"Irradiation Studies of Astrophysical Ice Analogues"

Philip D. Holtom

University College London

A Thesis submitted in partial fulfilment for the degree of Doctor of Philosophy

University Of London

2005

ProQuest LLC
789 East Eisenhower Parkway
P.O. Box 1346
Ann Arbor, MI 48106-1346

Abstract

In this thesis the formation of molecular species in cold icy mantles, typical of those in the interstellar medium (ISM) has been studied. The construction of an ultra high vacuum system for the formation and containment of these astrophysical ice analogues is described. The method of preparation of these ices is detailed and analysis methodologies are discussed.

VUV spectra of molecular ices (e.g. SO_2, CH_3NH_2, OCS) measured on the UV1 beam line of the Astrid Synchrotron facility at the University of Aarhus in Denmark, are presented. Molecular synthesis (e.g. CO_3, CO, H_2CO_3) induced by ion irradiated CO_2/H_2O ices using facilities at Queens University Belfast are also reported. In particular this thesis focuses on the irradiation studies of the binary ice mixture of Methylamine (CH_3NH_2) and Carbon Dioxide (CO_2). The results of irradiation of CH_3NH_2 and CO_2 binary ice mixtures by ultraviolet photons, and electrons are presented. The apparent production of the amino acid - glycine - in our irradiated samples is discussed together with possible production processes.

Acknowledgements

For Laura and for myself.

I would like to acknowledge all the people who have helped make this thesis possible

To Nigel Mason for his excellent supervision, encouragement , numerous trips abroad and for employing me in the first place. Grateful thanks to EPSRC for providing the funding for this PhD.

To all my friends at University College London and the Open University. In particular Anita Dawes, Robin Mukerji and Mike Davis who have helped immensely over the past 3 years. Also thanks to the former members of the group and everyone else at UCL and the OU who have helped me out. In particular Sam Eden, Paul Kendal, Paulo Limao Vieira, Ted Oldfield and the MAPS and glassblowing workshops at UCL.

Thanks to Jayesh Ramanlal, Paul Mealor, Leo Jenner and Dave Jenkins for keeping me amused with what must be getting on for 20,000+ e-mails and numerous pints of beer and cups of coffee over the past 7 years at UCL. To Jennifer Rosen and Cameron Adams for putting up with me and keeping in contact.

In Denmark: Søren Vrønning Hoffmann, Kate Andersen and Nykola Jones and everyone at ISA who helped us get through 3 week stretches underground for 15 hours a day. Particularly the unknown genius who installed the beer vending machine, where beer is cheaper than Coke....

In Belfast: Bob McCullough, and everyone in the Atomic And Molecular Physic Group at QUB for their hospitality and friendly and productive working atmosphere.

In Hawaii; Ralf Kaiser, Chris Bennett and Corry Jamison for their helpfulness and expertise.

Thanks also to my parents and family for support in particular to my fiancé Laura who has helped me get through this PhD !

Table of Contents

List of Figures

List of Tables

Chapter One

Introduction

"If it smells it's chemistry, if it crawls it's biology, if it doesn't work it's physics."
-- Anon.

The universal fascination with the origin of life has been a permanent fixture of mankind throughout history. Greek philosophers believed that life was inherent to matter, it appeared spontaneously (Brack 1998). It is only in recent times that we have started to understand our position in the universe and our own origins. This has lead to the new interdisciplinary subjects of Astrobiology and Astrochemisty. Their aim is to understand some of the fundamental processes in the universe that bring about the atoms and molecules we see around us and investigate how these simple building blocks can combine, eventually into complex organisms. There are two opposing views on where these prebiotoic molecules formed one which postulates that the molecules necessary to eventually create life were forged in the early universe and then seeded to Earth and the other that states the Earth itself was the site of formation of prebiotic molecules. The origins of life however are neither likely to be simple or clear cut, both of the two possibilities are equally valid and most likely played a role in the development of life on Earth. In this chapter we will give an overview of the interstellar medium and some of the topics of interest to astrobiology.

1.1 The interstellar medium (ISM)

The main focus of this thesis will be the investigation of the formation of molecules in the interstellar medium. We will present the design of an apparatus to simulate the conditions prevalent in the Interstellar Medium (ISM) (Chapter 3) and present our preliminary findings on the possible formation mechanisms of prebiotic and other important molecules in the ISM (Chapters 4-6) However initially it is necessary to give an overview of the Interstellar Medium and the discovery of molecules in space.

The interstellar medium is the vast expanse between the stars. It accounts for about a 10^{th} of the mass of our galaxy. 99 % of the interstellar medium is composed of gas and the most abundant gas by mass is hydrogen (approximately 75 %). The interstellar medium is extremely sparse and dilute, only 1 atom exists per cubic centimetre. The interstellar medium is not isotropic though. We see variations in all lines of sight in gas density. This results in clumps of matter known as clouds or nebulae.

1.2 Regions of the ISM

We will briefly define some of the common regions and features seen in the interstellar environment, in particular some of the nebulae in which astrophysical dust exists.

Emission nebulae occur around hot young stars. Stars are classified in terms of their spectral characteristics and luminosity An example from the Harvard Spectral classification scheme is given below. Table 1-1. Note that astronomers define HI as neutral hydrogen, HII as singly ionized hydrogen etc.

Table 1-1 The Harvard Spectral Classification Scheme for stellar objects

Spectral Type	Surface Temperature	Distinguishing Features
O	> 25,000K	H; HeI; HeII
B	10,000-25,000K	H; HeI; HeII absent
A	7,500-10,000K	H; CaII; HeI and HeII absent
F	6,000-7,500K	H; metals (CaII, Fe, etc)
G	5,000-6,000K	H; metals; some molecular species
K	3,500-5,000K	metals; some molecular species
M	< 3,500K	metals; molecular species
C	< 3,500K	metals; molecular species

Emission nebulae occur around hot stars, these OB type stars have a typical temperature in the range of 15,000 - 30,000 K (Table 1-1) and emit large amounts of ultraviolet radiation that heat the surrounding environment to high enough temperatures to ionise the surrounding hydrogen gas. In such a hot environment though there are few molecules of interest to astrobiology. Typical examples of such nebula are the M42 (Orion) and M20 (Trifid) nebulae. Figure 1-1

Figure 1-1 M20 (Trifid Nebula) showing the characteristic red glow of the H II regions of ionised hydrogen.

The characteristic red glow of the emission nebula is seen in Figure 1-1. The blue glow on the outer edge is caused by a reflection nebula.

Reflection Nebulae have a characteristic blue colour caused by light scattering from the interstellar dust particles. Blue light is scattered more effectively by dust particles due to their size. An example of a reflection nebular is seen around the Pleiades star cluster.

Absorption nebulae in contrast often appear dark, due to the low temperature of their environment (sometimes around 10 K). In this environment molecules can exist and dust grains can build up an icy mantle. An example of an absorption nebula is Barnard 68. (Di Francesco, Hogerheijde et al. 2002) report the abundances of $C_{18}O$, CS, NH_3, H_2CO, and C_3H_2) and one molecular ion, N_2H^+ in Barnard 68, showing the wide range of molecules present in an absorption nebula.

1.3 Interstellar Dust.

Recall that 99 % of the interstellar medium is the gas phase. There is however another component to the interstellar medium that we must consider, interstellar dust grains.

Look upon the stars and you will notice that the sky is mainly dark with the stars only covering a fraction of the sky. Considering the fact there are billions of stars along all lines of sight we could perhaps expect the night sky to be brighter than it is. Why then is the night sky so dim? The two possibilities are either there are no stars in these dark regions or the stars are being somehow obscured from our view. The latter of the two explanations is now understood to be true. Something is obscuring the starlight from us. This is due to the extinction of starlight by interstellar dust grains. These are small solid particles with a radius of about 10^{-7} m. Due to their small size they are capable of scatting the starlight from distant stars. In fact the total blocking of the light by interstellar dust grains can lead to "dark nebulae". A famous example of a dark nebula is the Horsehead nebula. Figure 1-2

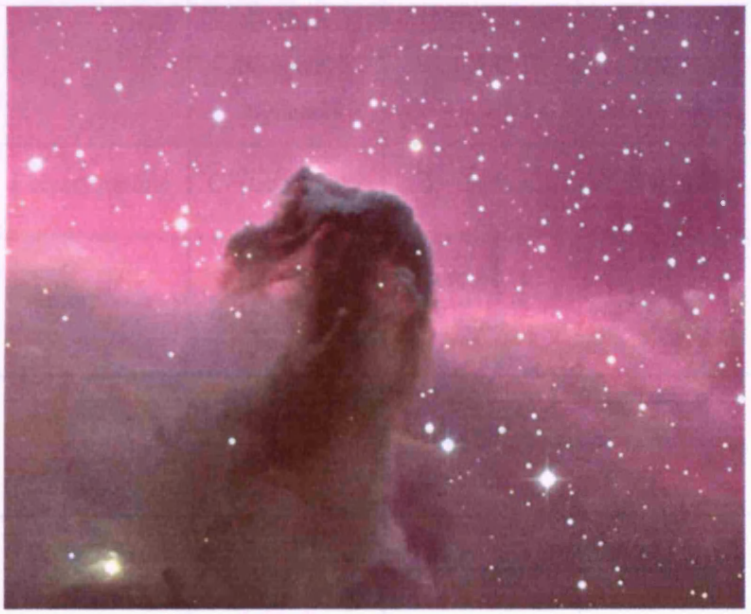

Figure 1-2 The Horsehead Nebula (Barnard 33) [1] showing the dark nebula against the background of emission nebulae IC 434 lit by Sigma Orionis (off screen)

[1] **Credit:** Nigel Sharp (NOAO), NSF; **Copyright:** AURA

Interstellar dust grains are thought to be carbonaceous or silicate in nature but we have yet to fully understand their true nature. We do know however that, despite their small size, they are most likely of immense importance in the creation of molecules in space. Interstellar dust grains exist in the cold environment of the ISM, temperatures of 10 K are common. At these low temperatures grains become sinks of molecules trapping most atoms and molecules that come into contact with the grain surface. This leads to a layer of ice building up on the grain surface. (Tielens and Allamandola 1987) give the composition of interstellar dust as in Table 1-2.

Table 1-2 Interstellar Dust Components (adapted from (Tielens and Allamandola 1987))

Component	Structure	Birth Site	Elemental Abundance	Rel. Volume	Spectral Signature
Silicates	Amorphous	O-Rich Giants & Nova	100 % Si 20 % O (Mg + Fe ?)	1	10,20 μm features
Graphite	Crystalline	C –Rich Giants (?)	> 25 % C	> 0.25	2200 Å Bump
Polycyclic Aromatic Hydrocarbons	Molecular Species	C- Rich Planetary Nebulae	1% C	0.01	3.3, 6.2, 7,7, 11.3 μm emission
Amorphous Carbon	Polycrystalline	C- Rich Giants	5 – 10 % C	~0.08	7.6 μm absorption
Icy Grain Mantles	Amorphous	Molecular Clouds	Up to 40 % C and I	Up to 2.8	3.1, 4.6, 6.0, 6.85, μm absorption
Organic Refractory Grain Mantles	Amorphous Polymer	Interstellar Medium,	24 % C, 6 % O	~0.8	3.4, 6.0 μm absorption
SiC	Crystalline	C-Rich Giants & Planetary Nebular	-	-	11.4 μm emission
MgS	Crystalline	C-Rich Giants & Planetary Nebular	-	-	30 μm emission

As well as being a site for molecule formation interstellar dust is also important as it plays a role in the heating and cooling mechanisms of clouds through the ejection of energetic photoelectrons, gas-grain collisions and the absorption and emission of radiation. (Tielens and Allamandola 1987).

Grain surface reactions play an important role in the astrochemistry of the ISM. We have already mentioned that grains become a sink for molecular material condensing upon them. Figure 1-3.

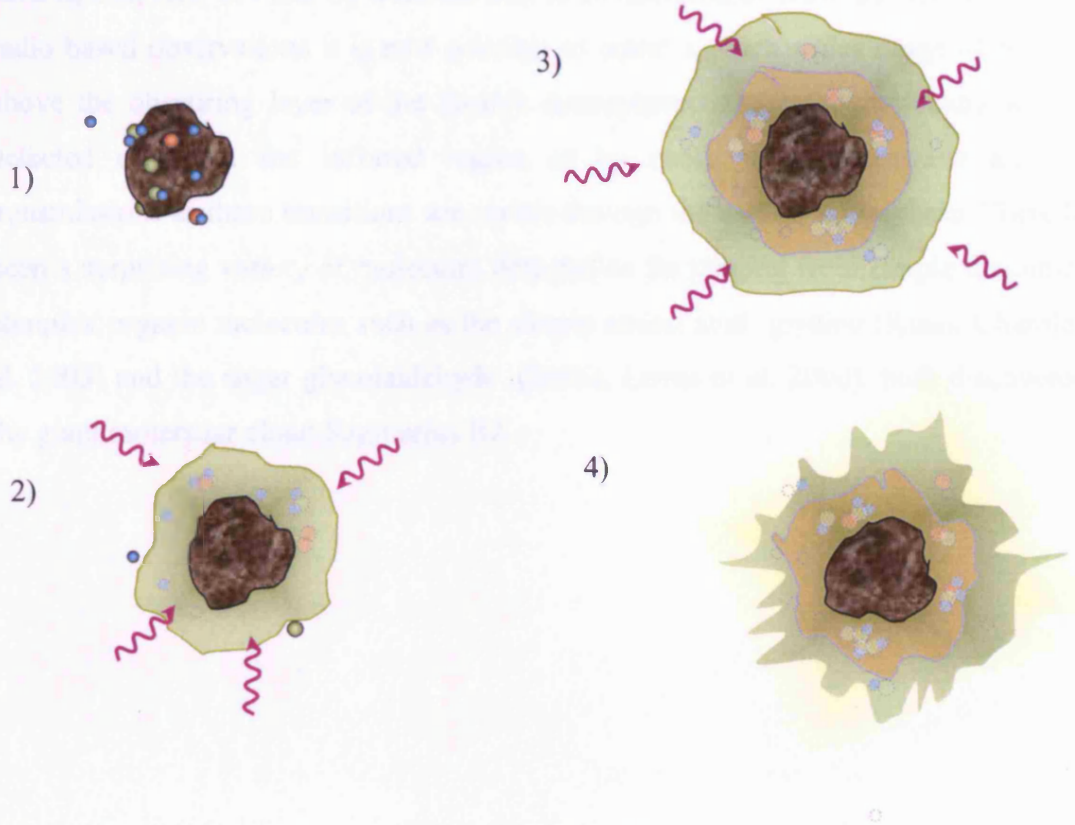

Figure 1-3 Schematic for grain surface reactions showing the formation of ice layers on a dust grain.

1) The solid grain cores begin to accrete molecular material from the ISM. An icy layer builds up.
2) The icy layer is exposed to irradiation events which modify the ice.
3) Further ice is accreted on top of earlier layers
4) Icy material and molecules are ejected from the ice into the gas phase through heating events such as shocks and grain–grain collisions.

1.4 Detection of molecules in the Interstellar medium

125 molecules are to date reported to have been observed in the interstellar medium and with improved detection methods more are being discovered each year. (Table 1-3) The very first molecules were discovered in the interstellar medium in the 1930's from the visible absorption of diffuse clouds. (Ehrenfreund and Charnley 2000). Simple radicals such as CH, OH, CN and C_2 were the first to be discovered. With the advent of modern radio based observations it is now possible to detect a much wider range of molecules above the obscuring layer of the Earth's atmosphere. Interstellar molecules are often detected either in the infrared region or by using their microwave and radio transmissions as these transitions are visible through the earth's atmosphere. There have been a surprising variety of molecules detected so far ranging from simple diatomics to complex organic molecules such as the simple amino acid glycine (Kuan, Charnley et al. 2003) and the sugar glycolaldehyde (Hollis, Lovas et al. 2000), both discovered in the giant molecular cloud Sagittarius B2.

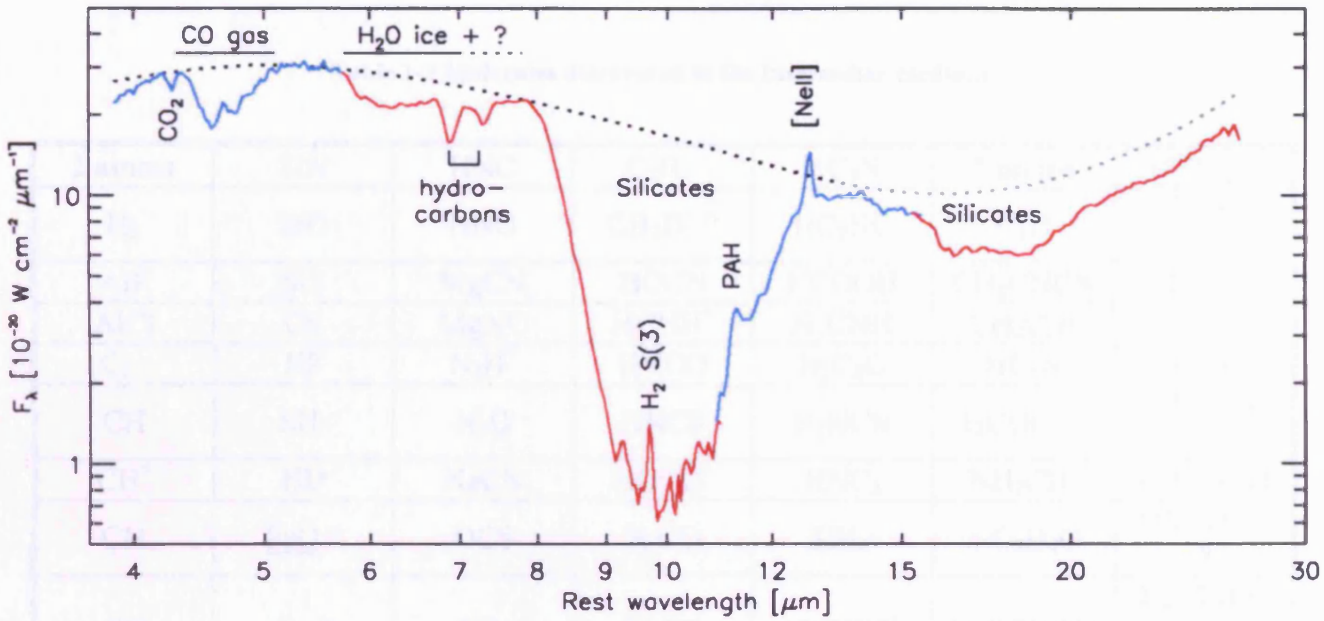

Figure 1-4 Spizter Telescope Infrared Spectrograph (IRS) low-resolution spectrum of the ultraluminous infrared galaxy IRAS F00183-7111 showing evidence for solid state features. [2]

Most of the molecules discovered are discovered in the gas phase and this makes up 99 % of the ISM but some molecules have also been discovered in the solid phase. Stars in the early phases of their life cycle provide the ideal method of observing solid phase ices. The infrared radiation given off by these Young Sellar Objects (YSO's) or Protostars allows us to detect the vibrational infrared transitions of molecules in the solid phase. For example (D'Hendecourt, Jourdain de Muizon et al. 1996) report the identification of the solid state features of H_2O, CO and CO_2 together with $^{13}CO_2$ and CH_4 towards the Protostellar object RAFGL 7009S from observations made using the ISO SWS (Short Wavelength spectrometer) instrument. Observations made using the Infrared Spectrograph instrument on Spizter are shown in Figure 1-4. Silicate and water ice features are clearly visible towards IRAS F00183-7111. In conclusion we can see that a wide array of molecules have been discovered in the astrophysical environment, both in the gas and solid phase. More progress is being made with new instruments on the detection of solid matter in the ISM. There is clearly a need for laboratory based work to simulate astrophysical ices and compare them to the spectra we observe in the interstellar medium.

[2] Taken from Spoon, H. W. W., L. Armus, *et al.* (2004). "Fire and Ice: Spitzer Infrared Spectrograph (IRS) Mid-Infrared Spectroscopy of IRAS F00183-7111." Astrophysical Journal Supplement Series **154**: 184-187.

Table 1-3 Molecules discovered in the Interstellar medium.

2 atoms	SiN	HNC	C_2H_2·	HC_3N	**7 atoms**	$(CH_3)_2O$
H_2	SiO	HNO	CH_2D^+ ?	HC_2NC	C_6H	CH_3CH_2OH
AlF	SiS	MgCN	HCCN	HCOOH	CH_2CHCN	HC_7N
AlCl	CS	MgNC	$HCNH^+$	H_2CNH	CH_3C_2H	C_8H
C_2··	HF	N_2H^+	HNCO	H_2C_2O	HC_5N	10 atoms
CH	SH·	N_2O	HNCS	H_2NCN	$HCOCH_3$	CH_3C_5N (?)
CH^+	HD	NaCN	$HOCO^+$	HNC_3	NH_2CH_3	$(CH_3)_2CO$
CN	FeO ?	OCS	H_2CO	SiH_4·	c-C_2H_4O	$(CH_2OH)_2$?
CO	O_2 ?	SO_2	H_2CN	H_2COH^+	H_2CCHOH	H_2NCH_2COOH Glycine ?
CO^+	**3 atoms**	c-SiC_2	H_2CS	**6 atoms**	**8 atoms**	CH_3CH_2CHO
CP	C_3·	CO_2·	H_3O^+	C_5H	CH_3C_3N	**11 atoms**
CSi	C_2H	NH_2	NH_3	l-H_2C_4	$HCOOCH_3$	HC_9N
HCl	C_2O	H^{3+}·	c-SiC_3	C_2H_4·	CH_3COOH	**12 atoms**
KCl	C_2S	H_2D^+, HD^{2+}	CH_3·	CH_3CN	C_7H	C_6H_6· (?)
NH	CH_2	SiCN	**5 atoms**	CH_3NC	H_2C_6	**13 atoms**
NO	HCN	AlNC	C_5·	CH_3OH	CH_2OHCHO	$HC_{11}N$
NS	HCO	**4 atoms**	C_4H	CH_3SH	l-HC_6H· (?)	
NaCl	HCO^+	c-C_3H	C_4Si	HC_3NH^+	CH_2CHCHO (?)	
OH	HCS^+	l-C_3H	l-C_3H_2	HC_2CHO	**9 atoms**	
PN	HOC^+	C_3N	c-C_3H_2	NH_2CHO	CH_3C_4H	
SO	H_2O	C_3O	CH_2CN	C_5N	CH_3CH_2CN	
SO^+	H_2S	C_3S	CH_4·	l-HC_4H*···· (?)		

1.5 The Solar System.

Besides the ices seen in the interstellar medium on the surface of dust grains there are ices located closer to home on the surfaces of planets in the solar system. Most of the outer planets that are far enough from the sun to sustain the temperatures needed for ice to form. It is worth pointing out at this stage that when we use the general term "ice" we do not necessarily mean water ice, H_2O. "Ice" in this context can be taken to mean any frozen gas.

1.5.1 Mars

Mars has always been of interest to those searching for clues to the origins of life. Currently there are two NASA rovers on the surface of Mars "Spirit" and "Opportunity". One of their main goals is to examine the surface of Mars to understand the history of water on Mars. As the Mars rovers examine the surface of the planet, the Mars global surveyor is currently imaging the entire planet from orbit. Mars is perhaps the one planet in the solar system closest to our own. It is believed it once held surface water like our own based on the features we have observed on the planet's surface. It has frozen polar ice caps like our own, but mainly composed of frozen carbon dioxide. The NASA Mars Odyssey orbiter though, reported that there may be evidence of water (H_2O) ice at both polar ice caps, trapped less than a meter below the surface. Images released from the Mars Odyssey satellite show just how abundant water on Mars may in fact be. Figure 1-5.

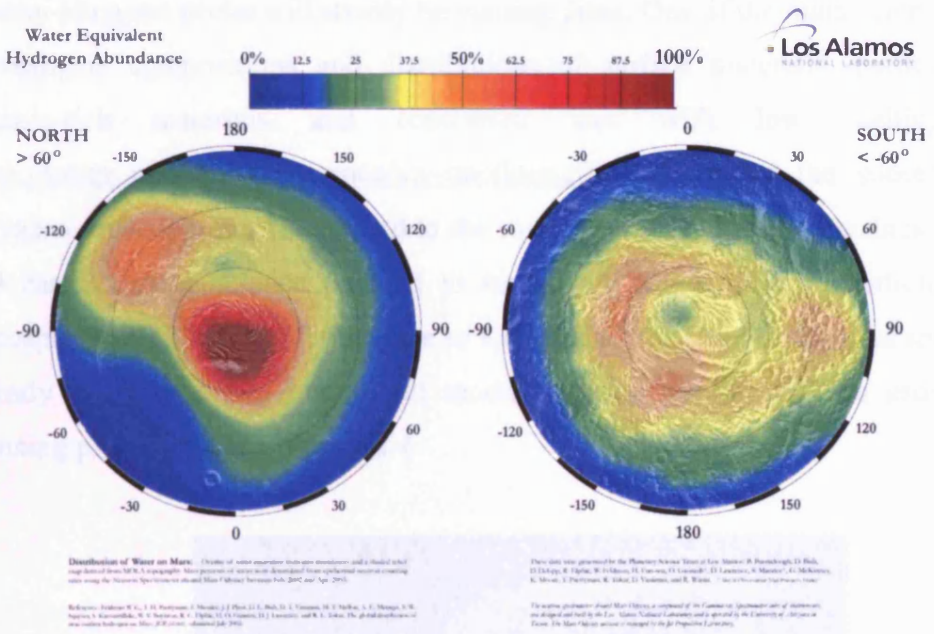

Figure 1-5 Map of Water Ice on Mars taken using the Neutron Spectrometer to locate deposits of water in the polar regions. Red shading indicates high density of water. [3]

1.5.2 The Gas Giants and their moons. Saturn, Titan, Jupiter and Io.

Although Mars has traditionally been the focus of a search for life in the solar system other candidates are promising. In particular the mysterious moon of Saturn, Titan. Discovered in 1655 by Dutch Astronomer Christiaan Huygens, it is the largest moon of Saturn and the second largest moon in the solar system. It has a thick atmosphere, with a temperature of 95 K and is predominantly made up of hydrocarbons and nitrogen compounds giving it a characteristic orange colour. The thick dense atmosphere has to date, made it impossible to penetrate the atmosphere and obtain information on the surface on the moon. The fact that Titan may have an atmosphere was first suggested in the 1900's and confirmed in 1944 by Kuiper who discovered evidence of methane in the atmosphere. Later space observations by Voyager revealed the presence of ethane, propane, acetylene, and other organic compounds. It is thought that this atmosphere may in fact be representative of the atmosphere on the early earth before early life forms began to increase the oxygen levels on the planet. In order to further study Titan the

[3] Image obtained from http://www.lanl.gov/worldview/news/photos/mars.shtml

Cassini-Huygens probe will shortly be visiting Titan. One of the main science aims is to "Investigate compositions and distributions of surface materials, particularly dark, organic-rich materials and condensed ices with low melting points." (http://saturn.jpl.nasa.gov/science/icy-satellites.cfm). On board the spacecraft is the Huygens probe which will descend to the surface of Titan through the thick atmosphere and carry a large science payload to investigate the exact composition of Titan's atmosphere and hopefully the surface as well. In fact the Cassni-Huygens spacecraft has already discovered two new small moons orbiting Saturn and has provided some stunning photos of Titan. Figure 1-6

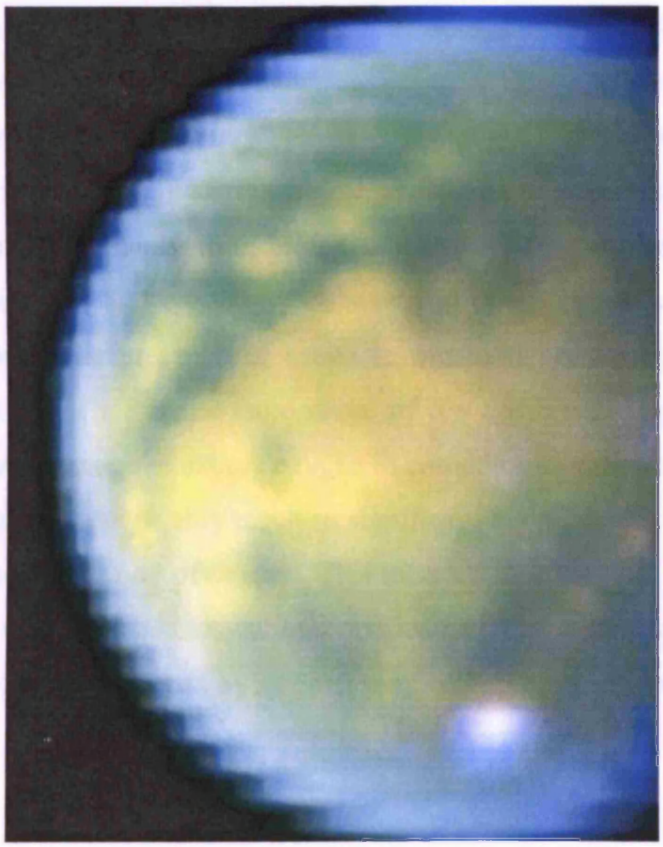

Figure 1-6 Titan false colour image by the Cassini-Huygens spacecraft. The yellow areas correspond to the hydrocarbon-rich regions, while the green areas are the icier regions. The bright white region is a methane cloud. [4]

The moons of Jupiter are also of interest, in particular Io which is the only currently volcanically active planet apart from the Earth. Io also has a thin atmosphere that is dominated by SO_2 emissions from the volcanoes. Unlike most of the outer solar system bodies which are dominated by H_2O ice such as Europa and Ganymede, Io appears to

[4] (Credits: NASA/JPL/University of Arizona)

mainly show a SO_2 dominated spectrum. ((Johnson and Quickenden 1997)). Traces of SO_2 have also been detected on the moon Europa, possibly caused by implantation of sulphur ions into water ice on the surface of the planet. Other moons of interest in the solar system are the moons of Saturn, Rhea and Dione. These satellites are rich in water ice, which also harbours trapped Ozone. ((Noll, Roush et al. 1997)). Rhea and Dione are exposed to particle irradiation from trapped ions in the magnetosphere of Saturn. Trapped oxygen molecules (O_2) in the ice may then form ozone, O_3 by exposure to charged particle and / or UV irradiation. Ozone is a significant molecule as it has been often cited as a candidate to identify planets with oxygen atmospheres in the search for Earth like extrasolar planets. It is quite difficult to directly detect oxygen as it is infrared inactive and any other detection methods such as detection of the 760 nm oxygen A-band become very difficult in an extrasolar environment due to the overwhelming light emitted from the star of any planetary system. It is thought that the presence of oxygen in a planetary atmosphere, for an Earth like planet, implies a continuous source of oxygen production (presumably from biological activity) (Leger, Pirre et al. 1994) as oxygen is a reactive gas and can easily be stored in other forms (e.g "locked up" in minerals and rocks). The presence of ozone in irradiated ices suggests oxygen as a source for this ozone. Thus if the atmosphere of the Earth was significantly derived from icy cometary impacts, the excess oxygen in cometary ices (implied because of the ozone detection) could conceivably result in significant ozone detection for a relatively low atmospheric concentration of oxygen. This means that it may not be sensible to use ozone as a tracer of a thick photosynthesis dominated oxygen atmosphere as even the small amount of oxygen delivered by a comet may be enough to allow enough ozone to be detected.

1.6 Comets.

Comets are the remnants of the early solar system formation. These "leftovers" of the early solar system are often described as "Dirty snowballs" A phrase coined by the late Professor Fred Whipple 50 years ago. Comets are important as they may be an indicator of the history of the physical and chemical processes that have occurred over the long history of the solar system. Comets consist of a nucleus, which is roughly a few kilometres across, composed of a mixture of ice and dust. Comets can either be short period comets that reside in or just outside of our solar system with orbital periods of ~200 years or less (for example the famous Halley's comet) or long period comets which have highly elongated orbits and orbital periods of up to 30 million years. For most of their lifetime these long period comets reside in the Oort cloud named after the Dutch astrometry Jan Oort who first proposed the existence of a reservoir of cometary materials at a great distance from the sun. For most of their lifetime comets are dark and unremarkable bodies, but as their orbits take them close to the sun they begin to warm and emit the characteristic "tails" most people associate with comets (in fact there are two tails, the ion tail and the dust tail from a comet) Figure 1-7.

Figure 1-7 Comet Hale-Bopp displaying dust and ion tails. The blue ion tail is caused by carbon monoxide ions and the white dust tail is produced from the disintegration of the comet nucleus. [5]

[5] ***Credit & Copyright: John Gleason (Celestial Images)***

In 1986 the Giotto probe, Europe's first deep space mission, was the first to capture pictures of a comets nucleus as it approached the comet Halley. In 2012 the ESA Rosetta lander will actually attempt to safely land on the nucleus of Comet 67P/Churyumov-Gerasimenk and probe the nucleus of the comet in situ.

During the long time that comets spend in the Oort cloud they will be subjected to long spells of irradiation by cosmic rays which may modify the chemical composition of the ice. Some theories of the origins of life on earth have postulated that comets striking the earth during the early bombardment phase of the earth may be the source of at least some of the Earths water content and possibly the origins of life. So a study of comets and in particular the irradiation of icy materials can be astobiologically relevant. For instance recent results reported by (Crovisier, Bockele-Morvan et al. 2004) show the comet Hale-Bopp to have over 22 molecules in the ice of the comet. The upper limits they derived for confirmed molecules and tentatively identified molecules are presented in Table 1-4.

Table 1-4 Summary of the molecular upper limits in comet Hale-Bopp (Taken from Crovisier, Bockele-Morvan et al. (2004))

Molecule	[X]/[H_2O]	Molecule	[X]/[H_2O]
H_2O	100	CH_2NH	<0.032
$(H_2O)_2$	<0.5	NH_2CN	<0.004
H_2O_2	<0.03	NH_2OH	<0.25
CH_3CCH	<0.045	HCNO	<0.0016
CH_2CO	<0.032	N_2O	<0.23
CH_3CHO	=0.025	NS	<0.01
c-C_2H_4O	<0.20	H_2CS	<0.04
C_2H_5OH	<0.10	CH_3SH	<0.05
CH_3OCH_3	<0.45	NaOH	<0.0003
CH_3COOH	<0.06	NaCl	<0.0008
CH_2OHCHO	<0.04	PH_3	<0.16
NH_2CH_2COOH I	<0.15	HDCO	<0.05
HC_5N	<0.003	CH_3OD	<0.07
C_2H_5CN	<0.010	CH_2DOH	<0.06
HDS	<0.3	NH_2D	<0.08

Another milestone in cometary research is the Stardust mission. A comet sample return mission devised by NASA. The Stardust spacecraft has collected material from the outgassing of the comet by trapping it in an "aerogel" which will then hopefully be safely returned to Earth in January 2006 for study. The comet Wild 2 was chosen as it is a relatively pristine comet. It only passed close to the Earth for the first time in 1974 and was perturbed by Jupiter, causing the comet to fall into a closer orbit. Having only made 5 trips around the sun Comet Wild 2 is a prefect comet to study as it is relatively unprocessed by interaction with solar radiation. Thus it should retain some of the characteristics of the early solar system. The returned material will allow us to study some of the characteristics of material formed early on and perhaps even outside the solar system, perhaps enabling us to determine the true composition of interstellar dust grains. Also the composition of a pristine comet like Wild 2 could shed light on some of the volatiles delivered to Earth in the early stages of its life cycle by comets, essential information to astrobiology and the determination of the origins of life.

Chapter Two

An Introduction To Astrochemistry and Molecular Structure.

If all else fails, immortality can always be assured by spectacular error.
-- John Kenneth Galbraith

2.1 Introduction

This chapter provides a background to the interdisciplinary subjects of Astrochemistry and astrobiology. We will also describe the theory underlying the experimental techniques of infrared and UV spectroscopy used in our experiments to monitor the molecular formation in ice. We will begin with an overview of possible mechanisms for the formation of molecules in the interstellar medium followed by a discussion on the detection of these molecules.

2.2 The Interstellar medium and chemical reactions at low temperatures

Over 125 molecules have so far been discovered in the interstellar medium (ISM) (Chapter 1) including many complex hydrocarbons and long chain molecules. For example the simplest amino acid glycine has been recently detected in the ISM (Kuan, Charnley et al. 2003). How do these complex organic molecules come to exist in the interstellar medium in the first place? Gas phase reaction chemistry can not account for the diversity and quantity of the observed constituents of the ISM. For instance even the simplest molecule H_2 can not form effectively in the gas phase at the low number densities present in the ISM. Three body reactions can stabilize the excited newly formed H_2 molecule but in most cases in the low densities of the ISM the molecule will

dissociated again. The simple gas phase reaction H+H $\rightarrow$ H_2 can not explain the observed abundances of H_2, instead dust grain surfaces can act as a catalyst to allow the newly formed H_2 molecule to release energy and stabilize. See for example, (Cazaux and Tielens 2004).

The interstellar medium is a diverse environment (See Chapter 1) containing wide fluctuations in temperature and density. One of the key components of the interstellar medium are dust grains. It is believed that these dust grains are the source of the molecules observed in the interstellar medium. Ice covered dust grains can act as a surface upon which to catalyse the reactions of molecules and as the icy material is exposed to solar radiation more photon induced chemistry becomes possible.
Interstellar dust grains are thought to be of a carbonaceous or silicate nature. In the ISM the typical grain temperature is of the order of 10 K. Hence when an atom or molecule strikes the grain they will stick to the grain. If we consider the rate of absorption of a background gas onto a substrate we obtain equation (1.1)

$$\text{Rate} = SnP/(2\pi mk_bT)^{1/2} \qquad (1.1)$$

where S is the sticking coefficient, n is the surface density of the absorbate layer (m^{-2}) P is the pressure (Pa), m is the mass of the molecule (kg) k_b is the Boltzmann constant and T is the temperature (K). (Collings, Dever et al. 2002) It is generally assumed that at low temperatures (10 K) the sticking coefficient is unity for all but the lightest species. (H_2, H and He).

Once a layer of ice has accreted onto the grain surface then it is possible for chemical reactions to occur within the ice as more diverse molecules attach to the grain and the grain is exposed to irradiation from stellar sources. However at such low temperatures and low number densities, the chemistry in the interstellar environment is quite different to that occurring on earth. We therefore need to consider certain new factors in order to determine if a chemical reaction is possible in such a cold, sparse environment. In particular we must understand the kinetics of a reaction (how "fast" a reaction will proceed) and secondly the reaction dynamics, for example the entrance and exit barriers involved in any reaction.

As a simple example we will consider a bimolecular reaction taking place at 10 K as illustrated in (1.2). Reactants A and BC combine to form AB and C as products.

$$A + BC \rightarrow AB + C \qquad (1.2)$$

The potential energy surface of the reaction is illustrated in Figure 2-1

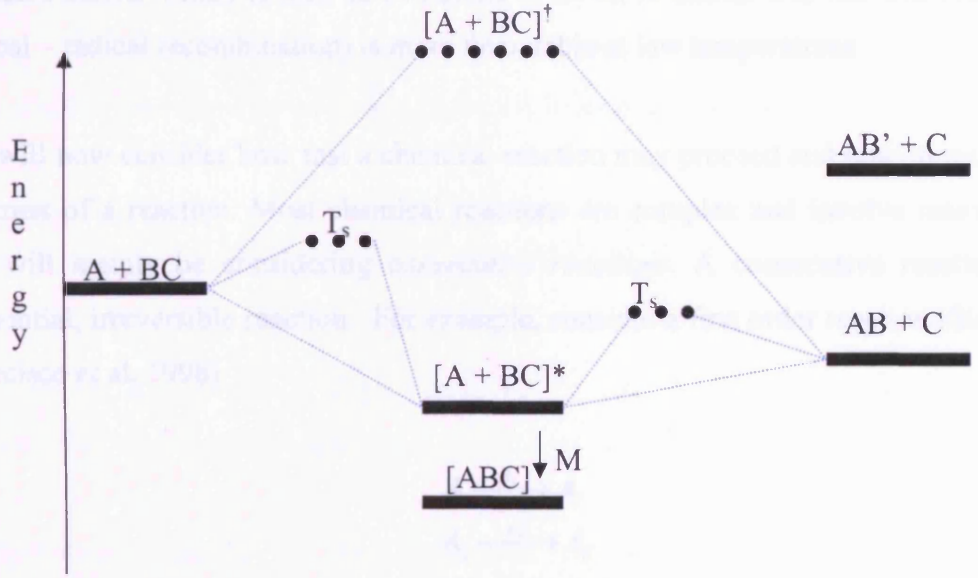

Figure 2-1 Potential Energy Surface of a Bimolecular reaction (adapted from (Kaiser 2002)) Transition states are indicated by dotted lines.

Considering the energetics of such a reaction two cases are apparent. Either the free energy of the products is lower than that of the reactants, the *exoergic* case or the free energy of the products is greater than that of the reactants, the *endoergic* case. The reaction may be *direct* or *indirect*. (Figure 2-1) A direct reaction will involve a transition state $[A + BC]^{\dagger}$. An indirect reaction will proceed via an intermediate [A +BC]*. There can be an exit or entrance barrier involved as shown in Figure 2-1. Due to energy and momentum conservation the free reaction energy can be channelled into rotational, vibronic or electronic energy. In the solid phase the intermediate product can also be stabilised as the vibrational modes can be coupled to phonon excitations in the

crystal stabilising the intermediate at low temperatures and making them spectroscopically detectable. An alternative scenario is that in a gas phase environment with a larger number density the intermediate can collide with another molecule M. This can channel the energy of the intermediate into the third body again stabilising the intermediate forming [ABC].

From this simple model we can say that in general for a reaction to occur at low temperatures we would expect the reaction to be exoergic and to have a negligible entrance barrier. This precludes direct reactions as these often involve a significant entrance barrier which is hard to overcome at 10 K. A barrier-less reaction (such as a radical – radical recombination) is more favourable at low temperatures.

We will now consider how fast a chemical reaction may proceed and how to model the progress of a reaction. Most chemical reactions are complex and involve many steps. We will mainly be considering *consecutive reactions.* A consecutive reaction is a sequential, irreversible reaction. For example, consider a first order reaction (Steinfeld, Francisco et al. 1998)

$$\begin{aligned} A_1 &\xrightarrow{k_1} A_2 \\ A_2 &\xrightarrow{k2} A_3 \end{aligned} \tag{1.3}$$

The values k_1 and k_2 are the *rate constants* for the reaction.

This is described by the rate expressions

$$\begin{aligned} \frac{d[A_1]}{dt} &= -k_1[A_1] \\ \frac{d[A_2]}{dt} &= k_1[A_1] - k_2[A_2] \\ \frac{d[A_3]}{dt} &= k_2[A_2] \end{aligned} \tag{1.4}$$

After integration we obtain the concentration of A_1 to be

$$[A_1] = [A_1]_0 e^{-k_1 t} \tag{1.5}$$

Thus the concentration of the initial reactant will decay as an exponential as the reaction proceeds.

The concentration of the product A_2 may then be obtained by solving the 2nd equation in (1.4). This leads to (1.6)

$$A_2 = \frac{k_1[A_1]_0}{k_2 - k_1}\left(e^{-k_1 t} - e^{-k_2 t}\right) \tag{1.6}$$

By conservation of mass we can obtain the expression for the concentration of A_3

$$[A_3] = [A_1]_0\left(1 - \frac{k_2}{k_2 - k_1}e^{-k_1 t} + \frac{k_1}{k_2 - k_1}e^{-k_2 t}\right) \tag{1.7}$$

This allows us to profile a simple chemical reaction and estimate how fast it will proceed from the observed quantities of the reactants and products.

Cosmic dust grains do not exist in a static environment, in dense clouds they are protected from the effects of UV irradiation which protects any synthesised molecules but in the interstellar medium dust grains may encounter UV photons and cosmic ray bombardment. This bombardment may induce further chemistry within the ice mantle. An ultraviolet photon may break a single bond of a molecule in the ice surface. Cosmic rays can penetrate further into the ice and can deposit up to 1 MeV inside the ice mantle and can generate highly reactive suprathermal (atoms with enough kinetic energy to be out of thermal equilibrium with the cold 10 K surroundings) carbon and oxygen particles (Kaiser 2002). Secondary electrons formed by ion irradiation can also play a role in the formation of new species. Newly formed species on the grain surfaces can then be released into the interstellar medium in a number of ways. (1) molecules may be directly ejected into the gas phase after formation (2) grain heating may release molecules into the ISM. Heating may be in the form of solar radation or grain collisions and shockwaves which heat the dust grains (3) photodesorption and cosmic ray desorption may free particles from the ice matrix.

From this overview of the possible chemical reactions in the interstellar medium we will now consider the structure of the molecules we will be observing. In this thesis we report results on the study of molecular formation in ice surfaces by photon, ion and electron induced processes. Detection of the product species is by infrared spectroscopy and UV spectroscopy. We therefore need to discuss the spectroscopy and structure of the molecules we detect.

2.3 Molecular Structure.

Before a discussion of the theory behind the spectroscopic observations upon which this thesis is based it is useful to briefly review the properties of atoms and molecules.

.

2.3.1 Atoms and Molecules

Quantum mechanics provides us with a description of an atom that allows us to visualise and predict the way that atoms and electrons behave. At first we will simply consider a hydrogen atom. In quantum mechanics an electron can be described by a *wave function,* ψ, which is found by solving the Schrödinger equation (1.8)

$$\frac{\partial^2\Psi}{\partial x^2}+\frac{\partial^2\Psi}{\partial y^2}+\frac{\partial^2\Psi}{\partial z^2}+\frac{8\pi^2 m}{h^2}(E-V)\Psi=0 \qquad (1.8)$$

The quantity ψ in fact represents the amplitude of the electron wave. The quantity of $\psi^*\psi$ dx represents the probability of finding the electron in a region of space dx. The solutions of this equation result in a series of quantum numbers. These are given as n, l, m and s. These quantum numbers are the basis for of a set of selection rules that govern the properties of an electron. Table 2-1 lists the values that the quantum numbers are allowed to take.

Table 2-1 Quantum Numbers

Quantum Number	Description	Allowed Values
n	Principle Quantum Number	1,2,3,4,... ∞
l	Angular Momentum	$l \leq (n-1)$
m	Magnetic	$m \leq \pm (l-1)$
s	Spin	± ½

Thus the principle quantum number n, describes the "Shell" of an electron orbital. defining its energy and size from the nucleus. This shell can be further divided into subshells of l and m. For historical reasons the quantum numbers of l are often written s,p,d or f for values of l=0,1,2,3 respectively. This gives us the familiar description of orbitals shown in Table 2-2

Table 2-2 The first atomic orbitals and their descriptions

Principle Quantum Number (n)	allowed *l* (0 to n-1)	Description
1	0	1s
2	0	2s
	1	2p
3	0	3s
	1	3p
	2	3d
4	0	4s
	1	4p
	2	4d
	3	4f

But what do these orbital actually mean? How can they be visualised? The Schrödinger equation results in a number of 3 dimensional "orbitals" that an electron cloud can occupy. Each of these has a distinct shape. The simplest of these is the 1s orbital. The 1s orbital has a spherical symmetry. The same applies to the 2s orbital and indeed all s orbitals. The 2s orbital has a spherically symmetric shape but is further away from the

nucleus than the 1s orbital. From Table 2-2 we see that if n=2 the value of l can be 0 or 1. If l= 1 we have a p orbital. Due to the considerations of the m quantum number the p orbital can have 3 degenerate states each orientated around the 3 axis as illustrated in Figure 2-2

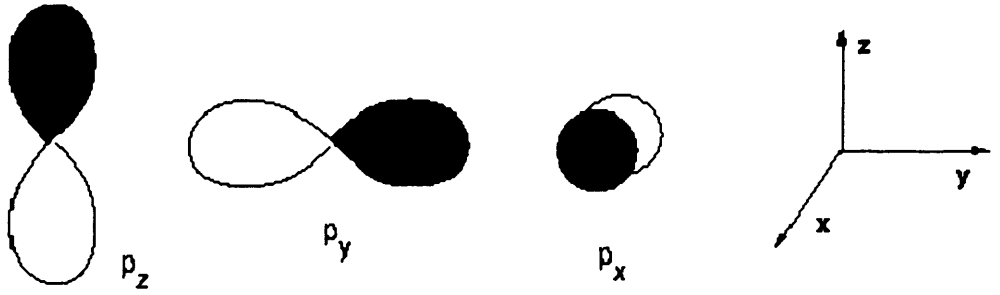

Figure 2-2 Diagrammatic representation of P orbitals.

The 3s and 3p orbitals likewise have a similar geometry to that of the 2s and 2p orbitals.

We have not yet considered the electron spin quantum number and the role it plays in determining electron position. Why don't all electrons simply occupy the lowest energy 1s orbital? The answer to this question lies in the spin quantum number and the Pauli Exclusion principle which states "Wave functions must be antisymmetric with respect to particle exchange" or " no two electrons can have the same set of quantum numbers" Thus only 2 electrons can occupy any orbital, one with spin +½ ,the other with spin -½. So if we follow the periodic table we can see that the electrons occupy the levels as shown in Table 2-3 as they sequentially fill the lowest energy orbital available

Table 2-3 Electronic Structure of the first elements of the periodic table

Atom	Electron Structure	Atom	Electron Structure
H	1s	C	$1s^2\ 2s^2\ 2p^2$
He	$1s^2$	N	$1s^2\ 2s^2\ 2p^3$
Li	$1s^2\ 2s$	O	$1s^2\ 2s^2\ 2p^4$
Be	$1s^2\ 2s^2$	F	$1s^2\ 2s^2\ 2p^5$
B	$1s^2\ 2s^2\ 2p$	Ne	$1s^2\ 2s^2\ 2p^6$

Note that convention dictates that the superscript indicates the number of electrons. For example fluorine has 5 electrons in the p orbitals. Electrons will always occupy empty orbitals before pairing up with other electrons. This is known as Hund's Rule. The full structure of Fluorine can therefore be written $1s^2\ 2s^2\ 2p_x^{\ 2}\ 2p_y^{\ 2}\ 2p_z^{\ 1}$. Hund's rule also gives rise to *Singlet* and *Triplet* states. A singlet state is a state with zero total spin angular momentum. A triplet state has a non zero spin total spin. For example the ground state of He is $1s^2$, the total spin angular momentum is zero so it is a singlet state. If we promote an electron to the 2s orbital we obtain a triplet state $1s^1\ 2s^1$ where the two electrons have parallel spin.

In order to describe the much more complex case of electrons in molecules we need to invoke the "Born-Oppenheimer Approximation." Here we separate the wave function into two parts, one describing the nuclei and one the electrons. With molecules we also have to consider that the energy of the molecule depends on the relative position of its nuclei. A typical potential energy curve is shown in Figure 2-3

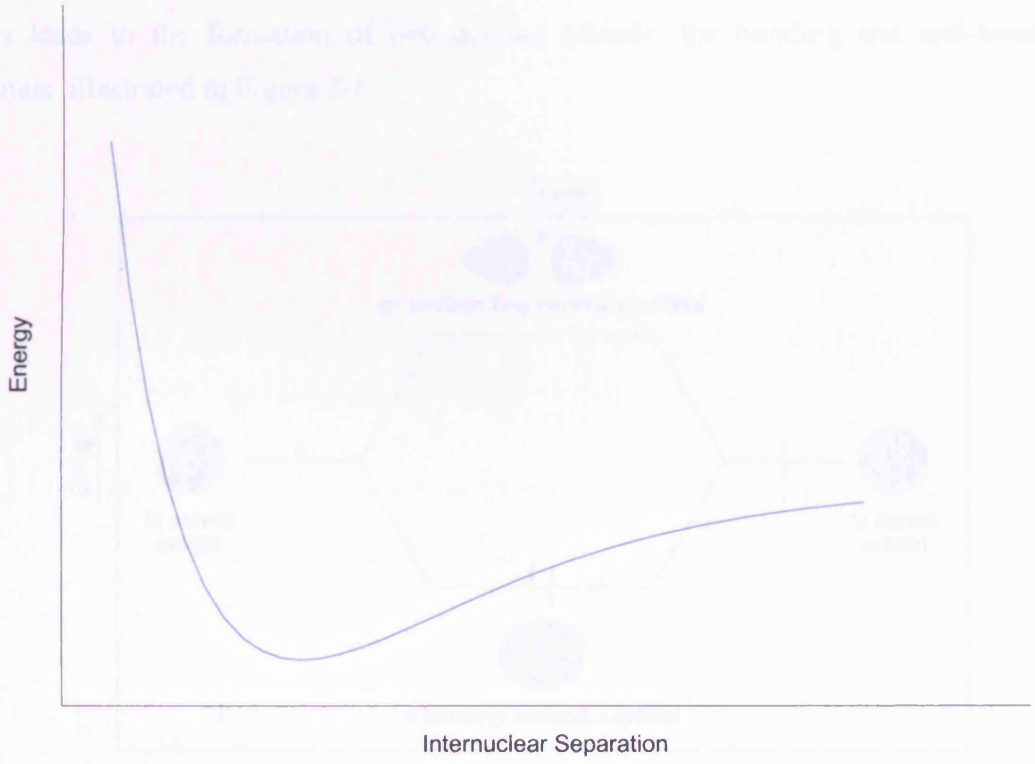

Figure 2-3 A Typical Molecular Potential Energy Curve (also known as a Morse Curve)

These potential energy curves are useful when visualising electronic transitions within diatomic molecules or atoms (Section 2.5.3)

The shape of a molecular orbital can be inferred from the *linear combination of atomic orbitals* (LCAO) approximation. In practice the approximate form of a molecular orbital can be obtained from the sums and differences of the atomic orbitals of the constituent atoms. (See (Banwell 1983) for a complete description). For example for a diatomic we can form molecular orbitals via two methods

$$\psi_{mo} = \psi_1 + \psi_2$$
$$\psi_{mo} = \psi_1 - \psi_2 \qquad (1.9)$$

For the hydrogen atom forming H_2 we have then

$$\psi_{H_2} = \psi_{1s} + \psi_{1s}$$
$$\text{or} \qquad (1.10)$$
$$\psi_{H_2} = \psi_{1s} - \psi_{1s}$$

This leads to the formation of two distinct orbitals, the bonding and anti-bonding orbitals illustrated in Figure 2-4

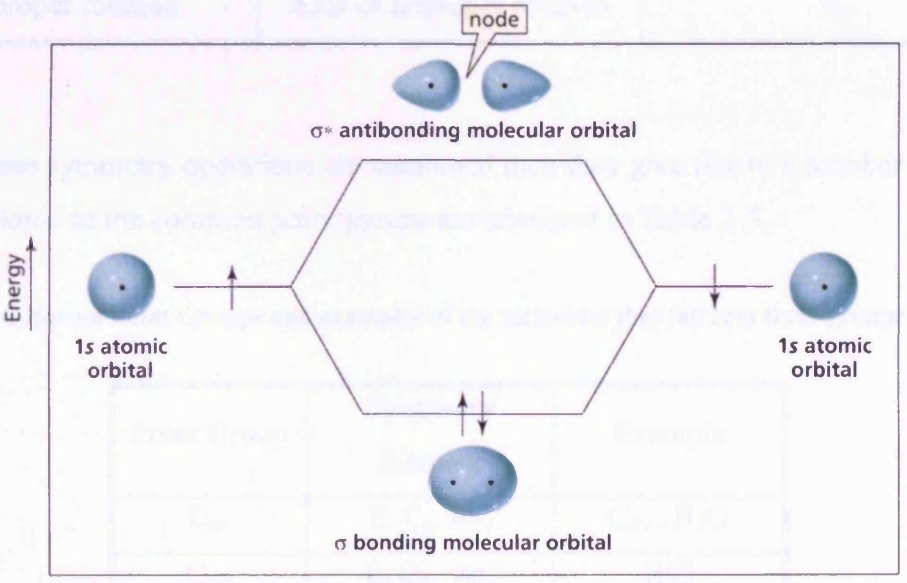

Figure 2-4 Formation of bonding and anti-bonding orbitals in Hydrogen [6]

[6] Reproduced from http://wps.prenhall.com/wps/media/objects/724/741576/chapter_01.html, Organic Chemistry, 4th Edition, P.Y. Bruice, Prentice-Hall Inc.

The bonding orbital is given the label σ. For the anti-bonding σ^* orbital we have a node of $\psi_{H2} = 0$ which leads to a higher energy and less favourable configuration.

2.4 Molecular Symmetry

Molecule's are often categorised in terms of their symmetry. To categorise a molecule in terms of its symmetry we assign it a point group. This point group is based upon a molecules response to a number of symmetry operations. This is a mathematical operation on the object that leaves it apparently unchanged. The 5 main operations are listed in Table 2-4

Table 2-4 Some Common Symmetry Operations

Symmetry Operation	Symmetry Element	Symbol
Identity	Whole body	E
n-fold rotation	n-fold axis of symmetry	C_n
Reflection	Plane of symmetry	$\sigma_v, \sigma_h, \sigma_d$
Inversion	Centre of symmetry	i
Improper rotation	Axis of improper rotation	S_n

When these symmetry operations are combined then they give rise to a number of point groups. Some of the common point groups are tabulated in Table 2-5

Table 2-5 Common Point Groups and examples of the molecules that fall into these groups

Point Group	Symmetry Element	Example
C_{nv}	E, C_n, $n\sigma_v$	C_{2v} - H_2O
$C_{\infty v}$	E, C_n, $\infty\sigma_v$	HCl
T_d	E,C_2, C_3, S_4, σ^d	CH_4, SiH_4
$D_{\infty h}$	E, *i*, $C_{\infty v}$, $\infty\sigma_v$,	CO_2

There are many more point groups than listed in Table 2-5. A full list can be found in (Atkins 1998)

2.5 UV and IR Spectroscopy of molecular Systems

In this section we will provide a theoretical overview of infrared and UV spectroscopy as applicable to the research described in this thesis.

2.5.1 Electromagnetic Radiation.

Both ultraviolet and infrared spectroscopy rely on electromagnetic radiation (Figure 2-5) as a medium to probe the properties of molecules.

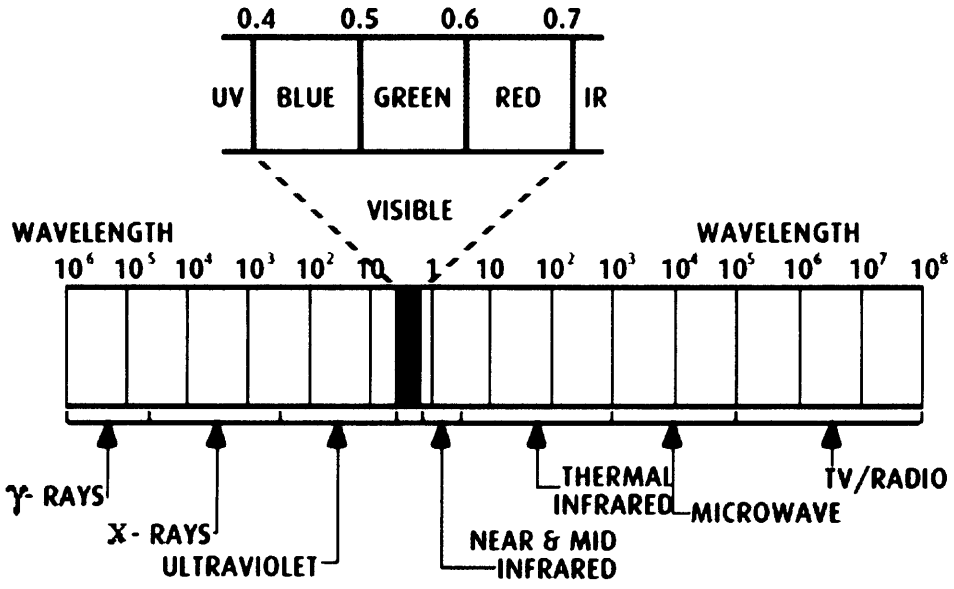

Figure 2-5 The Electromagnetic Spectrum

Atoms and molecules may absorb or emit radiation depending on the circumstances. This absorption or emission of radiation always happens in a quantised fashion. The energy of an absorbed or emitted photon is given by (1.11)

$$E = h\upsilon \tag{1.11}$$

where h is the Plank Constant ($h=6.626 \times 10^{-34}$ Js) and ν is the frequency of the photon.

2.5.2 Infrared spectroscopy

One of the most common techniques used for identifying molecules in low temperature environments in the laboratory is infrared spectroscopy. The infrared region extends from the "Near IR" 10,000-4,000 cm^{-1} (1-2.5 μm) to the "Mid IR" 4000-400 cm^{-1}(2.5-25 μm) and the "Far IR" 400 40 cm^{-1} (25 -250 μm)

At temperatures above 0 K molecules are able to rotate and vibrate. Though it should be noted that 0 K can never be reached due to the zero point energy of the molecule. Considering the case of the solid phase at 10 K we find that most molecular rotations are hindered due to the bonding and interactions between molecules but molecular vibrations are still free to occur. In the simplified case these vibrations are often thought of as being analogous to a system of masses joined by a spring. The bonds may be stretched and compressed with the frequency of these motions lying in the infrared, resulting in the characteristic absorption of infrared light by molecules containing a dipole moment. For example if we consider a non-linear polyatomic molecule such as H_2O, water, we have a total of 3N-6 vibrational modes possible where N is the number of atoms. (A linear molecule will possess 3N-5 modes) For water we have a total of 3 possible *fundamental* vibrations. (Figure 2-6)

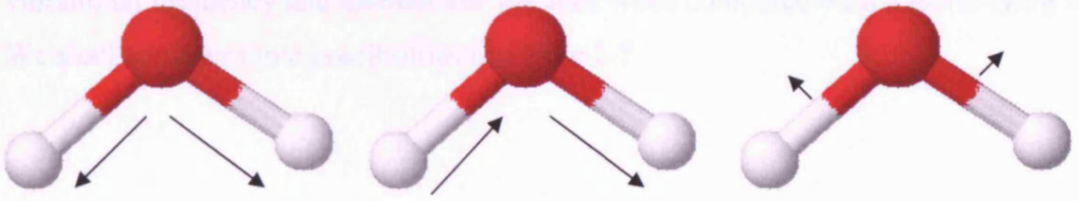

(a) symmetric stretch (b) asymmetric stretching (c) Bending

Figure 2-6 Vibrational modes of water

Each of these vibrations will cause a change in the dipole moment of the molecule. A large change will naturally give rise to a large absorption. The intensity of these infrared transitions is given in terms of an *infrared absorption coefficient*, usually given the symbol, A.

For each molecule there is a characteristic and unique infrared spectrum that can be used to identify the molecule and or some of the components of the molecule, i.e. each molecules has a "fingerprint". It should be noted that the infrared spectra of molecules may alter depending on its phase i.e. gas, liquid or solid phases and the solid phase in particular will be discussed later (Section 2.6)

2.5.3 UV Spectroscopy.

Ultraviolet spectroscopy involves transitions of the electrons within the outer orbitals of the molecule. Ultraviolet spectroscopy uses the wavelength range from the "Near Ultraviolet" from 380-200 nm moving into the Vacuum Ultraviolet range above 200 nm. Electrons occupy molecular orbitals and when an atom or molecule absorbs a photon an electron can be promoted to a higher energy atomic orbital. As the molecule relaxes photon emission may occur. These transitions occur in the ultraviolet energy range. One of the basic principles of electronic spectroscopy is the Franck-Condon Principle. This states that *"an electronic transition takes place so rapidly that a vibrating molecule does not change its internuclear distance appreciably during the transition"* The energy of a diatomic molecule can be represented by a Morse curve (section 2.3). If it undergoes a transition into an upper electronic state that is stable (with respect to the dissociation of the molecule) then we can represent that upper state by another Morse curve. This new upper state may have different parameters such as vibrational frequency and internuclear distance when compared with a lower lying state. We shall consider three possibilities in Figure 2-7

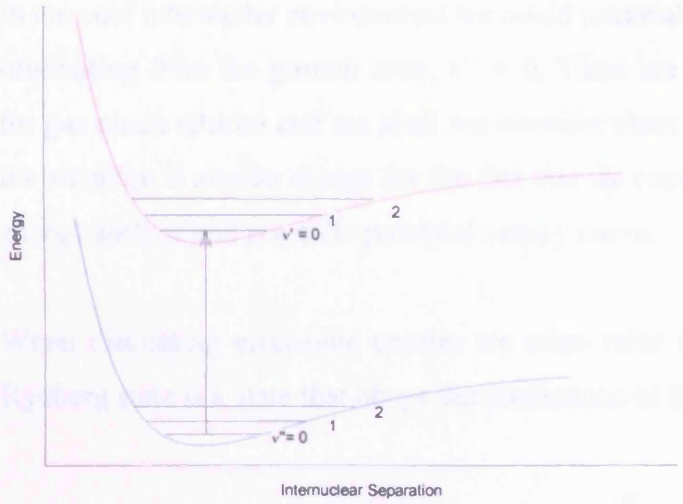

(a) Upper electronic state with the same internuclear distance and lower electronic (or ground) state.

The Frank-Condon principle suggests a vertical transition will occur in this case. This gives us a strong 0-0 transition.

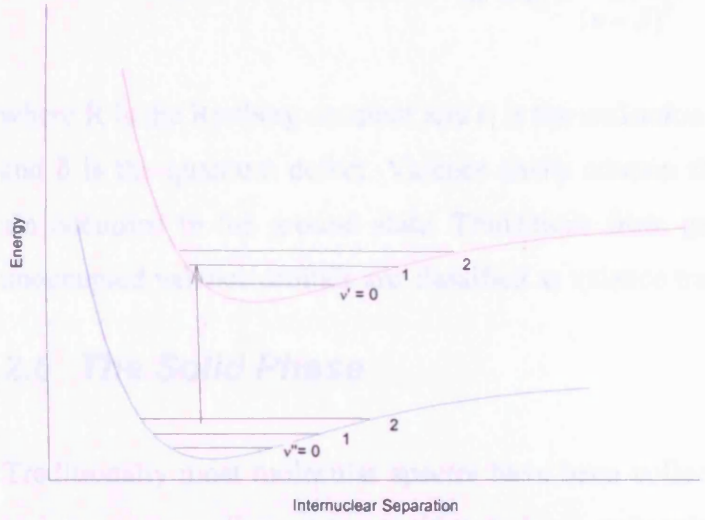

(b) A slightly increased internuclear separation in the upper state or lower/ground state.

In this case a vertical transition to the upper state will result in a strong transition to an higher upper vibrationally excited state.

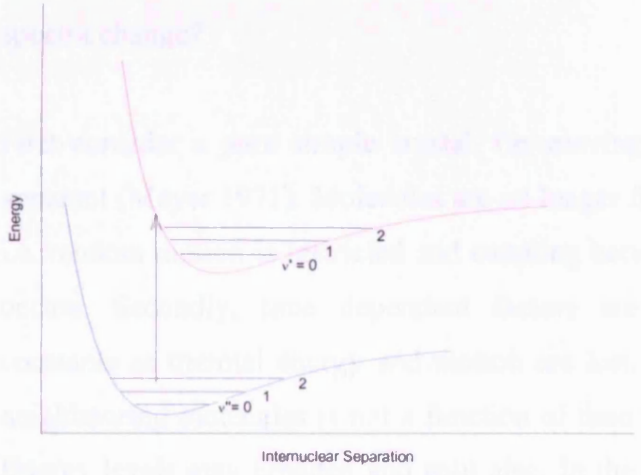

(c) Internuclear distance of the upper state is considerably greater than the ground state.

In this case transitions occur to a high value of v'. The molecule has an energy in excess of the dissociation threshold and the upper state is free to dissociate.

Figure 2-7 Application of the Frank-Condon Principle (adapted from (Banwell 1983))

In the cold interstellar environment we could reasonably only expect transitions to occur originating from the ground state, $v'' = 0$. There are unlikely to be any "hot bands" as for gas phase spectra and we shall not consider them further. For polyatomic molecules the situation is similar except for the fact that we consider a multi dimensional potential energy surface and not a 2D potential energy curve.

When discussing electronic spectra we often refer to *Rydberg* and *Valence* states. A Rydberg state is a state that obeys the predictions of the Rydberg formula. (1.12)

$$h\nu = \varepsilon_i - \frac{R}{(n-\delta)^2} \tag{1.12}$$

where R is the Rydberg constant and ϵ_i is the ionisation potential. n is an integer number and δ is the quantum defect. Valence shells contain the highest energy orbitals which are occupied in the ground state. Transitions from ground state valence orbitals into unoccupied valence orbitals are classified as valence transitions.

2.6 The Solid Phase

Traditionally most molecular spectra have been collected in the gas phase. Cryogenic techniques now allow us to consider studying molecular spectra in the solid phase or in an inert gas matrix. But what are the effects of freezing a gas sample? How will the spectra change?

First consider a pure simple crystal. On moving to the solid phase two changes are apparent (Meyer 1971). Molecules are no longer free to move in an unrestricted fashion i.e. random motion is restricted and coupling between molecular motion and excitation occurs. Secondly, time dependant factors are replaced by symmetry-determined constants as thermal energy and motion are lost. This means as the distance between neighbouring molecules is not a function of time then lines sharpen in the solid phase. Energy levels may broaden and split also. In the far infrared regions lattice vibrations may be observed (typically below 150 cm^{-1}) as we will not be observing in this region they will not be a further consideration however. We also note (Meyer 1971) that we expect electronic transitions to become red shifted from the gas phase and forbidden transitions may become enhanced.

When we consider infrared observations in the solid phase it is apparently that there is no rotational structure. Molecules are not free to rotate at temperatures in the region of 10 K and so the familiar P, Q and R branches seen in gas phase spectra collapse and appear as one broad band.

Spectral lines are observed as broad bands not the narrow lines we would expect for a transition from a single energy. This is due the phenomena of "line broadening".
The natural line width of a gaseous transition is determined by its lifetime. This lifetime is typically of the order of magnitude of 10^{-8} seconds leading to a line width of around 10^{-4} nm. (Meyer 1971; Banwell 1983) These lines are naturally broadened by a number of factors such as thermal motion, Doppler broadening, pre-dissociation, collisional broadening and molecular broadening. Collisional broadening mainly occurs in gases and liquids due to molecular motion. In a solid molecule such motion is restricted so collisional broadening is therefore restricted, resulting in sharper lines in the solid phase. Doppler broadening occurs due to the movement of the molecules. The Doppler effect causes a shift in the frequency as the source moves away or towards an observer related to the velocity of the molecule.

In the solid phase molecules interact with each other and their surroundings to a much greater degree than in the gas phase. This interaction can have an effect on the vibrations of a molecule which results in a shift in the vibrational position. The stronger the interaction with neighbouring species the larger the line shift. For instance the CO fundamental occurs at 2138 cm^{-1} which is 5 cm^{-1} lower than the gas phase value. In a mixture of CO, CH_3OH, NH_3, H_2O the CO peak is shifted to 2137 cm^{-1} (Tielens and Allamandola 1987) This suggests the CO does not have much interaction with the other molecules in the ice matrix. For molecules that interact strongly though such as water the shift can be much greater. For example the OH fundamental in water shifts ~ 400 cm^{-1} in the solid phase compared to the gas phase and is broadened by over 300 cm^{-1}.

2.6.1 Infrared (IR) Spectra in the condensed phase.

The infrared spectrum of a molecular solid will exhibit three regions (Quirico, Schmitt et al. 1996)

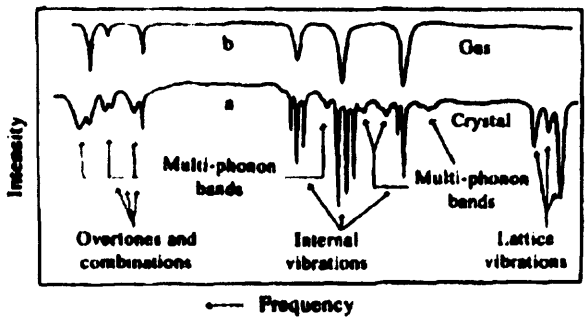

Figure 2-8 Spectrum of a molecular solid compared to a gas phase spectrum (taken from (Quirico, Schmitt et al. 1996))

The far infrared mode contains the crystal and phonon modes. There is no gas phase equivalent of these motions. As with the gas phase the fundamental modes of the molecule fall in the mid infrared range. This is the range we will be most concerned with. We generally observe a slight shift from the gas phase frequencies, crystal splitting effects may also be observed. In the near infrared we often observe overtone bands, which are also present in the gas phase.

2.6.2 UV Spectra in the condensed phase.

What is the fate of Rydberg transitions when we consider the condensed phase UV spectrum? It is known that Rydberg states are much more sensitive to perturbations from neighbouring molecules due to their large orbitals. (Robin 1974) describes how in the condensed phase Rydberg states are related to the electronic relaxation time relating to the electron mobility in that phase. For example in an organic crystal with low electron mobility the Rydberg states are broadened to such an extent as to be unobservable as the electronic relaxation time is short. (Robin 1974). We often observe a shift in the solid phase spectrum too and line broadening effects are also apparent in condensed phase spectra. So condensed phase UV spectra can be a tool for distinguishing between valence and Rydberg states. We will now consider condensed phase spectra in more general terms.

2.6.3 Amorphous and Crystalline States.

In the course of this research we encounter two different types of solids, amorphous and crystalline. (Figure 2-9) Amorphous solids are intrinsically disordered with no long range order. Crystal structures exhibit long range order.

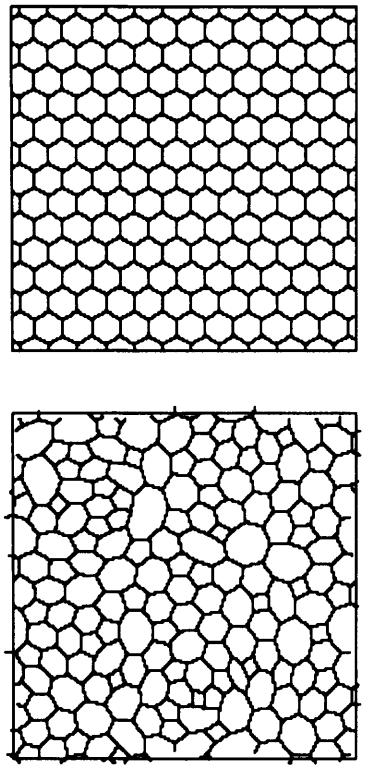

Figure 2-9 Diagram of an ordered Crystalline state (top) and a disordered amorphous state (bottom)

The structure of a solid can have a profound effect on its infrared and ultraviolet spectra. For example Water, H_2O has numerous crystalline structures each with a distinct spectrum. An example can be seen below. Figure 2-10

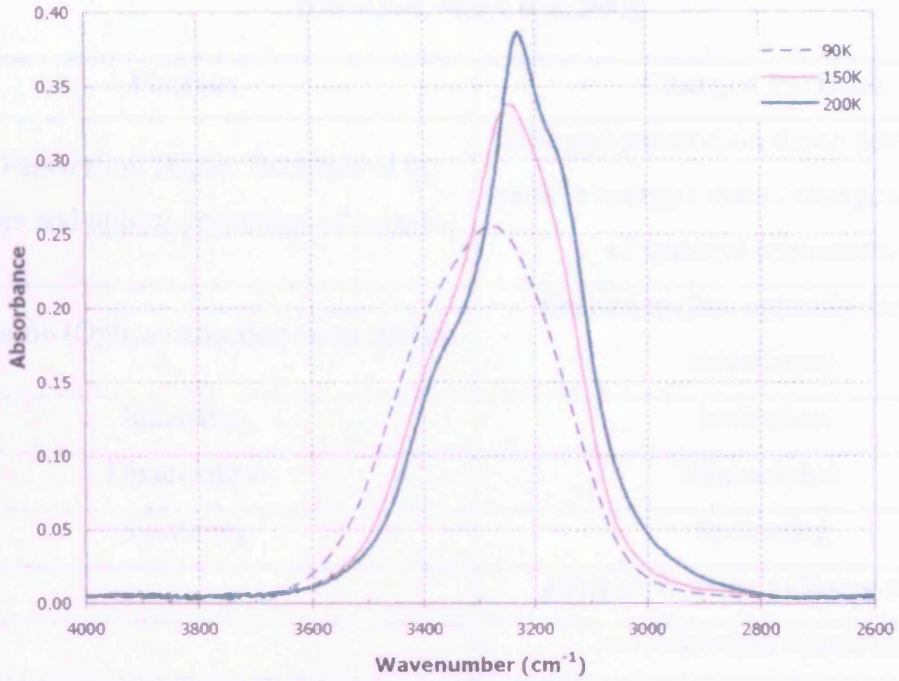

Figure 2-10 Infrared scan of the crystalline structures of water showing the amorphous (90 K), cubic (150 K) and crystalline states (200 K) (Taken from (Dawes 2003))

2.7 UV / Ion and Electron Chemistry.

The reactions induced by photons, and charged particles with solid matter are of vital importance in astochemistry. We can consider two cases, UV photons and charged particles.

In general UV photons do not penetrate far into a material. For instance in an Ort cloud comet (P.A. Gerakines, Moore et al. 2000) UV Photons may penetrate to a depth of 0.15 μm. In contrast they estimate that 41 eV molecule^{-1} is deposited in the upper 20 cm of ice from cosmic ray protons. A comparison between the two is illustrated in Table 2-6 and Figure 2-11

Table 2-6 Comparison of Photon and Charged particle effects (adapted from (Dawes 2003) & (Gerakines, Moore et al. 2001))

Photons	Charged Particles
Low Penetration Depth. Determined by structure and optical properties of material	Increased penetration depth determined by particle energy / mass / charge and density of material encountered.
Excitation (Optical selection rules apply)	Excitation (inc. optically forbidden transitions)
Ionisation	Ionisation
Dissociation	Dissociation
Sputtering	Sputtering
	Electron Capture / Charge transfer
	Ion- Molecule interactions
	Secondary effects – production of secondary electrons

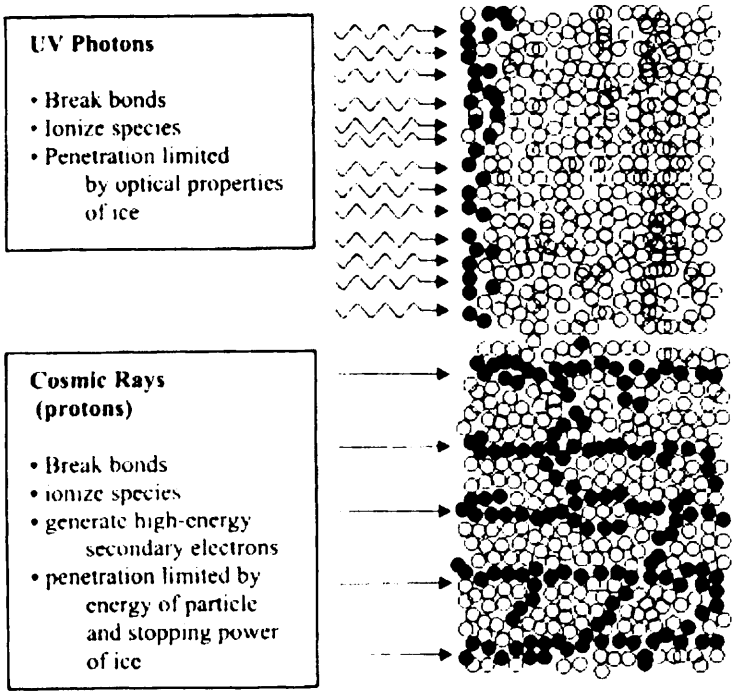

Figure 2-11 Comparison of Photon and Charged particle irradiation of a solid (adapted from (Gerakines, Moore et al. 2001))

The interactions of ions with solids are of particular interest in an astrophysical environment. When an ion penetrates a solid it will undergo a series of collisions with the solid target. As the ion collides with the target it will lose energy at a rate of dE/dx (typically of the order of a few to 100 eV per nm, dependant on conditions) (Nastasi, W. et al. 1996). This energy loss is dependant on screened column interactions with the target atoms and electrons. We can break these down into two loss interactions (1) nuclear *or elastic* collisions and (2) electronic *or inelastic* collisions. (1.13)

$$\frac{dE}{dx} = \left.\frac{dE}{dx}\right|_n + \left.\frac{dE}{dx}\right|_e \tag{1.13}$$

Nuclear collisions involve large energy losses and can involve significant angular deflection of the ion trajectory. Figure 2-12. Displacement of the target lattice atoms can also occur in these collisions.

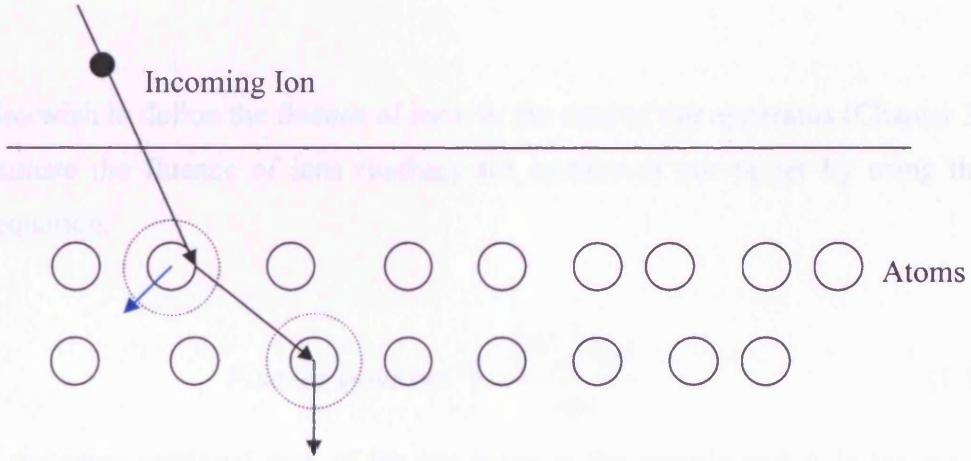

Figure 2-12 Ion Interaction with solid matter showing ion collisions and displacements. (Adapted from (Nastasi, W. et al. 1996))

Electronic collisions on the other hand are far less destructive in terms of creating lattice vacancies. They involve smaller energy losses per collision and there is negligible

deflection of the ion trajectory. Nuclear stopping dominates for low energy and high atomic number (Z). Electronic stopping will dominate for high energies and low values of Z.

When we consider the stopping of ions in matter it is useful to define the stopping cross section, S of an ion in matter.

This is defined as

$$S \equiv \frac{dE/dx}{N} \tag{1.14}$$

where N is the atomic density (atoms cm^{-3}).

We can also simply define the range, R of ions in matter as simply the rate of energy loss along the path of the ion.(1.15)

$$R = \int_{E_0}^{0} \frac{dE}{dE/dx} \tag{1.15}$$

We may also wish to define the fluence of ions. In the case of our apparatus (Chapter 3) we can estimate the fluence of ions reaching the surface of our target by using the following equation.

$$Fluence\ (ions\ cm^{-2}) = \frac{(a/A) I_{FC} t}{eqa} \tag{1.16}$$

where a is the cross sectional area of the ion beam at the sample and A is the cross section area the Faraday cup measuring the ion current. I_{FC} is the current on the faraday cup and e is the charge on an electron and q is the ion charge. In the case of our equipment $a/A=0.4^2/0.95^2$.

Stopping values and ranges may be obtained from literature for various ions or they may be calculated using the SRIM program (Ziegler 2003).

2.8 Computing Programs to support ion / electron irradiation of matter.

We will briefly describe some of the computer programs available currently that complement our research. It is sometimes useful to model the effects that ions and electrons have on matter. There are two programs available to do this.

The Stopping and Range of Ions in matter (SRIM) is a program written and published by James Ziegler and is also complimented by the program TRIM (the Transport of Ions in Matter). Using the "Core and Bond" model such that the "stopping powers in compounds can be predicted using the superposition of stopping by atomic "cores" and then adding the stopping due to the bonding electrons" (www.srim.org) SRIM is able to accurately predict the stopping and range of ions into a user specified target over a wide range of ion energies.

The CASINO (monte CArlo SImulation of electroN trajectory in sOlids) program is the electron equivalent of the SRIM program. The CASINO program is designed to simulate electron trajectories in solids especially low beam interactions. The casino program was used to simulate the electron interaction with solid layers of carbon dioxide and methylamine (Chapter 6) in order to estimate the electron energy loss into the solid ice layers.

2.9 Conclusions

In this chapter we have provided an overview of some of the underlying principles necessary to interpret our studies of the irradiation of astrophysical ice analogues. In the next chapter we will describe our equipment for the monitoring and preparing astrophysical ice analogues.

Chapter Three

Experimental Methods And Apparatus

"Hey, wait - I'm having one of those things. You know. A headache with pictures".

"An idea?"

--Futurama

3.1 Introduction

The apparatus described in this thesis was originally designed with the primary aim of being a portable system to simulate the environment of the Interstellar Medium (ISM). The benefits of a portable system are it allows us to easily move it to large irradiation facilities giving us options that fixed systems rarely have in terms of exposing our ice samples to conditions prevalent in the Interstellar medium. A portable design also allows for quick and easy reconfiguration of the system. For example, easily changeable substrates and a wide choice of molecules we can deposit. Also a small portable system allows the use of commercially available UV and infrared spectrometers. In order to simulate the conditions that a dust grain would experience in the ISM we must operate the system at low temperatures and pressures (Ultrahigh Vacuum, UHV) representative of the interstellar medium. Table 3-1

Table 3-1 - Typical conditions in the ISM and the Laboratory (after (Dawes 2003))

Parameter	Typical Conditions in the ISM	Typical Laboratory Conditions for our apparatus
Ice Temperature (K)	~10-70	>10
Ice Thickness (μm)	0.02-0.2	0.2 – 2
Condensation Rate	10^{5} -10^{7}	~10^{15} – 10^{17}
Ambient Pressure (mbar)	~10^{-17}	10^{-10} – 10^{-7}

Thus the major requirements of such a system are:

1) That the system is compatible with UV, Ion and electron irradiation of any astrophysical ice analogue.
2) That the system is capable of maintaining an ultrahigh vacuum environment of pressures greater than 10^{-9} mbar or greater.
3) That the system is compatible with ultraviolet and infrared spectroscopy, two of the main detection and identification methods used in experiments of this type.
4) That ices may be prepared and maintained at low (<30K) temperatures
5) That the system produces consistent and reproducible results from experiment to experiment.

In this chapter the apparatus will be described and the experimental methods and procedures used defined.

3.2 The "Ices Experiment"

A diagram of the UHV system used in these experiments is show in Figure 3-1. The chamber is based on a 6 way stainless steel cube with an internal diameter of 66 mm, (Manufactured by Kimbal Physics, Model number MCF275-SC600-A). Each face of the cube contains a Conflat, CF 40 flange to enable coupling to other devices. In order to allow IR and UV transmission spectroscopy two ports on the cube are fitted with transmitting Calcium Fluoride (CaF_2) windows mounted into the CF40 flanges. The remaining ports on the cube are used for sample deposition and irradiation sources.

Into this cube is inserted the sample holder, which consists of a cooling stage and transmitting CaF_2 substrate. The sample is able to rotate through 360° by mounting on a Caburn E-RMT-275 rotary feedthrough. The length of the cryostat is accommodated by attaching a stainless steel extension piece and a 6 way cross to the cube. The additional 6 way cross allows support and vacuum line connections to be attached to the chamber. The entire system is evacuated by a Leybold Turbovac TW-300 turbomolecular pump (pumping speed ~260 l s^{-1}) backed by an oil free Leybold EcoDry M15 dry pump (pumping speed ~14 $m^3 h^{-1}$). This ensures the chamber is free of oil contamination. The system is isolated from the pumping stage by a gate valve. This turbomolecular pump reaches a base pressure of the magnitude 10^{-7} mbar after one day of pumping . With the additional "cryopumping" effect of cooling the system a base pressure of ~10^{-9} mbar can be achieved with liquid helium. Pressure is measured by a combi-ion gauge (Leybold IONIVAC ITR-90) which has a range of 10^3 to ~5 x 10^{-10} mbar. The base pressure of 10^{-9} is suitable for the purposes described above as at this pressure the freezing out time of contaminates is long enough to enable us to perform irradiation experiments on ices without the problems of atmospheric gases freezing onto the coldhead. The system should be baked by application of heating tapes around the chamber (taking due care of the CaF_2 windows).

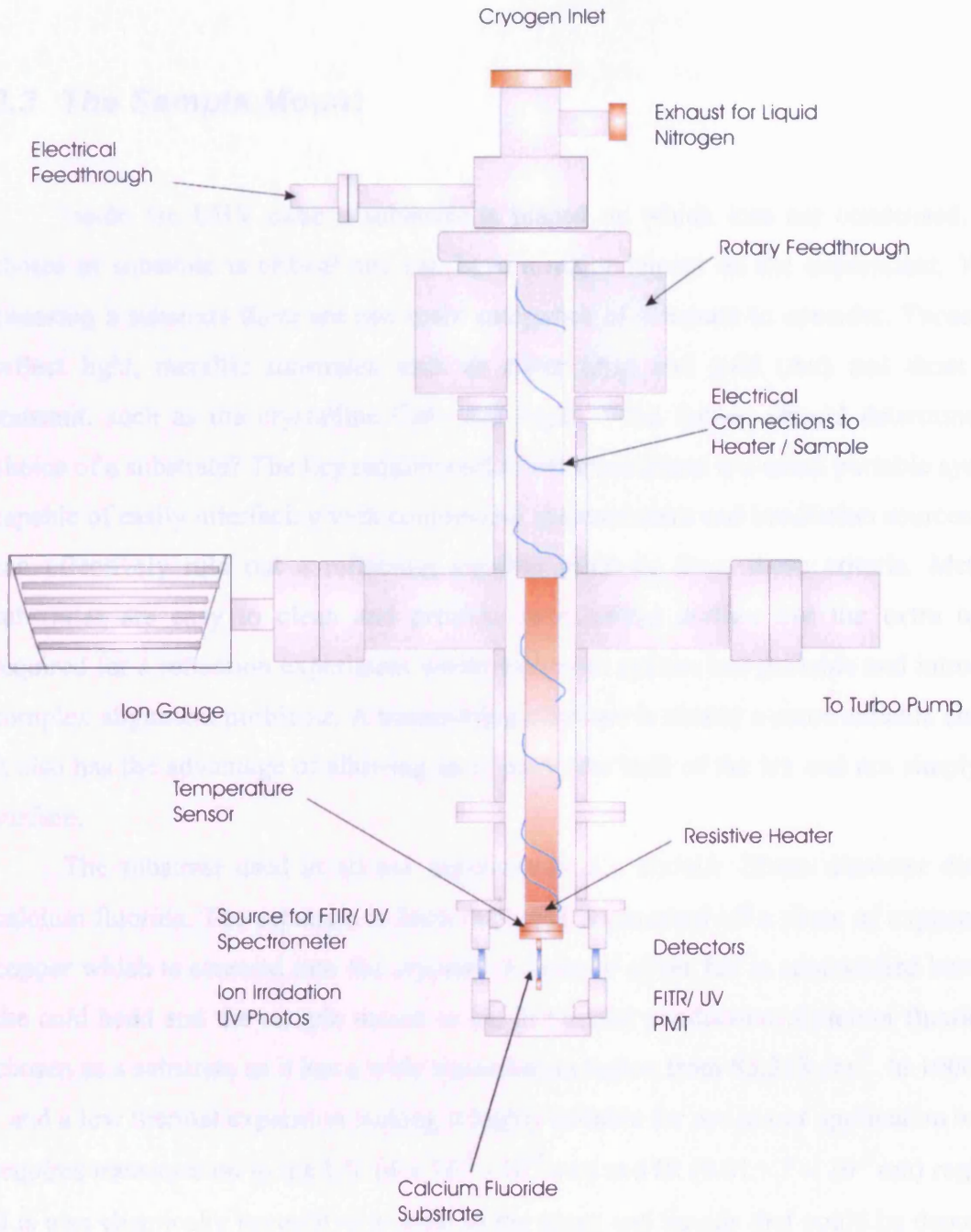

Figure 3-1 Diagram of the Vacuum Chamber (Not to Scale)

3.3 The Sample Mount

Inside the UHV cube a substrate is placed on which ices are condensed. The choice of substrate is critical and can have a major impact on the experiment. When choosing a substrate there are two main categories of substrate to consider. Those that reflect light, metallic substrates such as silver (Ag) and gold (Au) and those that transmit, such as the crystalline CaF_2 and MgF_2. What factors should determine the choice of a substrate? The key requirement in our experiment is a small portable system, capable of easily interfacing with commercial spectrometers and irradiation sources. We can effectively rule out a reflecting metallic substrate from these criteria. Metallic substrates are easy to clean and provide an excellent surface but the extra optics required for a reflection experiment would make our system less portable and introduce complex alignment problems. A transmitting substrate is clearly a more suitable choice. It also has the advantage of allowing us to probe the bulk of the ice and not simply the surface.

The substrate used in all our experiments is a circular 25mm diameter disk of calcium fluoride. The substrate is 2mm thick and is mounted off a piece of oxygen free copper which is screwed into the cryostat. A layer of silver foil is sandwiched between the cold head and the sample mount to aid in thermal conduction. Calcium fluoride is chosen as a substrate as it has a wide transmission region from 83,333 cm^{-1} to 1000 cm^{-1} and a low thermal expansion making it highly suitable for use in our application which requires transmission in the UV (4×10^{-5} - 10^{-7} cm) and IR (0.01 - 7×10^{-5} cm) regions. It is also chemically unreactive to most of the gases and liquids that could be deposited in our system. Our CaF_2 discs are supplied by Crystran Optics who supply CaF_2 in both UV and IR grades. The UV grade CaF_2 has a slightly extended range to allow transmission into the VUV. A sample of the transmission curve from one of the windows used in the experiment is shown in Figure 3-2 along with a transmission curve obtained from literature in Figure 3-3.There is excellent agreement between the two. The CaF_2 disc was originally held in place using 3 restraining screws and a washer. However this was eventually found to be impractical as the mounting arrangement either put excess pressure on the substrate causing cracks or allowed the substrate too much freedom of movement which we found caused irreproducible depositions and

lowered the sticking of molecules to the substrate. A photograph of this arrangement can be seen in Figure 3-4. The screw arrangement was eventually replaced by a copper disk which overlaps the edge of the substrate by a few mm and holds it firmly and evenly in place.

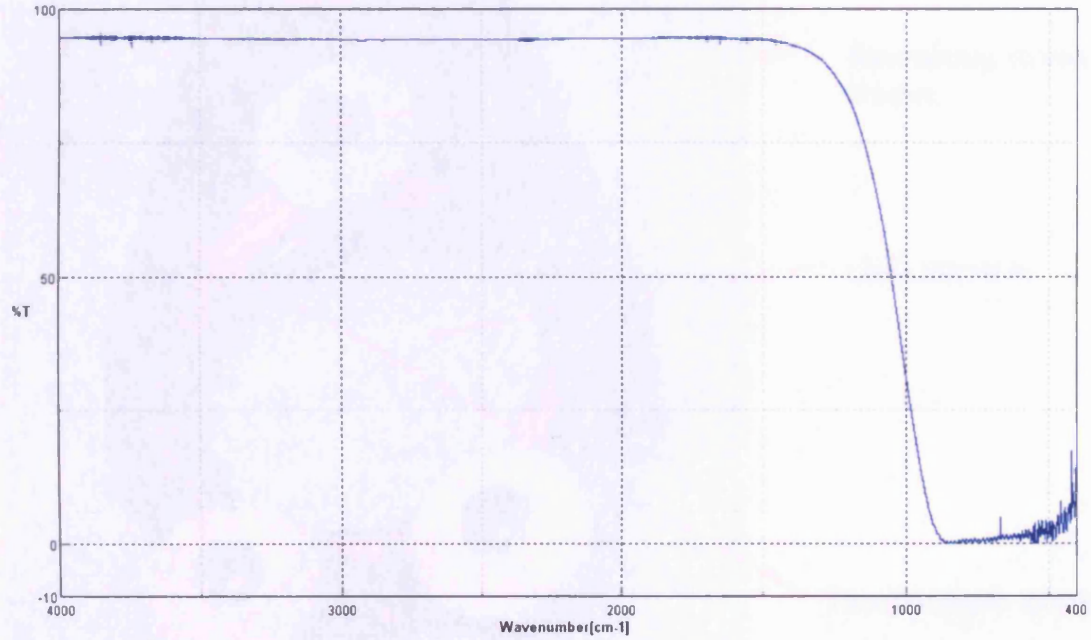

Figure 3-2 Infrared Transmission Spectra through a Calcium Fluoride window measured in the vacuum system using a Jasco 600 *Plus* FTIR at room temperature

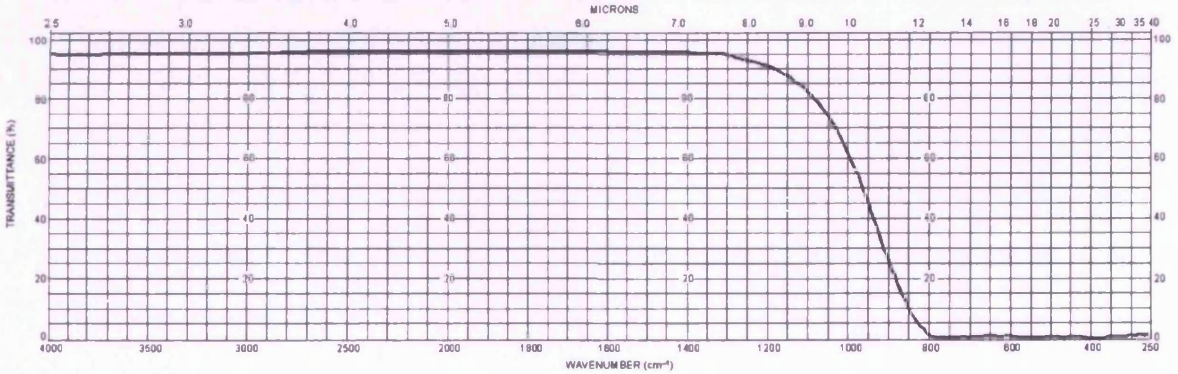

Figure 3-3 Transmission curve of CaF_2 in the Infrared obtained from Literature.

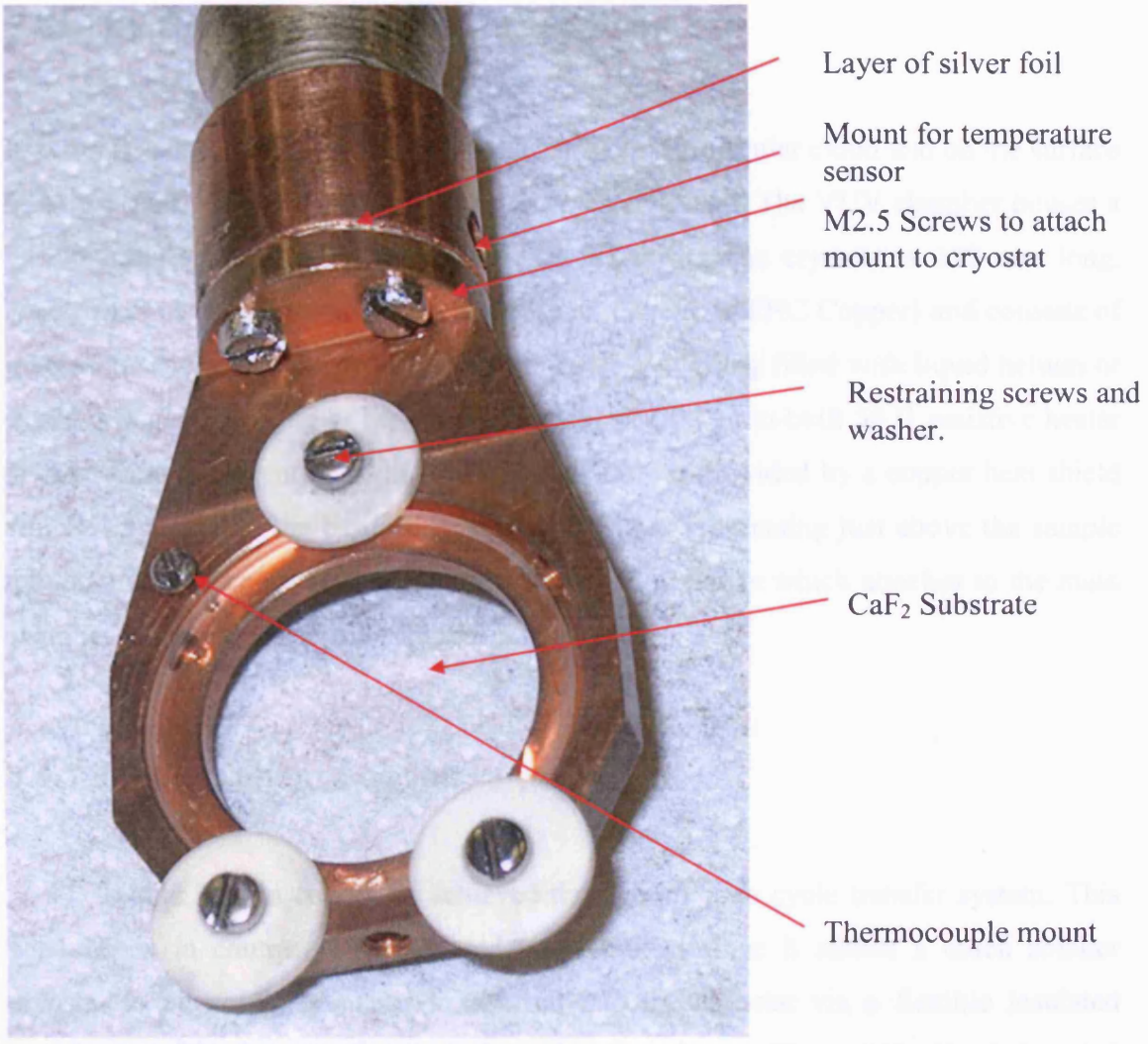

Figure 3-4 Photo of the original sample mount showing the retraining screws and the CaF_2 susbtrate. The mounting for a Rhodium iron temperature sensor is shown towards the top of the photo.

3.4 The Cryostat and Cooling system

In order to achieve temperatures typical of those in a molecular cloud and on the surface of a dust grain it is necessary to employ a cryostat system. The VUV chamber houses a custom built cryostat manufactured by AS Scientific. The cryostat is 250 mm long, constructed of Oxygen-Free High Conductivity Copper (OFHC Copper) and consists of a heat exchanger that sits upon a reservoir capable of being filled with liquid helium or liquid nitrogen. Heating of the cryostat is provided by an in-built 50 Ω resistive heater (1 A maximum current). Additional heat shielding is provided by a copper heat shield which is attached to the base of the heat exchanger, terminating just above the sample mount. The entire cryostat is mounted into a CF40 flange which attaches to the main chamber via an extension tube (Figure 3-1)

3.4.1 Liquid Helium Cooling

Liquid helium cooling is achieved through an open cycle transfer system. This was chosen in contrast with a closed cycle system since it allows a much smaller cryostat to be used. Helium is transferred into the cryostat via a flexible insulated transfer line. This is typically attached to a 100 litre dewar. The transfer line is inserted into the dewar and secured via a O-ring seal . The other end of the transfer line is inserted into the cryostat and secured with a similar seal. In order to remove the helium vapour produced during the cooling process a diaphragm pump is used to remove gaseous helium and to aid in the flow of helium from the dewar which, unlike conventional nitrogen dewars, is unpressurised. The helium flow rate is simply regulated by a needle valve attached to the diaphragm pump. The base temperature with liquid helium cooling is ~22 K.

3.4.2 Liquid Nitrogen Cooling

It is of course also possible to cool the cryostat using liquid nitrogen A custom built transfer line for this purpose can be attached to a pressurised nitrogen dewar. Flow into the cryostat is regulated via a liquid level sensor mounted into the cryostat insert. This controls a solenoid gate valve which allows a constant level of liquid nitrogen to remain in the reservoir of the cryostat. Nitrogen vapour is then expelled through a tube in the top of the cryostat. Base temperatures reached with liquid nitrogen cooling are around 82 K

3.5 Temperature Control and Sensing

Initially a Copper-Constantan thermocouple was used to measure the temperature at the substrate but this was subsequently replaced by a Rhodium-Iron temperature sensor (Oxford Instruments PHZ 0002). The sensor was mounted directly into the base of the cryostat by inserting it into hole bored through the copper mount. The sensor was pre-calibrated at 3 temperature points by the supplier, at liquid helium, liquid nitrogen and room temperature. This allowed us to use the sensor's full cryogenic range. It has a range from 0.5 to 500K with a quoted accuracy of 0.2 K. In order to use the new temperature sensor a temperature controller was purchased. An Oxford Instruments Model number ITC502 controller attaches to the Rhodium-Iron sensor. The temperature controller can also utilise two other thermocouples in concert with the Rhodium Iron sensor. One of the main disadvantages of the Rhodium-Iron sensor however is its fragile nature. Due to the rotatable nature of our cryostat the 4 pins from the temperature sensor had to be bent and the wires wrapped around the cryostat and fed up through the electrical feedthrough. This results in extra mechanical strain on the sensor and caused a failure of the sensor during one experiment. It was then decided a more robust temperature sensor should be mounted. A thermocouple is a more suitable choice as whilst not possessing the range and accuracy of the Rhodium-Iron sensor it is much more robust and can better withstand the movement required in our system. An N-type thermocouple and a Iron-Chromel/Gold thermocouple was therefore mounted on the substrate. They are attached to the two mounting screws that restrain the substrate onto the sample mount giving us two sensors allowing us to compare and calibrate the

sensors. The temperature controller also interfaces with the resistive heater on the cryostat allowing a balance between heating and cooling to be established and a constant temperature maintained. Operation of the ITC Temperature controller can be either via a PC or the front panel. The controller connects via a standard RS232 port and allows constant logging and monitoring of all 3 temperature sensors during the course of the experiment.

3.6 The Gas Dosing Line

A gas line is attached to the system in order to deposit molecules onto the substrate. Gas enters the UHV system from a 6 mm stainless steel tube which is welded onto a CF40 flange. The tube protrudes until it is 19 mm from the surface of the CaF_2 substrate. An diagram of the gas line can be seen below in Figure 3-5

Gas is fed into a mixing cell from a lecture bottle and liquid samples are drawn from a glass bulb using the vapour density. All connections on the gas line are Swagelok style and / or KF connectors. This allows the gas line to be easily reconfigured depending on where the experiment is being performed or the number and type of gas samples we wish to deposit. The mixing cell is a CF16 T-Piece which is isolated at both ends by a leak valve and an on-off valve. In order to read the pressure of gas in the cell a MKS baratron is attached to the other connector of the T-Piece. The flow of gas into the mixing cell is controlled by a needle valve and an on/off valve on each gas bottle. The needle valve allows a more precise flow of gas into the gas reservoir allowing us to fill the gas cell to ± 0.1 mbar (dependant on the molecule to be deposited. Some molecules such as water condense on the side of the cell or are "sticky" making deposition less accurate) Before filling the gas cell the line is evacuated using a Turbo pump backed by a rotary pump. The gas cell is then filled to a maximum base pressure of 12 mbar and sealed off. A precision leak valve then controls the flow of gas onto the substrate. During deposition the pressure in the main chamber is constantly recorded as an additional indication of the flow of gas into the chamber.

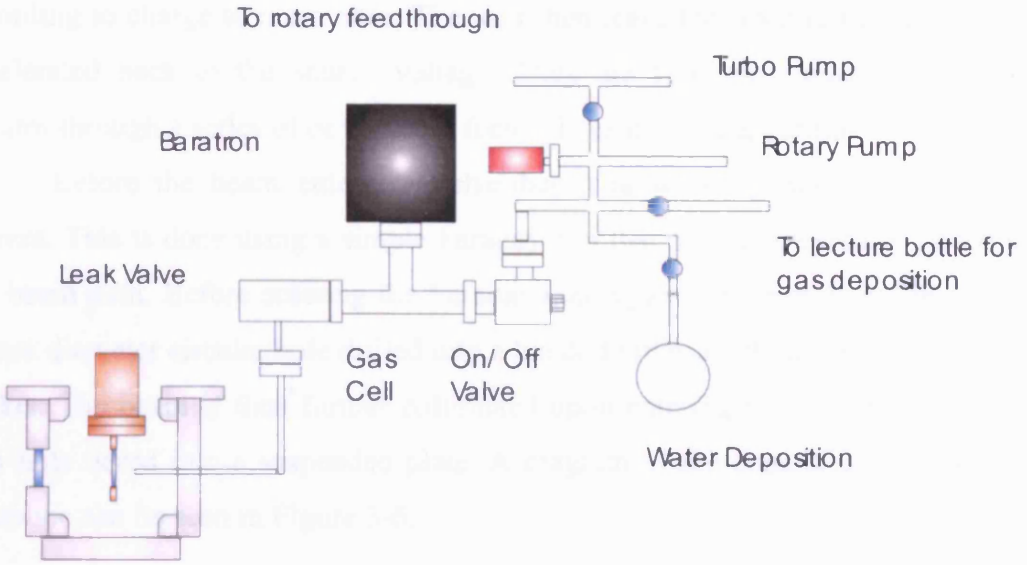

Figure 3-5 The Gas Deposition line

3.7 *Irradiation Sources*

In the course of this project three types of irradiation studies were used to mimic the radiation environment of the interstellar medium that a typical dust grain would be exposed to, Ion bombardment, ultraviolet irradiation and electron irradiation.

3.7.1 Ion Sources

Ion irradiation studies have been performed with the aid of the Electron Cyclotron Resonance Ion Source (ECRIS or ECR Source) or the 100 kv accelerator with oscillating electron source at Queen's University Belfast. The ECRIS is the preferred Ion source as it produces a wide range of low energy ions of single or multiple charge. A brief description of the operation of the ion source and the attachment of our system to the ion source is given below. The electron cyclotron resonance Ion source (ECRIS) at Queens University Belfast is used to produced multiply charged ions using a 9-10.5 GHz Electron Cyclotron Resonance Ion Source. (Trassl, Broetz et al. 1999) Electrons are excited in a plasma through a microwave discharge system and confined axially by a permanent magnet and radially by a multipole magnet. The electrons will then achieve resonant conditions when the microwave frequency matches the cyclotron frequency of the electrons in the plasma. Extraction of the ion beam from the source is then obtained by using a floating beamline accelerator. (The beamline is held at 4 kV potential) The ions are accelerated using a 90° analysing magnet which separates ions

according to charge to mass ratio. The ions then leave the floating beamline and are so decelerated back to the source voltage. They are then channelled via an electrical isolator through a series of deflection / focus plates into our apparatus.

Before the beam enters our chamber it is advantageous to measure the ion current. This is done using a simple Faraday cup that can be lowered or raised into the ion beam path. Before entering the Faraday cup region the beam is collimated using a 20mm diameter circular hole drilled into a blank double sided flange and a blank copper gasket. The beam is then further collimated upon entering the chamber by using an 8 mm hole bored into a suspended plate. A diagram of the apparatus as attached to the beamline can be seen in Figure 3-6.

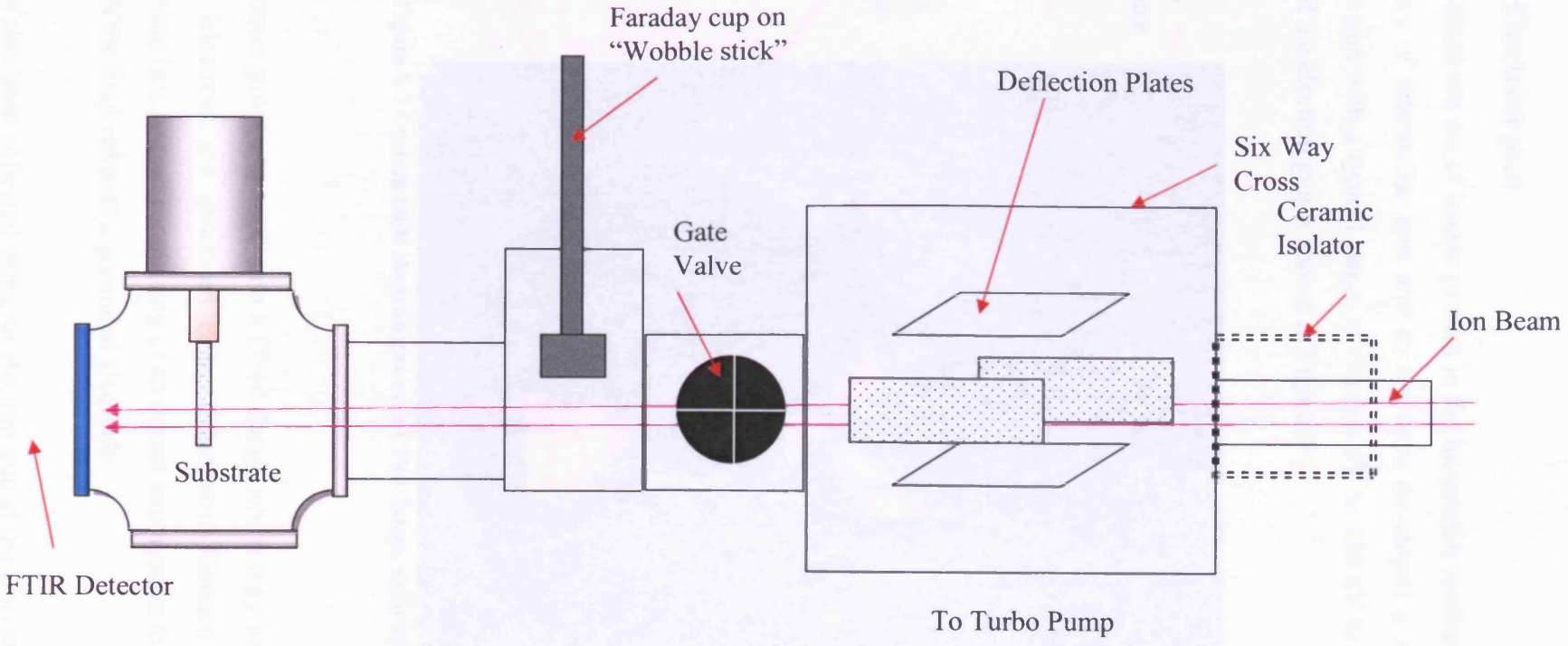

Figure 3-6 Diagram of the Ion Source attachment

3.7.2 Electron gun

Electrons are of course present in the interstellar medium and are involved in the chemistry of interstellar ices and so we have developed a custom built low energy electron gun with a typical range of ~ a few eV to 150 eV to irradiate our samples. A photo of the electron gun is shown in Figure 3-7

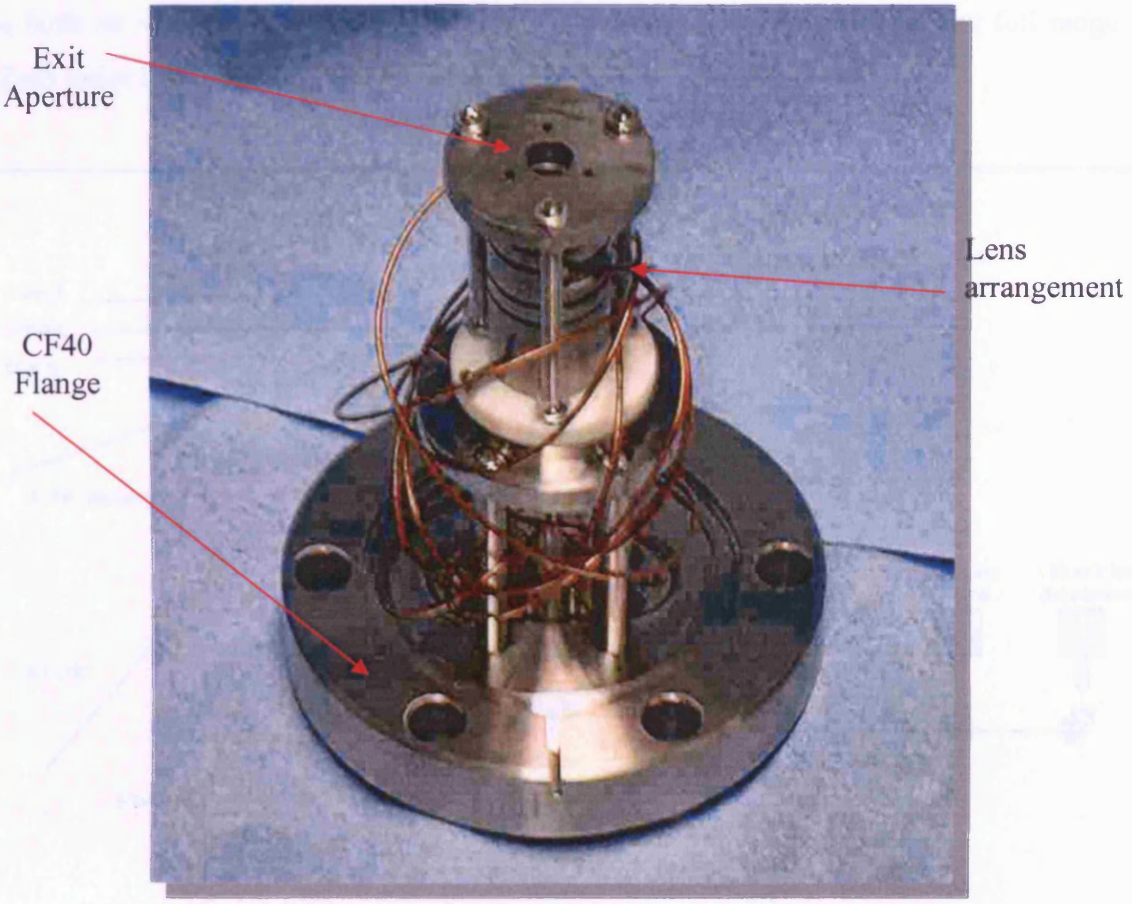

Figure 3-7 Custom built electron gun on a CF40 flange, showing the electron optics

The electron gun is mounted onto a CF40 flange which may be directly bolted onto the system. Electrons are generated using a tungsten filament and focused using an electrostatic lens system comprising of an Einzel lens system followed by a two element lens with the final element a grounded electrode.

Data has also been collected using an electron gun at the University of Hawaii at Manoa as the irradiation source. The University of Hawaii apparatus is described in detail in section 3.9

3.7.3 Ultraviolet Light

Ultraviolet photons are produced by the synchrotron radiation source at the Institute for Storage ring facilities (ISA) based at the University of Aarhus in Denmark as shown in Figure 3-8. The advantage of the Synchrotron source is that is can be used as both an irradiation source by "bathing" the sample in UV light over the full range (Zero order light) or as a VUV spectrometer (Section 3.8.3.2)

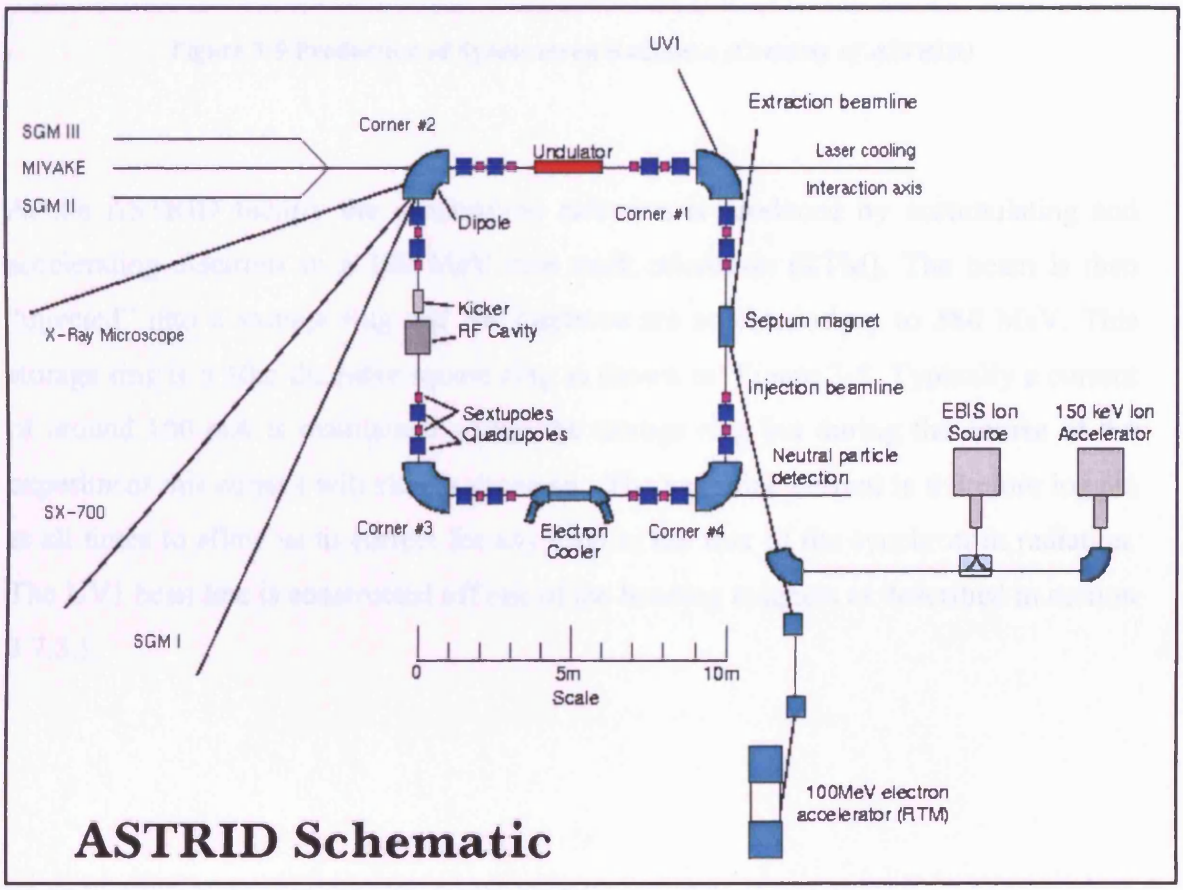

Figure 3-8 Diagram of the Astrid Source ***(Courtesy of ASTRID)***

Synchrotron radiation is produced when a magnetic field is applied normal to an electron beam travelling at relativistic speeds. As the electrons are deflected along a curved trajectory synchrotron radiation is emitted. (Figure 3-9)

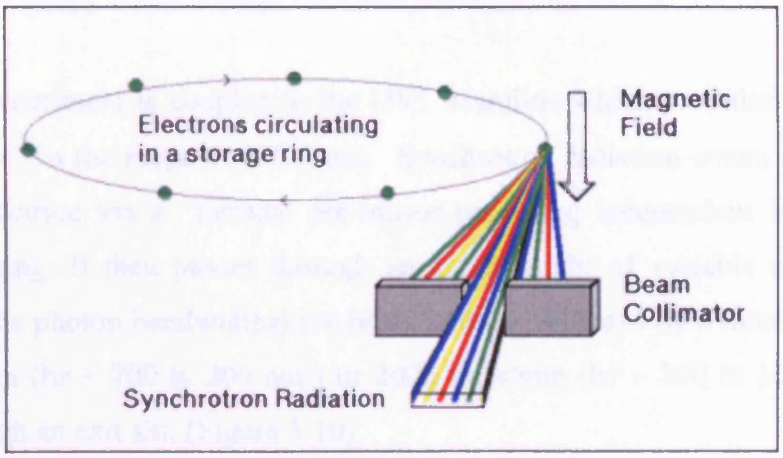

Figure 3-9 Production of Synchrotron Radiation ***(Courtesy of ASTRID)***

At the ASTRID facility the synchrotron radiation is produced by accumulating and accelerating electrons in a 100 MeV race track microtron (RTM). The beam is then "injected" into a storage ring and the electrons are accelerated up to 580 MeV. This storage ring is a 10m diameter square ring as shown in Figure 3-8. Typically a current of around 160 mA is maintained within the storage ring but during the course of the experiment this current will slowly decrease. The beamline current is therefore logged at all times to allow us to correct for any drop in the flux of the synchrotron radiation. The UV1 beamline is constructed off one of the bending magnets as described in section 3.7.3.1.

3.7.3.1 The UV1 Beamline

Our experiment is coupled to the UV1 beamline which provides a flux of 2 × 10^{11} photons s^{-1} in the range 100-700 nm. Synchrotron radiation enters the UV beam line and is focused via a toroidal pre-mirror providing independent horizontal and vertical focusing. It then passes through an entrance slit of variable size (allowing selection of the photon bandwidths) the beam is then dispersed by a toroidal grating of 1000 lines/mm ($h\nu$ ~ 700 to 200 nm) or 2000 lines/mm ($h\nu$ ~ 350 to 100 nm) before passing through an exit slit. (Figure 3-10)

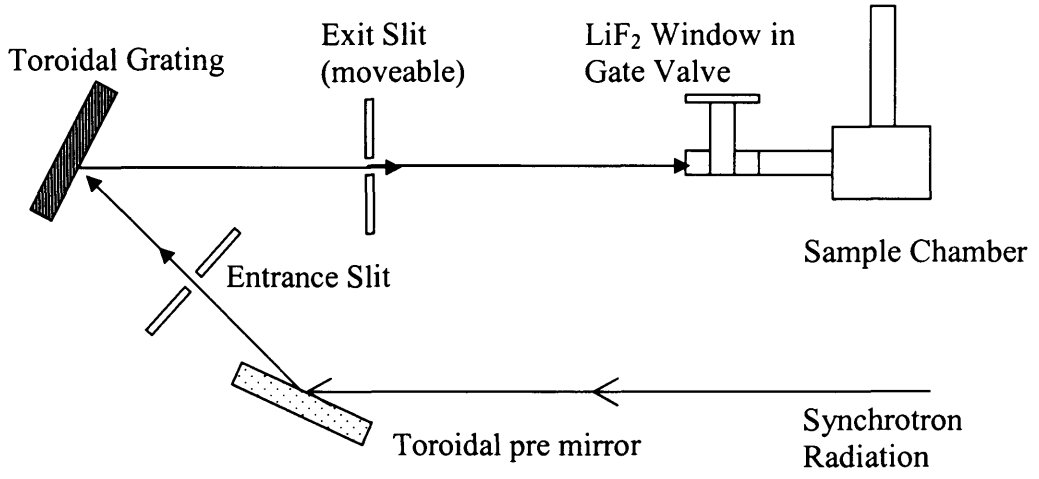

Figure 3-10 Schematic of the UV1 monochromator

In this work we used the high energy grating of 2000 lines/mm. The beam finally passes though an exit slit which is moveable in order to focus the beam. Thus scanning different wavelength regions requires moving the exit slit in order to obtain the best possible focus of the beam. The exit slit is repositioned by moving the entire experimental table. To scan a particular region the table therefore needs to be moved to an optimum position which can be determined from Figure 3-11

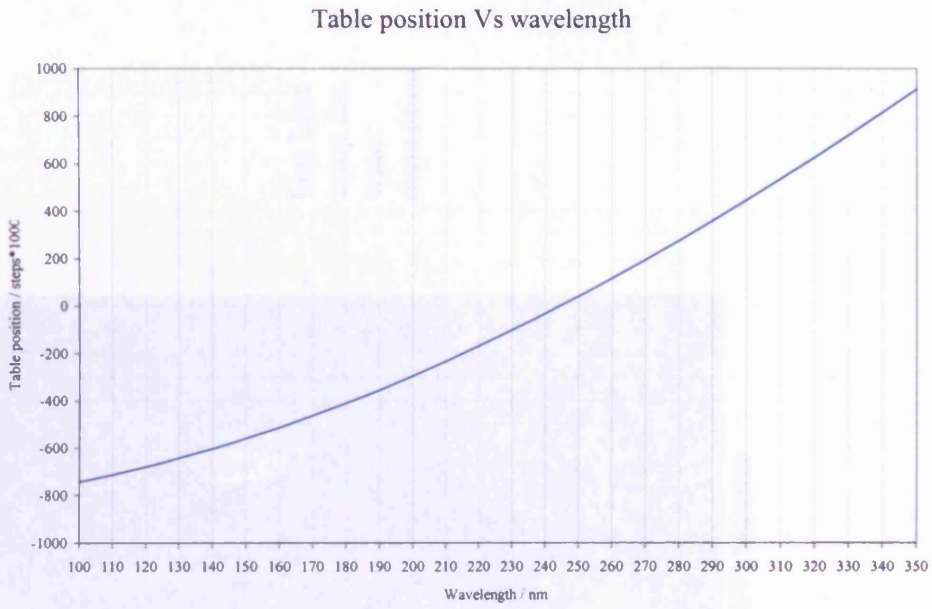

Figure 3-11 Table Position Vs. Wavelength for the UV1 Monochromator.

The UV1 beamline can be used in two complementary modes of operation either as an irradiation source or as a vacuum ultraviolet (VUV) spectrometer (section 3.8.3.2) In order to irradiate the sample the grating can be turned to act as a mirror allowing all wavelengths through the exit slit, this is known as "Zero Order" light. (A photograph of the apparatus can be seen in Figure 3-12)

UV photoabsorption data is recorded using a QL30F/RFI photo-multiplier tube (PMT) for photon detection. The wavelength scale was calibrated using fine structure present in the absorption bands of SO_2. Throughout the course of each experiment the beam current is also monitored. The beam current decays over the course of an experiment and the drop in the intensity of the synchrotron radiation is proportional to the loss of beam current. Due to the long timescales of irradiation in some experiments it is necessary to normalise to this beam current decay.

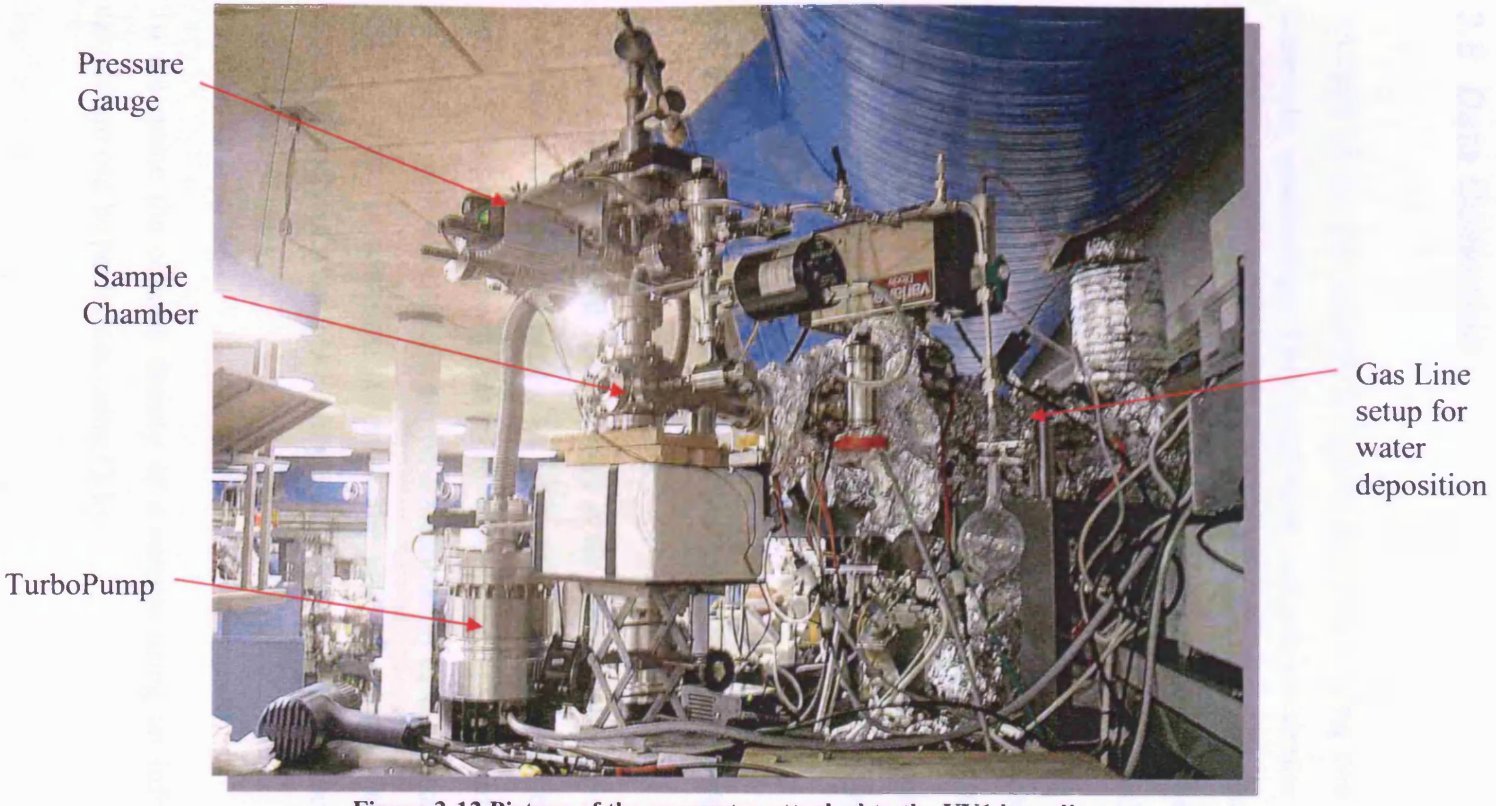

Figure 3-12 Picture of the apparatus attached to the UV1 beamline

3.8 Data Collection

Analysis of our ice samples is mainly performed using two techniques, infrared and ultraviolet spectroscopy. Data acquisition methods are similar in both cases with only a few minor variations due to software differences. However before any infrared or UV spectra can be meaningfully analysed and any complex irradiation studies performed it is necessary to gain an understanding of the physical properties of the ice. One major property of the ice is the ice thickness. It should be noted that the thickness of ice deposited per mbar of gas in our gas reservoir is not a constant from molecule to molecule. For each new molecule we deposit, we need to calibrate our dosing system. The most reliable method of calibration is to directly measure the ice thickness using either an FTIR spectrometer as described in section 3.8.1 below or preferably a He-Ne Laser (section 3.8.2)

3.8.1 Determining Sample thickness using infrared spectroscopy.

The strength of infrared spectroscopy is the number of physical properties that can be determined from an infrared scan of a molecule. Each molecule has a characteristic infrared "fingerprint" such that it can be identified from its infrared spectrum. It is also possible to gain information on the concentration of the absorbing molecules from an infrared scan. In astrophysical work the unit of column density is often used. The column density of a sample is simply a measure of the number of molecular absorbers along a line of sight.

To determine the column density of a sample using an infrared spectrum, a simple calculation can be performed using (3.1)

$$N = \ln 10 \frac{\int Abs(v)dv}{A} \qquad (3.1)$$

where N = column density in units of molecules cm^{-2}. A= integrated absorption coefficient (cm $molecule^{-1}$). $\int Abs(v)dv$ is the area of the infrared absorbing band at a specific frequency.

Note that when the infrared beam is not orthogonal to the substrate sample and enters at an angle θ (such as when using refection spectroscopy) then the effect of the reflection and incident angle can be taken into account by modification of (3.1) as follows

$$N = \ln 10 \frac{\int Abs(v)dv}{2A} \cos(\theta) \qquad (3.2)$$

From this column density it is possible to easily convert this into a sample thickness using the Beer-Lambert law.

$$d = \frac{NM}{N_A \rho} \qquad (3.3)$$

where d (cm) is the sample thickness, M is the molecular mass, N_A = Avogadro's number and ρ is the number density.

3.8.2 Determining sample thickness using He-Ne Laser measurements.

One disadvantage of the infrared method of determining sample thickness is that it requires knowledge of the absorption coefficient of the molecule , A. This absorption coefficient is dependant on very specific conditions, such as the purity of the sample and the temperature of the sample. As such they are only ever approximations. When calculating thickness using the infrared method it is usual to calculate the thickness using a number of different absorbing frequencies and average out the thicknesses obtained. The FTIR method also relies on a knowledge of the density of the solid, which is poorly known in most cases. Clearly an alternative method of determining the sample

thickness is required. One such method comes from the analysis of a thin film using a laser. At a fixed wave number the transmittance of a thin film will vary according to its thickness. The absorption / interference between the light reflected at the interfaces between ice / substrate and ice / vacuum determines an oscillation with decreasing amplitude of transmission versus thickness (Baratta and Palumbo 1998)

A Helium-Neon laser (λ=0.6328 μm) is directed from at the substrate as shown below in Figure 3-13 and in Figure 3-14

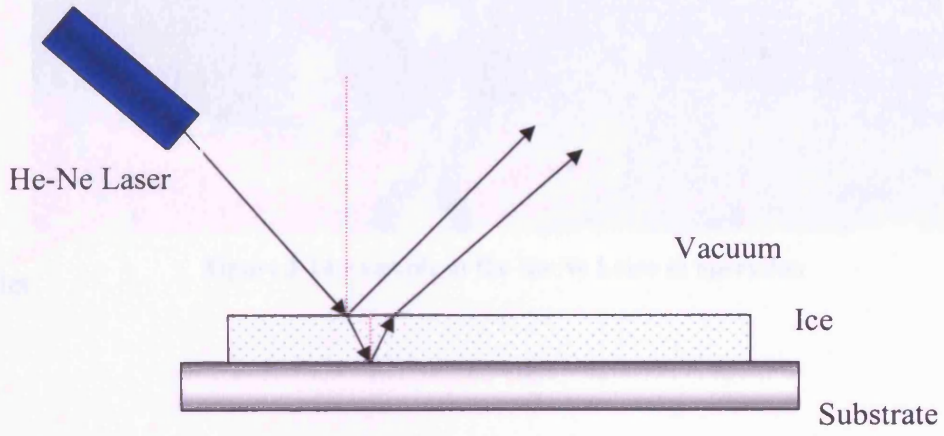

Figure 3-13 Setup of the He-Ne Laser

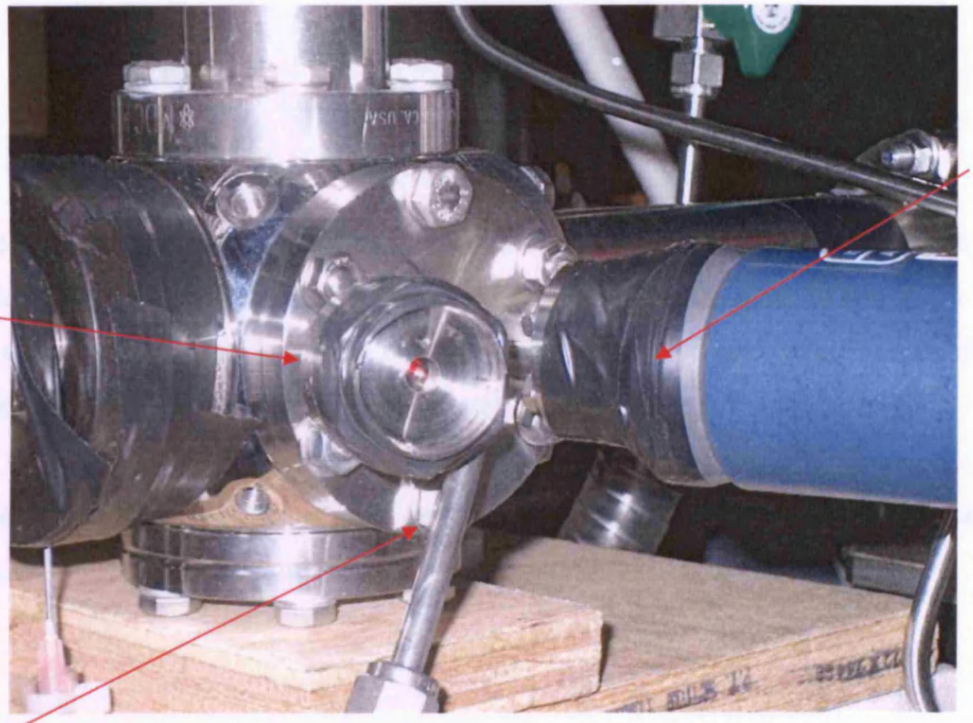

Figure 3-14 Example of the He-Ne Laser in operation

A photodiode is used to measure the output of the reflected beam. The laser enters the chamber via a modified CF40 flange. Two CF16 ports were welded onto the flange at an angle of 20° (Figure 3-14) They are then connected to a CaF_2 window. In between the two CF16 ports is a 6 mm swagelok tube used to dose the gas into the system so that we can deposit and take thickness measurements simultaneously. The procedure for taking measurements is as follows. Using the diode and a Keithly Electrometer we measure the base current on the diode. We align the angle of the substrate and the height of the laser to a constant and known position that maximises the signal on the diode. We then deposit a fixed amount of gas and measure the signal on the diode after deposition. This process is repeated several times so the thickness of the ice builds up and a clear sine wave pattern is visible from the plot of amount of gas deposited versus diode current. The period of this interference curve is then given by (3.4)

$$d = \frac{\lambda_0}{2n_f \cos\theta_f}$$ **(3.4) Thickness Equation (Baratta and Palumbo 1998)**

Where λ_0 is the laser wavelength, n_f is the refractive index of the ice and θ_f is the angle of reflection within the ice film. An estimate of the refractive index of the ice is found from the intensity ratio between minima and maxima of the interference fringes. (Baratta and Palumbo 1998), (Westley, Baratta et al. 1998)

The equation above can be simply derived by considering the interference patterns generated when light strikes a thin film on a substrate

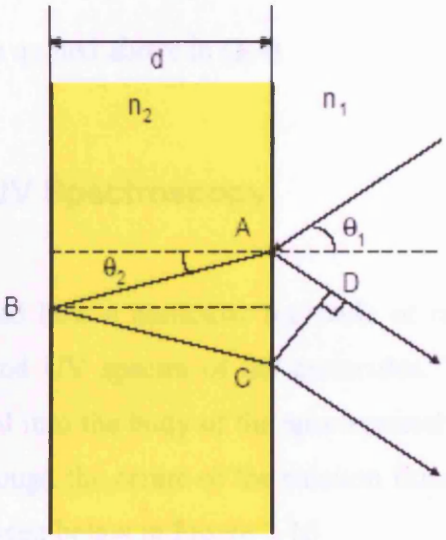

Figure 3-15 Thin Film Interference (Courtesy of Prof. A. H. Harker, UCL)

If we consider the path difference, Δ between paths AD and ABC we obtain

$$\Delta = n_2 (AB + BC) - n_1 (AD) \qquad (3.5)$$

Trigonometrically

$$AB = BC = d/\cos(\theta_2) \qquad (3.6)$$

From Snell's law

$$n_1 \sin(\theta_1) = n_2 \sin(\theta_2) \qquad (3.7)$$

Also

$$AD = AC \cos(90 - \theta_1) = AC \sin(\theta_1) \tag{3.8}$$

And

$$AC = 2\tan(\theta_2) \tag{3.9}$$

$$\begin{aligned}\Delta &= \frac{2n_2}{\cos(\theta_2)} - n_1 2d\frac{n_2}{n_1}\sin(\theta_2)\tan(\theta_2) \\ &= \frac{2dn_2}{\cos(\theta_2)}(1-\sin^2(\theta_2)) \\ &= 2n_2 d\cos(\theta_2)\end{aligned} \tag{3.10}$$

For interference to occur the path length difference must be equal to mλ

This leads us to the result quoted above in (3.4)

3.8.3 Infrared and UV Spectroscopy

Once we have determined how a particular molecule or mixture is deposited we can begin to take infrared and UV spectra of the molecules. In order to collect data the sample chamber is placed into the body of the spectrometer and aligned so that the UV or IR beam will pass through the centre of the calcium fluoride substrate. A diagram of this arrangement can be seen below in Figure 3-16

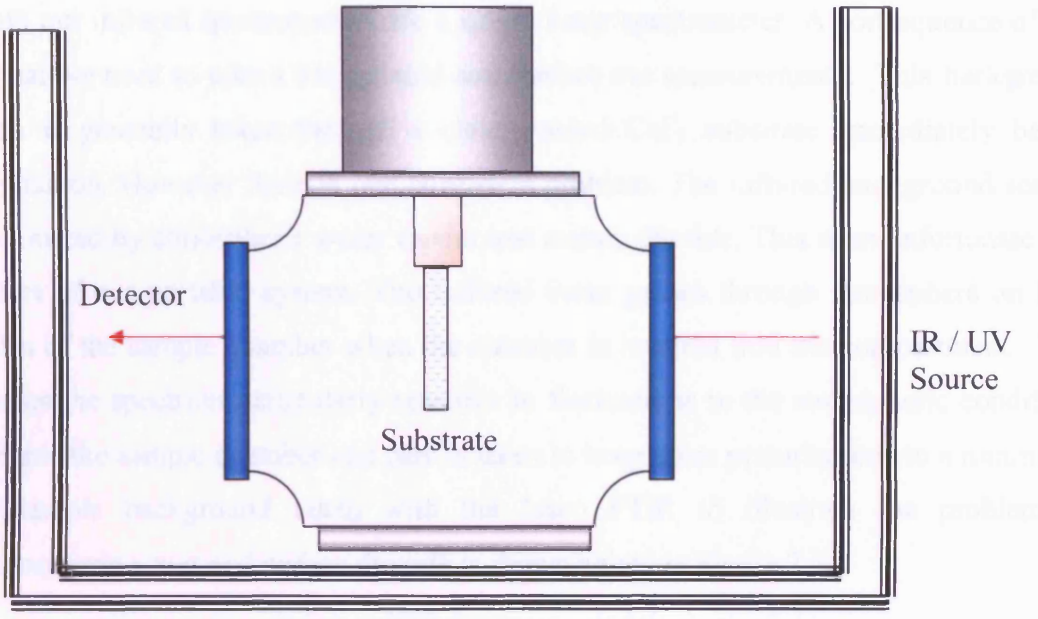

Figure 3-16 Arrangement of the chamber in the spectrometer compartment

Once the sample chamber is in place and aligned the experiment can be cooled and a background scan is taken at the working temperature. This is also a useful diagnostic for the condition of the substrate as any deviation from the expected background due to contamination from pervious experiments or atmospheric gases condensing on the substrate will be registered. In the next section the process of infrared and UV spectroscopy will be discussed in greater detail.

3.8.3.1 Infrared Spectroscopy.

Experiments performed at UCL, Queens University Belfast and the University of Aarhus initially used a Jasco 600*Plus* FTIR single beam spectrometer. The Jasco FTIR has a quoted optical range of 7800 – 350 cm^{-1}. However due to the CsI beam splitter, DLATGS detector and the presence of the CaF_2 windows which lead to a cut off at 1000 cm^{-1} we have an effective range of 4000- 1000 cm^{-1}. Later measurements were performed on a Nicolet FTIR. The Nicolet FTIR has a spectral range of 4000 to 1000 cm^{-1} again due to the CaF_2 windows used in our apparatus.

Both our infrared spectrometers are a single beam spectrometer. A consequence of this is that we need to take a background scan before our measurements. This background scan is generally taken through a clean cooled CaF_2 substrate immediately before deposition. However there is one consistent problem. The infrared background scan is dominated by atmospheric water vapour and carbon dioxide. This is an unfortunate side effect of our portable system. The infrared beam passes through atmosphere on both sides of the sample chamber when the chamber is lowered into the compartment. This makes the spectrum particularly sensitive to fluctuations in the atmospheric conditions outside the sample chamber and care is taken to keep these perturbations to a minimum. A sample background taken with the Jasco FTIR to illustrate the problem of atmospheric water and carbon dioxide is shown below in Figure 3-17

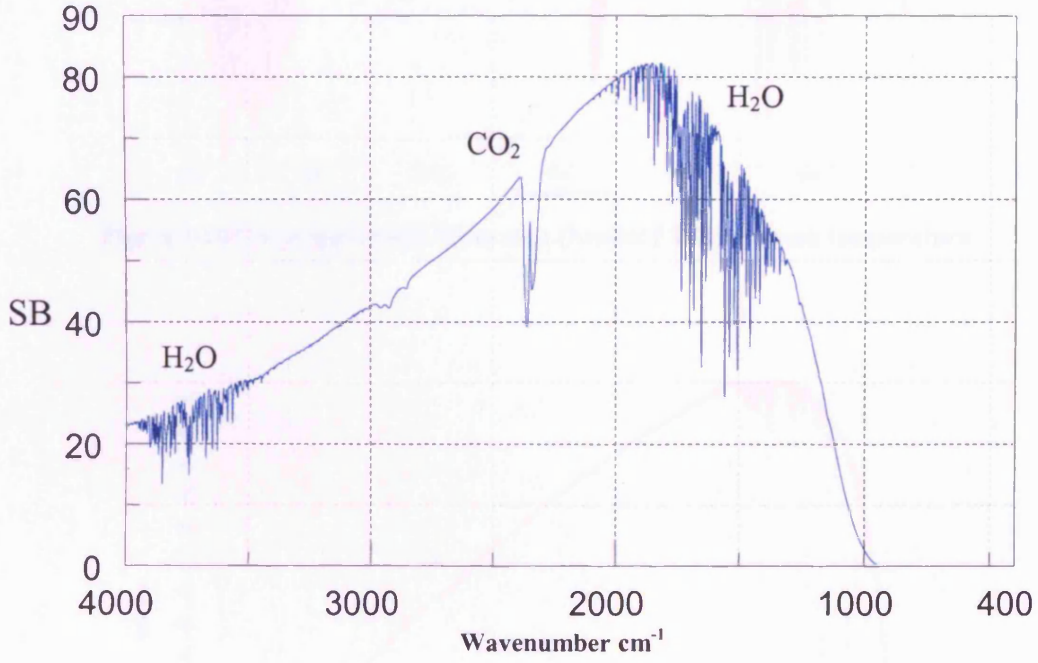

Figure 3-17 Sample background with Jasco 600*Plus* FTIR with no purge showing the large contamination problem of atmospheric water and carbon dioxide.

It can be seen that the main constituents of the background scan are atmospheric water and carbon dioxide and that the absorptions are significant. The Jasco FTIR provides a port for purging the internal optics of the sample chamber but the effect of purging is limited as the main contaminants come from the water and CO_2 present the beam path on either side of the CaF_2 windows in the spectrometer compartment.

For the new Nicolet FTIR however a purging system was purchased which allows the gap between CaF_2 windows and the infrared beam in the sample compartment to be purged with an infrared inert gas such as nitrogen, N_2. The effect of the purge is seen in Figure 3-18 and Figure 3-19. After an hour of purging the reduction in carbon dioxide and water in the spectrometer is readily visible.

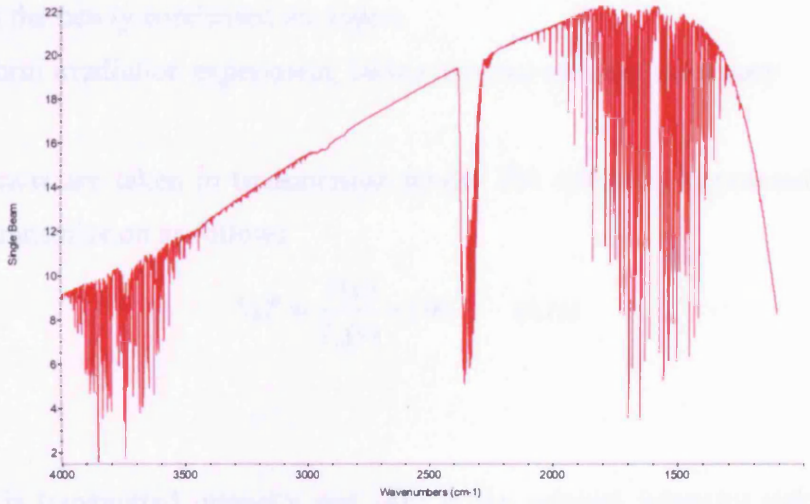

Figure 3-18 Un-purged single beam scan (Nicolet FTIR) at room temperature

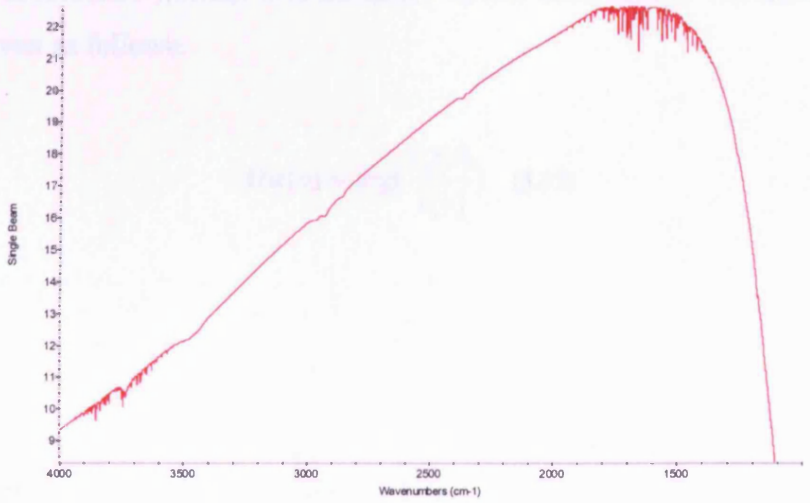

Figure 3-19 One Hour of Purging with Nitrogen (Nicolet FTIR) at room temperature

If the purge is maintained over a period of days combined with the use of a desiccant in the sample chamber then the reduction is water vapour and CO_2 is considerable.

A procedure for a typical scan would run as follows

1) Align the infrared beam with the centre of the substrate.
2) Take a background scan
3) Cool the substrate
4) Take a cool background
5) Prepare Ice layers
6) Scan the newly condensed ice layers.
7) Perform irradiation experiment, taking infrared scans as necessary

Generally scans are taken in transmission mode. The output is expressed in terms of percentage transmission as follows

$$\%T = \frac{I(\nu)}{I_0(\nu)} \times 100 \qquad (3.11)$$

Where I(v) is transmitted intensity and $I_0(v)$ is the original intensity (taken from the background scan). In some experiments (generally those using a silver mono crystal which does not transmit in the infrared and for comparison with published data much of which is in absorbance format) it is necessary to use absorbance. The absorbance of a sample is given as follows.

$$Abs(\nu) = \log(\frac{I_0(\nu)}{I(\nu)}) \qquad (3.12)$$

3.8.3.2 VUV and UV-VIS Spectroscopy.

In order to perform preliminary and test experiments in the laboratory at UCL a Shimadzu 2401PC spectrometer operating in the range 180 to 1010 nm was used. The spectrometer is capable of a resolution of 0.1 nm. The 180 nm cut off with all commercial UV-Vis spectrometers is due to absorptions by atmospheric gases. Purging with nitrogen can extend the range to 175 nm but this is rarely useful. Some preliminary tests on the system were done using the Shimadzu 2401PC spectrometer but all the UV spectra presented in this thesis were recorded using the ASTRID beamline.

In order to measure structure below the 180 nm range in the "Vacuum ultraviolet" range where a number of electronic transitions of interest occur we use the synchrotron radiation facility, the ASTRID UV1 beamline as a VUV spectrometer which allows us to extend our range to 125 nm . The cut off with UV1 is limited by the CaF_2 and LiF windows used in the system and in the beamline. A QL30F/RFI photomultiplier tube (PMT) is used to detect the UV light, which is scanned over the wavelength range ($120 < \lambda < 350$ nm) using a grating monochromator (as described in section 3.7.3.1) Unlike with infrared measurements the chamber is bolted directly onto the beamline. A LiF_2 window separates our chamber from the UV1 beamline reducing the risk of contamination of the storage ring from our sample. A diagram of the typical setup can be seen in Figure 3-20

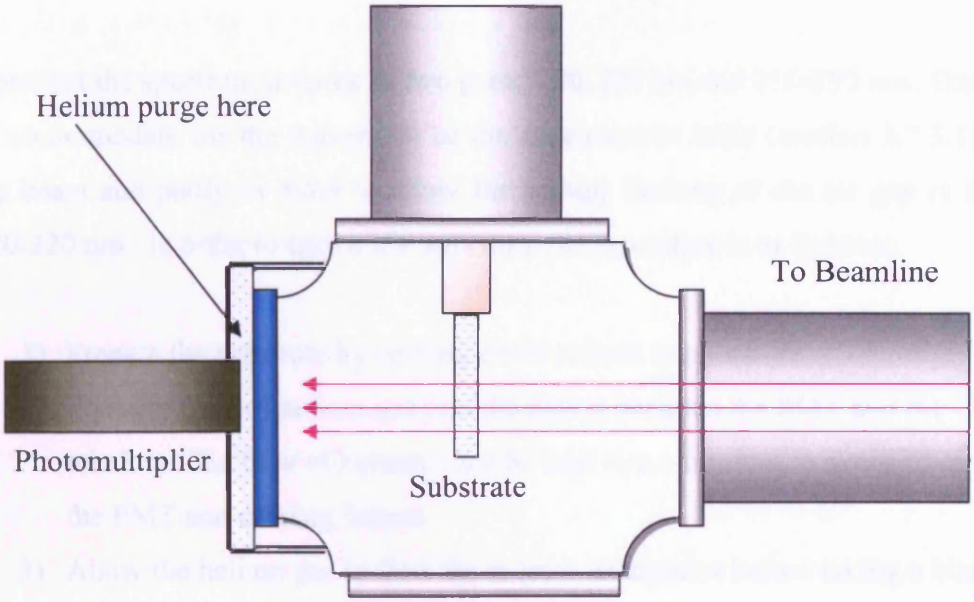

Figure 3-20 Typical setup of the chamber at the UV1 beamline

Between the CaF_2 window in our chamber and the PMT we enclose the area around the photomultiplier tube (PMT) with a rubber cap and purge the area with helium gas. This removes the absorption in our spectrum due to atmospheric oxygen lines. A typical purged background spectrum is shown in Figure 3-21

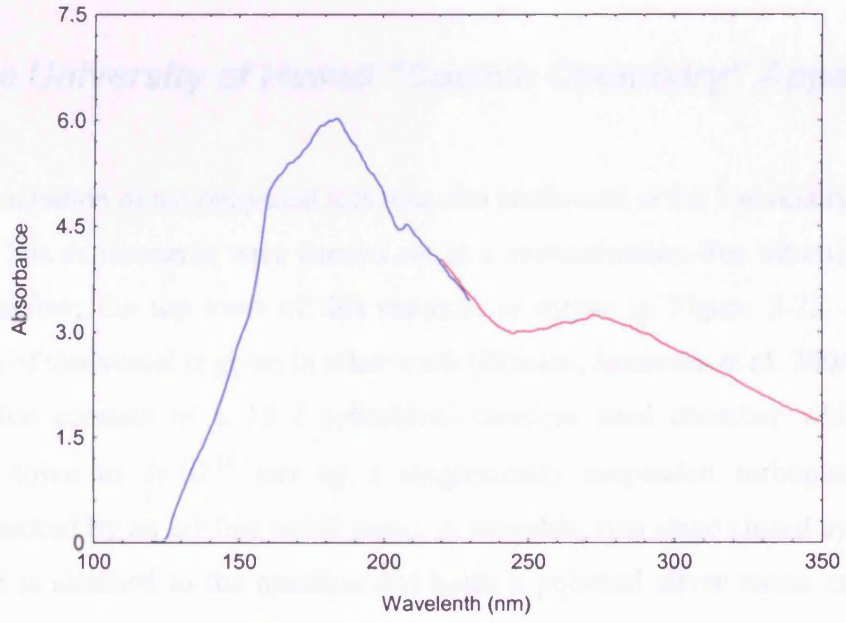

Figure 3-21 Sample UV Background with helium purge applied.

Note that the spectrum is taken in two parts. 120-220 nm and 210-350 nm. This is partly to accommodate for the movement of the spectrometer table (section 3.7.3.1) to focus the beam and partly in order to allow for helium flushing of the air gap in the region 120-220 nm. In order to take a UV spectrum the procedure is as follows:

1) Prepare the substrate by cooling down to base temperature
2) Start the flow of helium gas into the region between the PMT and the CaF_2 window. The flow of helium must be kept to a minimum to avoid "overloading" the PMT and causing failure.
3) Allow the helium gas to flow for at least 10 minutes before taking a blank background scan in the region 120-220 nm. Check the table position is located at -500 K
4) Repeat the above step to ensure consistency and that the helium purge is at a constant rate and there is no change in the background levels.
5) After taking the scan in the region 120-220 nm shut off the helium flow and scan the region 210-350 nm (Table position should be 250K)
6) Form ice surface by deposition gas / gases onto the substrate and perform the necessary irradiation / scans.

3.9 The University of Hawaii "Cosmic Chemistry" Apparatus

Electron irradiation of astrophysical ices was also performed at the University of Hawaii at Manoa. The experiments were carried out in a contamination-free ultrahigh vacuum (UHV) chamber; the top view of this machine is shown in Figure 3-22. A detailed description of this vessel is given in other work (Bennett, Jamieson et al. 2004)
The machine consists of a 15 *l* cylindrical stainless steel chamber which can be evacuated down to 2×10^{-10} torr by a magnetically suspended turbopump (Osaka Vacuum) backed by an oil-free scroll pump. A rotatable, two stage closed cycle helium refrigerator is attached to the machine and holds a polished silver mono crystal. This crystal is cooled to 10.8 ± 0.2 K and serves as a substrate for the ice mixture. The ice condensation is performed using a precision leak valve. The latter is connected to a gas reservoir and is attached on a linear transfer mechanism. During the gas condensation,

the deposition system is moved 5 mm in front of the silver target. This experimental arrangement guarantees a reproducible thickness and composition of the ices at 10 K. The electron gun used in all the experiments was Vacuum Technical Electron Source (model number EQ 22/35). All experiments were performed at 5keV electron energy. The electron beam is scanned over an area of 3.0 ± 0.4 cm^2 . The cryostat is heated by using a cartridge heater mounted into the cold head.

Infrared data was collected using a Nicolet 510 DX FTIR spectrometer (5000 - 500 cm^{-1}). Due to the use of a silver mono crystal we operate the FTIR in absorption–reflection–absorption mode at an angle of 75°. The infrared beam exits the spectrometer and is coupled via a mirror 'flipper' outside the spectrometer. It then passes through a differentially pumped potassium bromide (KBr) window into the ice sample, is reflected off the silver crystal and then exits the chamber via another differentially pumped KBr window. The infrared light is detected by an external liquid nitrogen cooled MCTB detector.

Simultaneously we have also collected mass spectrum data. A quadrupole mass spectrometer (Balzer QMG 420; 1–200 amu mass range) is used to detect gas phase products released from the ice matrix. The mass spectrum is tuned to suitable dwell times for the masses we are detecting in each experimental run (typically between 0.5 and 1s duration)

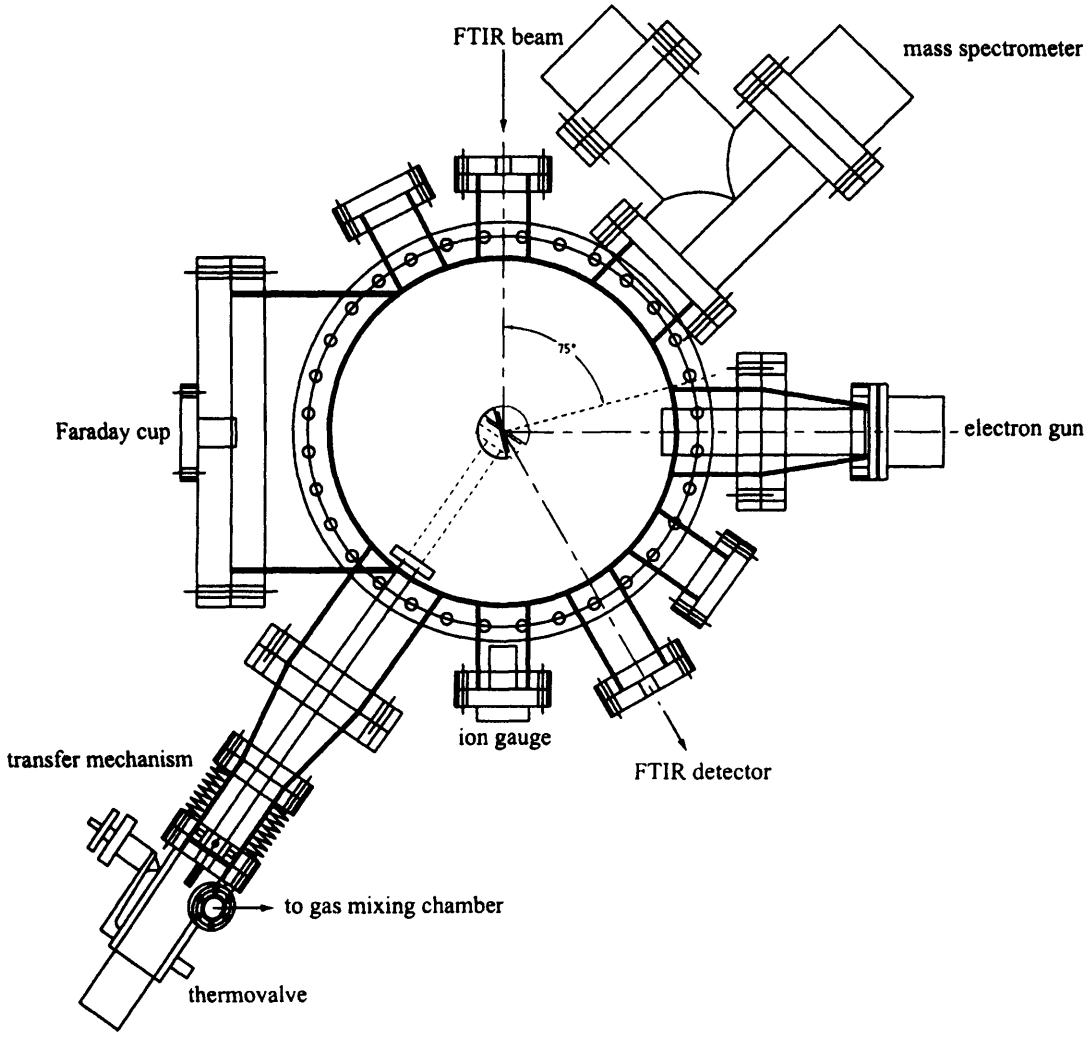

Figure 3-22 The University of Hawaii Apparatus

Chapter Four

Ion Bombardment Experiments

"Experiments should be reproducible – they should all fail in the same way."

--Anon

4.1 Introduction

Ion induced chemistry plays an important role in the formation of molecules in the interstellar medium. It is also particularly applicable to our own solar system in the case of Jupiter and the outer planets. It was known in the 1970's and 80's that Jupiter was a source of energetic ions and electrons from the Voyager probe flybys. The Cassini-Huygens probe has recently reported the Jovian moon Io as a possible source of these ions. (Krimigis, Mitchel et al. 2002) report the detection of H^+, He^+, He^{2+}, O^+, S^+, and SO_2^+ (or S_2^+) probably originating from volcanic out gassing on Io.

During the initial testing phase of our experimental apparatus we irradiated some simple mixtures of CO_2 and H_2O in order to test the attachment of our system to an ion source. We were then able to compare these results obtained to a previously published work on similar ice mixtures. Our preliminary experiments are detailed below.

4.2 Irradiation of Pure CO_2 ices

4.2.1 1 keV He^+ Irradiation of CO_2 ice films

This experiment was performed using the ECR ion source as described in Chapter 3. All data was collected using the Jasco 600 Plus FTIR operating in transmission mode. A calcium fluoride (CaF_2) substrate was cooled down using liquid helium as the cryogen. Due to cooling difficulties in the cryostat the liquid helium cooling achieved a base temperature of 90 K although due to later problems found in the temperature sensor this value may be subject to error. Later experiments with Liquid Helium achieved a base temperature of 22 K (See Chapter 5)

After cooling the substrate we recorded a background infrared scan. Spectral resolution was 1 cm^{-1}. A background scan before deposition and irradiation was recorded. We then deposited 10 mbar of CO_2 in 19 min 11 seconds. Figure 4-1, Table 4-1

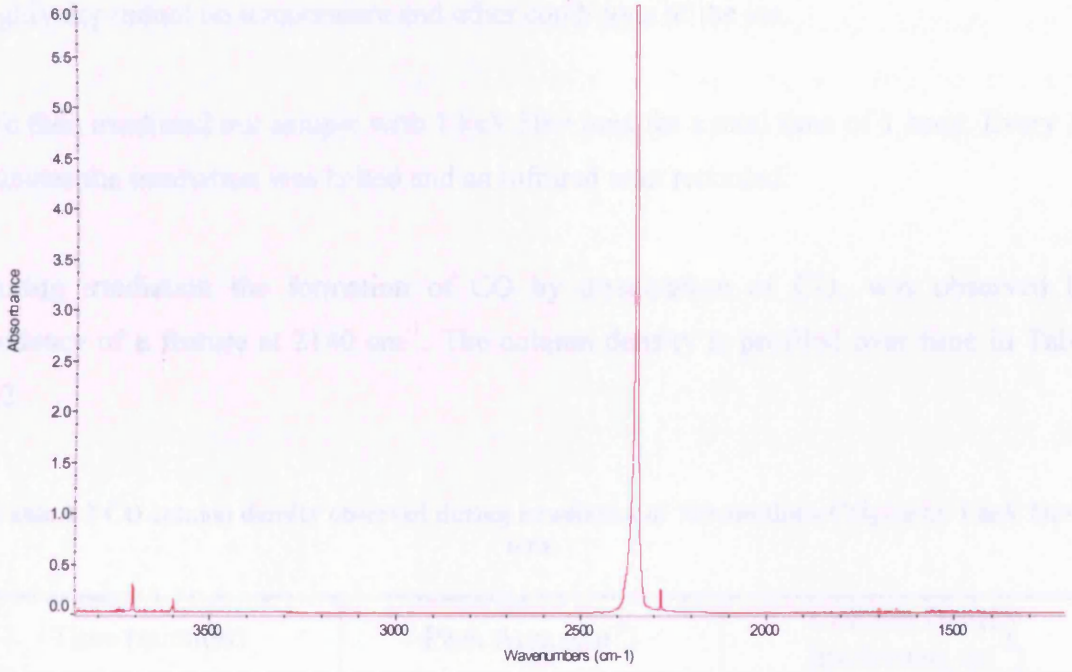

Figure 4-1 An IR spectrum recorded for 10 mbar CO_2 Ice at 90 K

Table 4-1 Features observed in IR spectrum of CO_2 ice at 90 K

Peak Position (cm^{-1})	Assignment	Absorption Coefficient (molecules cm^{-1})
3708	$\nu_1 + \nu_3$	1.4×10^{-18}
3600	$2\nu_2 + \nu_3$	4.5×10^{-19}
2343	ν_3 (asym. stretch)	-
2282	ν_3 ($^{13}CO_2$)	7.8×10^{-17}

Using the Beer-Lambert law (Chapter 3) and the integrated absorption coefficients of CO_2 in Table 4-1 we calculate a column density of $1.63 \pm 0.05 \times 10^{18}$ molecules cm^{-2}. Adopting a density of 1.7 g cm^{-3} for CO_2 (Klinger, Benest et al. 1985) this translates to a thickness of 700 ± 20 nm for our pure CO_2 ice sample. The error on the column density and ice thickness is calculated by averaging the column density calculated over 2 absorption peaks of CO_2. Note however that any error on the absorption coefficient is not taken into account. Absorption coefficients are by nature uncertain as they can be highly dependant on temperature and other conditions of the ice.

We then irradiated our sample with 1 keV He+ ions for a total time of 1 hour. Every 15 minutes the irradiation was halted and an infrared scan recorded.

During irradiation the formation of CO by dissociation of CO_2 was observed by evidence of a feature at 2140 cm^{-1}. The column density is profiled over time in Table 4-2.

Table 4-2 CO column density observed during irradiation of 700 nm thick CO_2 ice by 1 keV He+ ions.

Time (minutes)	Peak Area (cm^{-1})	Column Density (molecules.cm^{-2})
0	0	0
15	0.1063	1.44 E+16
30	0.1254	1.69 E+16
45	0.1458	1.97 E+16
60	0.1672	2.26 E+16

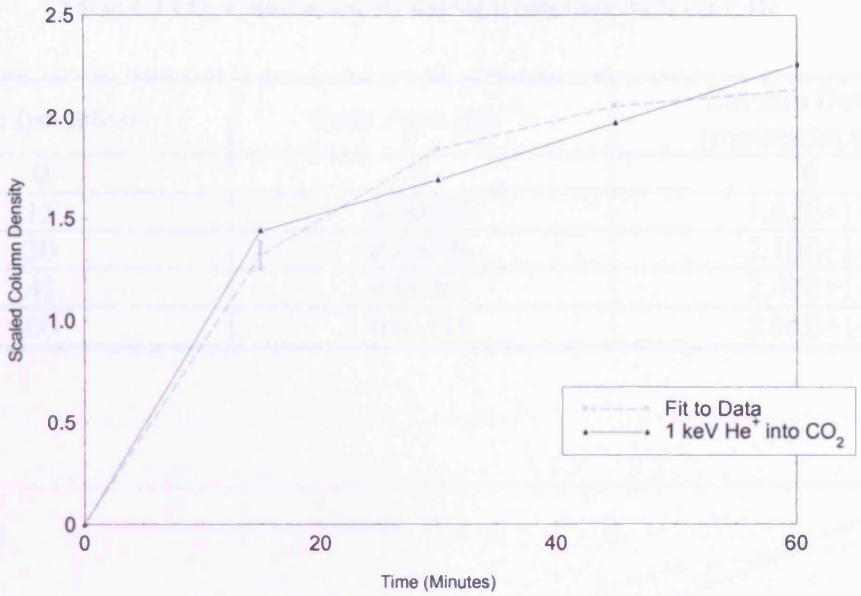

Figure 4-2 CO Column density during irradiation with 1 keV He^+

The rate of formation of CO is plotted in Figure 4-2. (Note that the column density is scaled by a factor of 1×10^{16} in the figure to allow for the fitting software used to perform the fit.) Recall from Chapter 2 the equation describing consecutive reactions. As we expect CO to be the direct product of CO_2 We can plot the formation of CO using the equation

$$[CO] = A(1 - \exp(-kx)) \tag{4.1}$$

This is shown by the blue line in Figure 4-2, the data fit predicts a value of A=2.18 and k= 0.0614

We also found evidence for formation of CO_3 in our sample at 2044 cm^{-1}. However we also have an unknown contaminant present at 2041 cm^{-1} which was present after deposition. This is assumed to have been at a constant level during the experiment and is subtracted from the CO_3 profile. The contaminant is most likely due to the age of the CO_2 gas bottle used in these preliminary experiments. Later experiments on the UV irradiation of CO_2 did not show this contamination. CO_3 column densities were calculated using an absorption coefficient of 8.7×10^{-17} cm $molecule^{-1}$. (Bennett, Jamieson et al. 2004)

Table 4-3 CO_3 Column density during irradiation with 1keV He^+

Time (minutes)	Peak Area (cm^{-1})	Column Density ($molecules.cm^{-2}$)
0	0	0
15	0.00689	1.82E+14
30	0.00794	2.10E+14
45	0.00941	2.49E+14
60	0.01116	2.95E+14

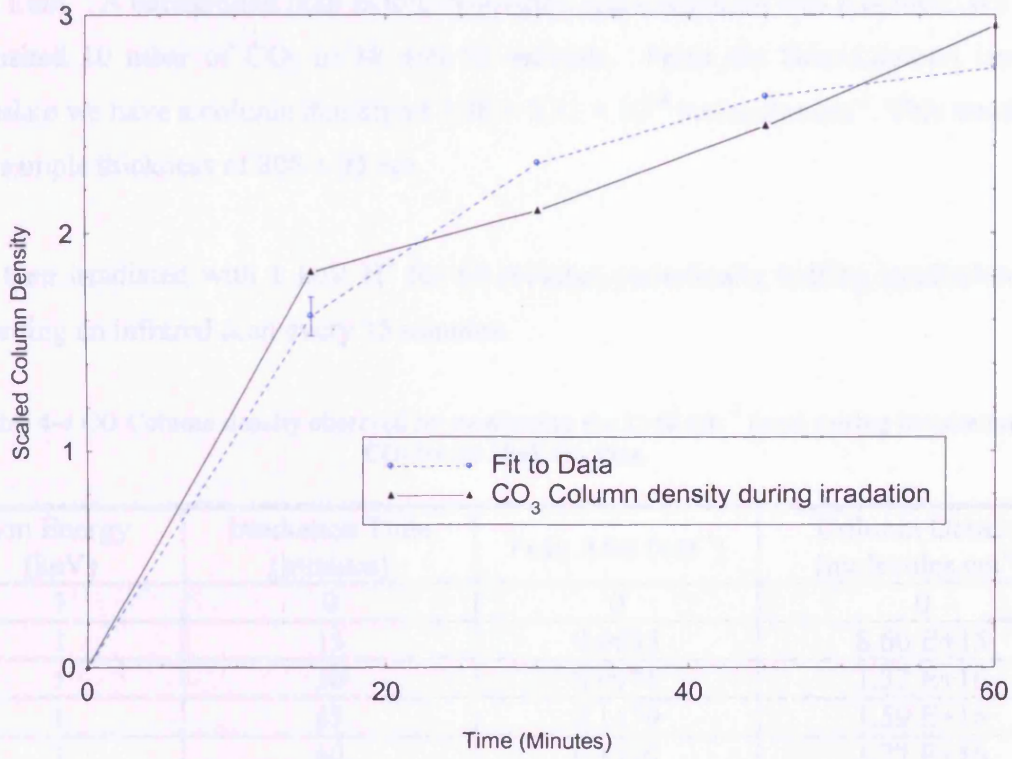

Figure 4-3 CO_3 column density during irradiation with 1 keV He^+

We can plot the formation of CO_3 using the equation

$$[CO_3] = C(1 - \exp(-jx)) \tag{4.2}$$

This is shown by the blue line in Figure 4-3. We obtain a value of C=2.85 and j= 0.0556

4.2.2 1 keV H^+ irradiation of pure CO_2 ices

This experiment was performed using the ECR ion source as described in Chapter 3. All data was collected using the Jasco 600 Plus FTIR operating in transmission mode. A calcium fluoride (CaF_2) substrate was cooled using liquid helium as the cryogen. We achieved a base temperature of 90 K.

After cooling the substrate we recorded a background infrared scan. Spectral resolution was 1 cm^{-1}. A background scan before deposition and irradiation was recorded. We then deposited 10 mbar of CO_2 in 18 min 53 seconds. From the Beer-Lambert law we calculate we have a column density of $1.88 \pm 0.21 \times 10^{18}$ molecules cm^{-2}. This translates to a sample thickness of 808 ± 95 nm.

We then irradiated with 1 keV H^+ for 60 minutes periodically halting irradiation and recording an infrared scan every 15 minutes.

Table 4-4 CO Column density observed by monitoring the 2140 cm^{-1} band during irradiation of CO_2 ice by 1keV H+ ions.

Ion Energy (keV)	Irradiation Time (minutes)	Peak Area (cm^{-1})	Column Density (molecules.cm^{-2})
1	0	0	0
1	15	0.0635	8.60 E+15
1	30	0.0976	1.32 E+16
1	45	0.1179	1.59 E+16
1	60	0.1310	1.77 E+16
2	75	0.2566	3.47 E+16
2	90	0.3143	4.25 E+16

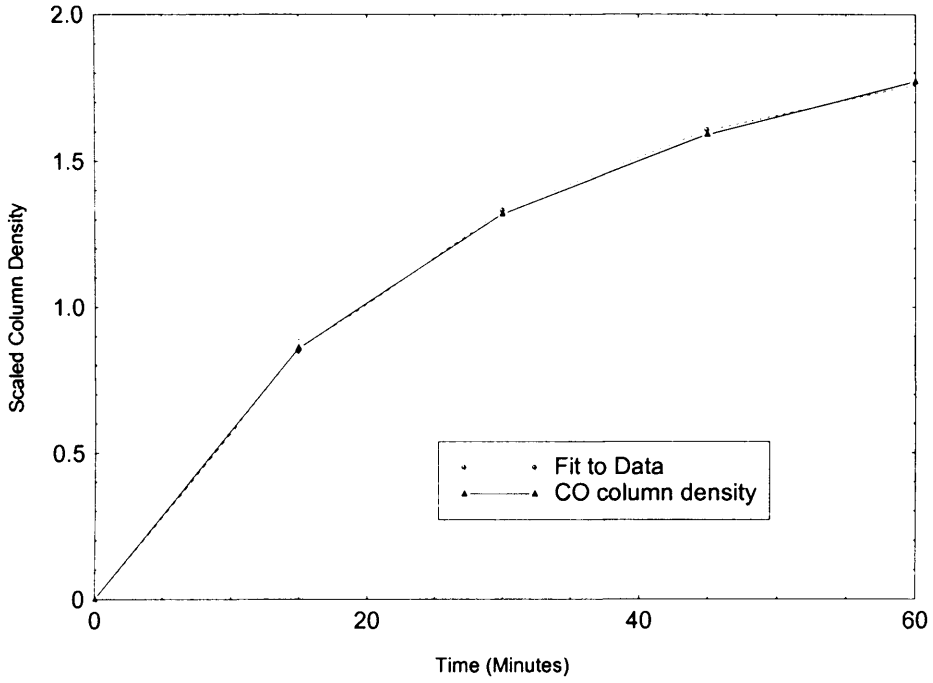

Figure 4-4 CO Column Density during irradiation of pure CO_2 ice with 1 keV H+

The CO column density for the 1keV irradiation was fit with equation (4.1). From this we obtain A=19.6 and k=0.0375

We also observe carbon trioxide, CO_3 in our ice at 2044 cm^{-1}. Table 4-5

Table 4-5 CO_3 Column density during irradiation of CO_2 Ice by 1 keV H^+ ions

Time (minutes)	Peak Area (cm^{-1})	Column Density (molecules.cm^{-2})
0	0	0
15	0.0308	8.15E+14
30	0.0343	9.08E+14
45	0.0359	9.50E+14
60	0.0362	9.58E+14

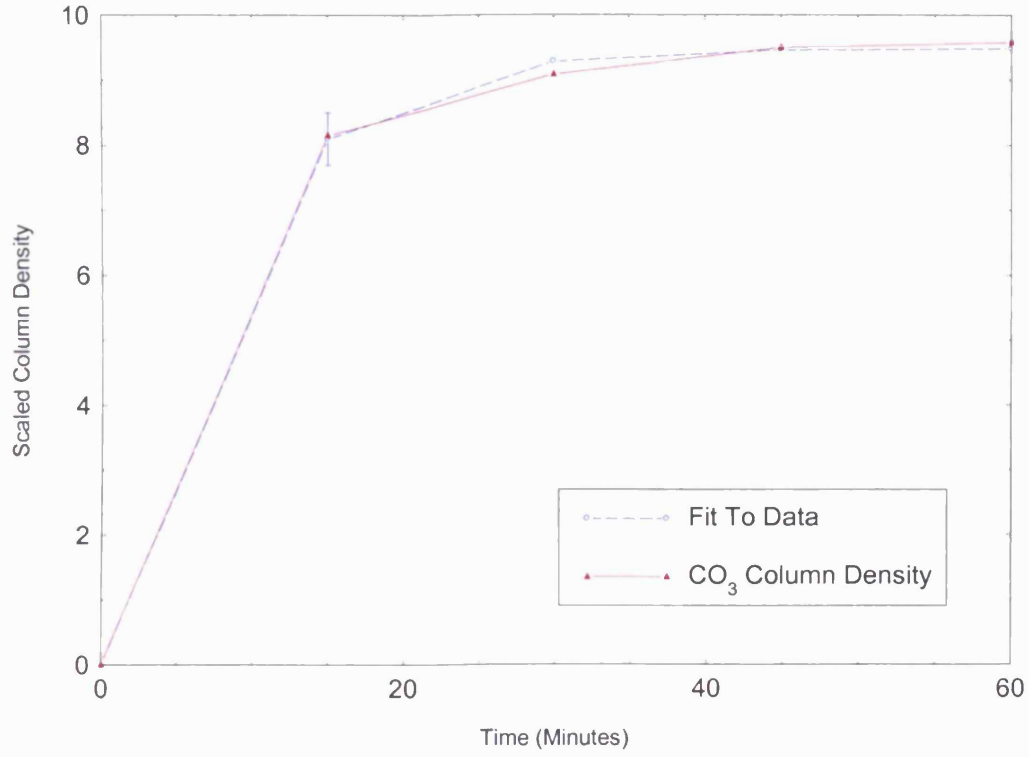

Figure 4-5 CO_3 Column Density During Irradiation of pure CO_2 ice with 1 keV H^+

We can plot the formation of CO_3 using the equation

$$[CO_3] = C(1 - \exp(-jx)) \tag{4.3}$$

This is shown by the blue line in Figure 4-5. From the we obtain a value of C=9.48 and j= 0.12

4.2.3 Discussion on CO formation in CO_2 irradiated ices

We may expect that carbon dioxide will dissociate in the following way when bombarded by ions

$$CO_2\ (X\ ^1\Sigma_g^+) \rightarrow CO\ (X\ ^1\Sigma^+) + O(^3P) \qquad (4.1)$$
$$CO_2\ (X\ ^1\Sigma_g^+) \rightarrow CO\ (X\ ^1\Sigma^+) + O(^1D)$$

The direct product of carbon dioxide dissociation is carbon monoxide, CO as observed in our ice layers.

Table 4-6 Summary of CO formation in CO_2 ice in both He^+ and H^+ irradiation.

Ion	Energy (keV)	Time (minutes)	CO Column Density (molecules cm^{-2})	Total Fluence (10^{15} ions cm^{-2})	A	k	Initial CO_2 Column Density (molecules cm^{-2})
He^+	1	0	0	0	2.18	0.0614	1.63×10^{18}
He^+	1	15	1.44×10^{16}	1.98			
He^+	1	30	1.69×10^{16}	4.36			
He^+	1	45	1.97×10^{16}	6.94			
He^+	1	60	2.26×10^{16}	9.71			
H^+	1	0	0	0	19.6	0.0375	1.8×10^{18}
H^+	1	15	8.60×10^{15}	2.18			
H^+	1	30	1.32×10^{16}	4.36			
H^+	1	45	1.59×10^{16}	6.54			
H^+	1	60	1.77×10^{16}	8.52			

In both H^+ and He^+ irradiation CO is observed. In the case of He^+ irradiation the formation of CO is almost twice as fast as for the case of H^+ irradiation. The reason for this could be simply due to the fact that He^+ is a non-reactive ion. Protons however can take part in subsequent chemical reactions for example adding to the C=O bond in CO_2. The slower formation of CO in the case of proton irradiation could indicate that the protons are being used in the formation of other products, or that CO is being converted to other products. One such product would be the addition of hydrogen to CO_2 forming HOCO. The ν_2 HOCO radical is predicted to be observable at 1848 cm^{-1} but we see no evidence for this in our spectrum. Previous studies of 1.5 keV H^+ irradiation of CO_2 have also suggested that H_2CO_3 carbonic acid may be produced (Brucato, Palumbo et al. 1997) during 10 K irradiation of CO_2 ice. We see no evidence for carbonic acid in our spectrum. This could possibly be due to the enhanced temperature and problems in cooling the sample.

We have also simulated the implantation of He^+ and H^+ ions into carbon dioxide using the SRIM (Stopping and Range of Ions in Matter) program. (Ziegler 2003)

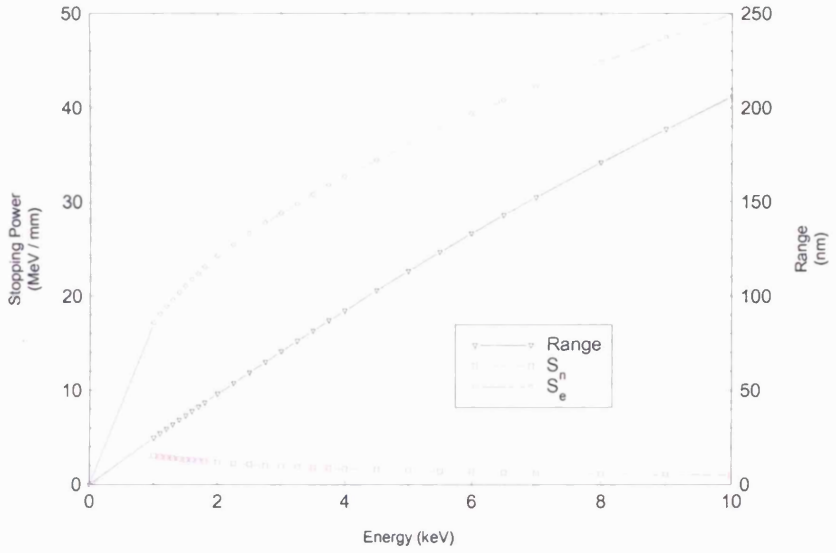

Figure 4-6 Range and Stopping Powers of H^+ into CO_2 ice as calculated by SRIM.

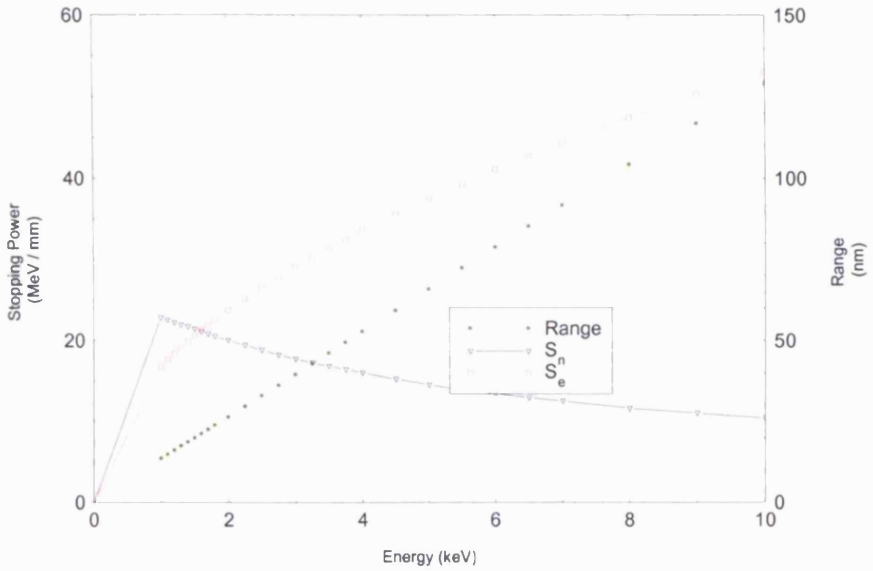

Figure 4-7 Range and Stopping Powers of He^+ into CO_2 ice

From the SRIM calculations we can see that we would expect the lighter hydrogen ions to penetrate further into the ice mass. At 1 keV we observe a greater contribution from electronic stopping than from nuclear stopping for H^+. The reverse is true for Helium. Overall as the final column densities after irradiation are so similar for He^+ irradiated and H^+ irradiated CO_2 ice it not possible to comment on the contribution from nuclear and electronic stopping for CO formation.

4.2.4 Discussion on CO_3 formation in CO_2 irradiated ices

The other spectroscopic product we can positively identify in our ice is CO_3. We observe the ν_1 2045 cm^{-1} CO_3 fundamental in both the He^+ irradiation and the H^+ irradiation.

Table 4-7 Summary of CO_3 formation.

Ion	Energy (keV)	Time (minutes)	CO_3 Column Density (molecules cm^{-2})	Total Fluence (10^{15} ions cm^{-2})	C	j	Initial CO_2 Column Density (molecules cm^{-2})
He^+	1	0	0	0	2.85	0.055	1.63×10^{18}
He^+	1	15	1.82E+14	1.98			
He^+	1	30	2.10E+14	4.36			
He^+	1	45	2.02E+14	6.94			
He^+	1	60	2.95E+14	9.71	9.48	0.12	1.8×10^{18}
H^+	1	0	0	0			
H^+	1	15	8.15E+14	2.18			
H^+	1	30	9.08E+14	4.36			
H^+	1	45	9.50E+14	6.54			
H^+	1	60	9.58E+14	8.52			

CO_3 is formed by the addition of oxygen radicals to CO_2. From (4.1) we observe there are two possibilities of forming oxygen radicals. Either in the ^1D state or the ^3P state. (Bennett, Jamieson et al. 2004) predict the reaction of $O(^1D)$ + CO_2 ($X\ ^1\Sigma_g^+$) → CO_3 (X^1A_1) to form the C_{2V} bridged structure of CO_3. There is an enhanced column density of CO_3 in the case of proton irradiation compared to helium ion bombardment. This could suggest that electronic inelastic collisions play a role in generating $O(^1D)$.

4.3 Irradiation of pure H_2O films.

Water ice was irradiated by protons and C^+ and C^{2+} ions. Unlike He^+ ions, C^+ and C^{2+} ions are reactive and can initiate chemical reactions as well as transferring energy to break chemical bonds.

4.3.1 4 keV C^+ Ions

Our ice samples were prepared at ~100 K. The water sample was purified to remove any trace gases by undergoing 2 or 3 cycles of freeze, pump, thawing. 10 mbar of water was then deposited on our cooled CaF_2 substrate in 50 seconds. Figure 4-8

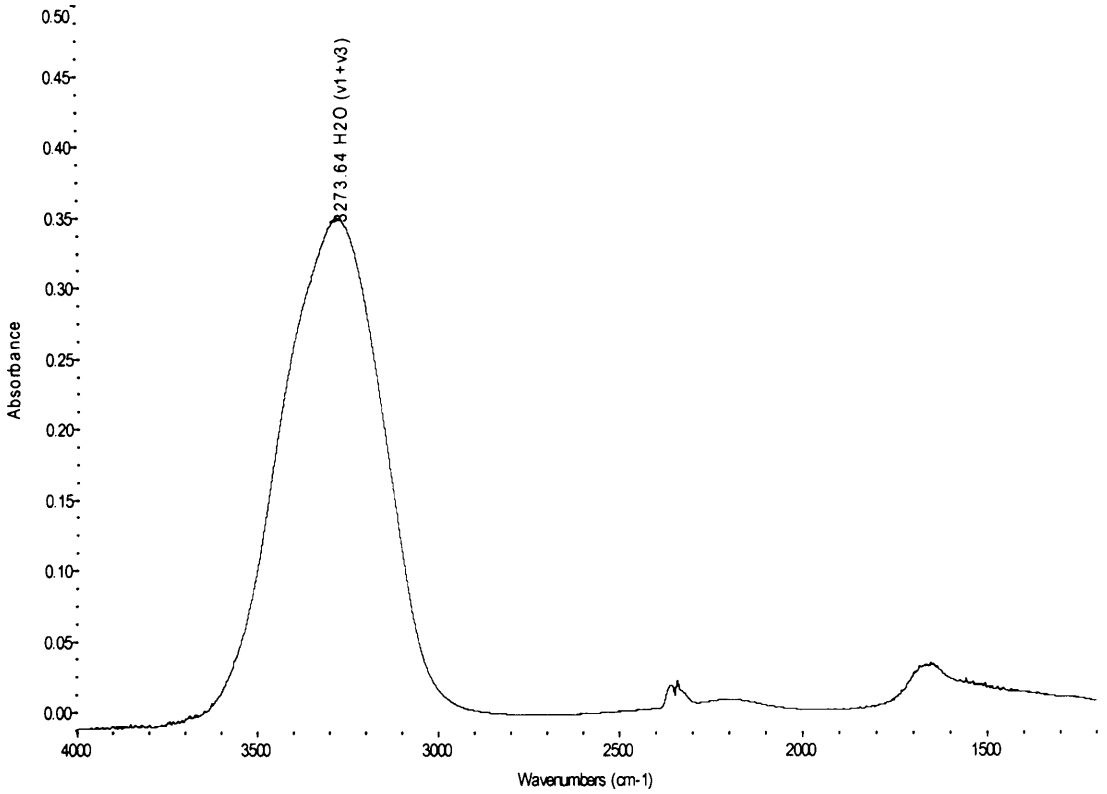

Figure 4-8 H_2O spectrum at ~100 K

Table 4-8 H_2O deposited at 100 K

Peak Position (cm^{-1})	Assignment
3278	ν_1, ν_3
2196	$\nu_2 + \nu_{libration}$ or $3\nu_{libration}$
1653	ν_2

4.3 Irradiation of pure H_2O films.

Water ice was irradiated by protons and C^+ and C^{2+} ions. Unlike He^+ ions, C^+ and C^{2+} ions are reactive and can initiate chemical reactions as well as transferring energy to break chemical bonds.

4.3.1 4 keV C^+ Ions

Our ice samples were prepared at ~100 K. The water sample was purified to remove any trace gases by undergoing 2 or 3 cycles of freeze, pump, thawing. 10 mbar of water was then deposited on our cooled CaF_2 substrate in 50 seconds. Figure 4-8

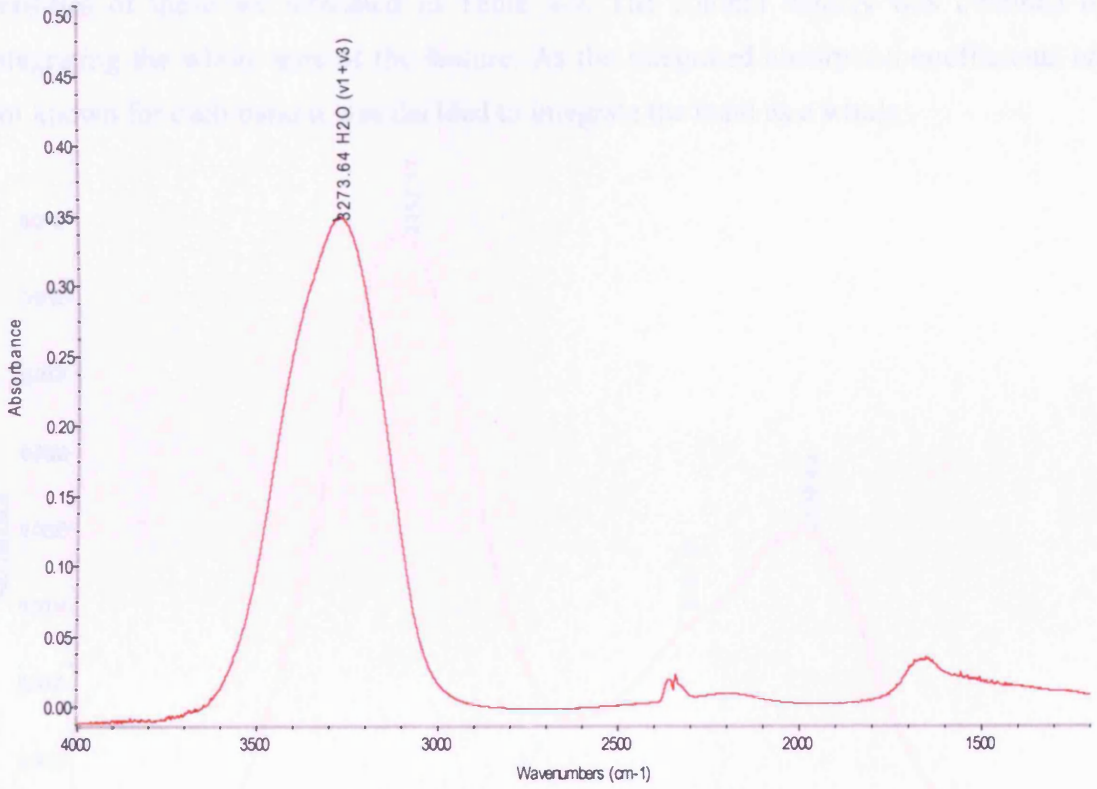

Figure 4-8 H_2O spectrum at ~100 K

Table 4-8 H_2O deposited at 100 K

Peak Position (cm^{-1})	Assignment
3278	ν_1, ν_3
2196	$\nu_2 + \nu_{libration}$ or $3\nu_{libration}$
1653	ν_2

We calculate the column density of water to be 1.3×10^{18} molecules cm^{-2}. This translates to a water ice thickness of 370 nm adopting an ice density of 1 gm cm^{-3} . (Using an absorption coefficient of $A=2.2 \times 10^{-16}$ cm $molecule^{-1}$ (Gerakines, Schutte et al. 1995)). We can assume an error of approximately 10 % on our calculated column density.

The ice sample was then irradiated for 90 minutes with 4 keV C^+ ions. At 15 minute intervals the irradiation was halted and an infrared spectrum of the ice recorded.

After irradiation we see several absorption bands in the ice film. We observe CO formation at 2152 cm^{-1} and 2136 cm^{-1} and a shoulder at 2140 cm^{-1}. The total column densities of these are tabulated in Table 4-9. The column density was obtained by integrating the whole area of the feature. As the integrated absorption coefficients are not known for each band it was decided to integrate the band as a whole

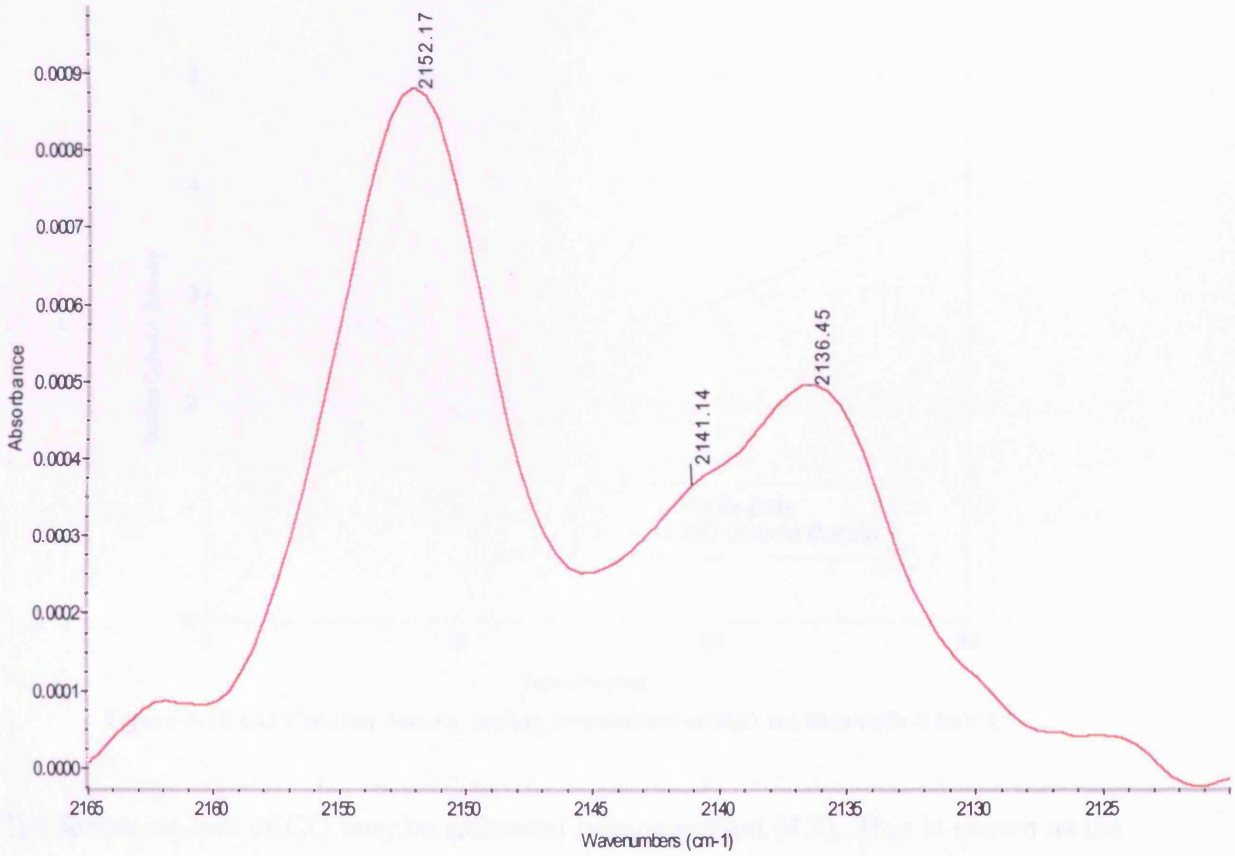

Figure 4-9 CO formation after 90 minutes of 4 keV C^+ irradiation of water ice film at ~100 K

Irradiation Time (minutes)	Peak Area (cm^{-1})	Column Density ($molecules.cm^{-2}$)
0	0	0
15	0.00544	1.39E+15
30	0.00737	1.88E+15
45	0.00917	2.30E+15
60	0.01134	2.90E+15
75	0.01346	3.44E+15
90	0.01603	4.10E+15

Table 4-9 CO Column densities during irradiation of H_2O ice film with 4 keV C^+ ions

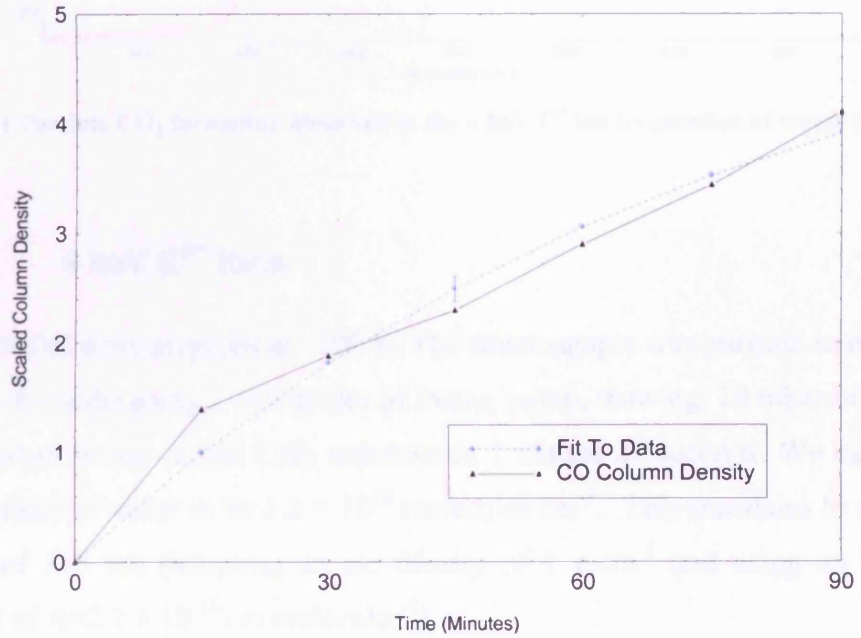

Figure 4-10 CO Column density during irradiation of H_2O ice film with 4 keV C^+

The formation rate of CO may be estimated using equation (4.2). This is shown as the blue line in Figure 4-10 From the we obtain a value of A=5.76 and k= 0.0126

We also observe tentative evidence for CO_2 formation in our irradiated ice. However there does appear to be a contaminant of CO_2 present in the original spectrum, most likely from atmospheric CO_2 present along the beam path and so it was not possible to gain any meaningful quantitative analysis from our data. The red line in Figure 4-11 shows the spectrum after 60 minutes of irradiation. The purple line is the initial spectrum before irradiation. There is no evidence for any other bands of CO_2 present.

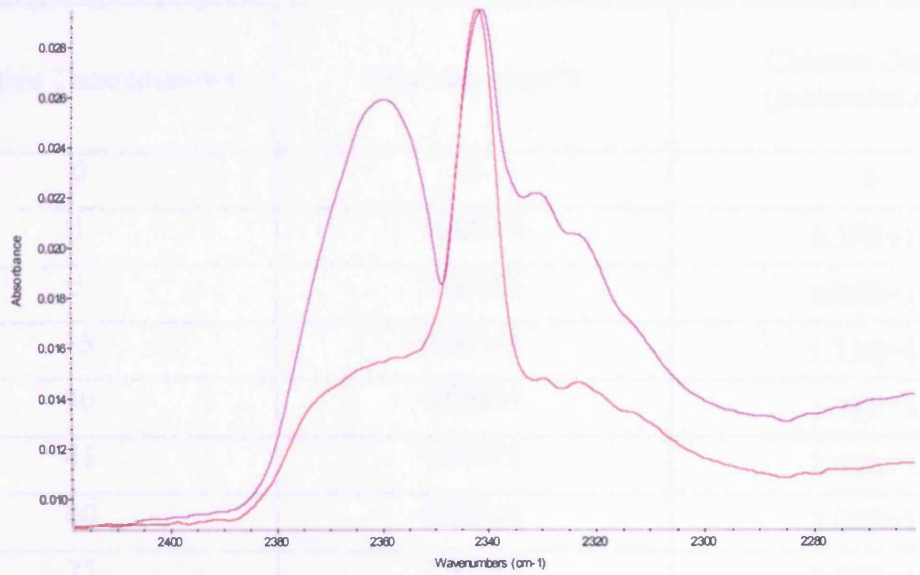

Figure 4-11 Possible CO_2 formation observed in the 4 keV C^+ ion irradiation of water ice at 100 K

4.3.2 4 keV C^{2+} Ions

Our ice samples were prepared at ~100 K. The water sample was purified to remove any trace gases by undergoing 2 or 3 cycles of freeze, pump, thawing. 10 mbar of water was then deposited on our cooled CaF_2 substrate in 1 minute 21 seconds. We calculate the column density of water to be 1.2×10^{18} molecules cm^{-2}. This translates to a water ice thickness of 350 nm (adopting an ice density of 1 $g.cm^{-3}$ and using an absorption coefficient of $A=2.2 \times 10^{-16}$ cm $molecules^{-1}$).

The ice sample was then irradiated for 120 minutes with 4 keV C^{2+} ions. The irradiation was periodically halted and an infrared spectrum recorded. After irradiation we see several new absorption bands in the ice film. We observe CO formation at 2149 cm^{-1} and 2139 cm^{-1}. The total column densities of these features are tabulated in Table 4-10. The column density was obtained by integrating the whole area of the feature. As the

integrated absorption coefficients are not known for each band it was decided to integrate the band as a whole.

Table 4-10 CO Column density after irradiation of 100 K water ice film with 4 keV C^{2+} ions

Irradiation Time (minutes)	Peak Area (cm^{-1})	Column Density (molecules.cm^{-2})
0	0	0
1	0.00328	8.39E+14
5	0.00385	9.85E+14
15	0.00441	1.13E+15
30	0.00697	1.78E+15
45	0.00972	2.49E+15
60	0.01208	3.09E+15
75	0.01517	3.88E+15
90	0.01680	4.30E+15
120	0.01698	4.34E+15

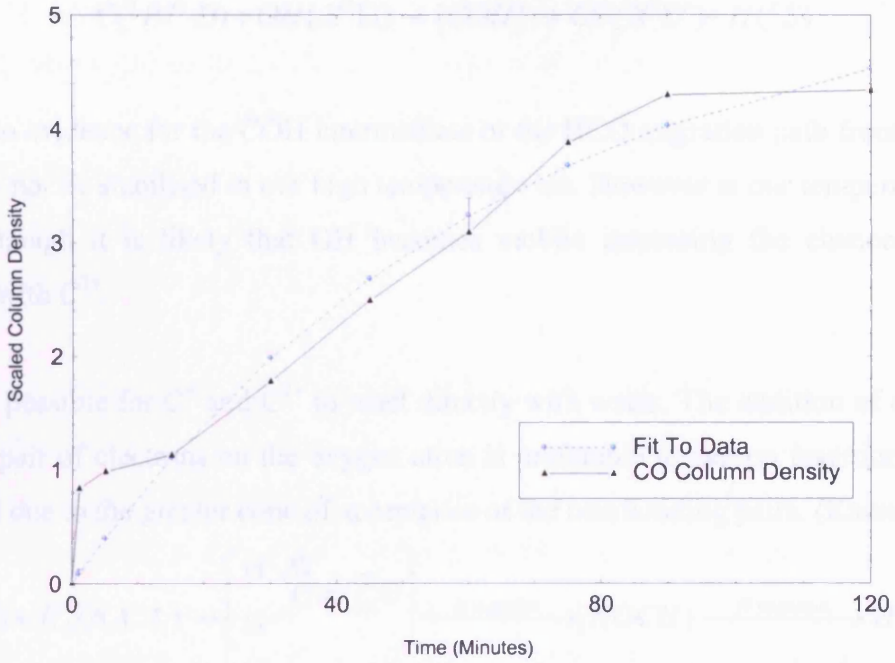

Figure 4-12 CO column density during irradiation of 100 K water ice film with 4 keV C^{2+}

We plot the formation of CO in Figure 4-12 (the column density is scaled by a factor of 10^{15}) and we fit an equation for the formation of CO using equation(4.3). This is shown by the blue line. From the we obtain a value of C=5.38 and j= 0.0152 .

Similarly as with the case of C^+ we can not gain any quantitative information on the formation of CO_2 due to contamination of the sample.

4.3.3 Discussion of H_2O irradiation.

The main product of carbon ion irradiation of H_2O ices is carbon monoxide CO. Upon irradiation water may dissociate into H + OH.

$$H_2O(X^1A_1) \longrightarrow H(^2S) + OH(X^2\Pi) \qquad (4.4)$$

Further dissociation of the OH molecule is possible forming O +H.
The implanted carbon ions may then react with oxygen atoms in the ice.

$$C + O(^3P) \rightarrow CO(X^1\Sigma^+) \qquad (4.5)$$

CO can also form from the reaction of carbon with OH radicals.

$$C(^3P/^3D) + OH(X^2\Pi) \rightarrow [COH] \rightarrow CO(X^1\Sigma^+) + H(^2S) \qquad (4.6)$$

We see no evidence for the COH intermediate or the HCO migration path from COH as these can not be stabilised in our high temperature ice. However at our temperatures of 100 K though it is likely that OH becomes mobile increasing the chances of OH reacting with C^{2+}.

It is also possible for C^+ and C^{2+} to react directly with water. The addition of carbon to the lone pair of electrons on the oxygen atom is preferable to carbon insertion into the OH bond due to the greater cone of acceptance of the non bonding pairs. (Kaiser 2002)

$$C(^3P/^1D) + H_2O(X^1A_1) \rightarrow \left[\begin{matrix} H \\ H \end{matrix} \!\!\diagdown\!\!\!\diagup \overset{\oplus}{O} = \underline{\overline{C}}^{\ominus} \right] \xrightarrow{H \text{ migration}} [HOCH] \xrightarrow{H \text{ migration}} H_2CO$$

We have observed that carbon monoxide is present in three possible locations in our water ice spectrum. We also note a small shift between the peak absorption positions in the case of C^+ and C^{2+} irradiation. It is well known that the CO molecule is a good indicator of the ice structure in which it is embedded. It is extremely sensitive to polar and non-polar ices. We define a polar ice as described in (Fraser, Collings et al. 2004). Polar ices are those dominated by hydrogen bonding networks and apolar ices are those with a typically Van der Waals bonding. Considering the C^+ case the 2152 cm^{-1} CO feature is often seen with CO in the presence of water as it is associated with CO bonded to OH dangling bonds in the water ice. (Fraser, Collings et al. 2004). The 2140 cm^{-1} feature is present as a small shoulder on the 2136 cm^{-1} band of CO. The 2140 feature is associated with pure CO. Finally the 2136 cm^{-1} feature of CO_2 is associated with CO embedded in a polar environment.

In the case of 4 keV C^{2+} irradiation we observe that the CO bonded to the OH dangling bond feature is seen at 2150 cm^{-1} and the pure CO absorption feature is seen at 2139 cm^{-1}, the polar CO component is seen as a shoulder at 2136 cm^{-1}.

What does this tell us about the structure of our ice and the formation of CO? The fact we see prominent bands centred at 2152 and 2136 cm^{-1} indicates we have at least two

sites of CO. As all our spectra are taken in transmission mode it is unlikely that we are seeing CO bonded to surface OH. We therefore need to consider the structure of water ice at our 100 K temperature. Water ice can take many structures often with large pores. (Ayotte, Smith et al. 2001) At 100 K we also expect that CO is free to diffuse within the ice matrix and may "fall into the pores" of our amorphous H_2O ice and the CO may bond to dangling OH bonds in the pores.

If we consider the 2140 cm^{-1} shoulder we can attribute this to CO in an apolar environment. Water itself is polar. Thus to see CO in an apolar environment it must be surrounded by other CO molecules or a non polar product such as CO_2. In order to form CO the carbon ion must come to a stop in the water ice. For C^+ we calculate this to be 25 nm into our ice. At a depth of 25 nm below the surface then we can expect to find a layer of CO. If enough water is converted to CO and or displaced we will form pockets of pure CO, giving rise to our "pure" CO signal at 2141 cm^{-1} (C^+ irradiation) and 2139 cm^{-1} (C^{2+} irradiation). However caution should be applied with the SRIM calculations. They do not assume any information on the structure of the ice. We have no way of modelling an amorphous or crystalline ice with SRIM so the penetration depth of 25 nm will not be accurate. However as we have an ice depth in excess of 350 nm the SRIM calculations allow us to confirm that we are in the regime of ion implantation and it is unlikely our ions are passing through the water ice.

As we currently have no knowledge of the absorption coefficients of the CO bonded in different environments then we are currently unable to say quantitatively how much CO is located in each environment. However we have some information from previous studies of CO in polar and apolar mixtures, allowing us to estimate the absorption coefficients of the 2140 and 2136 cm^{-1} band of CO. For example (Palumbo and Strazzulla 1993) estimate the absorption coefficient of CO in water ice to be 1×10^{-17} molecules cm^{-2} for the pure 2140 cm^{-1} band and 1.7×10^{-17} molecules cm^{-2} for the 2136 cm^{-1} band. It appears there is not too much fluctuation in the absorption coefficients of CO at different sites so our estimate for the column density may be within acceptable limits.

We can however try to estimate an upper limit for the formation of CO. If we assume that water will dissociate as via (4.4) and all oxygen atoms formed then react with the

implanted carbon ions we can estimate from the destruction of H_2O a limit for the formation of CO. In the case of C^+ irradiation before irradiation we have a column density of 1.3×10^{18} molecules cm^{-2}. After irradiation we have a H_2O column density of 6.3×10^{17} molecules cm^{-2} a loss of 6.7×10^{17} molecules. Thus we can have a maximum column density of $\sim 6.7 \times 10^{17}$ molecules cm^{-2}. Integrating the band area of the CO absorption features produces a column density of 4.10×10^{15} molecules cm^{-2}, this figure is of course inaccurate as we do not know the absorption coefficient of CO in all 3 locations in our ice. From these figures we can then estimate that as little as 0.6 % of the implanted carbon ions will react to form CO. We must also bear in mind that each implanted carbon ion can break more than one H_2O bond. If the oxygen atoms produced by the dissociation of H_2O are not forming CO then what other species can they form? Pervious studies of C^+ irradiation by (Strazzulla, G. et al. 2003) who implanted $^{13}C^+$ ions into 1 μm film thickness of water at 77 K have reported the formation of CO_2, CO and H_2O_2. Due to the aforementioned problems with the contamination of our sample with atmospheric CO_2 lines and water lines it is not possible to estimate the true level of CO_2 formed in our ice samples. We observe no evidence of H_2O_2 formation in our ice either. It is possible that that some of the oxygen atoms are in the form of infrared inactive O_2 or other oxygen baring species we can not detect.

SRIM predicts that 4 keV C^+ ions will have a range of 25 nm in our water ice. This represents a penetration into just 6 % of the bulk of the ice. Sputtering of the ice is negliable at this energy. Unfortunately SRIM can not simulate multiply charged ions so we have no way of estimating the penetration depth of our C^{2+} ions. Comparing the two ion irradiation cases (Table 4-11)

Table 4-11 Summary of C^+ and C^{2+} formation of CO in water ice films at 100 K.

Ion	Energy (keV)	Time (minutes)	CO Column Density (molecules cm^{-2})	Total Fluence (10^{16} ions cm^{-2})	A	k	Initial H_2O Column Density (molecules cm^{-2})
C^+	4	0	0	0	5.76	0.0126	1.3×10^{18}
C^+	4	15	1.39E+15	1.19			
C^+	4	30	1.88E+15	2.3			
C^+	4	45	2.30E+15	3.57			
C^+	4	60	2.90E+15	4.75			
C^+	4	75	3.44E+15	5.94			
C^+	4	90	4.10E+15	7.13			
C^{2+}	4	0	0	0	5.38	0.0152	1.2×10^{18}
C^{2+}	4	1	8.39E+14	0.02			
C^{2+}	4	5	9.85E+14	0.10			
C^{2+}	4	15	1.13E+15	0.29			
C^{2+}	4	30	1.78E+15	0.57			
C^{2+}	4	45	2.49E+15	0.86			
C^{2+}	4	60	3.09E+15	1.14			
C^{2+}	4	75	3.88E+15	1.44			
C^{2+}	4	90	4.30E+15	1.73			
C^{2+}	4	120	4.34E+15	2.29			

Upon first inspection there appears to be very little difference in either the rate or yield of CO between C^+ and C^{2+}. However if we take into account the fluence of the ions then it becomes apparent that approximately double the amount of CO is formed by the C^{2+} ions for the same fluence of ions. Another difference in C^+ and C^{2+} irradiation is the destruction of water. We note from our observations that C^{2+} ions do not destroy as much water as C^+ ions. There is negligible water loss when comparing like fluences in the case of C^{2+}. This suggests that C^{2+} ions do not break as many H-OH bonds during their passage into the ice. This could suggest a shallower penetration depth for the

higher charged ions. Neutralisation of the C^{2+} ions is likely to generate a larger number of excited $C(^1D)$ atoms (Dawes, Davis et al. 2004) which could in turn lead to a greater formation of CO.

4.3.4 Metastable states

It should be noted that the discussion on possible formation mechanisms is all based on the assumption that the ion beam consists of ground state ions. In reality this is unlikely to be the case. Our conclusions on the relative formation of CO with the C^{2+} ion compared to the C^+ ion do not take into account the metastable fraction and the effects this may have. The internal energy of the metatstables in the ion beam may affect our results. Previous studies have shown our ion beam may have a metastable fraction of 0.25 to 0.45 of C^{2+} (^3P) and an estimated fraction of 0.67 C^+ (^4P). These have an internal excitation energy of 17.04 and 5.33 eV respectively. Ideally the experiments should be repeated with a ground state beam. (Chapter 7)

4.4 *Irradiation of H_2O:CO_2 mixtures by rare gas ions*

All experiments were performed under similar conditions using similar deposition methods and times. The procedure for each experiment was as follows.

Before deposition the liquid water is degassed by freezing, pumping then thawing the water. The water vapour is then drawn into the mixing cell before the addition of carbon dioxide in a 1:1 gas ratio. This mixture is then deposited onto our cooled CaF_2 substrate. The base temperature was recorded to be ~95 K. Using the CO_2 bands at 3702, 3595 and 2279 cm^{-1} we estimated a CO_2 column density of $6.3 \pm 2.3 \times 10^{17}$ molecules cm^{-2} and a H_2O column density of $4.9 \pm 1.5 \times 10^{17}$ molecules cm^{-2}. This translates to a thickness of 270 ± 98 nm of CO_2 ice and 150 ± 44 nm H_2O ice. A binary ice thickness of 420 ± 140 nm.

After deposition we recorded an infrared scan using the Jasco 600 Plus FTIR. (Figure 4-13)

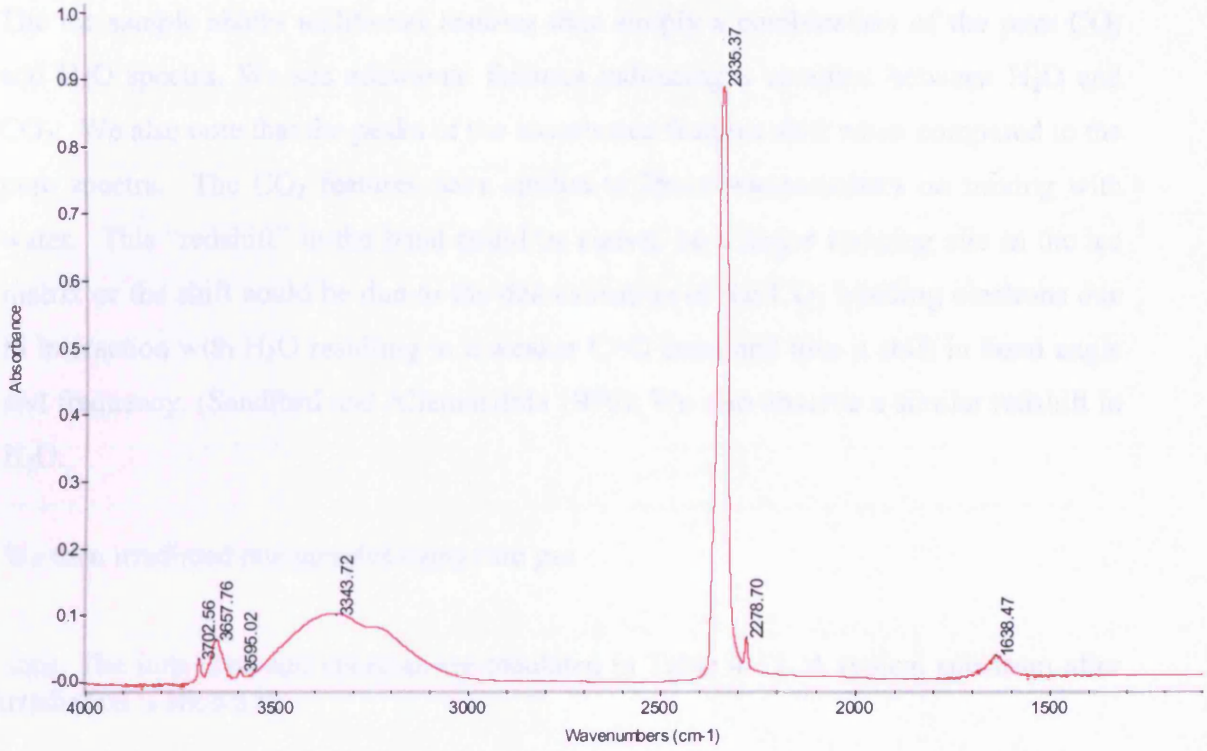

Figure 4-13 H_2O:CO_2 mixture deposited at 95 K

We see the following infrared absorptions at ~100 K before irradiation .
Table 4-12

Table 4-12 Infrared Absorptions of unirradiated CO_2:H_2O ice at 100 K.

Species	Frequency (cm^{-1})	Assignment	Characterisation
CO_2	3702	$\nu_1 + \nu_3$	
H_2O:CO_2	3657	(?)	H_2O:CO_2 complex
CO_2	3595	$2\nu_2 + \nu_3$	
H_2O	3344	ν_1, ν_3	Sym & Asym O-H stretch
H_2O:CO_2	3227	ν_1, ν_3	H_2O:CO_2 complex
CO_2	2335	ν_3	C=O asym stretch
CO_2	2279	ν_3	^{13}C=O asym stretch
H_2O	1639	ν_2	Bending mode

The ice sample shows additional features than simply a combination of the pure CO_2 and H_2O spectra. We see additional features indicating a complex between H_2O and CO_2. We also note that the peaks of the absorbance features shift when compared to the pure spectra. The CO_2 features have shifted to lower wavenumbers on mixing with water. This "redshift" in the band could be caused be a larger trapping site in the ice matrix or the shift could be due to the delocalisation of the CO_2 bonding electrons due to interaction with H_2O resulting in a weaker C=O bond and thus a shift in bond angle and frequency. (Sandford and Allamandola 1990). We also observe a similar redshift in H_2O.

We then irradiated our samples using rare gas

ions. The ions used and energies are tabulated in Table 4-13. A typical spectrum after irradiation is shown in

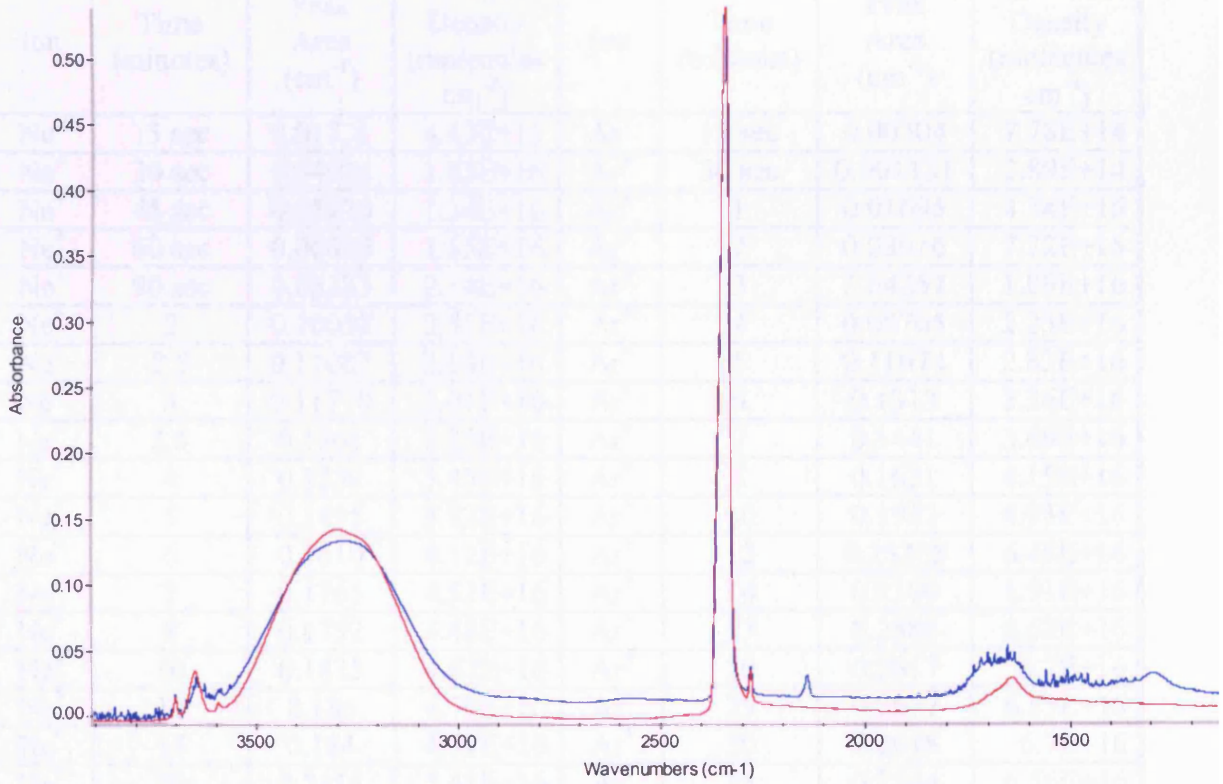

Figure 4-14 Sample spectra after irradiation. Red spectrum is unirradiated ice sample. Blue spectrum is H_2O:CO_2 ice irradiated for 40 mins with Kr+.

Table 4-13 Summary of the rare gas irradiation of H_2O:CO_2 icy mixture at 100 K.

Ion	Total Irradiation Time (minutes)	Total Fluence (ions cm^{-2})	Ion Atomic Number
4 keV Ne+	30	5.98×10^{15}	20
4 keV Ar+	35	7.44×10^{15}	40
4 keV Kr+	40	8.60×10^{15}	83
4 keV Xe+	60	4.92×10^{15}	131

We have monitored the formation of CO in the region 2200 to 2260 cm^{-1}. The column density of CO formed for each ion irradiation case is tabulated in Table 4-14

Table 4-14 CO Formation during irradiation of H_2O : CO_2 ice mixtures by heavy ions at 4 keV.

Ion	Time (minutes)	Peak Area (cm^{-1})	Column Density (molecules cm^{-2})	Ion	Time (minutes)	Peak Area (cm^{-1})	Column Density (molecules cm^{-2})
Ne^+	15 sec	0.01731	4.43E+15	Ar^+	15 sec	0.00304	7.78E+14
Ne^+	30 sec	0.04024	1.03E+16	Ar^+	30 sec	0.001131	2.89E+14
Ne^+	45 sec	0.05230	1.34E+16	Ar^+	1	0.01695	4.34E+15
Ne^+	60 sec	0.06070	1.55E+16	Ar^+	2	0.03016	7.72E+15
Ne^+	90 sec	0.08383	2.14E+16	Ar^+	3	0.04257	1.09E+16
Ne^+	2	0.10052	2.57E+16	Ar^+	4	0.08705	2.23E+16
Ne^+	2.5	0.11087	2.84E+16	Ar^+	5	0.11074	2.83E+16
Ne^+	3	0.11770	3.01E+16	Ar^+	6	0.1313	3.36E+16
Ne^+	3.5	0.1261	3.23E+16	Ar^+	7	0.1441	3.69E+16
Ne^+	4	0.1339	3.43E+16	Ar^+	8	0.1621	4.15E+16
Ne^+	5	0.1495	3.82E+16	Ar^+	10	0.1927	4.93E+16
Ne^+	6	0.1610	4.12E+16	Ar^+	12	0.25205	6.45E+16
Ne^+	7	0.1765	4.52E+16	Ar^+	14	0.2309	5.91E+16
Ne^+	8	0.1752	4.48E+16	Ar^+	17	0.2586	6.62E+16
Ne^+	10	0.1825	4.67E+16	Ar^+	20	0.2617	6.7E+16
Ne^+	12	0.186	4.76E+16	Ar^+	25	0.2677	6.85E+16
Ne^+	15	0.184	4.71E+16	Ar^+	30	0.2618	6.7E+16
Ne^+	20	0.2113	5.41E+16	Ar^+	35	0.2564	6.56E+16
Ne^+	30	0.2092	5.35E+16				

Ion	Time (minutes)	Peak Area (cm^{-1})	Column Density (molecules cm^{-2})	Ion	Time (minutes)	Peak Area (cm^{-1})	Column Density (molecules cm^{-2})
Xe^+	15 sec	0.00551	1.41E+15	Kr^+	15 sec	0.00678	1.73E+15
Xe^+	30 sec	0.01015	2.6E+15	Kr^+	30 sec	0.01448	3.7E+15
Xe^+	60 sec	0.01763	4.51E+15	Kr^+	1	0.02010	5.14E+15
Xe^+	90 sec	0.02394	6.12E+15	Kr^+	2	0.03230	8.26E+15
Xe^+	2	0.03558	9.1E+15	Kr^+	3	0.04407	1.13E+16
Xe^+	3	0.04939	1.26E+16	Kr^+	4	0.05635	1.44E+16
Xe^+	4	0.06425	1.64E+16	Kr^+	5	0.06248	1.6E+16
Xe^+	5	0.06795	1.74E+16	Kr^+	6	0.06860	1.76E+16
Xe^+	6	0.07495	1.92E+16	Kr^+	7	0.07379	1.89E+16
Xe^+	7	0.08394	2.15E+16	Kr^+	8	0.07872	2.01E+16
Xe^+	8	0.10000	2.56E+16	Kr^+	10	0.09319	2.38E+16
Xe^+	10	0.1267	3.24E+16	Kr^+	12	0.09976	2.55E+16
Xe^+	12	0.1448	3.7E+16	Kr^+	14	0.10666	2.73E+16
Xe^+	14	0.1598	4.09E+16	Kr^+	17	0.11143	2.85E+16
Xe^+	17	0.1697	4.34E+16	Kr^+	20	0.12375	3.17E+16
Xe^+	20	0.1824	4.67E+16	Kr^+	25	0.12903	3.3E+16
Xe^+	25	0.1854	4.74E+16	Kr^+	30	0.13358	3.42E+16
Xe^+	30	0.1957	5.01E+16	Kr^+	40	0.1281	3.28E+16
Xe^+	40	0.2150	5.5E+16	Kr^+			
Xe^+	50	0.2083	5.33E+16	Kr^+			
Xe^+	60	0.2235	5.72E+16	Kr^+			

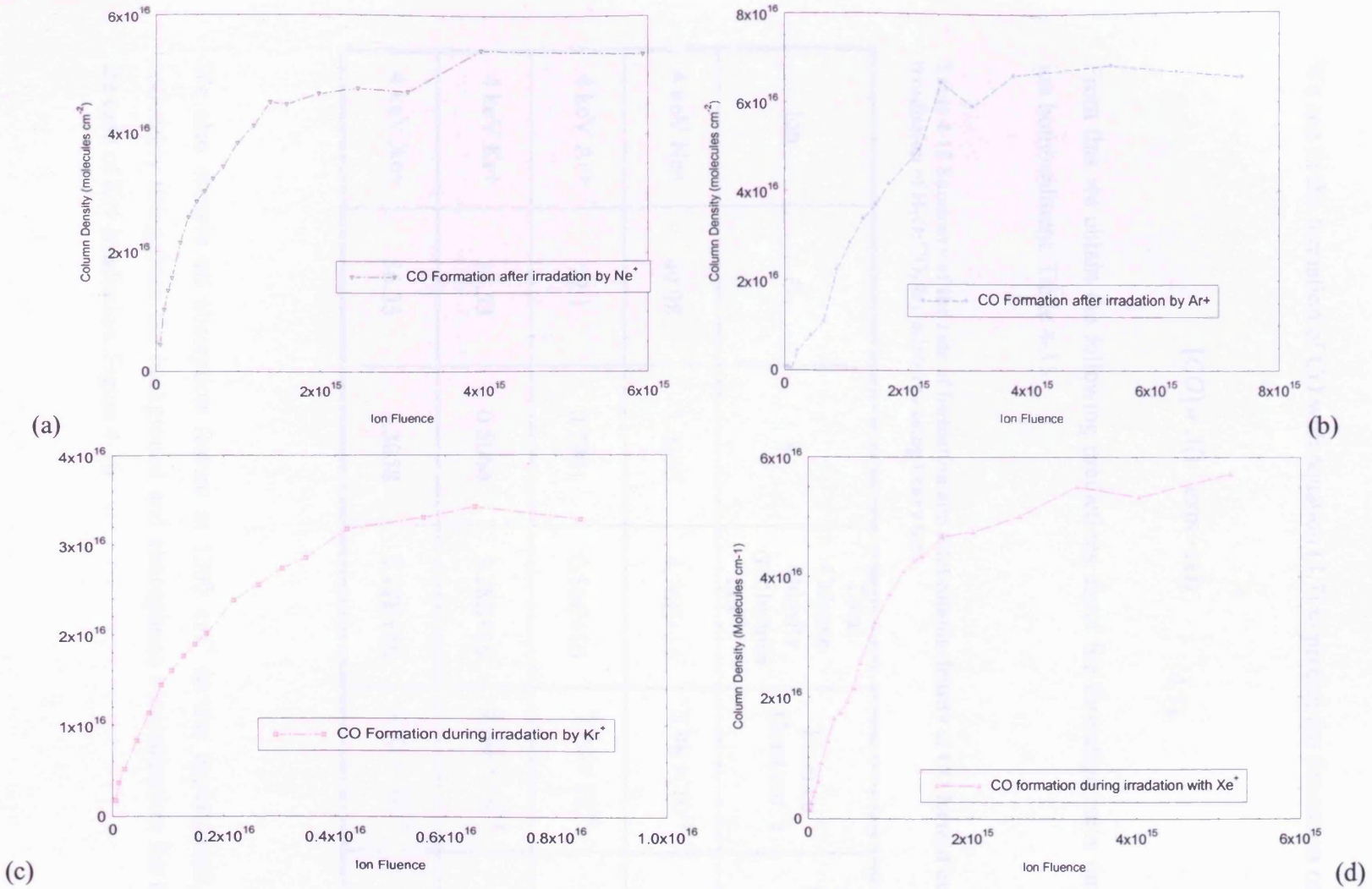

Figure 4-15 Formation of CO during heavy ion irradiation (a) Ne^+ (b) Ar^+ (c) Kr^+ (d) Xe^+. Ion fluences are in units of ions cm^{-2}

We can fit the formation of CO with equation (4.7) to predict the formation rate of CO

$$[CO] = A(1 - \exp(-k\alpha)) \qquad (4.7)$$

From this we obtain the following predictions about the formation rates during heavy ion bombardment. Table 4-15.

Table 4-15 Summary of the rate of formation and total column density of CO formed during irradiation of H_2O:CO_2 icy mixtures using heavy ions

Ion	A	k	Total Column Density (molecules cm^{-2})	Fluence (Ions cm^{-2})	Column Density / Fluence Ratio
4 keV Ne+	49.98	1.0395	4.76E+16	5.98×10^{15}	7.9
4 keV Ar+	72.1	0.7901	6.56E+16	7.44×10^{15}	8.8
4 keV Kr+	33.53	0.8064	3.28E+16	8.60×10^{15}	3.81
4 keV Xe+	56.35	1.3058	5.72E+16	4.92×10^{15}	11.6

We also observe an absorption feature at 1300 cm^{-1} in our experiments, which is noticeably rising from the background and atmospheric contamination for instance in the case of Kr+ irradiation. Figure 4-16

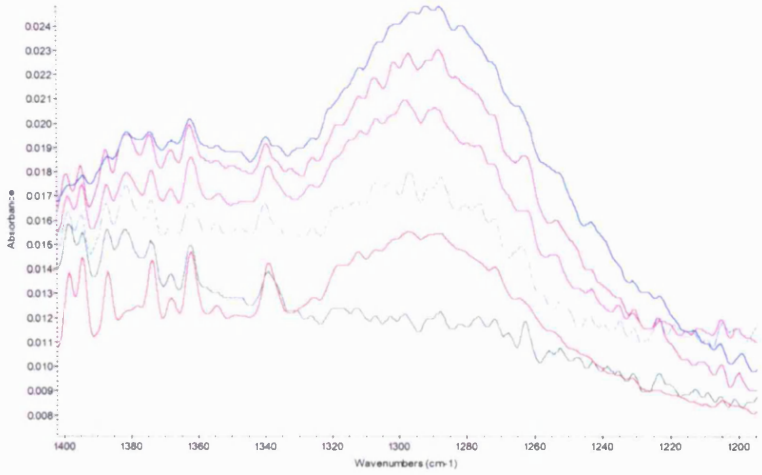

Figure 4-16 Absorption peak at 1300 cm^{-1} during Kr^+ irradiation of H_2O CO_2 ice mixtures at ~ 100 K. Selected data sets are shown.

We can attribute the absorption feature at 1300 cm^{-1} to methane, CH_4 or carbonic acid H_2CO_3. For the reasons outlined in the discussion below we have assigned the feature to H_2CO_3. However as can be seen in Figure 4-16 the atmospheric contamination from water features is considerable in this region making an accurate column density difficult to measure. From the available data we estimate the column density of H_2CO_3 formed by heavy ion irradiation of a H_2O:CO_2 ice mixture to be as shown in Table 4-16. Column densities were calculated assuming an absorption coefficient of 1.0×10^{-16} molecules cm^{-2} (Gerakines, Moore et al. 2000)

Table 4-16 Final Column density of H_2CO_3 during H_2O:CO_2 ice irradiation by heavy ions by monitoring the C-OH in plane bend of H_2CO_3 at 1300 cm^{-1}

Ion	Area at end of irradiation (cm^{-1})	Final Column Density (molecules cm^{-2})	Fluence (Ions cm^{-2})	Column Density / Fluence Ratio
4 keV Ne+	0.14689	3.4×10^{15}	5.98×10^{15}	0.56
4 keV Ar+	0.16924	2.5×10^{15}	7.44×10^{15}	0.33
4 keV Kr+	0.1932	4.45×10^{15}	8.60×10^{15}	0.52
4 keV Xe+	0.16924	3.0×10^{15}	4.92×10^{15}	0.60

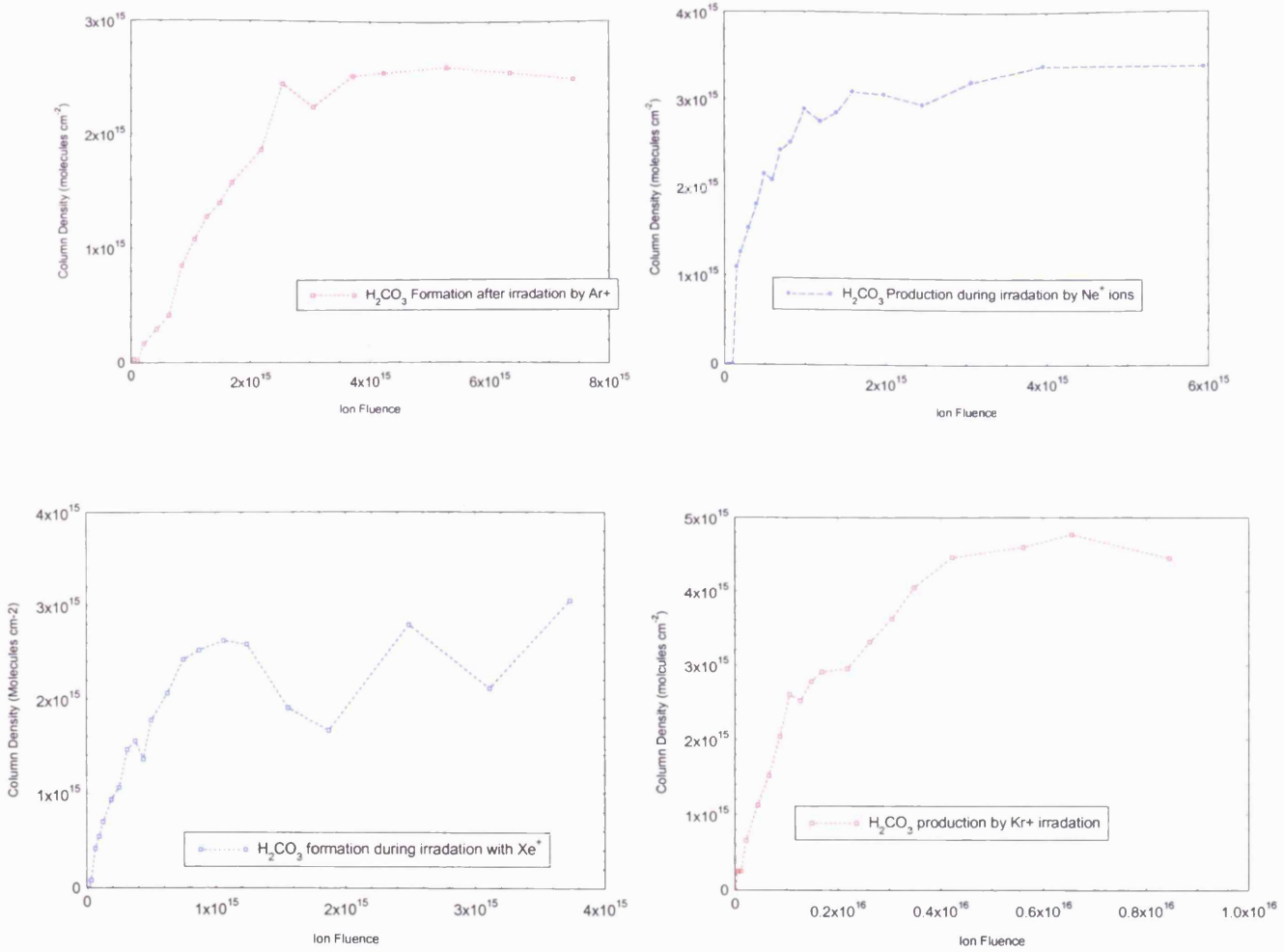

Figure 4-17 H_2CO_3 production during H_2O:CO_2 ice irradiation by heavy ions by monitoring the evolution of the C-OH in plane bend of H_2CO_3 at 1300 cm^{-1} Ion fluences are in units of ions cm^{-2}

4.4.1 Discussion on heavy ion bombardment of H_2O:CO_2 ice mixtures

We will now discuss the effect of ion mass on the formation rate and column density of CO formed. From the column density to fluence ratio it is clear that Xenon is the most efficient ion in terms of producing a high yield of CO. Followed by Ar, then Ne and Xe. The production of CO in the case of Kr^+ irradiation seems to be anomalously low, despite the greater fluence of ions the yield of CO was the smallest.

The SRIM program can be used to predict some of the properties of ions in water ice and carbon dioxide mixtures. We have calculated the range of the ions into H_2O / CO_2 ice. Table 4-17. With increasing ion mass the range of the implanted ion decreases, with the exception of krypton which has the smallest range of all. A possible reason for the low yield of CO during irradiation by Kr^+ could be due to saturation effects. As the Kr+ ions can not penetrate as far into our ice layer we may have exhausted our supply of CO_2 resulting in a low yield of CO. It is also possible the other products are being formed and competing with CO yields. Due to the purging difficulties regions of the spectrum are contaminated by atmospheric water and carbon dioxide absorptions, making the identification of other products formed from our irradiation studies difficult. The CO molecule absorbs in a region free from atmospheric water and carbon dioxide contamination, partly the reason for the focus on CO in our initial experiments.

Table 4-17 Approximate Range and Stopping powers for heavy ions into a H_2O CO_2 mixture calculated by SRIM 2003

Ion	dE/dx Electric (MeV /mm)	dE/dx Nuclear (MeV /mm)	Range (Å)
4 keV Ne^+	24.92	188.1	175
4 keV Ar^+	37.68	335.6	131
4 keV Kr^+	32.52	482.5	125
4 keV Xe^+	31.4	521.7	134

In terms of the production rate we find that this increases with increasing ion mass with the exception of neon. There seems to be no obvious correlation between ion mass and the yield of CO, but with the exception of Neon there seems to be a trend in ion mass and the rate of formation of CO. The CO spectrum itself only exhibits one peak at 2140 cm^{-1} which is assigned to pure CO. There are no sites in the mixed H_2O CO_2 ice for CO to bond to dangling OH bonds or exist in a polar environment. This suggests all our CO production is localised to the range of the ion beam. i.e. a layer of CO forms at the penetration depth of the ion beam.

For feature at 1300 cm^{-1} due to the contamination of the spectra we have not attempted to fit a profile to the evolution of this carrier. As can be seen particularly in the case of the Xe^+ irradiation Figure 4-17 there are large errors on the measurement of the column density as we see large variations in the measured column density that can only be explained in terms of the atmospheric contamination of the spectrum. The yield of the 1300 cm^{-1} feature does not seem to be affected by the ion mass in any meaningful way. The fact though that we may have produced methane is interesting in itself. Methane is often produced by organic organisms and has at times been seen of a good indicator of a possible source of biological activity on a planet. Production of methane by non-organic means has implications for the search for signs of life on other planets. We should however look for other possibilities for the origin of the 1300 cm^{-1} band. Infrared spectroscopy is a powerful tool for the identification of unknown species but care needs to be taken when basing an absolute identification on IR data alone. There are two candidates for the 1300 cm^{-1} absorption band. These are the ν_4 fundamental of methane and the C-OH In plane bend of carbonic acid H_2CO_3. We compare the two molecules in Table 4-18

The three strongest absorptions of H_2CO_3 are at 2626, 1719, 1307 cm^{-1}. If we attribute the 1307 cm^{-1} feature to H_2CO_3 then we could reasonably expect to see the 2626 and 1719 absorptions also. Any feature at 1719 cm^{-1} would be partially obscured by the ν_2 H_2O bending mode. There is no evidence of any feature rising above the ν_2 mode of H_2O. In some of the spectra there is evidence for a broad spectral feature centred around 2600 cm^{-1}. This could be evidence of the 2626 cm^{-1} OH stretch of H_2CO_3.

Table 4-18 Comparison of the infrared fundamentals of CH_4 and H_2CO_3. H_2CO_3 assignments are from experimental data (P.A. Gerakines, Moore et al. 2000), CH_4 assignments are from B3LYP 6-311G* Theory (Johnson, Richter et al. 2003)

H_2CO_3 Position (cm^{-1})	H_2CO_3 Vibrational Mode	H_2CO_3 Band Strength, A (10^{-17} cm molecule^{-1})	CH_4 Mode Number	CH_4 Scaled Frequency (cm^{-1})	CH_4 IR Intensity (km mol^{-1})
2840+2761	O-H stretch	9.8 ± 0.4	ν_1	2913	0
2626	O-H stretch	16. ± 0.8	ν_2	1523	0
1719	C=O stretch	11 ± 1	ν_3	3014	32.6
1508	C-OH asym stretch	6.5 ± 0.6	ν_4	1304	19.8
1307	C-OH in-plane. bend	10 ± 2			
1038	C-OH sym stretch	0.14 ± 0.02			
908	C-OH out of plane bend	5.6 ± 0.8			
813	CO_3 out of plane bend	?			
690	CO_3 in plane bend	1.3 ± 0.2			

We see no evidence for the ν_3 band of methane as it is obscured by H_2O absorptions in the same region. If we compare the column density of the features of the band at 1300 and 2600 cm^{-1} we find they are of similar orders of magnitude suggesting an assignment to H_2CO_3 for both features.

H_2CO_3 has previously been observed in ion irradiated H_2O:CO_2 mixtures ((Brucato, Palumbo et al. 1997; Gerakines, Moore et al. 2000; P.A. Gerakines, Moore et al. 2000)). To date though there has not been a study involving the heavy ion irradiation of water / carbon dioxide mixtures. (Brucato, Palumbo et al. 1997) reported on the irradiation of a frozen mixture of H_2O:CO_2 by 1.5 keV protons and 3 keV He at 10 K. They found that the yield of CO was roughly the same for both cases. In our heavy ion irradiation experiment we have observed that there is no trend in the yield of H_2CO_3 with increasing ion mass. SRIM predictions show that the most noticeable effect of

increasing the ion mass is an increased nuclear stopping power. There seems to be no correlation between increased nuclear stopping power and production of H_2CO_3.

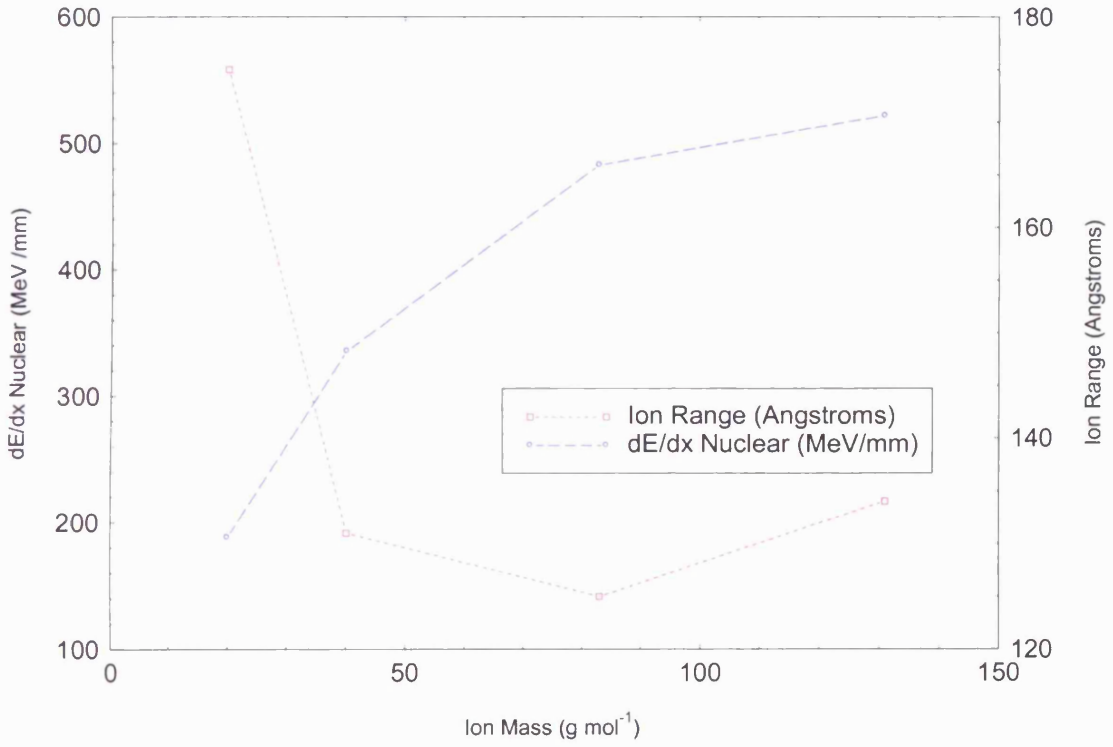

Figure 4-18 SRIM predictions showing the effect of increased mass of the 4keV ions Ne, Ar, Kr and Xe on the nuclear stopping and Ion range.

One possible route to H_2CO_3 formation was suggested by (Gerakines, Moore et al. 2000)

$$H_2O \xrightarrow{ions} H + OH \tag{4.8}$$

They then postulate that secondary electrons may form negative ions such as CO_2^-

$$CO_2 + e^- \longrightarrow CO_2^- \; and \; OH + e^- \longrightarrow OH^- \tag{4.9}$$

The formation of the bicarbonate ion then occurs

$$CO_2^- + OH \longrightarrow HCO_3^- \text{ and / or } OH^- + CO_2 \longrightarrow HCO_3^- \tag{4.10}$$

Finally

$$HCO_3^- + H^+ \longrightarrow H_2CO_3 \tag{4.11}$$

However none of the intermediate products of this reaction scheme were observed by (Gerakines, Moore et al. 2000) or by ourselves so it is impossible to confirm this pathway at present.

4.5 Conclusions

This chapter has focused on the ion irradiation of water and carbon dioxide, two of the most common and simple molecules found in the interstellar medium and highly relevant to astrobiology. We have irradiated a mixture of water and carbon dioxide for the first time with a succession of heavy ions to investigate the formation of carbon monoxide CO and investigated the effect of charge dependence on the formation of CO in water ice. In the next chapter we will present the results of the UV spectroscopy of a range of astrophysical ices.

Chapter Five

Ultraviolet Spectroscopy of Astrophysical Ice Analogues.

"Never express yourself more clearly than you are able to think."

– Niels Bohr.

This chapter describes the ultraviolet (UV) spectroscopy of ice films. All experiments were performed at the Institute for Storage Ring Facilities at the University of Aarhus in Denmark. Experiments used the UV1 beam line as a tuneable source of UV photons. The UV1 beam line has a resolving power of 1,000 to 5,000 with a typical flux of 2 x 10^{11} photons/sec. The accessible wavelength used in the experiments (details of the experimental setup are given in Chapter 3) from the beam line is 120 to 700 nm being limited by the CaF_2 windows used for both the cell and the substrate. In this chapter the UV transmission spectroscopy of several astrophysical ices will be presented.

5.1 VUV Photoabsorption of Methane at 25K

Methane, CH_4 ($X\ ^1A_1$) (Figure 5-1) is amongst the most common species found on Earth and associated with a wide range of organic activity making it an important molecule from an (astro)biological perspective. However it was only discovered in the interstellar medium comparatively recently. In 1991 (Lacy, Carr et al. 1991) detected the 7.6 μm absorption (ν_4) from gaseous methane towards NCG 7539 IRS 9. Lacy, Carr et al. also reported the probable detection of solid methane along the same line of sight.

At the time of its discovery the detection of methane in the interstellar medium provided additional confirmation of the role of reactions on dust grains, Methane had long been thought to be formed on dust grains (Lacy, Carr et al. 1991);(d'Hendecourt, Allamandola et al. 1985) and references therein) by reactions of hydrogen atoms with carbon, successively building up to the CH_4 molecule. The high abundances of solid CH_4 found in the observations of (Lacy, Carr et al. 1991) was seen as confirmation that CH_4 could indeed be formed on grain mantles. Methane is also abundant in cometary bodies (Mumma, Disanti et al. 1996) and in the atmospheres of the gas giants. (Strobel 1969). The Voyager spacecraft observed that the atmosphere of Titan (which is similar to a prototypical early earth) is composed of 2 to 3 % methane and the Cassini-Huygens space craft will shortly be able to probe this in greater detail.

The methane molecule itself is a T_d symmetry type molecule with a tetrahedral structure. The ionization potential is 12.99 eV (Herzberg 1966), the dissociation energy $D(CH_3\text{-}H)$=4.40 eV (Herzberg 1966). The molecular properties of methane are summarised in Table 5-1

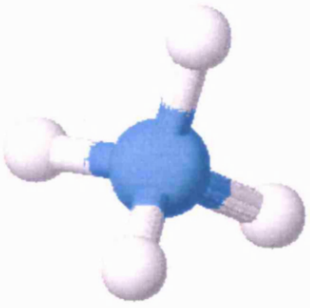

Figure 5-1 Methane, CH_4 ($X\ ^1A_1$)

The VUV spectrum of gaseous methane has been investigated by many authors and numerous measurements of room temperature methane cross sections exist for use in terrestrial atmospheric studies. However to date, there have been comparatively few measurements of the low temperature VUV spectra of solid methane, particularly at those temperatures relevant to astrophysical ices. The gas phase electronic absorption spectrum of methane begins at around 140 nm (~8.8 eV). (Wang, Liu et al. 2000). The lowest energy excited state of methane is identified as a degenerate $^1T_2$ state formed from $3s \leftarrow 1t_2$ excitations (Mebel, Lin et al. 1997). This $^1T_2$ state correlates with the

dissociation of CH_4 to CH_2 ($^1B_1$) + H_2. The next excited state is expected to lie at much higher energies above our present cut off. The VUV spectrum of methane in the region of the UV1 beamline is therefore expected to be simple and well defined. Recording the VUV spectrum of methane will therefore allow us to test our system and compare it with an established result.

Table 5-1 Molecular Properties of Methane (CH_4) (Taken from (Herzberg 1966))

State	Point Group	T_0 (cm^{-1})	Vibrational Frequencies (cm^{-1})				Electronic Configuration	Observed Transitions (nm)
			ν_1	ν_2	ν_3	ν_4		
A ($^1F_2$)	(T_d)	(68730)						A↔X (1455-500 Angstroms)
$X\ ^1A_1$	T_d	0	2916.5	1533.6	3019.49	1306.2		IR

5.1.1 Experimental Procedure

Before measuring any UV transmission spectra it is necessary to calibrate the instrument and determine the thickness of the ice film deposited on the substrate per mbar of gas pressure in our gas reservoir. In order to do this we have developed a laser interference method (Chapter 3).

5.1.1.1 Calibration of the film thickness

In order to calibrate our dosing system for each new molecule it is necessary to deposit a sample of our target molecule while recording the reflection from the ice surface from a He-Ne laser. We have deposited from 0 to 6 mbar of CH_4 onto our cooled CaF_2 substrate. The base pressure was $\leq 10^{-9}$ mbar with a temperature of 25 K. The deposition is shown in Table 5-2 and plotted in Figure 5-2.

Table 5-2 Thickness measurements of CH_4

Amount CH_4 deposited (mbar)	Time for deposition (seconds)	Total CH_4 deposited (mbar)	Laser current (mA)
0.0	0	0.0	27.30
0.2	22	0.2	25.70
0.2	14	0.4	23.30
0.2	24	0.6	20.80
0.2	14.7	0.8	19.20
0.2	21.3	1.0	19.10
0.2	17	1.2	20.50
0.2	23.6	1.4	23.10
0.2	23.4	1.6	25.80
0.2	22.9	1.8	27.70
0.2	27.6	2.0	28.40
0.2	12.8	2.2	27.90
0.2	20.3	2.4	25.80
0.2	13.6	2.6	23.50
0.2	15.7	2.8	20.90
0.2	16.6	3.0	19.40
0.2	24.1	3.2	19.50
0.2	23.7	3.4	21.10
0.2	21.6	3.6	23.60
0.2	24.7	3.8	26.20
0.2	15.5	4.0	27.90
0.2	20.8	4.2	28.40
0.2	23.4	4.4	27.50
0.2	23.8	4.6	25.50

0.2	23	4.8	22.80
0.2	18.8	5.0	20.40
0.2	22.4	5.2	19.20
0.2	20.1	5.4	19.50
0.2	22.8	5.6	21.30
0.2	23.9	5.8	23.80
0.2	20	6.0	26.20

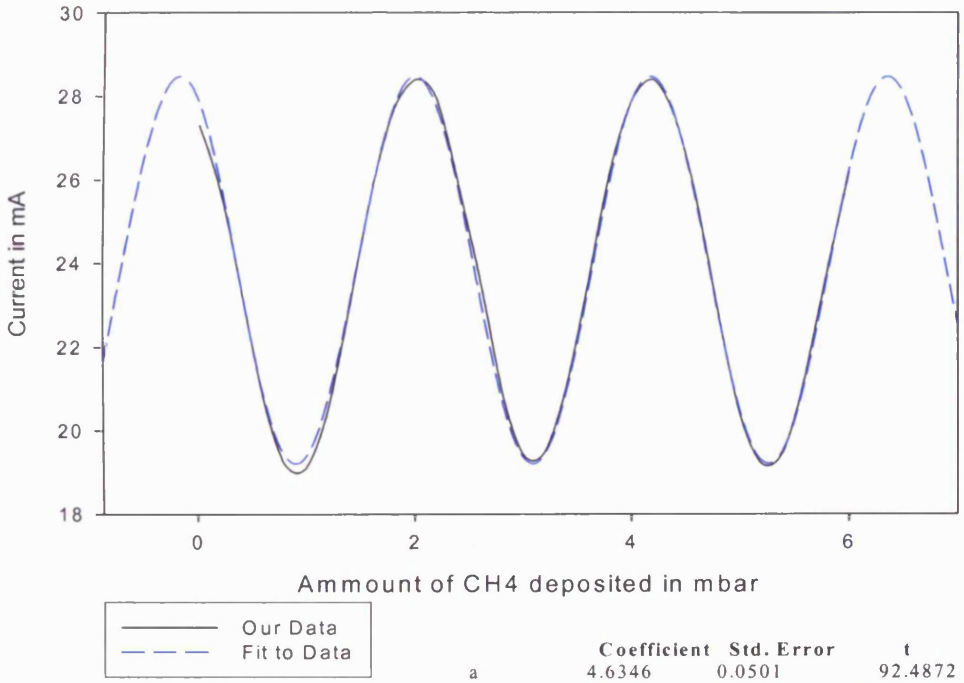

	Coefficient	Std. Error	t	P
a	4.6346	0.0501	92.4872	<0.0001
b	2.1797	0.0043	502.5051	<0.0001
c	2.1010	0.0204	103.2068	<0.0001
y0	23.8297	0.0356	668.7521	<0.0001

Figure 5-2 Thickness measurements of CH_4, deposited at 25 K.

Using the method discussed in Chapter 3 we can calculate the thickness of CH_4 ice that corresponds to the deposition of 1mbar of CH_4 from our dosing system. We fit a sine wave of the form

$$y = y_0 + A\sin\left(\frac{2\pi x}{b+c}\right) \qquad \textbf{(5.1)}$$

The sine curve was fit to the data using Sigma Plot (SPSS Software 2002). Where y_0 is the offset, and A, b and c are constants. Using these parameters it is possible to

determine the thickness and refractive index of CH_4 . The refractive index can be estimated from the ratio of the maximum and minimum intensity (Westley, Baratta et al. 1998) See section 3.8.2 for a detailed description of this method. Using the maximum and minimum amplitudes of our sine wave and averaging over periods we find the refractive index of our sample at 25 K to be n= 1.46.

Applying this to (3.4) we find the period of the sine curve corresponds to

$$d = \frac{\lambda_0}{2n_f \cos\theta_f} = \frac{0.6328}{2 \times 1.46 \times \cos(40)} = 0.28\ \mu\text{m}$$

Note that θ_f is the angle of the laser *within the ice* (which is calculated using Snell's law). Thus one period of the since curve corresponds to 0.28 μm of CH_4 ice. Using Figure 5-2 we observe one period also corresponds to 2.17 mbar of CH_4 deposited. So we can conclude that for every mbar of CH_4 deposited this represents 0.13 μm of ice.

We have studied the UV spectrum of methane ice between 120 to 150 nm. Before deposition we recorded a background spectrum at 25K using a cooled clean CaF_2 substrate. Subsequent measurements are referenced to this using the Beer Lambert law to calculate the absorption of the ice film. The spectrum was taken on the UV_1 beamline at ASTRID using 0.5 nm resolution. 2 mbar of methane was dosed in 219 seconds. This corresponds to an ice thickness of 0.26 μm. The base temperature during deposition was 25 K. The VUV spectrum is shown in Figure 5-3.

The cross sections may be derived from the Beer Lambert law (Section 3.8.3) in the form shown in (5.2) where c is the sample concentration (in molecules cm^{-3}) and l is the path length (sample thickness in cm) and σ is the cross section (cm^2)

$$\ln\left(\frac{I_0}{I_t}\right) = \sigma c l \quad (5.2)\ \text{Beer Lambert Law}$$

The calculated cross sections for methane are tabulated in Table 5-3. In order to calculate the concentration of methane molecules we have adopted a density of 0.4224 $g.cm^{-3}$ (Hagiwara, Hikasa et al. 2002)

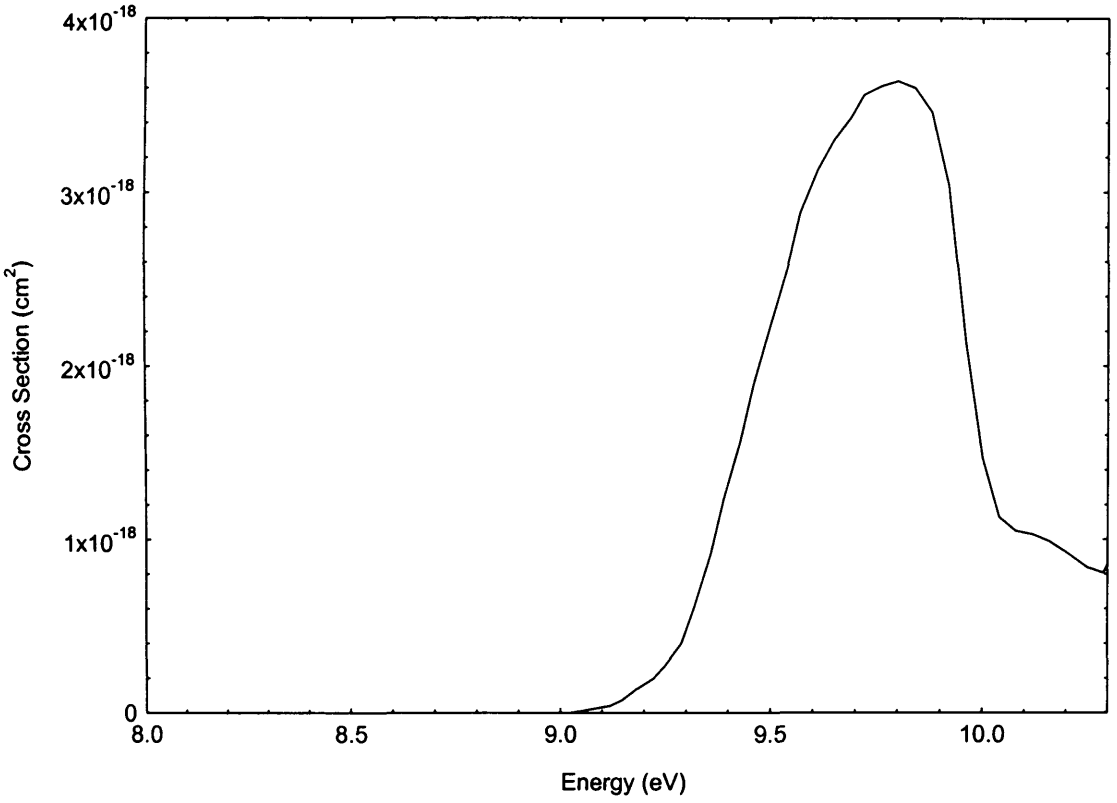

Figure 5-3 Cross sections of methane ice deposited at 25 K

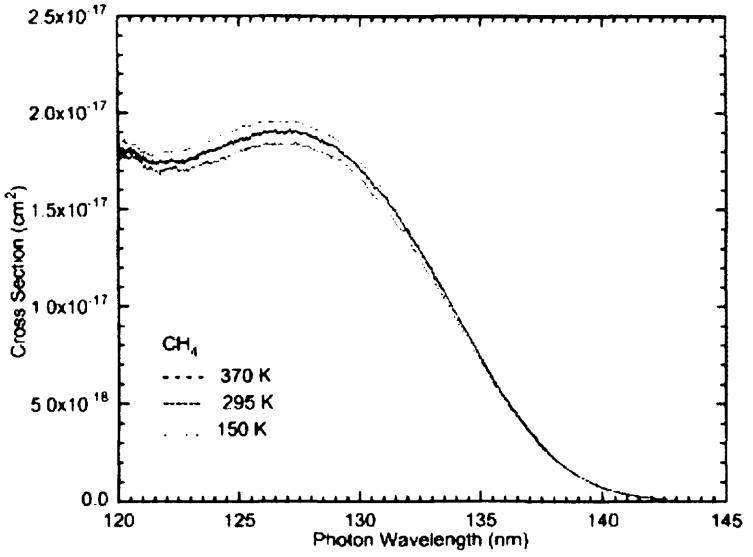

Figure 5-4 Cross section of CH_4 at 150 K as reported by (Chen and Wu 2004). The dotted curve shows the spectrum at 150 K.

Table 5-3 Comparison of our cross sections of methane at 25 K to room temperature gas phase cross sections (Chen and Wu 2004)

Wavelength (nm)	Energy (eV)	Absorbance	Cross section at 25 K (cm^2)	Room Temperature Cross Sections. (cm^2)
120	10.33	0.485508	1.01×10^{-18}	1.80×10^{-17}
120.5	10.29	0.408128	8.08×10^{-19}	
121	10.25	0.451187	8.41×10^{-19}	1.77×10^{-17}
121.5	10.2	0.494018	9.28×10^{-19}	
122	10.16	0.507045	9.90×10^{-19}	1.74×10^{-17}
122.5	10.12	0.531759	1.03×10^{-18}	
123	10.08	0.552657	1.05×10^{-18}	1.76×10^{-17}
123.5	10.04	0.610626	1.13×10^{-18}	
124	10	0.827297	1.47×10^{-18}	1.80×10^{-17}
124.5	9.96	1.26667	2.14×10^{-18}	
125	9.92	2.13667	3.04×10^{-18}	1.85×10^{-17}
125.5	9.88	2.71116	3.46×10^{-18}	
126	9.84	3.12723	3.60×10^{-18}	1.90×10^{-17}

126.5	9.8	3.42234	3.64×10^{-18}	
127	9.76	3.6083	3.61×10^{-18}	1.90×10^{-17}
127.5	9.72	3.72515	3.56×10^{-18}	
128	9.69	3.77779	3.43×10^{-18}	1.88×10^{-17}
128.5	9.65	3.77464	3.30×10^{-18}	
129	9.61	3.71533	3.12×10^{-18}	1.82×10^{-17}
129.5	9.57	3.57453	2.88×10^{-18}	
130	9.54	3.33114	2.57×10^{-18}	1.70×10^{-17}
130.5	9.5	2.97899	2.24×10^{-18}	
131	9.46	2.55643	1.89×10^{-18}	1.58×10^{-17}
131.5	9.43	2.06803	1.57×10^{-18}	
132	9.39	1.58712	1.23×10^{-18}	1.38×10^{-17}
132.5	9.36	1.16885	9.20×10^{-19}	
133	9.32	0.820386	6.07×10^{-19}	1.11×10^{-17}
133.5	9.29	0.553626	4.02×10^{-19}	
134	9.25	0.360543	2.71×10^{-19}	9.60×10^{-18}
134.5	9.22	0.227567	1.94×10^{-19}	
135	9.18	0.135663	1.34×10^{-19}	7.30×10^{-18}
135.5	9.15	0.0755973	7.56×10^{-20}	
136	9.12	0.0381569	4.06×10^{-20}	5.20×10^{-18}

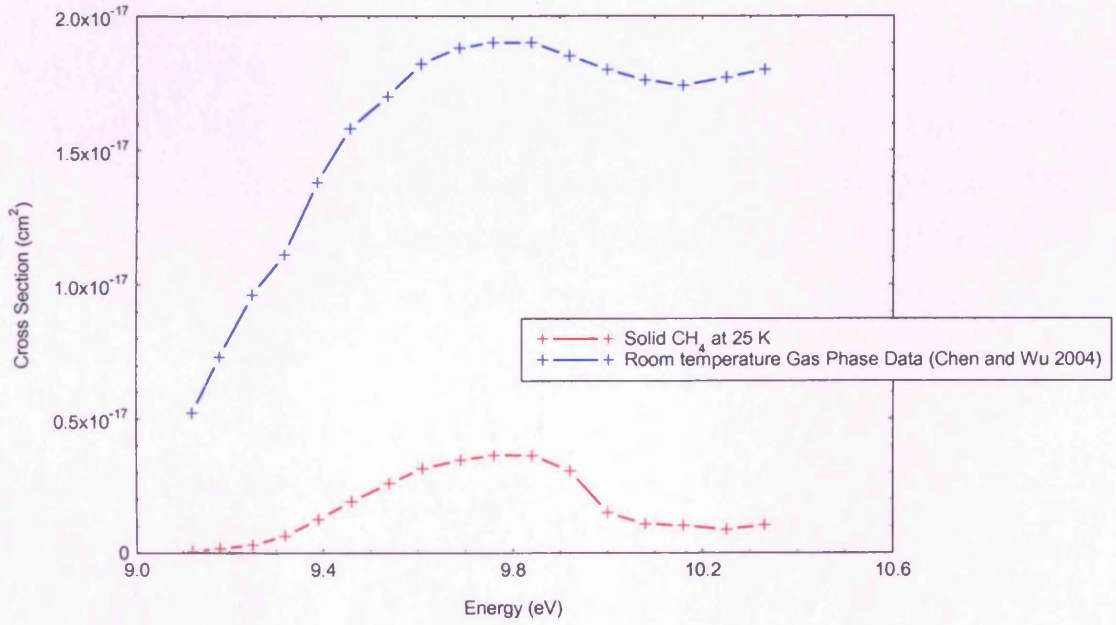

Figure 5-5 Comparison between gas phase room temperature cross sections and the cross sections of solid methane at 25 K

5.1.2 Results

The UV spectrum of methane exhibits a single band in the region 120 to 135 nm. This single broad continuum has been identified by (Mebel, Lin et al. 1997) as originating from the $3s(C_{2v}) \leftarrow 1t_2$ transition. It should be noted that this is near to the cut off of our spectral range caused by the Calcium Fluoride substrate and windows, such that we have low sensitivity in this region (See Figure 3-3) However the band seems to be well defined and the shape of the curve is in excellent agreement with previous studies by Chen and Wu (2004) measured at 150 K (Figure 5-4). Their study found little temperature variation in the cross sections between their gaseous samples of CH_4 at temperatures in the range 150 to 370

K. Our data however shows a reduction in the cross sections when methane is in the solid phase (Figure 5-4 and Figure 5-5) by a factor of 10 compared to the gas phase. There is no noticeable shift in the position of the band compared to the gas phase though the lack of vibrational structure makes it hard to judge any possible shifts.

5.2 VUV Photoabsorption of OCS at 25 K

Carbonyl sulphide, OCS ($X^1\Sigma^+$) is a surprisingly common molecule in the interstellar medium. It has been detected in our local solar system on Venus (Krasnopolsky and Pollack 1994), in comets and extragalactically making it the heaviest molecule discovered outside our galaxy. (Mauersberger, Henkel et al. 1995). It has an ionization potential of 11.24 eV and and dissocation energy D(OC-S) ≤3.71 eV (Herzberg 1966)

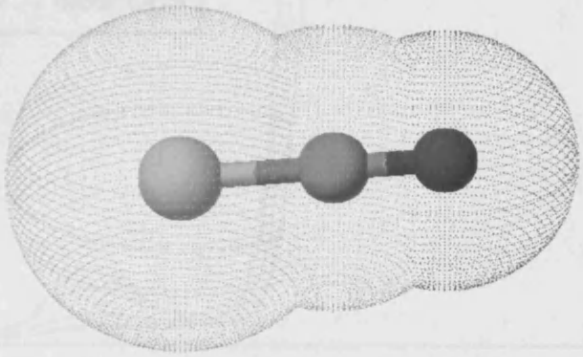

Figure 5-6 Carbonyl sulphide, OCS ($X^1\Sigma^+$)

5.2.1 Experimental Procedure

We initially recorded a background scan in the region 120 to 340 nm on a clean CaF_2 substrate at 25 K. Our samples were grown by dosing OCS onto the 25 K CaF_2 substrate. We dosed OCS onto our substrate in intervals from 1 mbar to 6 mbar sequentially (Table 5-4). After each dose we recorded an ultraviolet spectrum. Spectral resolution was 1 nm. As our experiments on OCS were the last taken in a set of data on the UV1 beam line there was unfortunately no time to perform laser thickness measurements.

Table 5-4 Deposition of OCS at 25 K from 1 to 6 mbar.

Time for Deposition (seconds)	Total Amount Deposited (mbar)	Time for Deposition (seconds)	Total Amount Deposited (mbar)
81	1	130	4
48	2	192	6

5.2 VUV Photoabsorption of OCS at 25 K

Carbonyl sulphide, OCS ($X^1\Sigma^+$) is a surprisingly common molecule in the interstellar medium. It has been detected in our local solar system on Venus (Krasnopolsky and Pollack 1994), in comets and extragalactically making it the heaviest molecule discovered outside our galaxy. (Mauersberger, Henkel et al. 1995). It has an ionization potential of 11.24 eV and and dissocation energy D(OC-S) ≤3.71 eV (Herzberg 1966)

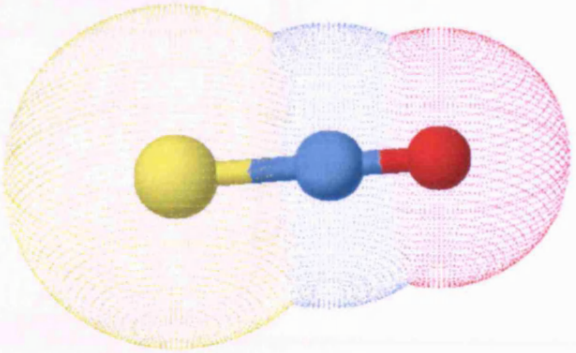

Figure 5-6 Carbonyl sulphide, OCS ($X^1\Sigma^+$)

5.2.1 Experimental Procedure

We initially recorded a background scan in the region 120 to 340 nm on a clean CaF_2 substrate at 25 K. Our samples were grown by dosing OCS onto the 25 K CaF_2 substrate. We dosed OCS onto our substrate in intervals from 1 mbar to 6 mbar sequentially (Table 5-4). After each dose we recorded an ultraviolet spectrum. Spectral resolution was 1 nm. As our experiments on OCS were the last taken in a set of data on the UV1 beam line there was unfortunately no time to perform laser thickness measurements.

Table 5-4 Deposition of OCS at 25 K from 1 to 6 mbar.

Time for Deposition (seconds)	Total Amount Deposited (mbar)	Time for Deposition (seconds)	Total Amount Deposited (mbar)
81	1	130	4
48	2	192	6

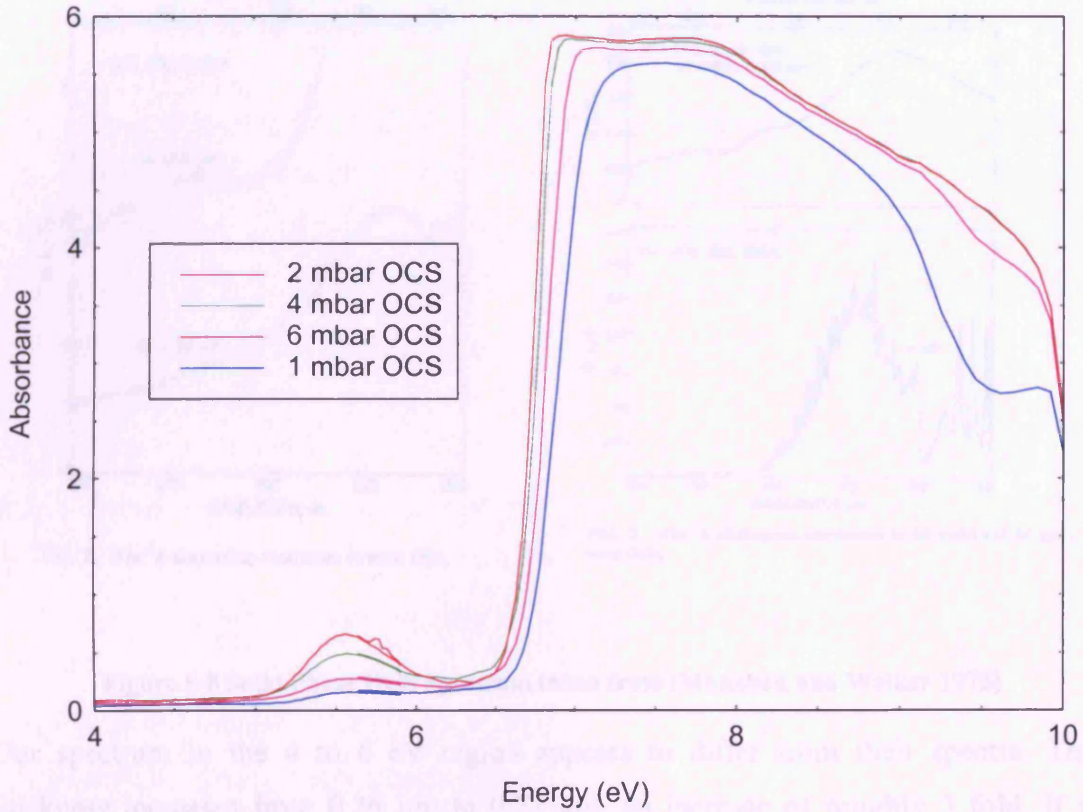

Figure 5-7 VUV Spectrum of Solid OCS at 25 K. OCS was deposited from 1 to 6 mbar pressure in our mixing cell.

5.2.2 Results

Solid OCS exhibits two broad bands, from 5 to 6 eV and from 6.5 to 10 eV. There has been a complimentary study of solid OCS at 53 K by (Monahan and Walker 1975). They identify the transitions observed as transitions from the $^1\Sigma^+$ ground state to the $^1\Delta$ and $^1\Pi$ states respectively. The spectra they recorded are shown in Figure 5-8

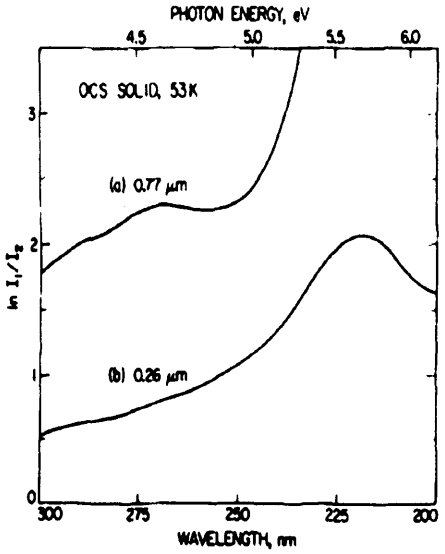

FIG. 2. The $^1\Delta$ absorption continuum in solid OCS.

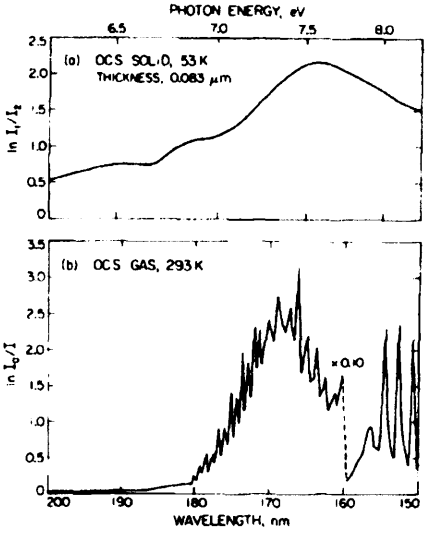

FIG. 3. The $^1\Pi$ absorption continuum in (a) solid and (b) gaseous OCS.

Figure 5-8 Solid Phase OCS Spectrum taken from (Monahan and Walker 1975)

Our spectrum in the 4 to 6 eV region appears to differ from their spectra. Their thickness increases from 0.26 μm to 0.77 μm, an increase of roughly 3 fold. If we assume that increasing the amount of gas deposited onto the substrate from 1 to 6 mbar represents a six fold increase in thickness (which may not be strictly true, but will serve as an approximation) then we can see that our spectra do not match theirs for the thicker sample. However our spectra may be saturated as can be seen at the 8 eV peak. The 0.77 μm spectra of Monahan and Walker (Figure 5-8) shows spectral peaks at 4.3 and 4.7 eV while the thinner sample shows a stronger peak at 5.73 eV which is lacking in our thinner sample. But as we have no indication of the thickness of our sample it is impossible to accurately compare them. In contrast our spectra show an absorption peak at 5.57 eV with no spectral features at 4.3 or 4.7 eV even in our thickest samples. Monahan and Walker assigned the 4.3, 4.7 and 5.73 eV transmissions to $^3\Sigma^+$, $^3\Delta$ and $^1\Delta$ states. On the basis of this we will assign the feature in the region 4 to 7 eV as the transition from the $^1\Sigma^+$ to the $^1\Delta$ state. We find a shift of 0.13 eV from the gas state $^1\Delta$ transition in contrast to Monahan and Walker (1975) who found a shift of 0.29 eV.

5.3 VUV Photoabsorption of SO_2 at 25 K

SO_2 has recently been observed for the first time in the extragalactic medium by Martín et al. (2003), who reported five SO_2 transitions detected towards NGC 253 with a total column density of 7 x 10^{13} cm^{-1}. SO_2 is present in the atmospheres of Venus and Io and on the surface of Europa. Solid phase SO_2 has been suggested as the source for the 4.05-4.08 μm feature of SO_2 seen in Io's spectrum by Smythe et al (1979)

Sulphur dioxide, SO_2 (X_1A_1) is a C_{2v} molecule that is strongly polar with a bond angle of 120°. (Figure 5-9) Its valence ground state molecular configuration may be written as

$$(5a_1)_2(3b_2)_2(6a_1)_2(2b_1)_2(7a_1)_2(4b_2)_2(5b_2)_2(1a_2)_2(8a_1)_2$$

The ionization potential of SO_2 is 12.34 eV and the dissociation energy D(OS-O) = 5.61 eV. (Herzberg 1966) It has a boiling point of 263.1 K . A summary of the molecular properties of SO_2 is given in Table 5-5.

Table 5-5 Molecular Constants of SO_2 from (Herzberg 1966)

State	Point Group	T_0 (cm^{-1})	Vibrational Frequencies (cm^{-1}) ν_1	ν_2	ν_3	Electronic Configuration	Observed Transitions (nm)
H		87100					H← X (114-112)
G							G← X (130-120)
F		74100					F← X (135-131)
E		63570					E← X (160-140)
D	C_s	42264	756.8	393	890.5		D↔X
C	C_s	41413 / 42573.45[b]	963 / 960[b]	377 / 377[b]	279[a] / 220[b]		C↔X (235-180)
$A(^1B_1)$	C_{2v}	29622		317.5	813	$(a_2)^2(b_2)^2(a_1)(b_1)$	A↔X (340-260)
$a(^3B_1)$	C_{2v}	25766.9	905.7	359.8		$(a_2)^2(b_2)^2(a_1)(b_1)$	a↔X (390-340)
X^1A_1	C_{2v}	0	1151	517.6	1361.7	$(a_2)^2(b_2)^2(a_1)^2$	IR

[a] Taken from (Robert Wu, Yang et al. 2000)

[b] Taken from (Brand, Chiu et al. 1976)

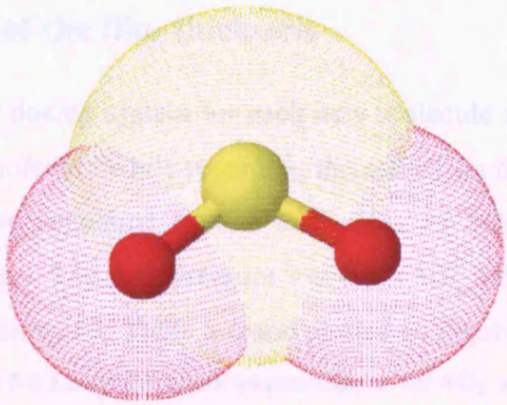

Figure 5-9 Sulphur Dioxide, SO_2

There have been numerous gas phase photoabsorption studies of SO_2 but to date there are few studies of SO_2 ice in the ultraviolet. It is important to have accurate information on the low temperature spectrum of solid SO_2 to aid in the detection of solid phase SO_2 and its mixtures in ices. Therefore we have performed experiments to characterise the deposition profile of SO_2 ices and determine its UV spectrum at temperatures ranging from 25 K to 90 K. We performed four experiments on SO_2 ice.

1) A "Fast" deposition of SO_2 at 25 K
2) A "Fast" deposition of SO_2 at 25 K and heating of the ice sample (annealing) to 90 K
3) A "Fast" deposition of SO_2 at 80 K
4) A "Slow" deposition of SO_2

5.3.1 Experimental Procedure

Before measuring any UV transmission spectra it is necessary to calibrate the instrument and determine the thickness of the ice film deposited on the substrate per mbar of gas pressure in our gas reservoir. In order to do this we have developed a laser interference method (Chapter 3)

5.3.1.1 Calibration of the film thickness

In order to calibrate our dosing system for each new molecule it is necessary to deposit a sample of our target molecule while recording the reflection from the ice surface from a He-Ne laser. We have deposited from 0 to 5 mbar of SO_2 onto our cooled CaF_2 substrate in 0.2 mbar steps. The base pressure was 6.4 x 10^{-9} mbar with a temperature of 25 K. The deposition is shown in Table 5-6 and plotted in Figure 5-10.

Table 5-6 Laser thickness measurements for SO_2 at 25K

Time for deposit (seconds)	Total deposited (mbar)	Diode Current (mA)
0	0.0	28.30
13	0.2	29.90
31	0.4	29.10
31	0.6	28.40
27	0.8	27.10
32	1.0	26.80
20	1.2	27.50
23	1.4	28.70
21	1.6	29.70
24	1.8	30.10
29	2.0	30.00
26	2.2	29.20
19	2.4	28.00
19	2.6	27.20
6	2.8	27.00
12	3.0	27.20
25	3.2	28.00
26	3.4	29.20
32	3.6	29.70
18	3.8	29.20
20	4.0	28.40
22	4.2	27.30
15	4.4	26.50
13	4.6	26.20
17	4.8	26.50
21	5.0	27.20

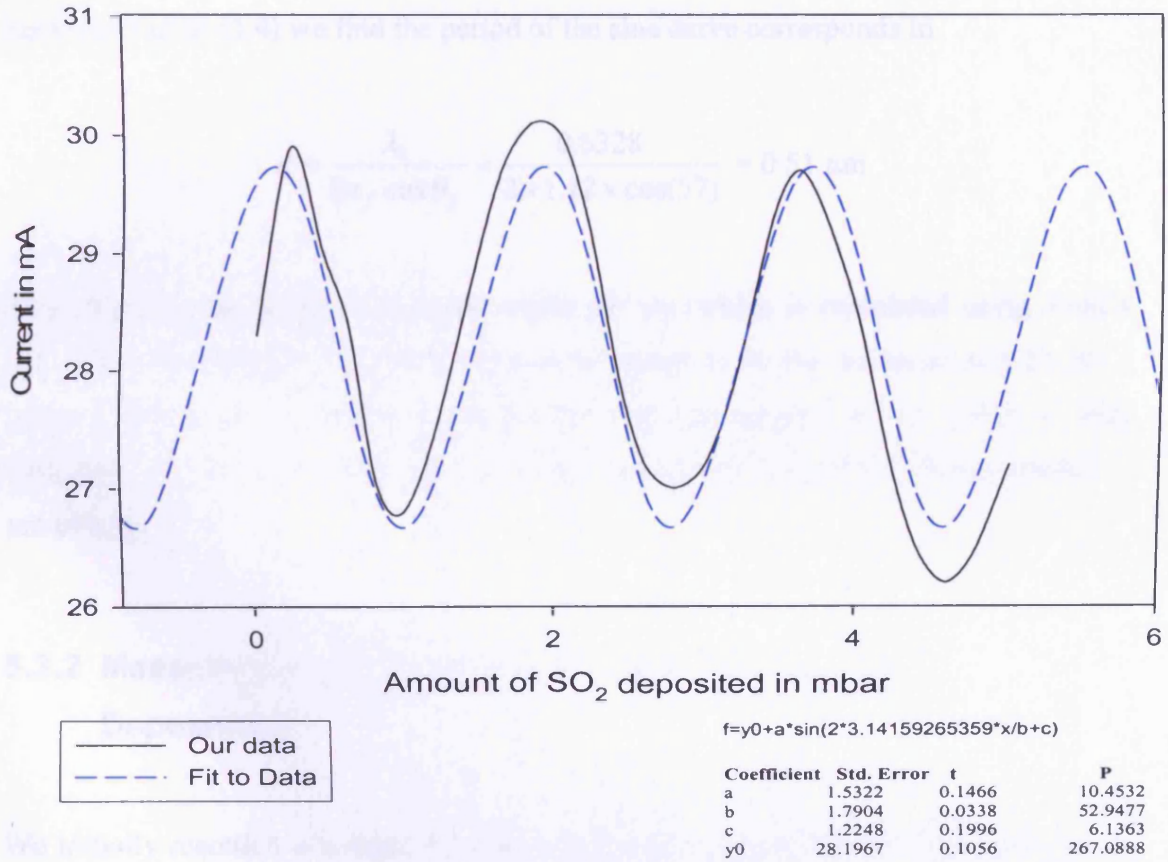

Figure 5-10 Deposition Curve of SO_2 ice deposited at 25 K from 0 to 6 mbar pressure of SO_2 in our mixing cell.

The interference pattern in Figure 5-10 may be fitted using a sine curve of the form

$$y = y_0 + A\sin\left(\frac{2\pi x}{b+c}\right) \qquad \textbf{(5.3)}$$

A sine curve was fitted to the data using Sigma Plot (SPSS Software 2002), using equation (5.3) where y_0 is the offset, and A, b and c are constants. Using these parameters it is possible to work out the thickness and refractive index of SO_2 . The refractive index can be estimated from the ratio of the maximum and minimum intensity

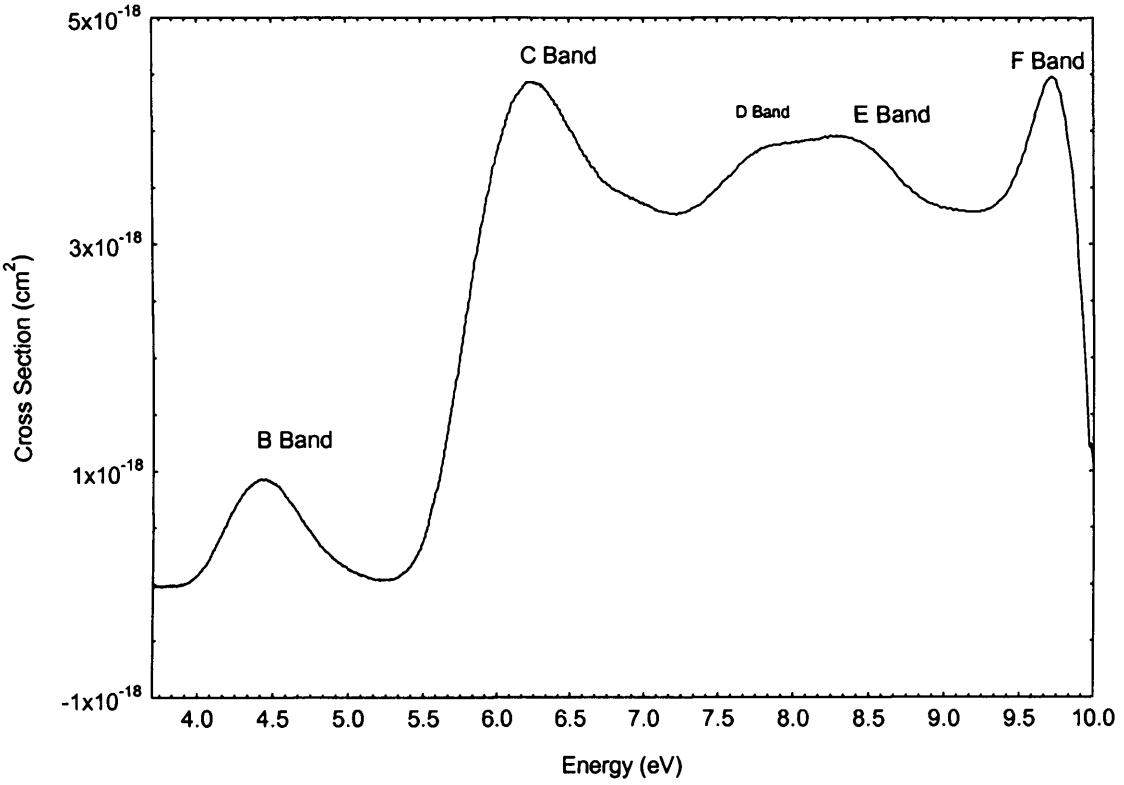

Figure 5-11 Cross sections of SO_2 at 25 K ("Fast Deposition")

5.3.2.1 The 3.6 to 5.2 eV region (B Band)

The gas phase transition in this region has been attributed to the $\tilde{B}^1B_1 - \tilde{X}^1A_1$ electronic transition (Robert Wu, Yang et al. 2000). In the solid phase at 25 K it is characterised by a single broad featureless absorption peak centred at 4.43 eV. A comparison between gas phase data obtained by (Vandaele 1994) is shown in Figure 5-13. The vibrational progressions clearly seen in the gas phase are not present in the condensed phase of SO_2. The solid phase spectrum is also shifted by 20 nm from peak to peak comparison with the gas phase. We note however that the magnitude of the cross sections is similar in the case of the gas and solid phase.

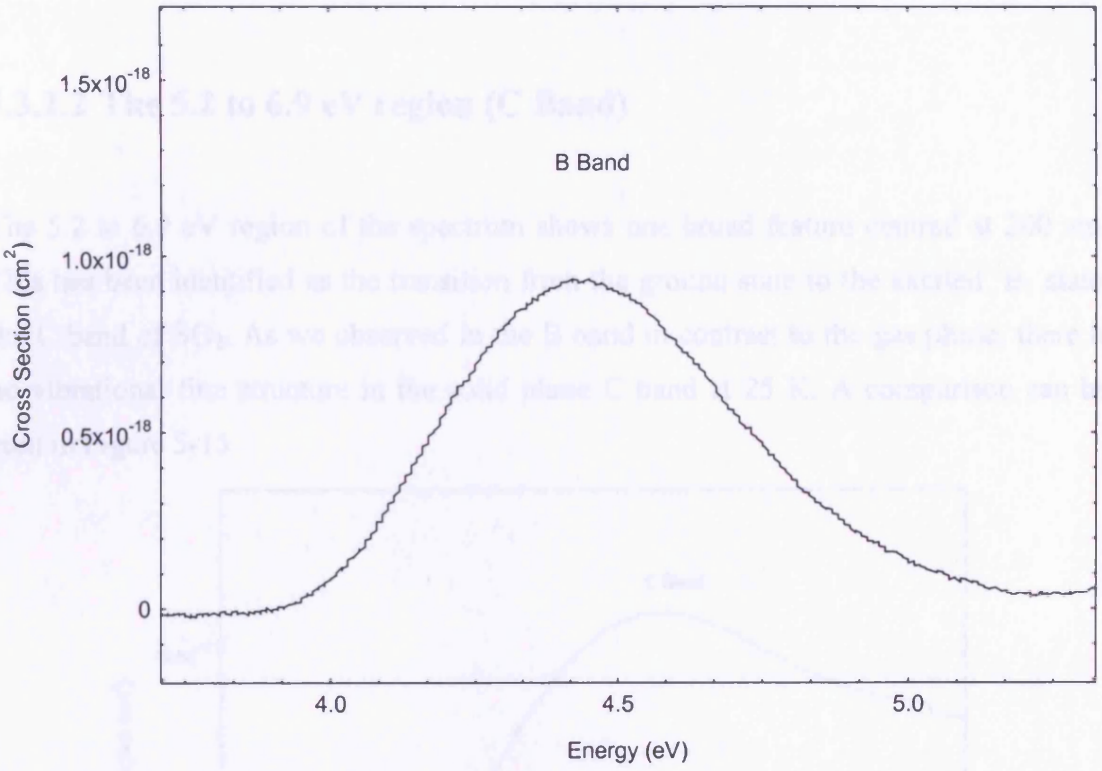

Figure 5-12 The B Band of SO_2 deposited at 25K

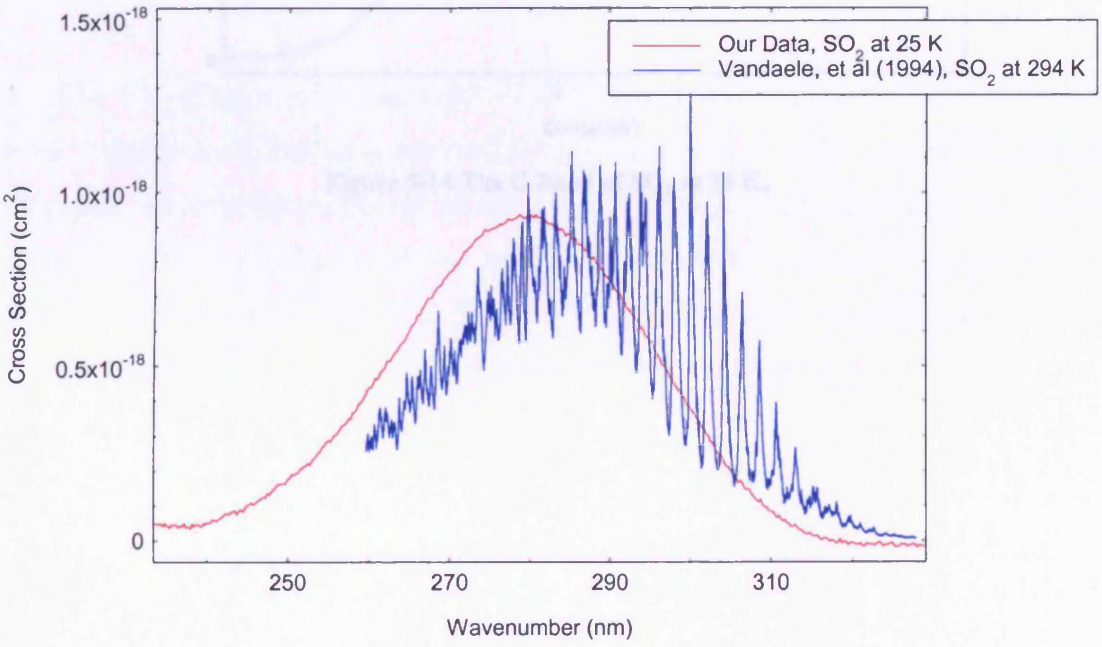

Figure 5-13 Comparison between gas and solid phase B band of SO_2

5.3.2.2 The 5.2 to 6.9 eV region (C Band)

The 5.2 to 6.9 eV region of the spectrum shows one broad feature centred at 200 nm. This has been identified as the transition from the ground state to the excited $^1B_1$ state, the C band of SO_2. As we observed in the B band in contrast to the gas phase, there is no vibrational fine structure in the solid phase C band at 25 K. A comparison can be seen in Figure 5-15

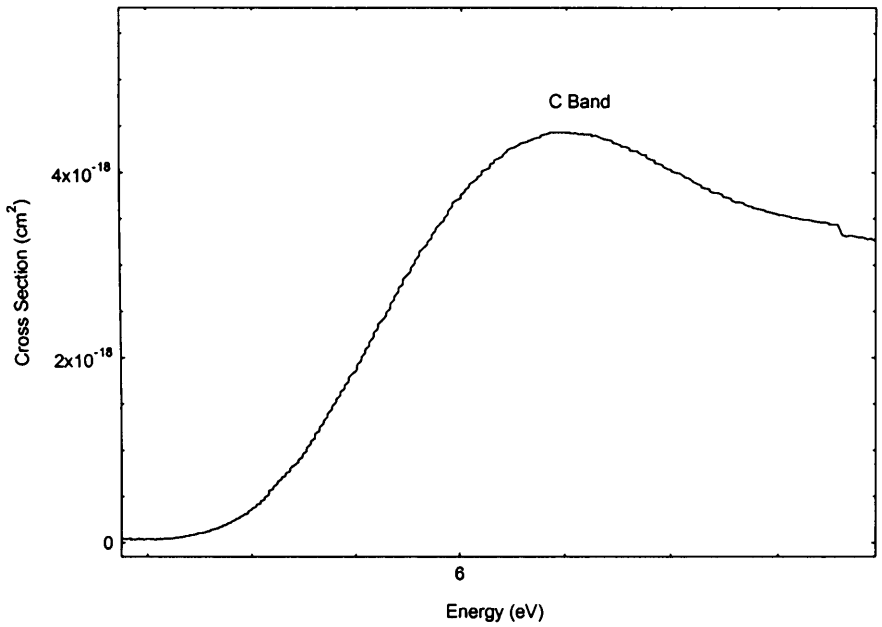

Figure 5-14 The C Band of SO_2 at 25 K.

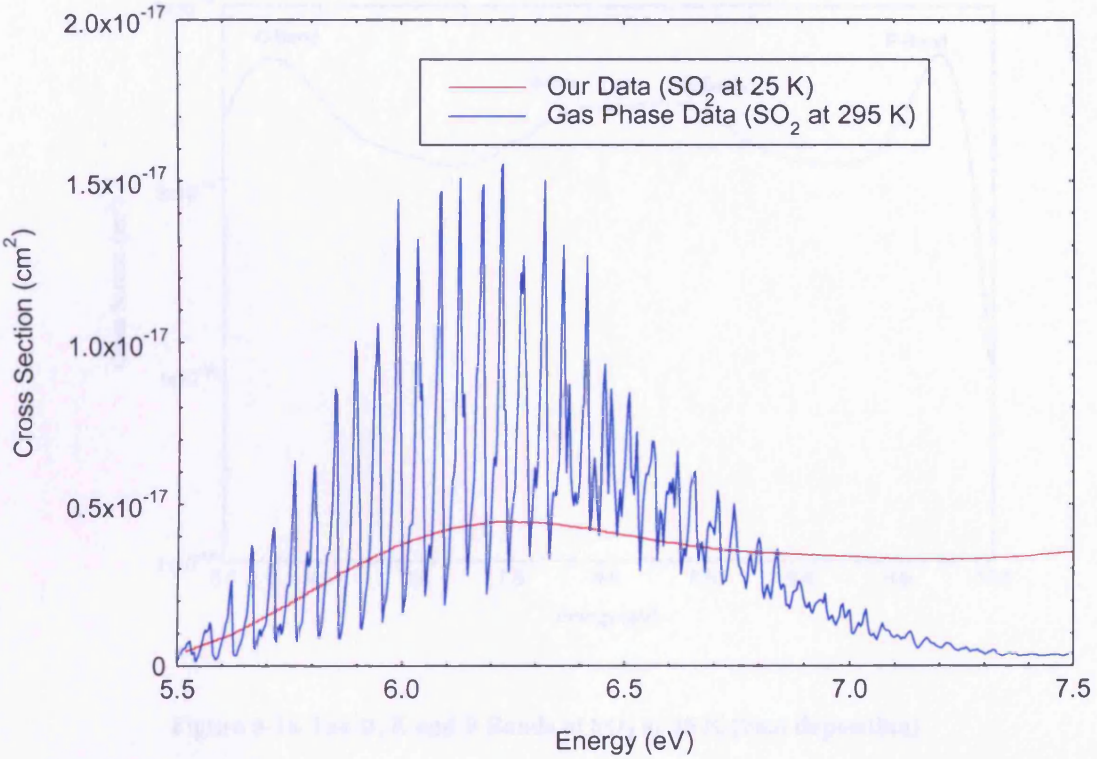

Figure 5-15 Comparison between gas and solid phase C band of SO_2. (Gas phase data courtesy of S.V. Hoffman (Private communication))

5.3.2.3 The 7 to 10 eV range

The 7 to 10 eV range encompasses 3 bands. (Figure 5-16) Namely the D, E, and F bands. It should be noted that the F band is too close to our cut off region and the data in this region is unreliable so will not be discussed. Herzberg (1966) comments that SO_2 is transparent between 135 and 180 nm apart from 3 diffuse bands near 155 nm. This is clearly not the case with solid phase SO_2 and the 3 diffuse bands are greatly enhanced in the solid phase, having cross sections comparable with the C band.

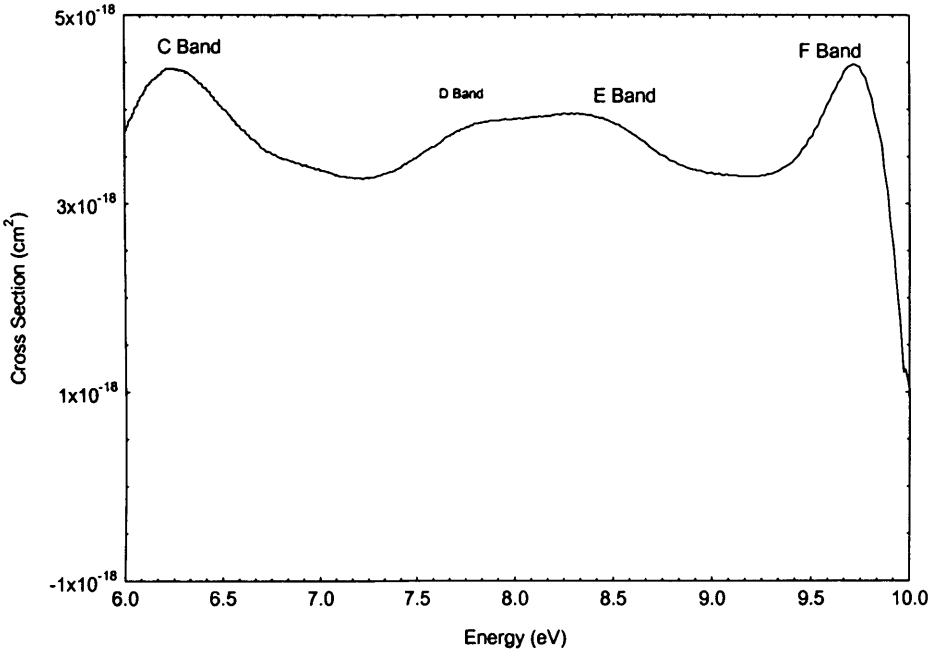

Figure 5-16 The D, E and F Bands of SO_2 at 25 K (Fast deposition)

(Golomb, Watanabe et al. 1961) have studied the SO_2 spectrum in the region 105 to 217 nm (11.8 to 5.71 eV) in the gas phase. Figure 5-17

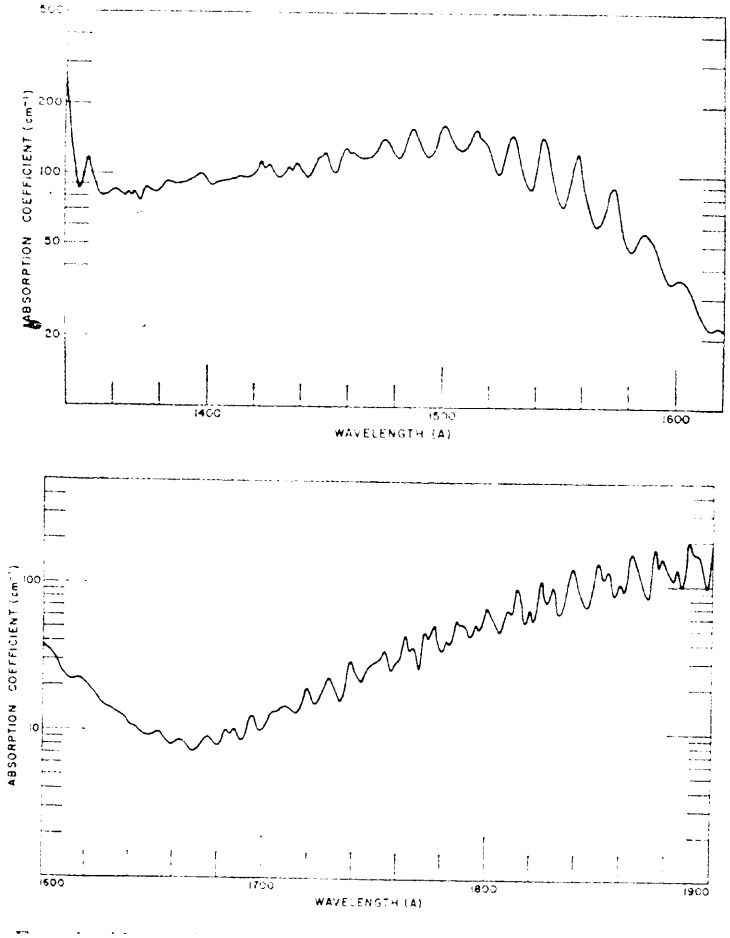

Figure 5-17 Gas Phase SO_2 in the region 134 to 190 nm taken from (Golomb, Watanabe et al. 1961)

Considerable vibrational features are present in the gas phase which is again not present in the solid phase spectrum.

5.3.3 VUV Spectrum of SO_2 after annealing

In space the ice covered grain mantles may be subject to rapid heating (e.g. by a shock). In order to mimic this effect we annealed our SO_2 sample by heating the SO_2 to a temperature of 90 K, maintaining this temperature for one minute and then cooled the sample back down to our base temperature of 25 K. The results of annealing the sample can be seen in Figure 5-18 which depicts a spectrum of a fast deposition of SO_2 at 25 K then heated to 90 K and re-cooled to record the spectrum. All spectra in this section are presented in absorbance as we can not say how the heating of the SO_2 has affected the parameters such as the thickness and density of the SO_2 sample.

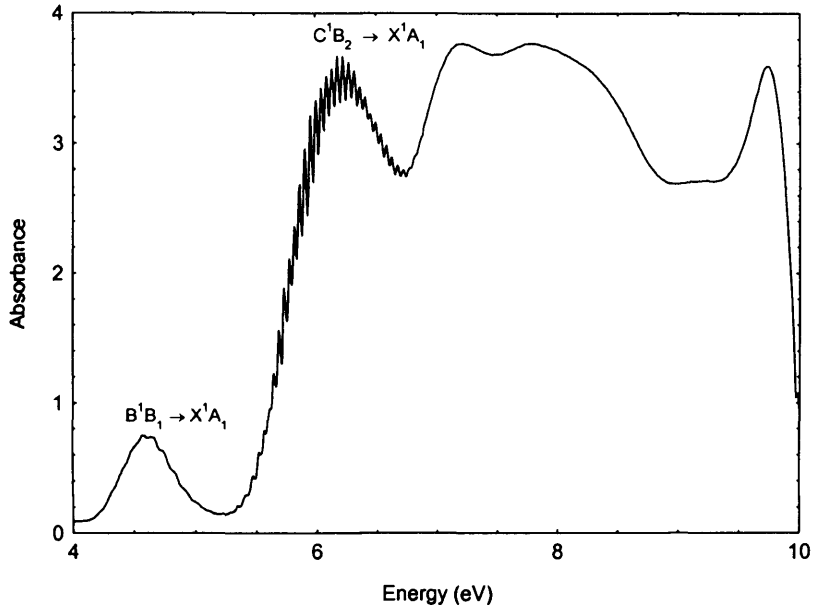

Figure 5-18 SO_2 deposited at 25 K, heated to 90 K, re-cooled to 25 K

After annealing there are once again 5 distinct bands visible. However there are now clear vibrational progressions similar to those observed in the gaseous spectrum of SO_2. These features remain "frozen in" to the ice when it is re-cooled to 25K

5.3.3.1 The 3.6 to 5.2 eV region (B Band)

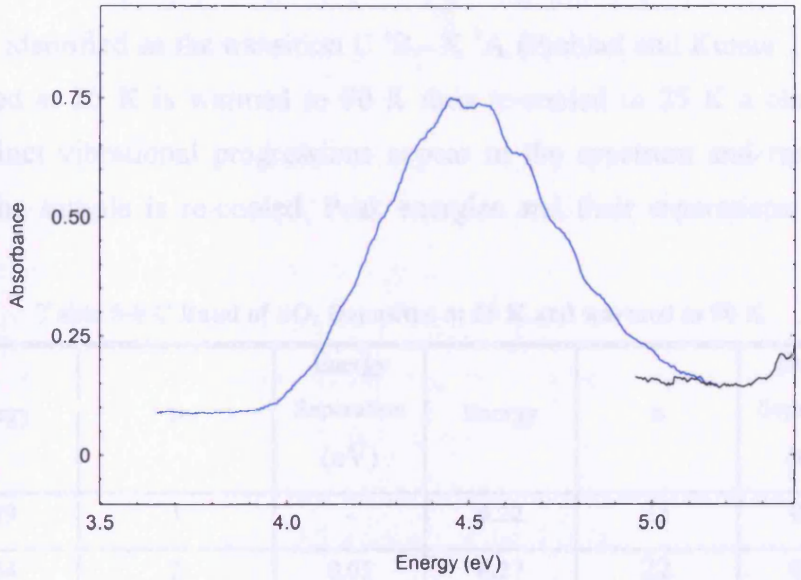

Figure 5-19 The 3.6 to 5.2 eV region of annealed SO_2 ice at 25 K

The onset of the B band is given as 312.95 nm or 3.9618 eV by (Clements 1935). Our onset appears to occur at ~ 3.92 eV. After the annealing process there is evidence for emergence of vibrational structure within the band. The peaks are listed in Table 5-7

Table 5-7 Peaks of the B Band of SO_2 deposited at 25 K and warmed to 90 K

Peak location (eV)	Our Band assignment	Energy separation between successive peaks (eV)
4.45	1	
4.55	2	0.1
4.65	3	0.1
4.76	4	0.11
4.87	5	0.11

The energy separation of the bands could be consistent with either the ν_1 or ν_3 vibrations of SO_2. Due to the close frequency of their vibrations it is currently not possible to assign the progression seen on the B band to either of these vibrations.

5.3.3.2 The 5.2 to 6.9 eV region (C Band)

This band is identified as the transition C $^1B_2$– X $^1A_1$ (Prahlad and Kumar 1997). When SO_2 deposited at 25 K is warmed to 90 K then re-cooled to 25 K a clear change is visible. Distinct vibrational progressions appear in the spectrum and remain "frozen out" when the sample is re-cooled. Peak energies and their separations are listed in Table 5-8

Table 5-8 C Band of SO_2 Deposited at 25 K and warmed to 90 K

Energy	n	Energy Separation (eV)	Energy	n	Energy Separation (eV)
5.29	1	-	6.22	21	0.04
5.34	2	0.05	6.27	22	0.05
5.42	3	0.08	6.32	23	0.05
5.47	4	0.05	6.36	24	0.04
5.52	5	0.05	6.41	25	0.05
5.57	6	0.05	6.45	26	0.04
5.61	7	0.04	6.49	27	0.04
5.64	8	0.03	6.54	28	0.05
5.69	9	0.05	6.58	29	0.04
5.74	10	0.05	6.63	30	0.05
5.78	11	0.04	6.68	31	0.05
5.82	12	0.04	6.72	32	0.04
5.87	13	0.05	6.77	33	0.05
5.91	14	0.04	6.82	34	0.05
5.96	15	0.05			
6.00	16	0.04			
6.04	17	0.04			
6.09	18	0.05			
6.13	19	0.04			
6.18	20	0.05			

The energy separation of the peaks is 0.05 eV. A separation of 50 meV corresponds to the ν_2 frequency of the C state. $\nu_2 = 377$ cm^{-1} = 0.046 eV in the gas phase. (Table 5-5) This suggests the absorption features seen in the 90 K spectrum are representative of a vibrational progression in ν_2. In order to view the vibrational structure a physical change to the structure of the SO_2 ice must have occurred to allow the progression to become active.

The gas phase (0,0,0) onset of the C band is listed in (Brand, Chiu et al. 1976) as occurring at 42573.45 cm^{-1} or 5.278 eV and also by (Robert Wu, Yang et al. 2000) as 5.279 eV. The onset of our progression begins at 5.29 eV and we assign this to (0,0,0), the small difference being ascribed to the shift in electronic energy levels in moving from the gas to solid phase. Assuming the value of the C state $\nu_2 = 377$ cm^{-1} and (0,0,0) to be located at 5.279 eV we assign the bands as follows in Table 5-9

Table 5-9 Assignments to SO_2 Bands

Peak Value SO_2	Assignment (ν_1, ν_2 ,ν_3)	Assignment from literature (peak location in eV)
5.29	0 0 0	
5.34	0 1 0	0 1 0 (5.32) [a]
5.42	0 3 0	0 3 0 (5.42) [a]
5.47	0 4 0	0 4 0 (5.47) [b]
5.52	0 5 0	0 5 0 (5.52) [b]
5.57	0 6 0	0 6 0 (5.56) [b]
5.61	0 7 0	0 7 0 (5.60) [b]
5.64	0 8 0	0 8 0 (5.65) [b]
5.69	0 9 0	
5.74	0 10 0	
5.78	0 11 0	
5.82	?	
5.87	?	
5.91	?	

5.96	?	
6.00	?	
6.04	?	
6.09	0 17 0	
6.13	0 18 0	
6.18	0 19 0	
6.22	0 20 0	
6.27	0 21 0	
6.32	0 22 0	
6.36	0 23 0	
6.41	0 24 0	
6.45	0 25 0	
6.49	0 26 0	
6.54	0 27 0	
6.58	0 28 0	
6.63	0 29 0	
6.68	0 30 0	
6.72	0 31 0	
6.77	0 32 0	
6.82	0 33 0	

[a] (Robert Wu, Yang et al. 2000) [b] (Bludsky, Nachtigall et al. 2000)

It is clear that the energy spacing between the vibrational levels should eventually decrease as the electron is excited towards the continuum. A more complete quantum mechanical treatment of the C band has been partially undertaken by (Bludsky, Nachtigall et al. 2000). Their assignments are given in Table 5-9. and are in agreement with ours. We are however lacking the (0,2,0) band in our spectrum. Closer investigation of the spectrum suggests it may be blended into (0,3,0) band.(Figure 5-20) The reason for this is unclear.

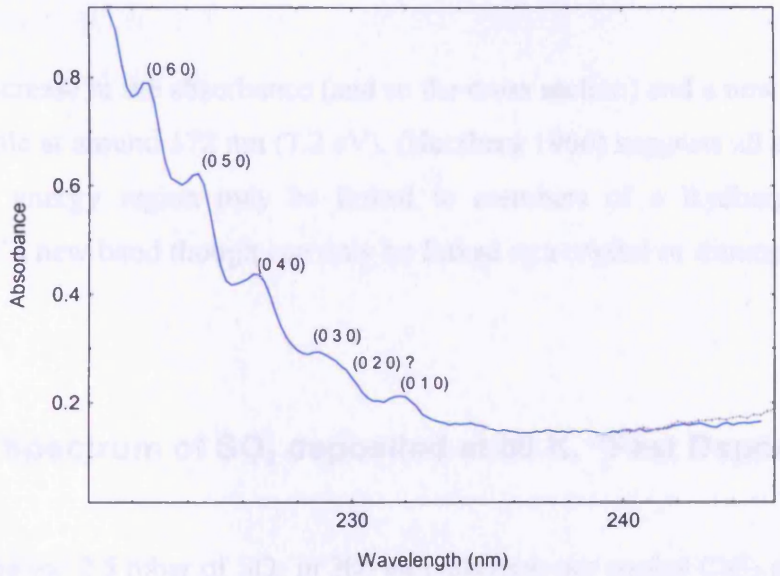

Figure 5-20. The first 6 peaks of the progression in the C band of annealed SO_2 at 25 K. Note the merging of the (0,3,0) and (0,2,0) peaks.

5.3.3.3 The 7 to 10 eV range (D, E, F Bands)

A clear change in the spectrum in this region is also observed on annealing and is illustrated in Figure 5-21

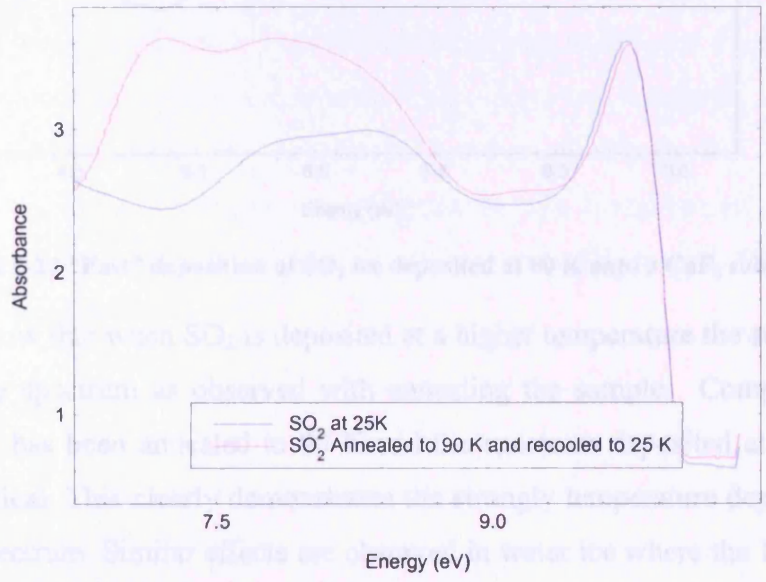

Figure 5-21 The 7 to 10 eV range annealed spectrum shown before and after annealing of the SO_2 sample originally deposited at 25 K

There is an increase in the absorbance (and so the cross section) and a new broad feature becomes visible at around 172 nm (7.2 eV). (Herzberg 1966) suggests all of these bands lying in this energy region may be linked to members of a Rydberg series. The appearance of a new band though can only be linked to a crystal or dimmer effect in the SO_2

5.3.4 VUV Spectrum of SO_2 deposited at 80 K. "Fast Deposition"

We have deposited 2.5 mbar of SO_2 in 386 seconds onto our cooled CaF_2 substrate at 80 K. This translates to a thickness of 0.44 μm. The results of our deposition are shown in Figure 5-22.

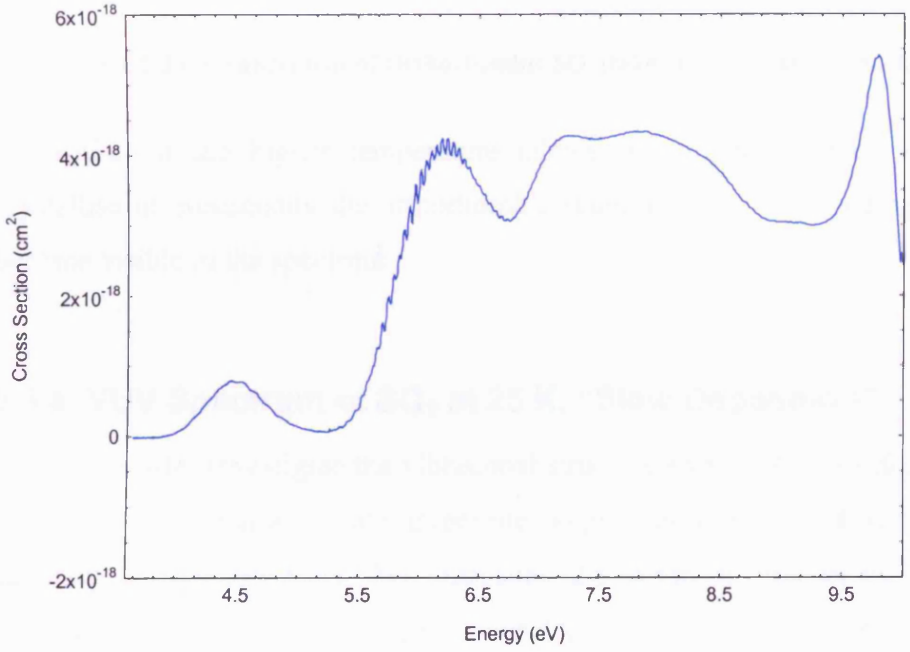

Figure 5-22 "Fast" deposition of SO_2 ice deposited at 80 K onto a CaF_2 substrate.

Our results show that when SO_2 is deposited at a higher temperature the structure is still evident in the spectrum as observed with annealing the sample. Comparison of the spectrum that has been annealed to 90 K and the spectrum deposited at 80 K reveals they are identical. This clearly demonstrates the strongly temperature dependant nature of the SO_2 spectrum. Similar effects are observed in water ice where the IR spectrum is strongly dependant on the deposition temperature and hence crystalline structure of the

molecules. (Westley, Baratta et al. 1998) At ~140 K SO_2 is known to have an orthorhombic structure Figure 5-23

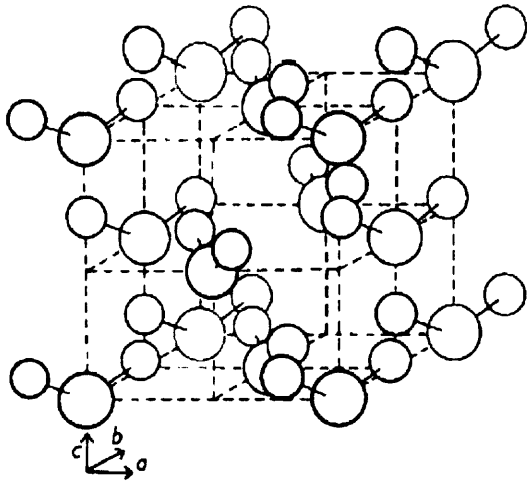

Fig. 2. Arrangement of molecules in one unit cell.

Figure 5-23 Arrangement of Orthorhombic SO_2 (taken from (Post, Schwartz et al. 1952)

Deposition at the higher temperature allows the sulphur dioxide enough time to crystallise in presumably the orthorhombic state, allowing the bending progression to become visible in the spectrum.

5.3.5 VUV Spectrum of SO_2 at 25 K. "Slow Deposition"

In order to fully investigate the vibrational structure seen in SO_2 we deposited SO_2 at a much slower condensation rate. Experimental procedures and conditions matched those described in Section 5.3.1. We deposited 2.5 mbar of SO_2 in 123 minutes. This translates to a thickness of 0.44 μm in our deposition. The deposition rate was therefore 0.21 μm per hour contrasting to a rate of 2.8 μm per hour. The results of this deposition are shown in Figure 5-24.

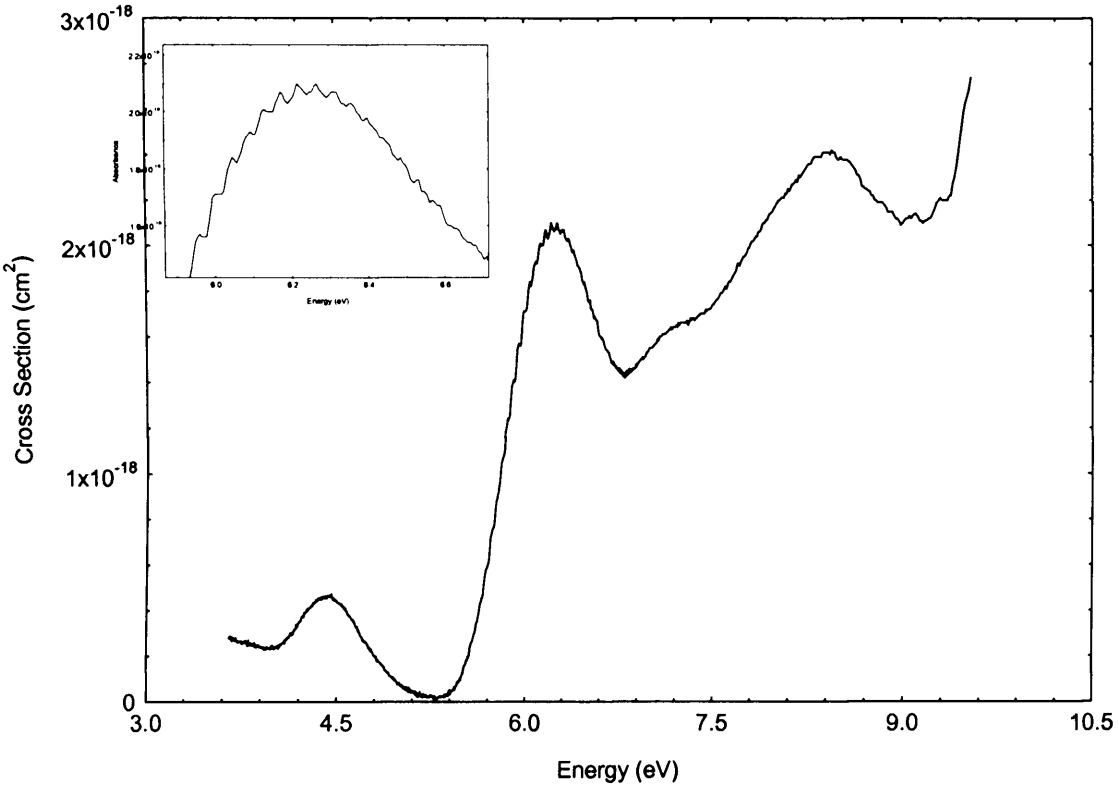

Figure 5-24 UV spectrum of SO_2 deposited at 25 K with a slow deposition rate. An enlarged view of the C-Band of SO_2 at ~6.3 nm is shown in the inset.

It is clear from the spectrum that unlike the fast deposition at 25 K there are signs of vibrational structure in our low temperature spectrum. A comparison between the slow and fast deposition is shown in Figure 5-25. Note that the upturn at ~ 4 eV in the cross section is most likely an experimental artefact, perhaps due to fluctuations in the beam current or undulator movement on the beamline.

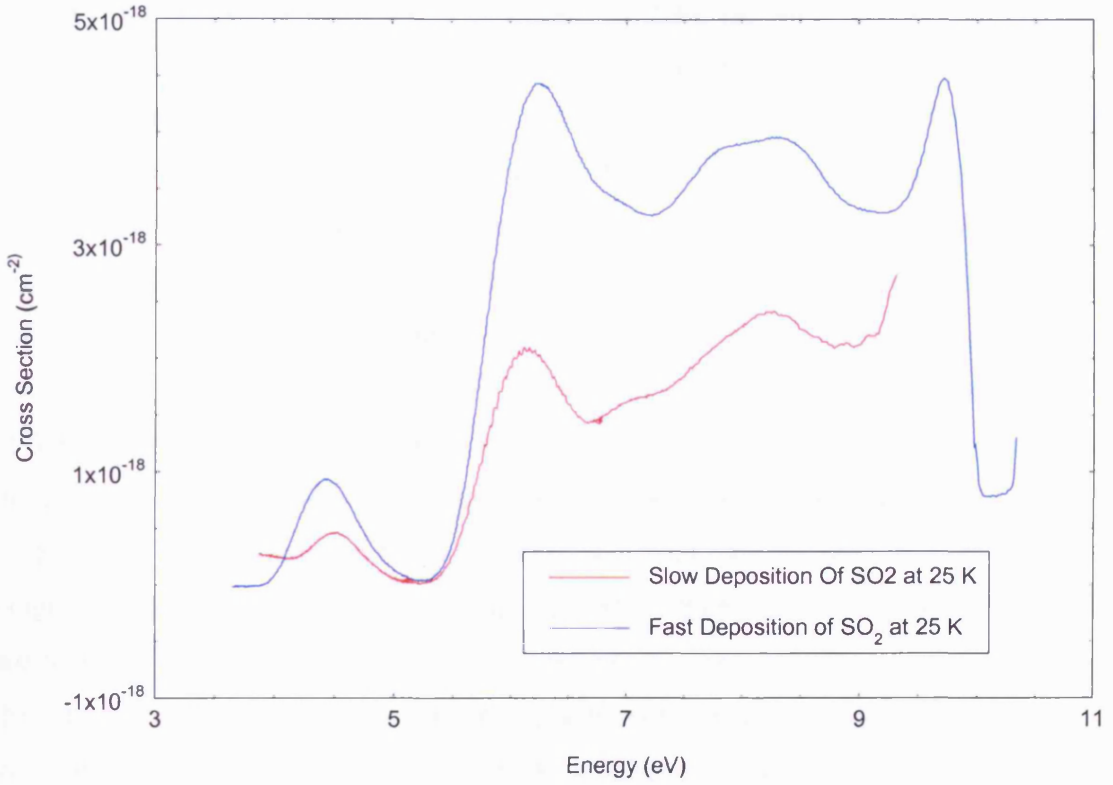

Figure 5-25 Comparison between the slow and fast deposition of SO_2 at 25 K

There is a shift in the energy of the bands between the slow and fast depositions. The shift is approximately 0.1 eV towards higher energy from the slow deposition to the fast deposition. Some of the structure in the D and E band of SO_2 has also been altered by the fast deposition. There is no longer a small peak at 7.5 ev. Instead the spectrum rises smoothly to a peak at 8.25 eV. There is also a notable decrease in cross section for the slow deposition but this could be due to a change in density of the SO_2 molecule in different crystalline configurations. When calculating the cross section for both deposition rates we assumed a density of 1.98 g cm^{-3}.

The spectrum of SO_2 highlights the importance of deposition rate when studying condensed phase ices. Fast deposition rates will produce an amorphous solid with little vibrational structure. SO_2 molecules may be in any orientation and so all vibrations become washed out and form broad bands. Crystalline solids are formed at longer deposition rates.

Most of the research concentrated on deposition rates has been directed at the water molecule. (Kouchi, Yamamoto et al. 1994) set out some of the conditions for an amorphous ice to form. "Amorphous ice forms if the molecules are "frozen" in the vicinity of the adsorption points and can not settle to the crystalline configuration. I.e. the diffusion distance during the deposition time must be smaller than the lattice constant of the ice for an amorphous ice to form. It is clear from our ice samples that a similar thing is happening with SO_2. A fast deposition will produce an amorphous ice. Our evidence for the amorphous nature of low temperature (with a high deposition rate) of SO_2 comes from considering the nature of an amorphous solid. In an amorphous solid there is *no long range order.* This means there is no coupling between molecules. The order in any solid depends on the orientation and distribution of the molecules. No long range order in an amorphous solid suggests that random orientations and distributions are possible. This random orientation frees the SO_2 ice from any constraints placed upon the vibrations of the SO_2 and so no selection rules apply and it is possible to excite all vibrational modes directly by single-mode processes (Henning and Mutschke 1997). Thus, absorption spectra of amorphous materials reflect the whole density of vibrational states which is itself broadened due to the statistical variation in bond length and angle. In contrast in a crystalline state we have coupling between the molecules. (Whalley and Bertie 1967) state that coupling can increase the intensity of infrared features (and thus we assume their UV counterparts) by propagating a particular vibration through the crystal lattice. From this argument it seems clear that when we observe vibrational structure in our ice we must be viewing a crystalline structure.

5.4 VUV Photoabsorption of CO at 20 K

Carbon monoxide, CO ($X^1\Sigma^+$) is a simple linear molecule, a common substance found on earth and in space. For instance (Federman, Lambert et al. 2003) report the ultraviolet signature of CO towards ρ Oph A and χ Oph recorded using the Goddard High Resolution Spectrograph on the Hubble Space Telescope. After H_2, CO is the most abundant molecule in the Interstellar Medium. (van Dishoeck and Black 1988). The rotational lines of CO are often widely used as a tracer of molecular material in interstellar clouds in Astronomy. The CO "Fourth Positive Band system" ($A^1\Pi - X^1\Sigma^+$) has also been observed in the sun, the planets and the ISM. The air glow spectrum of Mars and Venus shows evidence of these emissions from the impact of photoelectrons and the effects of solar UV photons. (Beegle, Ajello et al. 1999)

The carbon monoxide ground state may be written as:

$$(1\sigma)^2(2\sigma)^2(3\sigma)^2(4\sigma)^2(1\pi)^4(5\sigma)^2 \qquad (5.4)$$

5.4.1 Experimental Procedure

Before the deposition of CO we cooled our CaF_2 substrate to a base temperature of 20 K. We then recorded a background scan. Experimental constraints due to the lack of a He-Ne laser at the time of data collection prevented us from recording a laser thickness measurement of CO deposition. We deposited 0.5 mbar CO in 30 seconds and recorded a UV spectrum. Figure 5-26.

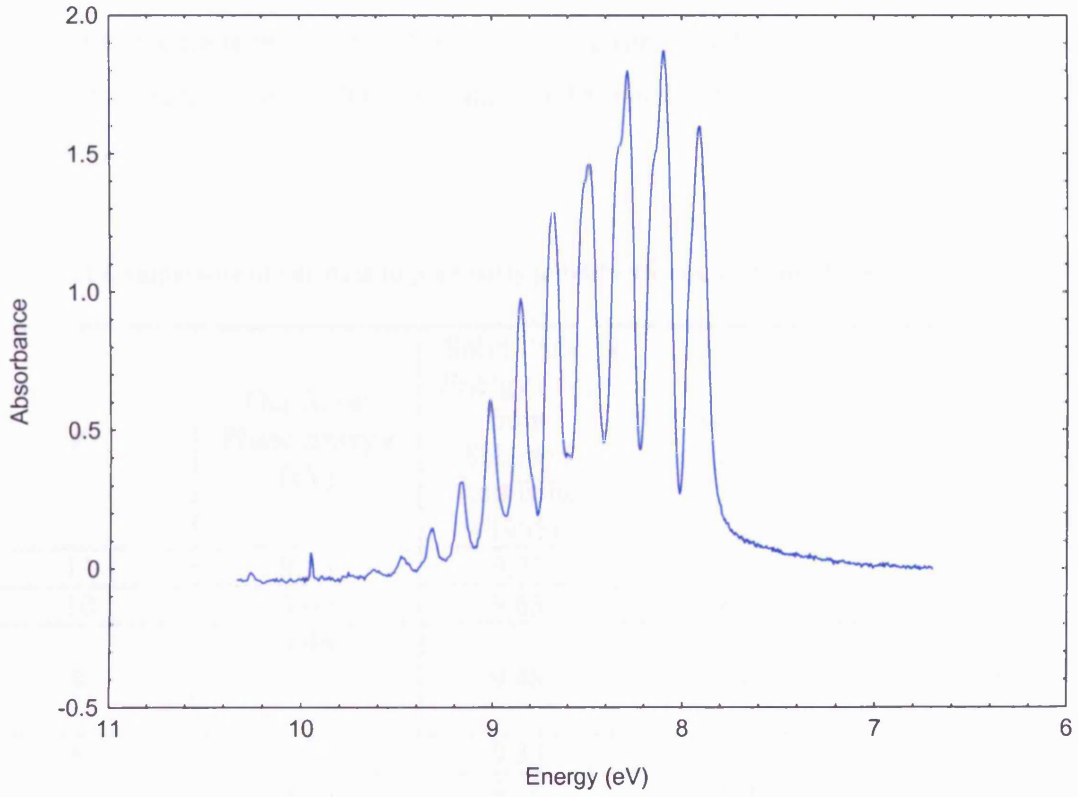

Figure 5-26 UV spectrum of CO at 20 K

5.4.2 Results

CO deposited at 20 K exhibits vibrational features. These are tabulated in Table 5-10. Peak splitting is also evident and the split peaks are listed in parentheses in Table 5-10 and Table 5-11

Table 5-10 Vibrational Progression in CO at 20 K

Band Number	Energy (eV)	Peak Separation (eV)	Band Number	Energy (eV)	Peak Separation (eV)
1	9.78	-	7	8.88	0.13
2	9.62	0.16	8	8.68	0.2
3	9.48	0.14	9	8.48 (8.51)	0.2
4	9.31	0.17	10	8.29 (8.33)	0.19
5	9.16	0.15	11	8.09 (8.14)	0.2
6	9.01	0.15	12	7.90 (7.96)	0.19

We identify the transition as the ($A^1\Pi - X^1\Sigma^+$) transition and have compared our work to pervious results on solid CO. The data of (Brith and Schnepp 1965) is shown in Table 5-11

Table 5-11 Comparison of our data to previously published work on solid phase and gas phase CO.

v'	Our Solid Phase Energy (eV)	Solid Phase Energy (eV) from Schnepp And Brith (1965)	Gas Phase Energy (eV)	ΔE (Gas- Solid)
11	9.78	9.77	9.95	0.18
10	9.62	9.63	9.81	0.18
9	9.48	9.48	9.67	0.19
8	9.31	9.33	9.53	0.20
7	9.16	9.18	9.38	0.20
6	9.01	9.02	9.22	0.20
5	8.88	8.86	9.07	0.21
4	8.68	8.69	8.90	0.21
3	8.48 (8.51)	8.49 (8.54)	8.74	0.26
2	8.29 (8.33)	8.29 (8.35)	8.57	0.28
1	8.09 (8.14)	8.10 (8.17)	8.39	0.30
0	7.90 (7.96)	7.91 (7.97)	8.21	0.31

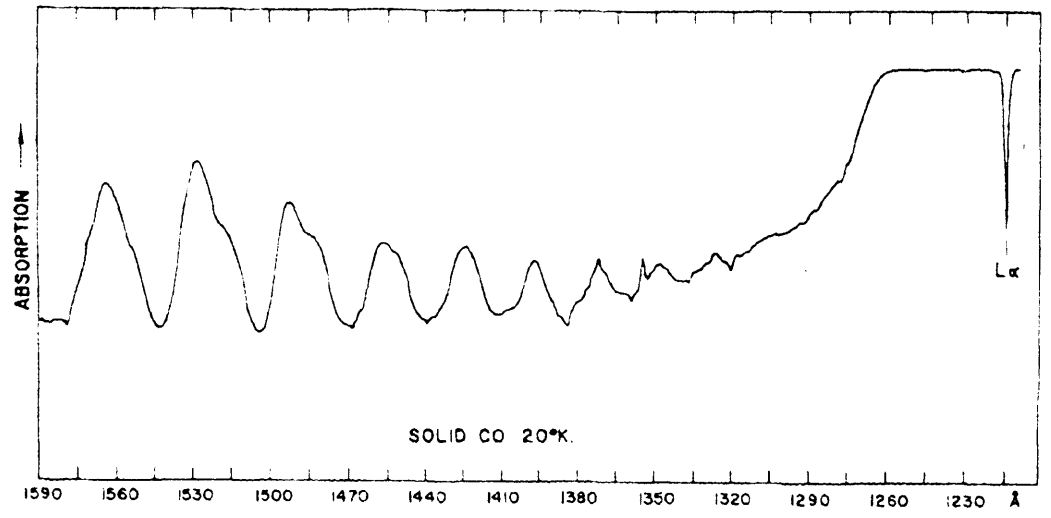

Figure 2. Tracing of the absorption spectrum of solid CO at 20°K. Transition : $A\ ^1\Pi \leftarrow X\ ^1\Sigma^+$.

Figure 5-27 Tracing of the absorption spectrum of solid CO at 20 K as reported by (Brith and Schnepp 1965)

5.4.3 Discussion.

The spectrum of solid CO was reported by (Brith and Schnepp 1965) Figure 5-27. Our results are in excellent agreement with theirs as can be seen in Table 5-11. Our progression contains 12 bands identified as (0,0) to (11,0). We do not see the (12,0) transition as observed by (Brith and Schnepp 1965) due to our low sensitivity in the high energy region. We note the (0,0) transition is shifted 0.31 eV from the gas phase with the shift becoming increasingly smaller until the (4,0) transition where the shift remains constant. The (0,0) to (3,0) bands of CO exhibit a crystal field splitting identified as Davydov splitting ((Brith and Schnepp 1965)). Davydov splitting is defined as "*The splitting of bands in the electronic or vibrational spectra of crystals due to the presence of more than one (interacting) equivalent molecular entity in the unit cell*". As we currently have no thickness information for our CO sample we can not make any comments on the photoabsorption cross section but this will be addressed in future work.

5.5 VUV Photoabsorption of CO_2 at 25 K

Carbon dioxide, CO_2 ($X_1\Sigma_g^+$) is an important constituent of cometary bodies, the atmospheres of planets and interstellar dust grains. It has been detected in all three locations. A thorough knowledge of its UV spectrum is therefore essential. CO_2 has been detected in both solid and gaseous form in the Interstellar medium. (Gerakines, Whittet et al. 1999; Sandford, Bernstein et al. 2001).

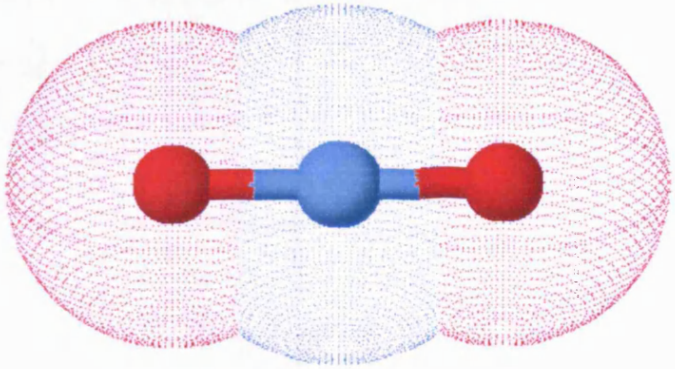

Figure 5-28 The Carbon Dioxide (CO_2) Molecule

Observations using the Infrared Space Observatory (ISO) have detected solid CO_2 towards numous sources detecting both polar (CO_2 mixed with water, with H_2O dominant) and one nonpolar (CO_2 dominant) forms of CO_2 ice. (Gerakines, Whittet et al. 1999)

A summary of the properties of CO_2 is given in Table 5-12.

Table 5-12 Summary of the Molecular Properties of CO_2 from (Herzberg 1966)

State	Point Group	T_0 (cm^{-1})	Vibrational Frequencies (cm^{-1}) ν_1	ν_2	ν_3	Electronic Configuration	Observed Transitions (nm)
$\tilde{B}\begin{Bmatrix}{}^1B_1(\Sigma_g^-)\\ {}^1A_1(\Delta_g)\end{Bmatrix}$	C_{2v}	73100 72480	1225			$\begin{Bmatrix}..b_1a_1^2a_2^2b_2^2a_1\\ ..b_1^2a_1a_2^2b_2^2a_1\end{Bmatrix}$	B↔ X (139 -122)
$A^1B_2(\Delta_u)$	C_{2v}	46000				$...1\pi_u^4a_2^2b_2a_1$	A↔ X
$X^1\Sigma_g^+$	$D_{\infty h}$	0	1388.17	667.40	2349.16	$...4\sigma_g^23\sigma_u^21\pi_u^41\pi_g^4$	IR

5.5.1 Experimental Procedure

Before measuring any UV transmission spectra it is necessary to calibrate the instrument and determine the thickness of the ice film deposited on the substrate per mbar of gas pressure in our gas reservoir. In order to do this we have developed a laser interference method (Chapter 3)

5.5.1.1 Calibration of the film thickness

In order to calibrate our dosing system for each new molecule it is necessary to deposit a sample of our target molecule while recording the reflection from the ice surface from a He-Ne laser. We have deposited from 0 to 6 mbar as recorded in Table 5-13. The substrate temperature was 25 K during deposition and the chamber pressure was 5 x 10^{-9} mbar before deposition commenced.

Table 5-13 Laser Thickness Measurements for CO_2 at 25K

Time for Deposit (seconds)	Total Deposited (mbar)	Diode Current (mA)
-	0.0	27.40
22	0.2	25.90
35.5	0.4	23.30
20.2	0.6	20.80
22.5	0.8	19.20
30	1.0	19.00
26.1	1.2	20.50
23.3	1.4	23.00
26.4	1.6	25.80
24.8	1.8	27.80
20.4	2.0	28.60
22	2.2	27.70

27.5	2.4	25.50
25	2.6	22.60
22.8	2.8	20.00
26.3	3.0	18.50
20	3.2	18.80
32.8	3.4	20.90
10.6	3.7	26.30
17.9	3.8	27.80
31.6	4.0	29.10
24.9	4.2	28.70
28.1	4.4	26.70
20.5	4.6	23.40
32.5	4.8	21.00
28.6	5.0	18.80
22.7	5.2	18.40
24.6	5.4	19.70
28	5.6	22.50
23.2	5.8	25.40
21.3	6.0	27.50

This data is plotted in Figure 5-29.

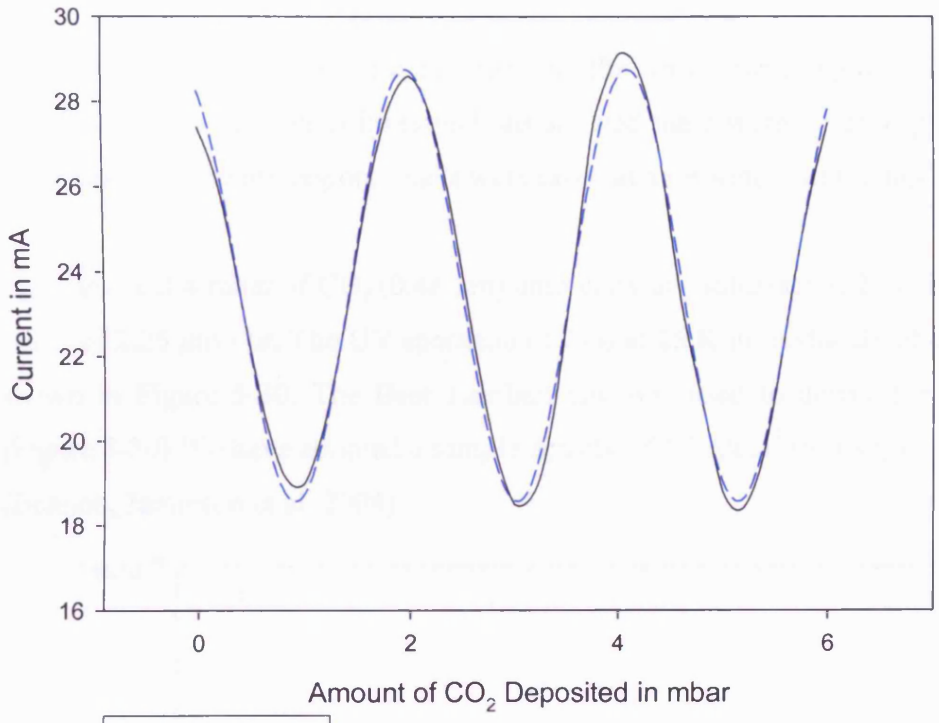

f=y0+a*sin(2*3.14159265359*x/b+c)

	Coefficient	Std. Error	t	P
a	5.0893	0.0985	51.6655	<0.0001
b	2.1190	0.0077	274.9023	<0.0001
c	2.0156	0.0377	53.4115	<0.0001
y0	23.6502	0.0713	331.8719	<0.0001

Figure 5-29 Deposition Curve of CO_2

Using the data in Table 5-13 we determine the refractive index of CO_2 at 25K to be 1.54. The compares to a value of 1.4 for CO_2 ice at 53 K given in (Monahan and Walker 1975) which was obtained from a Kramers-Kronig analysis by the authors.

From this the thickness of our ice sample is

$$d = \frac{\lambda_0}{2n_f \cos\theta_f} = \frac{0.6328}{2\times 1.54\times\cos(37)} = 0.26\ \mu\text{m}$$

Note that θ_f is the angle of the laser *within the ice* (which is calculated using Snell's law). Thus one period of the since curve corresponds to 0.26 μm of CO_2 ice. Using Figure 5-29 we observe one period also corresponds to 2.1 mbar of CO_2 deposited. So we can conclude that for every mbar of CO_2 deposited this represents 0.12 μm of ice.

5.5.2 Results

VUV absorption spectra were recorded in the wavelength region 120 to 180 nm. Preliminary low resolution investigations showed there were no absorption features in the longer wavelength region. Scans were taken at a resolution of 0.2 nm

We deposited 4 mbar of CO_2 (0.48 μm) onto our CaF_2 substrate at 25 K in 780 seconds, a rate of 2.25 μm / hr. The UV spectrum of CO_2 at 25 K immediately after deposition is shown in Figure 5-30. The Beer Lambert law was used to derive the cross sections (Figure 5-30) We have adopted a sample density of 1.7 g/cm^3 for CO_2 in this calculation (Bennett, Jamieson et al. 2004)

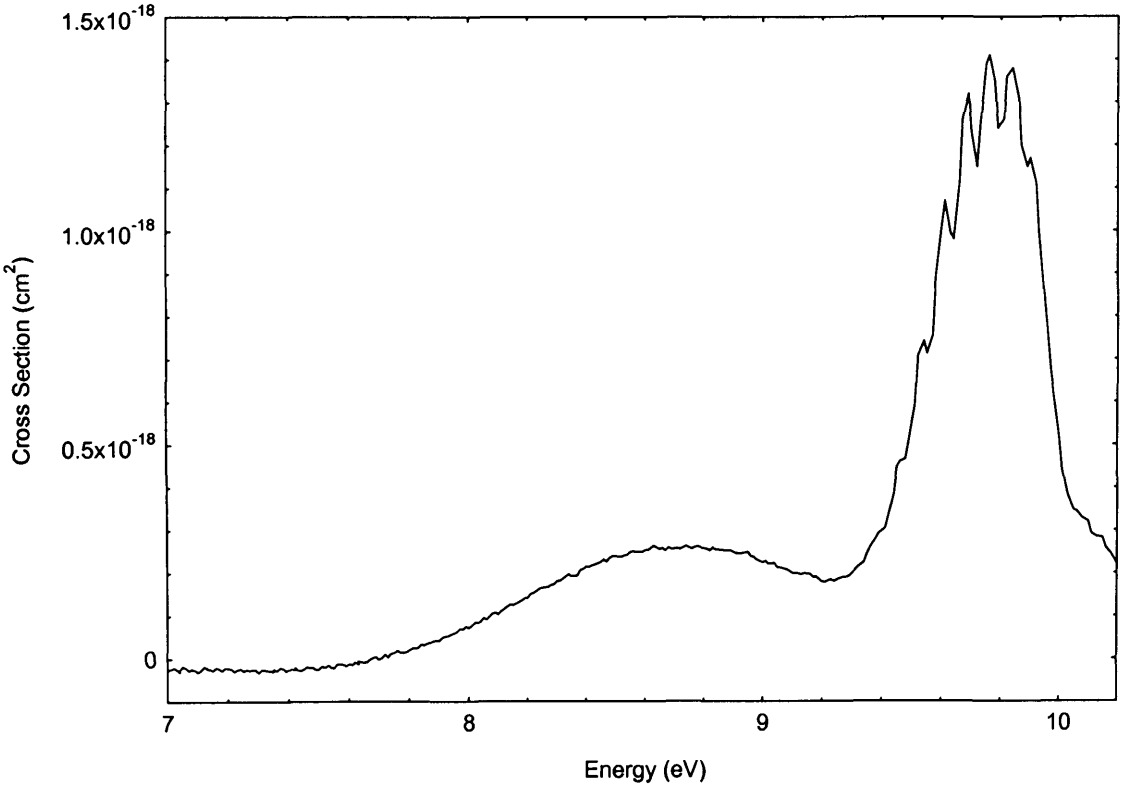

Figure 5-30 Cross Sections of CO_2 deposited at 25 K

The solid phase UV spectrum of CO_2 has been previously studied by (Monahan and Walker 1974) and (Monahan and Walker 1975). There are two regions in our spectra which are identified as the $^1\Pi_g \leftarrow {}^1\Sigma_g^+$ transition centred at 9.8 eV (126 nm), and the

broad transition centred at 8.67 eV has been identified as $^1\Delta_u \leftarrow {}^1\Sigma_g^+$ (Monahan and Walker 1974)

Table 5-14 Vibrational Structure in CO_2 at 25K

Peak Position, Our Data (eV)	Peak Separation (eV)	Monahan Data Solid (eV) [a]	Monahan Gas Peak Position (eV) [a]	$\Delta E_{(sold - gas)}$ Our data (eV)
9.38				
9.45	0.07			
9.54	0.09	9.53	9.50	0.04
9.62	0.08	9.59	9.58	0.04
9.69	0.07	9.67	9.66	0.03
9.77	0.08	9.74	9.74	0.03
9.85	0.08	9.82	9.82	0.03
9.91	0.06	9.90	9.89	0.02

a Taken from (Monahan and Walker 1974)

The vibrational structure seen in the spectrum is tabulated in Table 5-14 and is attributed to the ν_2 bending progression (Rabalais, McGlynn et al. 1971) When compared with gas phase data of (Monahan and Walker 1974) (Figure 5-31) it shows a shift of ~ 0.03 eV towards higher energies. This contrasts to the findings of (Monahan and Walker 1974) who observed little to no shift in the bending progression of CO_2 but did see a shift in the continuum of more than 0.5 eV (the continuum is due to the dissociation along the asymmetric stretch coordinate). This shift in the continuum is best shown in Figure 5-32. Gas phase data on CO_2 at 195 K is taken from (Yoshino, Esmond et al. 1996)).It is clear that the $^1\Pi_g \leftarrow {}^1\Sigma_g^+$ transition is shifted by a large amount compared to the gas phase (approximately 0.5 eV). The $^1\Delta_u \leftarrow {}^1\Sigma_g^+$ continuum shifts by a much smaller amount, 0.34 eV is quoted by (Monahan and Walker 1975), and we find a shift of 0.13 eV from our data to the gas phase data of (Yoshino, Esmond et al. 1996)

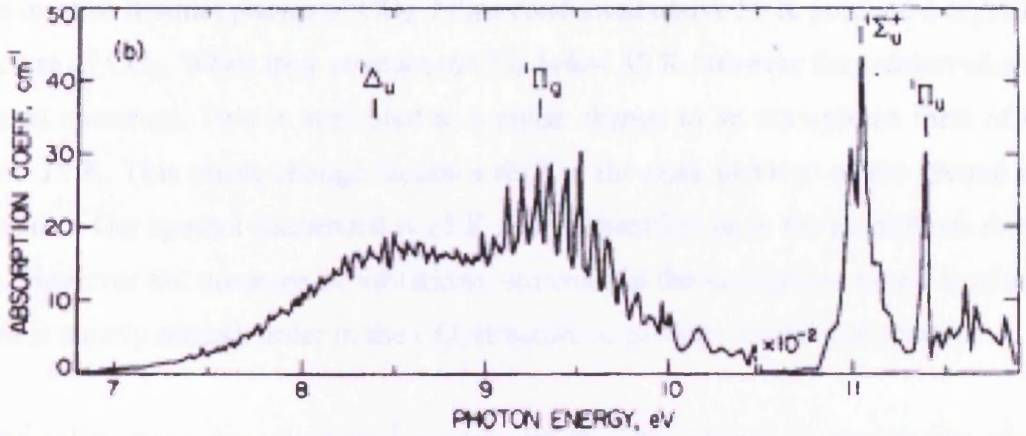

Figure 5-31 Gas Phase Spectrum of CO_2 obtained by (Monahan and Walker 1974)

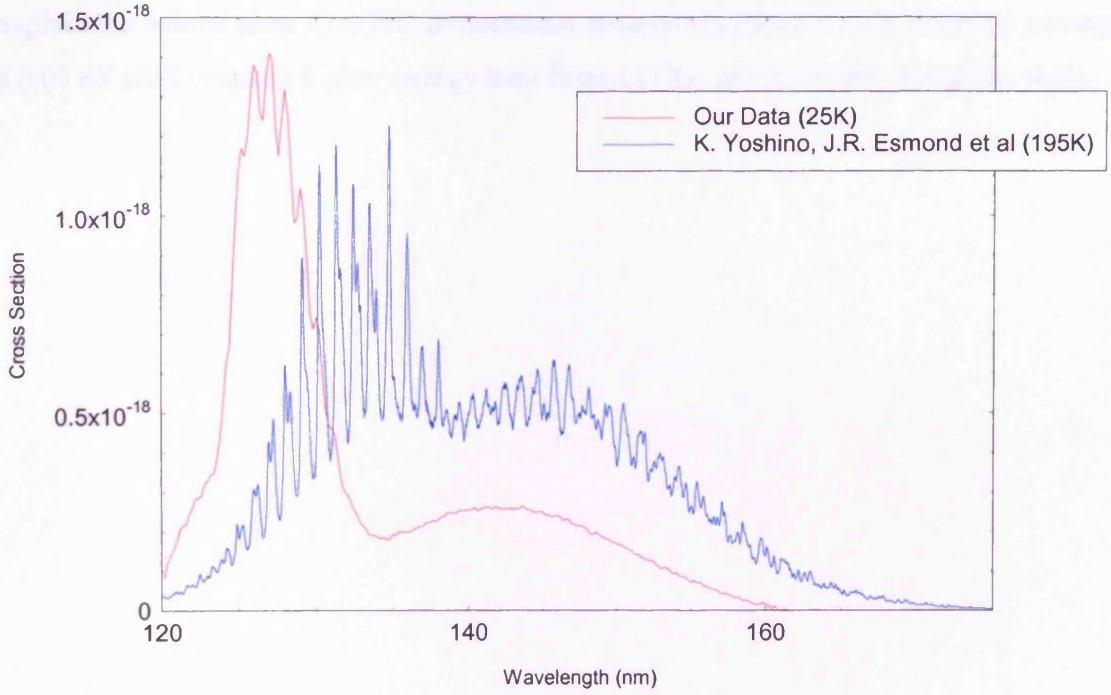

Figure 5-32 Comparison between gas and solid phase CO_2 (Gas phase data from (Yoshino, Esmond et al. 1996))

This shift in the band spacing from gas to solid could be explained by a change in the physical properties of the CO_2. The data of (Monahan and Walker 1974) was taken at a temperature of 53 K. Infrared studies of ice films by (Falk 1987) show that

there are two distinct phases of CO_2. Films condensed *above* 50 K produce a crystalline structure of CO_2. When they condensed CO_2 *below* 35 K however they observed a new infrared spectrum. This is attributed to a phase change to an amorphous form of CO_2 below 35 K. This phase change causes a shift in the peak position of the ground state vibrations. Our spectra condensed at 25 K should therefore be in the amorphous form of CO_2. However the presence of vibrational structure in the amorphous phase is unusual. There is clearly enough order in the CO_2 structure to produce vibrational features.

In the solid phase the vibrational modes and thus the electronic spectra are closely coupled with the physical state of the solid. Deposition rate and angle all affect the structure of the deposited solid. These differences between the two experiments could explain the results seen. Our low temperature amorphous films of CO_2 show on average a 0.03 eV shift towards higher energy than films of CO_2 grown in the crystalline state.

5.6 VUV Photoabsorption of CH_3NH_2

Methylamine, CH_3NH_2 (X_1A') is a C_s molecule. (Figure 5-33) It has been detected in gaseous form in the interstellar medium (Fourikis, Takagi et al. 1974; Kaifu, Morimoto et al. 1974). It is regarded as an important molecule from an astrobiology perspective as it is a precursor of the amino acid glycine. (Chapter 6) .The gas phase spectrum is known to exhibit two bands in the VUV region centred at 5.7 and 7.2 eV (Hubin-Franskin, Delwiche et al. 2002). It is suggested that the two electronic states in this region correspond to the lowest lying (3s, A') Rydberg state and a valence state of symmetry A".

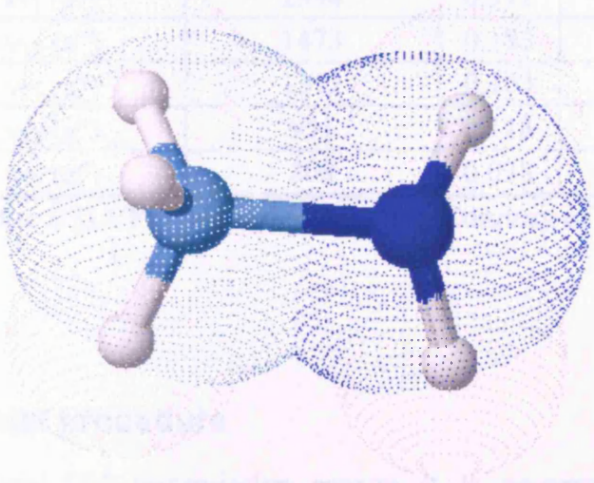

Figure 5-33 CH_3NH_2 Molecule

The low lying excited states of methylamine have been investigated in detail by (Taylor and Bernstein 1995). They calculated the fundamental frequencies expected for the 3s A' Rydberg state and concluded that the two lowest states of excited CH_3NH_2 are planar in nature about the C-NH_2 bond.

Table 5-15 Calculated ground state methylamine vibrational modes and infrared intensities.

Species	Vibration Number	Scaled Frequency cm^{-1}	Energy eV	Intensity Km mol^{-1}	Characterisation
CH_3NH_2 ($X\ ^1A'$) [(a)]	ν_1 (a')	3383	0.419	2	NH_2 sym. str.
	ν_2 (a')	2960	0.367	42	CH_3 asym. str.
	ν_3 (a')	2860	0.355	103	CH_3 sym. str.
	ν_4 (a')	1619	0.201	23	NH_2 scissor
	ν_5 (a')	1452	0.180	7	CH_3 deform
	ν_6 (a')	1418	0.176	2	CH_3 umbrella
	ν_7 (a')	1137	0.141	7	CH_3 rock
	ν_8 (a')	1024	0.127	8	CN str.
	ν_9 (a')	827	0.103	164	NH_2 umbrella
	ν_{10} (a")	3455	0.428	0	NH_2 asym. str.
	ν_{11} (a")	2994	0.371	38	CH_2 asym. str.
	ν_{12} (a")	1473	0.183	3	CH_3 deform
	ν_{13} (a")	1312	0.163	0	NH_2, CH_3 rock
	ν_{14} (a")	951	0.118	0	NH_2, CH_3 rock
	ν_{15} (a")	308	0.038	39	torsion

(a) Calculated using the B3LYP/6-311G(d,p) basis set. Courtesy of Prof. Yoshihiro Osamura.

5.6.1 Experimental procedure

Before measuring any UV transmission spectra it is necessary to calibrate the instrument and determine the thickness of the ice film deposited on the substrate per mbar of gas pressure in our gas reservoir.

5.6.1.1 Calibration of the film thickness

In order to calibrate our dosing system for each new molecule it is necessary to deposit a sample of our target molecule while recording the reflection from the ice surface using a He-Ne laser. We have deposited from 0 to 7.2 mbar of CH_3NH_2 onto our cooled CaF_2 substrate. The base pressure was $\leq 10^{-9}$ mbar with a temperature of 25 K. The deposition is shown in Table 5-16 and plotted in Figure 5-35. We find the refractive index of our sample to be 1.78.

Table 5-16 Laser Thickness Measurements for CH_3NH_2

Amount Deposited (mbar)	Time for deposit (seconds)	Total deposited (mbar)	Laser Current (mA)
0.0	-	0.0	29.25
0.2	17	0.2	28.72
0.2	11	0.4	27.07
0.2	15	0.6	24.5
0.2	13	0.8	21.7
0.2	21	1.0	18.97
0.2	23	1.2	17.24
0.2	20	1.4	16.61
0.2	20	1.6	17.37
0.2	18	1.8	19.09
0.2	17	2.0	21.65
0.2	19	2.2	24.33
0.2	25	2.4	26.67
0.2	22	2.6	27.99
0.2	25	2.8	28.4
0.2	17	3.0	27.4
0.2	20	3.2	25.4
0.2	24	3.4	22.8
0.2	16	3.6	20.1
0.2	15	3.8	17.76
0.2	20	4.0	16.25
0.2	19	4.2	15.95
0.2	24	4.4	17
0.2	19	4.6	19
0.2	19	4.8	21.57
0.2	19	5.0	24.1
0.2	23	5.2	26.1
0.2	18	5.4	27.1
0.2	26	5.6	27
0.2	21	5.8	25.8
0.2	21	6.0	23.7
0.2	15	6.2	21.1
0.2	17	6.4	18.49
0.2	24	6.6	16.36
0.2	22	6.8	15.2
0.2	22	7.0	15.24
0.2	22	7.2	16.53

Applying this to (3.4) we find the thickness of our ice sample to be

$$d = \frac{\lambda_0}{2n_f \cos\theta_f} = \frac{0.6328}{2 \times 1.78 \times \cos(31)} = 0.21\ \mu\text{m}$$

Note that θ_f is the angle of the laser *within the ice* (which is calculated using snell's law). Thus one period of the since curve corresponds to 0.21 μm of CH_3NH_2 ice. Using Figure 5-34 we observe one period also corresponds to 2.7 mbar of CH_3NH_2 deposited. So we can conclude that for every mbar of CH_3NH_2 deposited this represents 0.07 μm of ice.

We grew CH_3NH_2 using a deposition of 7 mbar which translates to a thickness of 0.53 μm. We then recorded VUV adsorption spectra in the region 120-220 nm at a resolution of 0.20 nm Figure 5-35

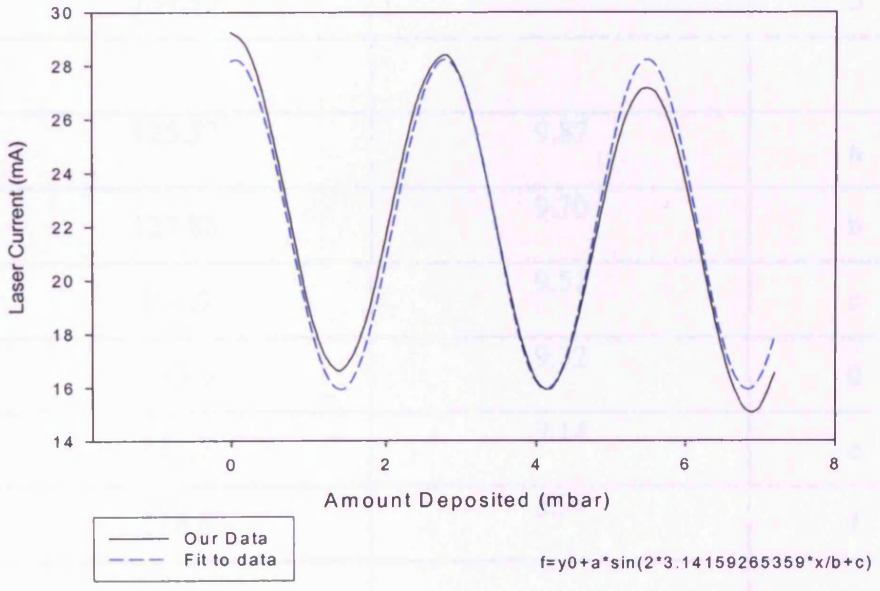

Figure 5-34 Deposition Curve for CH_3NH_2 at 25K

5.6.2 Results

The VUV spectrum of CH_3NH_2 collected immediately after gas deposition at 25 K is shown in Figure 5-35. We see clear vibrational structure. (Table 5-17), three vibrational progressions can be identified (in Figure 5-36 and Figure 5-37) which we have labelled 1-6, a-f. and I to VI

Table 5-17 Vibrational progressions is CH_3NH_2 at 25 K

Wavelength (nm)	Wavelength (eV)	Label	ΔE (eV)
124.71	9.94	1	
127.01	9.76	2	0.17
129.39	9.58	3	0.17
131.8	9.41	4	0.16
134.39	9.22	5	0.17
125.57	9.87	a	
127.85	9.70	b	0.17
130.3	9.51	c	0.17
133.0	9.32	d	0.18
135.7	9.14	e	0.17
138.6	8.94	f	0.18
178.34	6.95	I	0.05
179.60	6.90	II	0.05
180.9	6.85	III	0.05

182.40	6.80	IV	0.06
183.97	6.74	V	0.06
185.77	6.67	VI	0.05

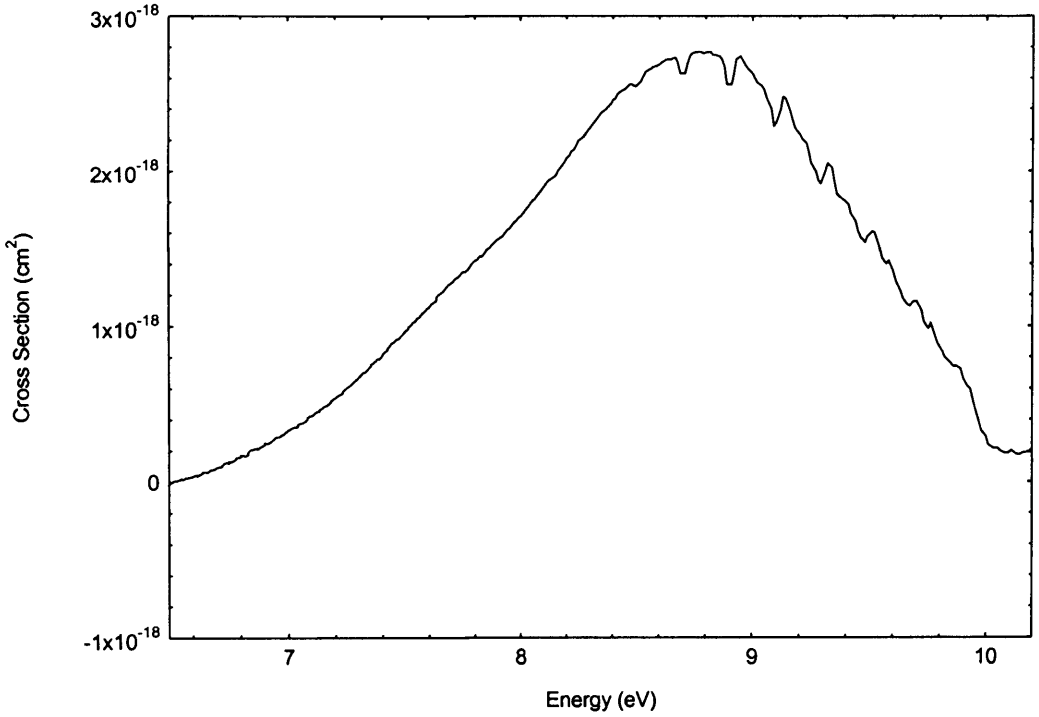

Figure 5-35 VUV Spectrum of CH_3NH_2 at 25K

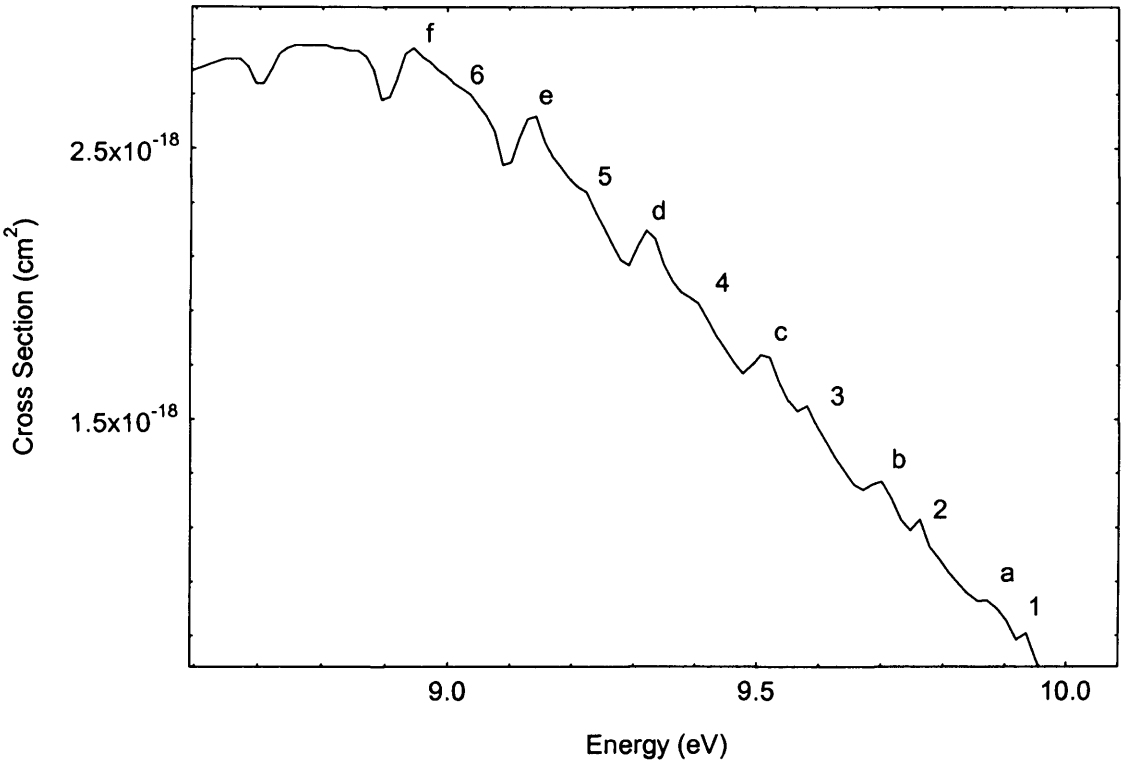

Figure 5-36 Scaled view of CH_3NH_2 at 25 K

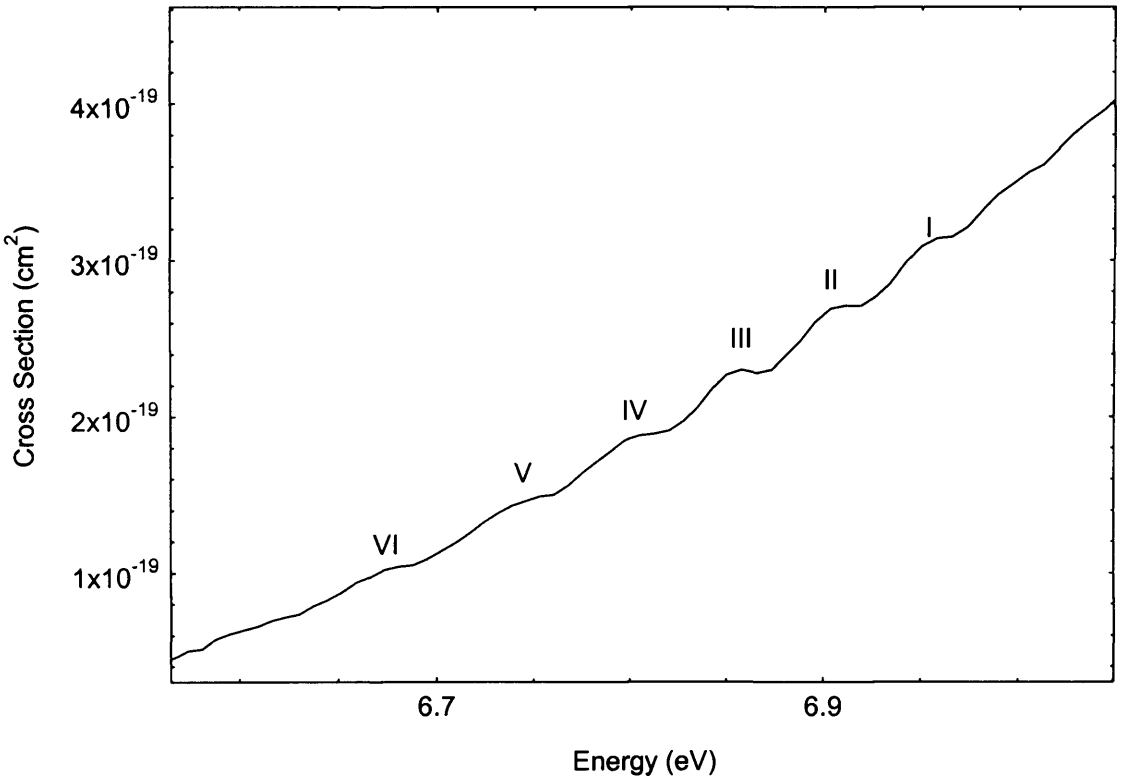

Figure 5-37 Scaled view of Progression in CH_3NH_2 at 25 K

The two vibrational progressions 1-6 and a-f have an average separation of 0.17 eV. This corresponds to 1371 cm^{-1}. This suggests that the underlying progression can be attributed to the ν_6 CH_3 umbrella mode of the methylamine molecule at 1377 cm^{-1}

(Taylor, Walker et al. 1980). There is however what appears to be two progressions (1-6) and (a-f), The spacing indicates the second progression (a-f) could be built upon $n\nu_6 + \nu_{15}$. The progression labelled I to VI has an average spacing of 0.045 eV. (363 cm^{-1}). The only vibrational mode this could correspond to is the ν_{15} torsion fundamental. (Table 5-15). Alternatively we could be seeing a progression in $n\nu_9$ and $n\nu_9 + \nu_{15}$ as the spacing between I and III (Table 5-17) corresponds to 0.1 eV which is ~ ν_9.

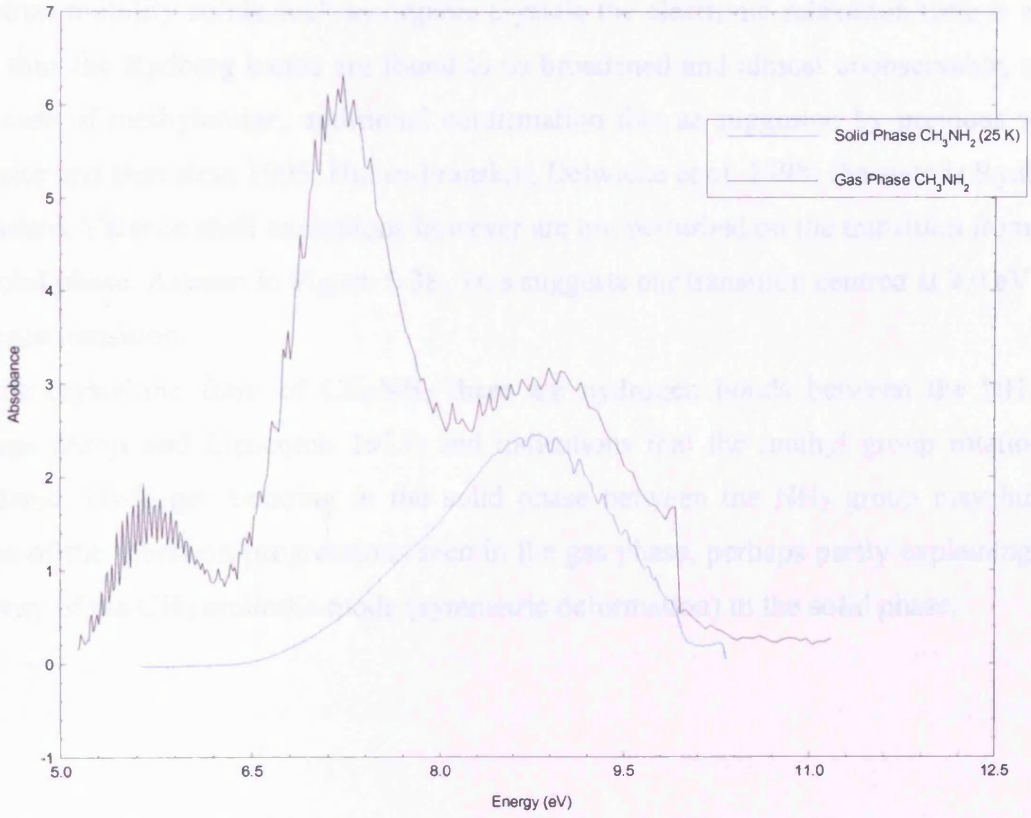

Figure 5-38 Comparison between gas and solid phase (25 K) UV spectrum of CH_3NH_2

When the gas and solid phase spectra of CH_3NH_2 are compared (Figure 5-38) it is clear that there is a substantial change caused by the solidification of the CH_3NH_2.

We would naturally expect a shift of the electronic spectrum on the transition between the solid and gaseous phase (Robin 1974). However the spectrum of CH_3NH_2 in the solid phase is radically different to the gaseous phase. Our solid phase spectrum exhibits only one broad peak as opposed to the 3 seen in the gas phase. In the gaseous phase the predominantly optically active modes are the ν_9 NH_2 wag and the ν_7 CH_3 rocking modes. (Baek, Choi et al. 2002);(Hubin-Franskin, Delwiche et al. 1998; Hubin-Franskin, Delwiche et al. 2002). In the solid phase, in the progression labelled a-f and 1-

6 the separation of the quanta in the vibrational spacing does not suggest an assignment to the ν_9 NH_2 wag and the ν_7 CH_3 rocking modes as for the gas phase. Rather the ν_6 CH_3 umbrella mode of the methylamine molecule is now active. The low intensity in the solid phase of the first two bands seen in the gas phase is not unexpected. Recall that the two transitions seen in the gas phase are thought to be attributed to a Rydberg excitation.(Hubin-Franskin, Delwiche et al. 1998). (Robin 1974) observes that in low electron mobility solids such as organic crystals the electronic relaxation time is short and thus the Rydberg bands are found to so broadened and almost unobservable, as in the case of methylamine, additional confirmation that as suggested by previous work (Taylor and Bernstein 1995; Hubin-Franskin, Delwiche et al. 1998) the state is Rydberg in nature. Valence shell excitations however are not perturbed on the transition from gas to solid phase. As seen in Figure 5-38. This suggests our transition centred at 9.0 eV is a valence transition.

In the crystalline form of CH_3NH_2 there are hydrogen bonds between the NH...N groups (Atoji and Lipscomb 1953) and indications that the methyl group rotation is hindered. Hydrogen bonding in the solid phase between the NH_2 group may hinder some of the vibration progressions seen in the gas phase, perhaps partly explaining the activity of the CH_3 umbrella mode (symmetric deformation) in the solid phase.

5.7 VUV Spectroscopy and Irradiation Studies of CH_3NH_2 and CO_2 mixtures.

5.7.1 Introduction.

Methylamine and carbon dioxide are possible precursors of the amino acid glycine. In Chapter 6 we will present a full overview of the possible reaction pathways to glycine from electron irradiated CH_3NH_2 and CO_2. To compliment this we have recorded the VUV spectra of a mixture of methylamine and CO_2 ice for the first time and we will present preliminary results of the UV irradiation of a mixture of CH_3NH_2 and CO_2 in Chapter 6.

5.7.2 Experimental

Before deposition we cooled a clean CaF_2 substrate to 25 K and recorded spectra of our cooled blank CaF_2 disk at 25 K. Spectra were recorded in the region 120-200 nm at a resolution of 0.2 nm. We have dosed a mixture of 1.5:1 (gas phase ratio) of CH_3NH_2:CO_2 onto a cooled CaF_2 substrate at 25 K. The mixture was prepared by allowing the two gases to combine in our mixing cell before deposition. We deposited a 10 mbar pressure of the mixture from our mixing cell onto the substrate in 1630 seconds. The chamber pressure before deposition was 1.4×10^{-8} mbar. After deposition we have recorded the VUV spectrum of the mixture at 25 K. We then underwent an annealing process with our sample, simulating some of the heating and cooling events an interstellar ice could be expected to receive. The sample was subjected to successive heating and cooling phases, each time recording a spectrum until the sample temperature reached 100 K and the mixture desorbed from the surface.

5.7.3 Results.

The VUV spectrum of the CO_2 : CH_3NH_2 mixture deposited at 25 K is shown in Figure 5-39. An overlay of the UV spectra of the components of the mixture is shown in Figure 5-39

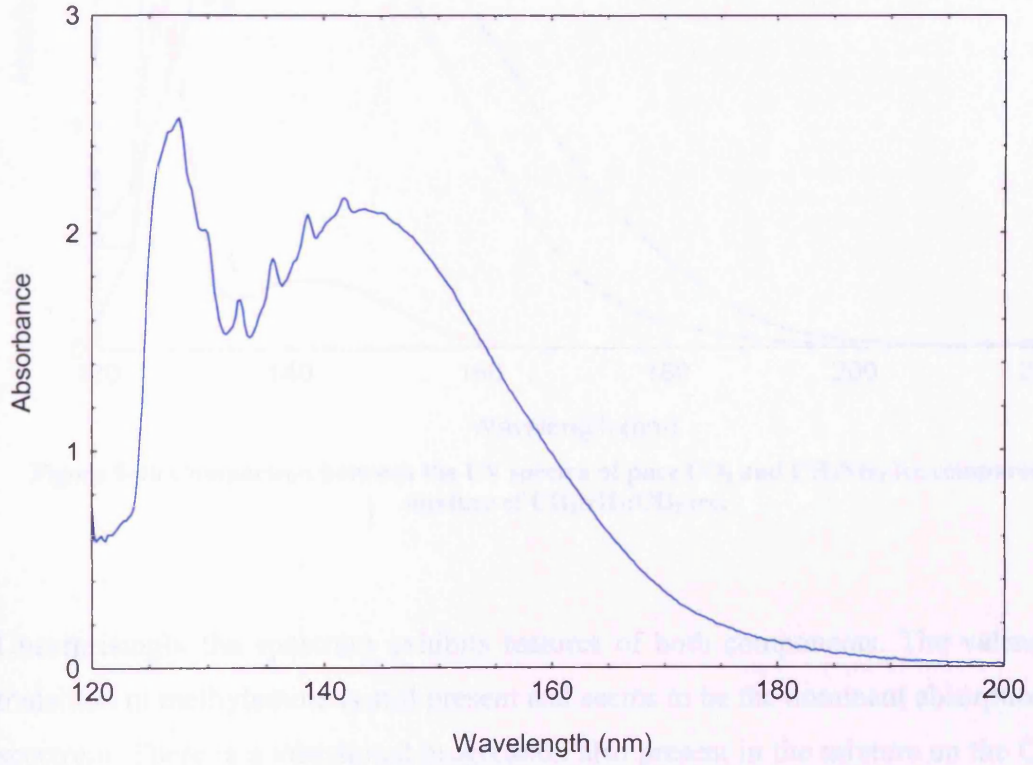

Figure 5-39 VUV Spectrum of CH_3NH_2 and CO_2 mixture at 25 K after dosing.

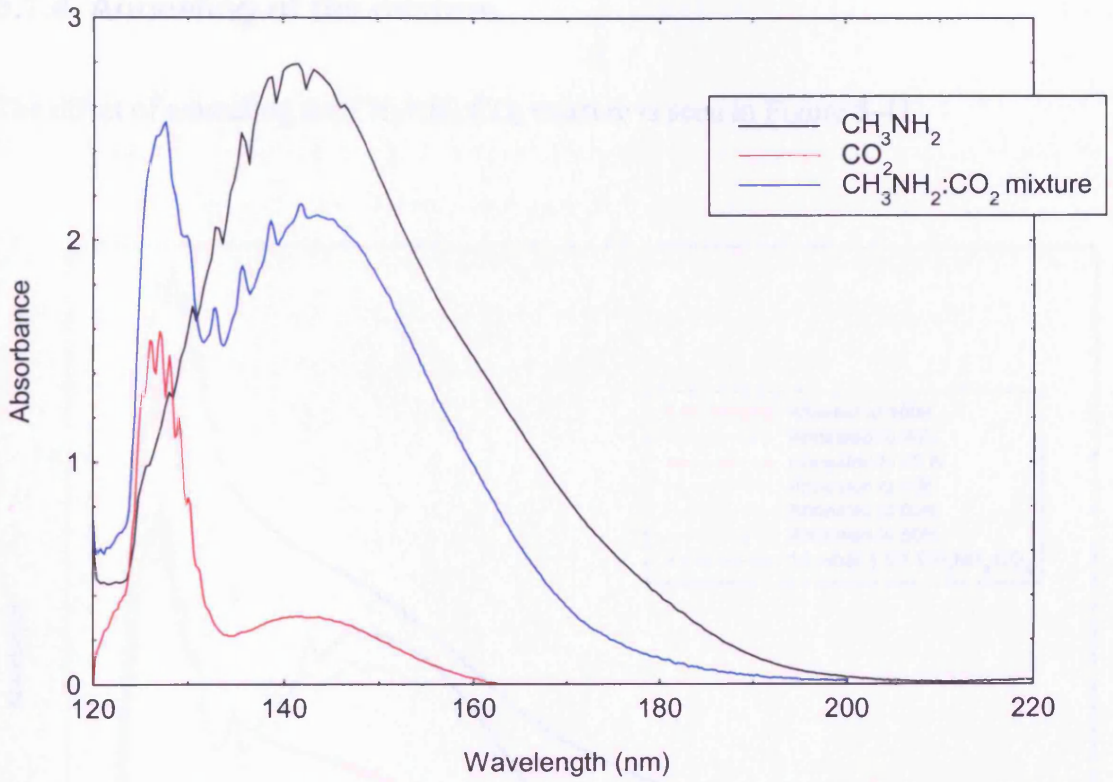

Figure 5-40 Comparison between the UV spectra of pure CO_2 and CH_3NH_2 ice compared to a mixture of CH_3NH_2:CO_2 ice.

Unsurprisingly the spectrum exhibits features of both components. The valence state transition in methylamine is still present and seems to be the dominant absorption in the spectrum. There is a vibrational progression also present in the mixture on the CH_3NH_2 band. The CO_2 $^1\Pi_g \leftarrow {}^1\Sigma_g^+$ transition is still active but has lost much of the vibrational progression present in the pure sample. This is progression is attributed to the ν_2 bending mode of CO_2. (Rabalais, McGlynn et al. 1971). In the case of the mixture we propose that the addition of the CH_3NH_2 to the ice matrix may restrict this bending mode by "trapping" the CO_2 within the ice matrix preventing the vibrational progression in CO_2 from becoming active.

5.7.4 Annealing of the mixture.

The effect of annealing the CH_3NH_2:CO_2 mixture is seen in Figure 5-41

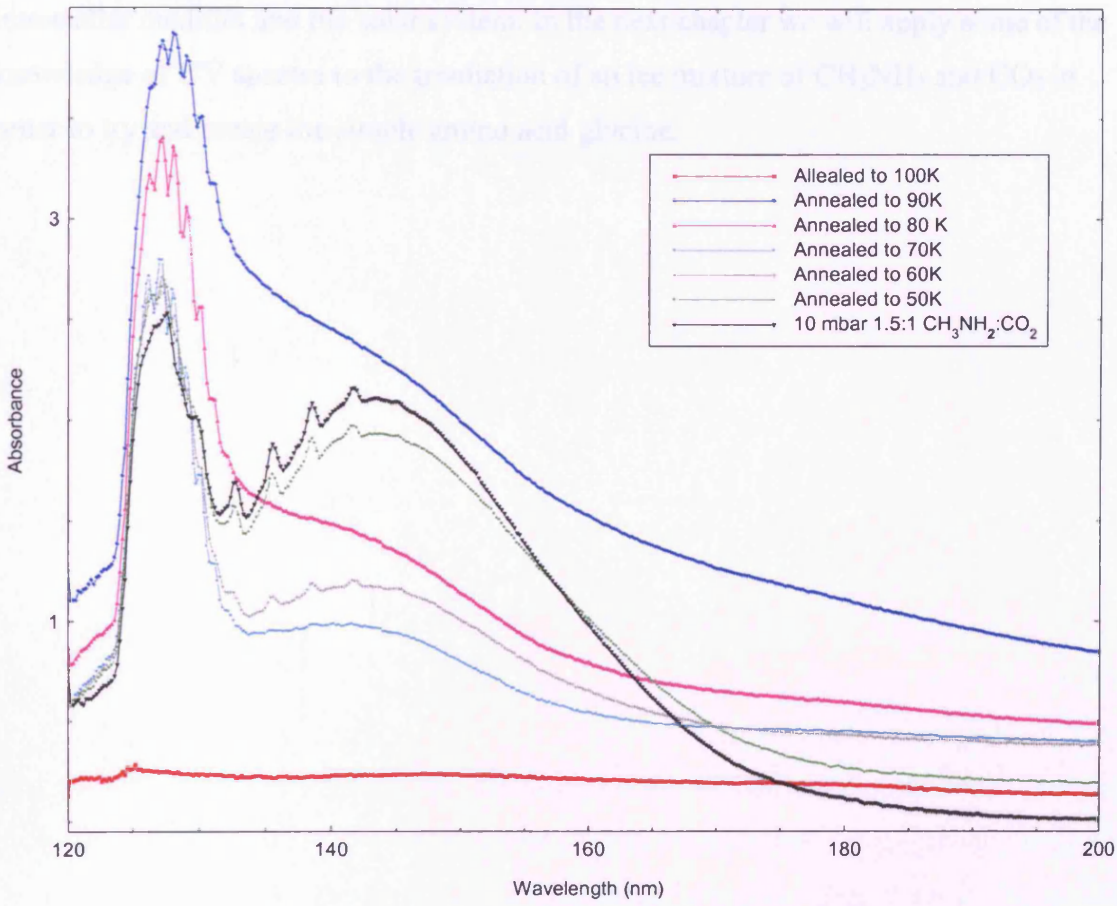

Figure 5-41 Annealing of the CH_3NH_2:CO_2 mixture

The structure of the CO_2 band changes as the temperature is raised. On heating to 50 K we notice that the vibrational progression becomes active. This could indicate either a change in the physical structure of the ice matrix of the desorbtion of the methylamine. However the band structure at 145 nm indicates CH_3NH_2 is still present so the latter is unlikely. The spectra indicate there is no noticeable shift in band position upon heating. Once the sample has reached 70 K the vibrational structure in CH_3NH_2 is lost and a broad featureless band is seen in place.

5.8 General conclusions and comments

In this chapter we have presented, in some cases for the first time, the ultraviolet spectra of a number of molecules in the condensed phase. Knowledge of the ultraviolet spectra of these molecules can play an important part in attempting to detect them in the interstellar medium and the solar system. In the next chapter we will apply some of the knowledge of UV spectra to the irradiation of an ice mixture of CH_3NH_2 and CO_2 in order to try and create the simple amino acid glycine.

Chapter Six

Studies on the formation of Glycine in the ISM.

"Theft from a single author is plagiarism – from three or more it is research."

--Anon

6.1 Introduction

Electron induced processes play an important role in interstellar ice chemistry. Electron tracks induced by cosmic ray bombardment or UV photoionisation can profoundly alter the composition of the icy mantle of an interstellar dust grain. (See Chapter 1). In this chapter we explore electron and photon irradiation of ices to probe the formation of a simple amino acid, glycine, in the interstellar medium. Amino acids are the building blocks of proteins which are essential to all known life on earth. One of the persistent theories in astrobiology is the concept of 'panspermia'. The idea that the building blocks of life were not formed on earth but are formed in the ISM and are therefore universally present throughout the universe. Panspermia postulates that life began on the Earth due to the delivery of these essential chemicals and components of life from space in the form of meteorite and comet impacts on the primitive earth. Astronomers, whether they adhere to this theory or not, have long searched for signs of complex organic molecules in the interstellar medium. In particular the search for the simplest amino acid glycine (NH_2CH_2COOH) has been ongoing since the confirmation of the microwave spectrum of glycine in the laboratory in the late 70's. (Brown, Godfrey et al. 1979) conducted a

radio search for glycine in hot molecular cores.Whilst not absolutely confirming the presence of glycine from their initial observations they tentatively estimated a glycine column density limit of 10^{12} cm^{-2} to 10^{14} cm^{-2} in Sgr B2 and Ori A. Surveys for interstellar glycine are however hampered by the intrinsic weakness of the lines being searched for and the problems of overlapping of spectra of other molecules (Kuan, Charnley et al. 2003). However (Kuan, Charnley et al. 2003) recently reported the results of a search of the hot molecular cores of Sgr B2 (N-LMH), Orion KL, and W51 e1/e2. They reported evidence for 27 glycine lines in 19 different spectral bands with column densities of about 10^{14} cm^{-2}; this translates to fractional abundances with respect to hydrogen of 2.1×10^{-10} for Sgr B2, 1.5×10^{-9} for Orion, and 2.1×10^{-10} for W51. This finding has prompted a search for the possible formation mechanism of glycine in the interstellar medium.

Recent speculation on the formation of glycine has identified CH_2NH_2 as a possible precursor to glycine in the Interstellar medium. (Woon 2002). An obvious source of CH_2NH_2 is the molecule Methylamine, CH_3NH_2 which has already observed in the interstellar medium in Sgr B2 (M) and Ori MC-1. (Fourikis, Takagi et al. 1974; Kaifu, Morimoto et al. 1974);(Turner 1989; Turner 1991)). (Woon 2002) predicts that the direct recombination of CH_2NH_2 radicals with COOH radicals will yield glycine in an astrophysical environment. Extrapolating back from this we can postulate that a simple binary mixture of CH_3NH_2 and CO_2, both possible components of astrophysical ice, could yield glycine upon irradiation to form the CH_2NH_2 and COOH radicals.

This chapter will describe electron and photon irradiation experiments on the irradiation of mixtures of CH_3NH_2 and CO_2 and discuss our conclusion that glycine can indeed formed in such an ice under the right conditions.

6.2 Electron Irradiation of a pure Methylamine (CH_3NH_2) Ice film.

6.2.1 Introduction

In order to fully understand the processes involved when irradiating ice mixtures it is desirable to understand the irradiation of the component ices in their pure state. (Bennett, Jamieson et al. 2004) have studied the electron irradiation of pure CO_2 ice using the same apparatus and under the same conditions as the present study and so our initial experiments on the formation of glycine focused on the irradiation of pure CH_3NH_2 ice. (Bennett, Jamieson et al. 2004) concluded from the 5 keV electron irradiation of pure CO_2 ice at 11K that CO, CO_3 and O_3 were the main products of electron irradiation of CO_2 with the C_{2V} symmetric, cyclic CO_3 structure being formed

6.2.2 Experimental

Experiments were performed using the apparatus at the University Of Hawaii at Manoa (described in more detail in Chapter 3). The machine consists of a 15 *l* cylindrical stainless steel chamber which can be evacuated down to 8×10^{-11} torr by a magnetically suspended turbopump backed by an oil-free scroll pump. A polished silver mono crystal is used as the substrate for our experiments. This crystal is cooled to 10.8 ± 0.2 K using a rotatable, two stage closed cycle helium refrigerator. Our spectra are collected in reflection mode due to the use of the metal substrate. We use a Nicolet FTIR to collect the infrared spectra constantly throughout the experiment. Mass spectrum data is also recorded using a Quadrupole Mass Spectrometer (QMS). Before the desposition of any ice layers we recorded a background infrared scan. (Figure 6-1). We condensed a film of pure CH_3NH_2 (99.99 % purity) ice at 11 K at a chamber pressure of 1×10^{-8} torr by depositing for 10 minutes. After deposition the ice is irradiated for 60 minutes with 5 keV electrons at a current of 1 μA. The ice is then kept isothermal at 11K for a further 60 minutes before being subjected to heating at a rate of 0.5 K per minute until the sample temperature reaches 300 K. From the infrared spectrum of the deposited ice at

11 K (Figure 6-2) we can calculate the thickness of the ice deposited using the Beer-Lambert Law (Chapter 3). We assume a methylamine density of 0.85±0.05 gcm^{-3} (Atoji and Lipscomb 1953) and averaging over the absorptions due to the ν_6 and ν_8 fundamentals we can calculate an ice thickness of 156 ± 10 nm with a column density of $2.6 \pm 0.2 \times 10^{17}$ molecules cm^{-2} . (The infrared absorption coefficients for CH_3NH_2 can be found in Table 5-15)

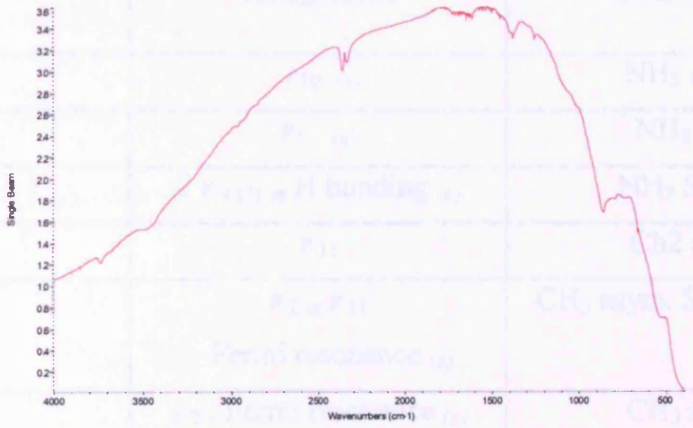

Figure 6-1 Background scan of Ag Substrate at 11 K

Figure 6-2 shows an infrared spectrum from a pure methylamine ice film at 11 K. The measured peaks are tabulated and identified in Table 6-1

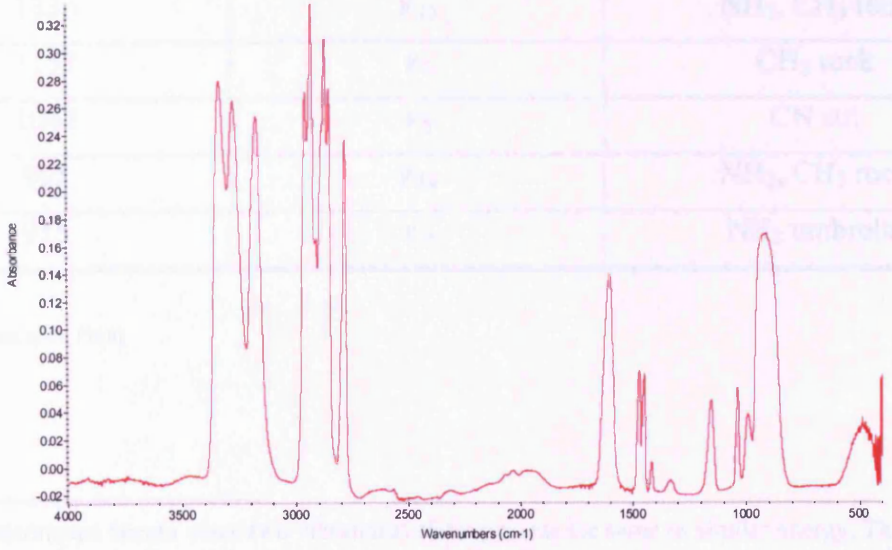

Figure 6-2 Spectrum of Pure CH_3NH_2 ice at 11 K

Due to the problems of numerous fundamentals, Fermi resonances [7] and overtones present it is often hard to identify the features. The assignments tabulated are therefore compiled and interpreted from previous studies on CH_3NH_2.

Table 6-1 Pure CH_3NH_2 ice film deposited at 11 K

Frequency (cm^{-1})	Assignment	Characterisation
3342	ν_{10} (a)	NH_2 asym. str.
3282	ν_1 (a)	NH_2 sim. str.
3181	2 $\nu_{4\,(?)}$ or H bonding (a)	NH_2 Scissor (?)
2965	ν_{11}	Ch2 asym. str
2941	ν_2 or ν_{11} + Fermi resonance (a)	CH_3 asym. Str or CH_2 asym. str.
2881	ν_2 + Fermi resonance (a)	CH_3 asym (?)
2861	$\nu_{2\,(?)}$	CH_3 asym (?)
2791	$\nu_{3\,(a)}$	CH_3 sym str.
1612	ν_4	NH_2 Scissor
1477	ν_5	CH_3 deform
1453	ν_{12}	CH_3 deform
1420	ν_6	CH_3 umbrella
1336	ν_{13}	NH_2, CH_3 rock
1157	ν_7	CH_3 rock
1042	ν_8	CN str.
995	ν_{14}	NH_2, CH_3 rock
915	ν_9	NH_2 umbrella

(a) (Durig, Bush et al. 1968)

[7] A Fermi resonance occurs when two vibrational states possess the same or similar energy. This degeneracy results in an interaction between the two states. For example when an overtone and a fundamental have similar vibrational frequency.

After electron irradiation for 1 hour new infrared absorptions features appear. These are tabulated in Table 6-2. We observe the CN^- ($X\ ^1\Sigma$) radical at 2062 cm^{-1} and its overtone band at 4130 cm^{-1}. We also observe methane, CH_4 ($X\ ^1A_1$) at 1300 cm^{-1} and methanimine, CH_2NH ($X\ ^1A'$) at 1677 cm^{-1}. The strong absorption of methylamine (CH_3NH_2) dominates a large region of the spectrum masking additional fundamentals of these product species.

Table 6-2 New Infrared absorptions at 11 K after 1 hour of irradiation of CH_3NH_2 with 5 keV electrons.

Frequency (cm^{-1})	Molecule	Assignment	Absorption Coefficient (km. mol^{-1})	Column Density (molecules cm^{-2})
2062	CN^-	σ	7	1.8×10^{17}
1677	CH_2=NH	υ_4	22	2.2×10^{16}
1638	C-NH_3	υ_3	77	2.9×10^{16}
1300	CH_4	υ_4	17	6.3×10^{15}
4130	CN^-	2σ	-	-

6.2.3 Discussion

Comparison with pervious experiments on the photodissociation of gaseous CH_3NH_2 (Hubin-Franskin, Delwiche et al. 2002), suggest that after irradiation we might expect CH_3NH_2 to dissociate as follows.

$$CH_3NH_2(X^1A') \rightarrow CH_2NH_2(X^2A') + H(^2S_{1/2}) \quad (a)$$

$$CH_3NH_2(X^1A') \rightarrow CH_3NH(X^2A') + H(^2S_{1/2}) \quad (b)$$

$$CH_3NH_2(X^1A') \rightarrow CH_3(X^2A'') + NH_2(X^2B_1) \quad (c)$$

However due to the intense and numerous absorptions of the CH_3NH_2 ice it is impossible to observe the CH_2NH_2 and CH_3NH absorptions. Similarly we see no evidence for CH_3 or NH_2 absorptions. We do however see secondary products of the irradiation. In particular we see the CH_2=NH molecule, C-NH_3 and the CN^- molecule which could be formed by the removal of hydrogen from the CH_2NH molecule.

As it is the closest species to CH_3NH_2 we have monitored production of the CH_2NH molecule over time and attempted to fit a time profile to it. (Figure 6-4)
Assuming the CH_3NH_2 reacts as expected from photon irradiation studies we can assume the following reaction scheme based on the observed products in our ice matrix.

$$CH_3NH_2 \rightarrow CH_2NH_2 / CH_3NH + H \rightarrow CH_2NH + 2H \qquad (6.1)$$

This reaction is a consecutive reaction (Chapter 2) and can be modeled, using the equation

$$[A_3] = [A_1]_0 \left(1 - \frac{k_2}{k_2 - k_1} e^{-k_1 t} + \frac{k_1}{k_2 - k_1} e^{-k_2 t} \right) \qquad (6.2)$$

where k_1 and k_2 are the rate constants and $[A_1]$ and $[A_3]$ are the concentration of the reactants.

The absorption of the CH_2NH molecule overlaps with the ν_4 CH_3NH_2 absorption. In order to profile the CH_2NH column density we need to deconvolute the spectrum to obtain the peak area of each of the features. The deconvolution is made using a Gaussian fit to the data, as this better simulates the broadening we expect in the solid phase as opposed to using a lorentizan fit which is typical of gas phase data. We use the software PAN[8] to deconvolute the peaks. A sample of this is shown in Figure 6-3. After all the data files have been deconvoluted we fit equation (6.2) to the time evolution of the column density of CH_2NH as shown in Figure 6-4.

[8] Dimeo, R. (2003). PAN: Peak Analysis, http://www.ncnr.nist.gov/staff/dimeo/panweb/pan.html

The small absorptions of the molecule prevent an accurate deconvolution for early time scales. We estimate an error of ± 0.3 × 10^{14} molecules cm^{-2} on our column density at 1 hour. The fit to the data gives us rate constants of 1.9 × 10^{-5} s^{-1} and 1.1× 10^{-5} s^{-1} for k_1 and k_2 respectively for the reaction shown in (6.1).

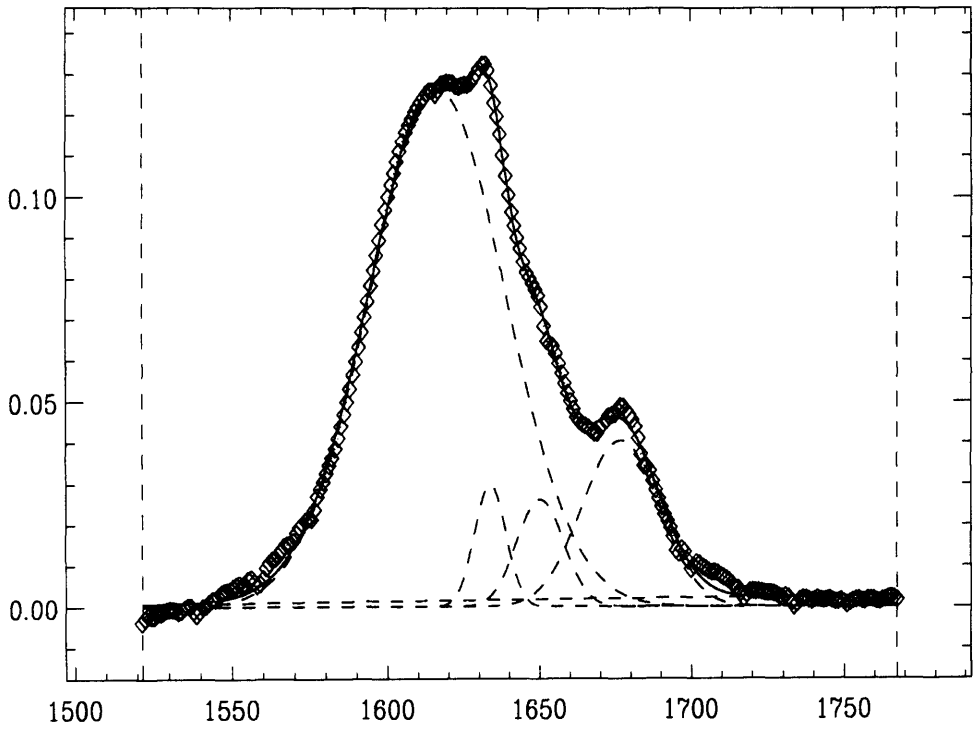

Figure 6-3 Sample Deconvolution. The original spectra is seen as the diamond shaped line. Dotted lines represent the best fit to the data to produce the spectrum.

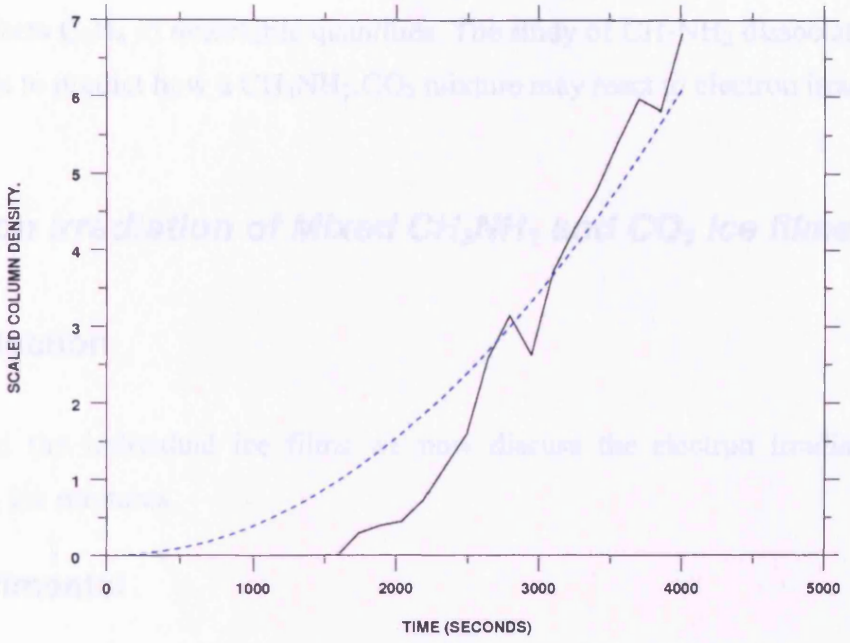

Figure 6-4 Evolution of the CH_2NH column density and fit (column density scaled by 1×10^{14}). The fit is denoted by the blue dotted line. Experimental data by the solid black line.

6.2.4 Conclusions.

Our preliminary studies on the electron irradiation of CH_3NH_2 at 11 K have shown us some of the products we can expect from the dissociation of CH_3NH_2 by electrons. It is clear that CH_3NH_2 fragments readily and hydrogen abstraction occurs easily upon irradiation. There is some evidence for cleavage of the C-N bond of CH_3NH_2. The presence of methane suggests that the C-N bond has been cleaved results in the formation of a CH_3 radical which hydrogen can easily add to forming CH_4.

$$CH_3(X^2A'') + H(^2S_{1/2}) \rightarrow CH_4\,(X^1A_1) \qquad (6.3)$$

We would also expect the radical – radical reaction of CH_3 to form Ethane, C_2H_6. We do not observe C_2H_6 in our spectrum though. After comparison of the irradiated CH_3NH_2 spectrum with a sample spectrum of pure C_2H_6 recorded on the same equipment we see no evidence for C_2H_6 formation at 11 K. On warming of the spectra some bands are evident which may be attributed to C_2H_6 but it is not possible to confirm this at present. This suggests that the CH_3 radicals are not free to recombine at 11 K.

Perhaps due to reduced mobility at 11 K. They may not be correctly orientated to recombine to form C_2H_6 in detectable quantities. The study of CH_3NH_2 dissociation has given us a basis to predict how a CH_3NH_2:CO_2 mixture may react to electron irradiation

6.3 Electron irradiation of Mixed CH_3NH_2 and CO_2 ice films.

6.3.1 Introduction

Having studied the individual ice films we now discuss the electron irradiation of CH_3NH_2 / CO_2 ice mixtures.

6.3.2 Experimental

We prepared our ice mixture by allowing CH_3NH_2 and CO_2 into a mixing cell then depositing this binary mixture of gas onto our cooled silver substrate at 11 K. We deposited methylamine CH_3NH_2; (15 torr; 99.99 %) and carbon dioxide, CO_2; (10 torr, 99.999 %) at a main chamber pressure of 10^{-8} torr for 10 minutes. The spectrum after deposition is shown in Figure 6-5 and absorptions are listed in Table 6-3. We have calculated the thickness of the ice using the Beer-Lambert law. We integrated the infrared absorption features of carbon dioxide at 3708 cm^{-1} (integral absorption coefficient A= 1.4×10^{-18} cm $molecule^{-1}$) and 3600 cm^{-1} (A=4.5×10^{-19} cm $molecule^{-1}$) and of methylamine at 1600 cm^{-1} (A=4.3×10^{-18} cm $molecule^{-1}$) and 1150 cm^{-1} (A=1.5×10^{-18} cm $molecule^{-1}$). This suggests a methylamine to carbon dioxide ratio in the ices of about 30. Accounting for the column densities and the densities of carbon dioxide (1.7±0.1 $g.cm^{-3}$; (Klinger, Benest et al. 1985)) as well as of methylamine of (0.85±0.05 gcm^{-3}; (Atoji and Lipscomb 1953)), we have an optical thicknesses of 9±6 nm in carbon dioxide ice and 436±13 nm in methylamine ice, i.e. a thickness of the binary ice mixture of 445±19 nm.

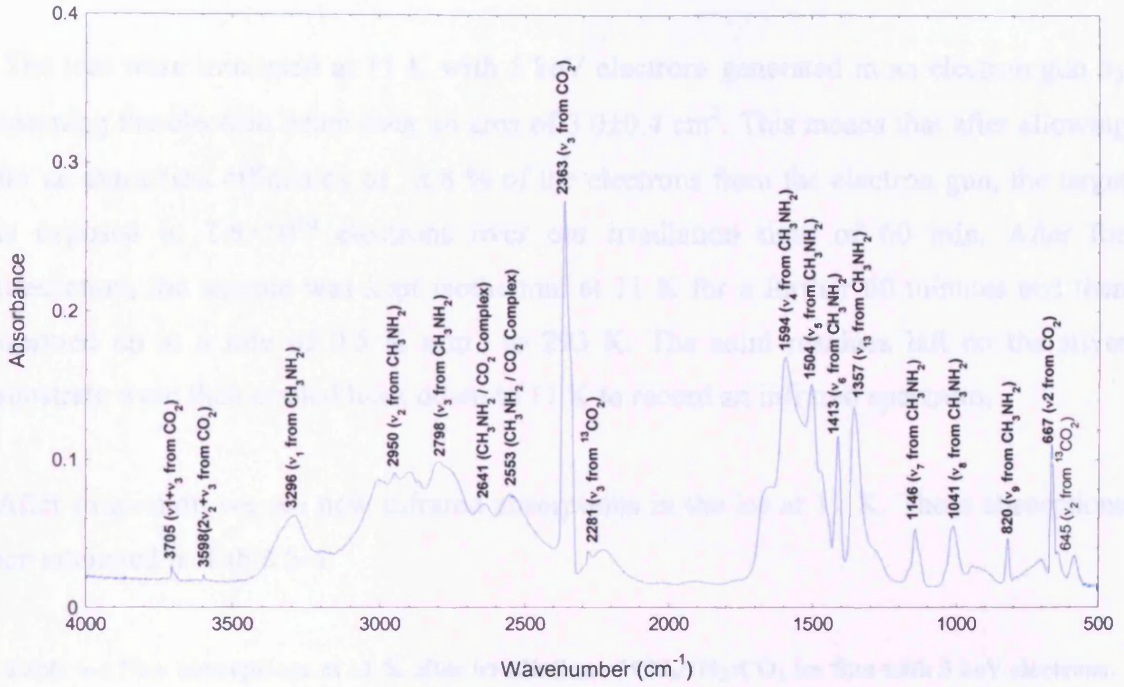

Figure 6-5 CH_3NH_2 : CO_2 spectrum at 11 K

Table 6-3 Absorptions of the CH_3NH_2:CO_2 ice mixture as seen at 11 K

Frequency (cm^{-1})	Molecule	Assignment	Characterization
3705	CO_2	$\upsilon_1 + \upsilon_3$	combination
3598	CO_2	$2\upsilon_2 + \upsilon_3$	combination
3296	CH_3NH_2	υ_1	NH_2 symmetric stretch
3001/2995	CH_3NH_2	υ_{11}	CH_3 antisymmetric stretch
2950	CH_3NH_2	υ_2	CH_3 antisymmetric stretch
2798	CH_3NH_2	υ_3	CH_3 symmetric stretch
2363	CO_2	υ_3	asymmetric stretch
2281	$^{13}CO_2$	$\upsilon_3(^{13}CO_2)$	isotope peak
1594	CH_3NH_2	υ_4	NH_2 scissor
1504	CH_3NH_2	υ_5	CH_3 antisymmetric deformation
1475	CH_3NH_2	υ_{12}	CH_3 antisymmetric deformation
1413	CH_3NH_2	υ_6	CH_3 symmetric deformation
1357	CH_3NH_2	υ_{13}	NH_2 Twist
1167	CH_3NH_2	υ_{14}	CH_3 rocking (shoulder)
1146	CH_3NH_2	υ_7	CH_3 rocking
1041	CH_3NH_2	υ_8	CN stretching (shoulder)
820	CH_3NH_2	υ_9	NH_2 wagging
667	CO_2	υ_2	in plane/out of plane bending
645	CO_2	$\upsilon_2(^{13}CO_2)$	isotope peak

The ices were irradiated at 11 K with 5 keV electrons generated in an electron gun by scanning the electron beam over an area of 3.0±0.4 cm^2. This means that after allowing for an extraction efficiency of 78.8 % of the electrons from the electron gun, the target is exposed to 1.8×10^{16} electrons over our irradiation time of 60 min. After the irradiation, the sample was kept isothermal at 11 K for a further 60 minutes and then warmed up at a rate of 0.5 K min^{-1} to 293 K. The solid residues left on the silver substrate were then cooled back down to 11 K to record an infrared spectrum.

After irradiation we see new infrared absorptions in the ice at 11 K. These absorptions are tabulated in Table 6-4

Table 6-4 New absorptions at 11 K after irradiation of CH_3NH_2:CO_2 ice film with 5 keV electrons.

Frequency (cm^{-1})	Molecule	Assignment	Characterization	Column density at end of irradiation. (molecules cm^{-2})
789	$CH\text{-}NH_2$	υ_9	NH_2 Out of plane	1.93×10^{14}
	H_2CNO	(?)	(?)	(?)
	O_3^-	υ_3	Asym. Stretch	(?)
	HNCO	υ_4		
1381	$NH_3^+CH_2COO^-$	$\upsilon_s COO$	symmetric CO_2 stretch	1.20×10^{13}
1657*	CO_2^-	υ_3	OCO asymmetric stretch	(?)
1846*	HOCO	υ_2	CO stretch	(?)
2139	CO	υ_1	CO stretch	1.31×10^{15}
2164	OCN-	υ_1	CN stretch	1.62×10^{15}
2078	CN-	σ	CN stretch	1.75×10^{14}

*** These products were seen when during irradiation of a similar ice mixture with higher electron currents. They are listed here as an observation.**

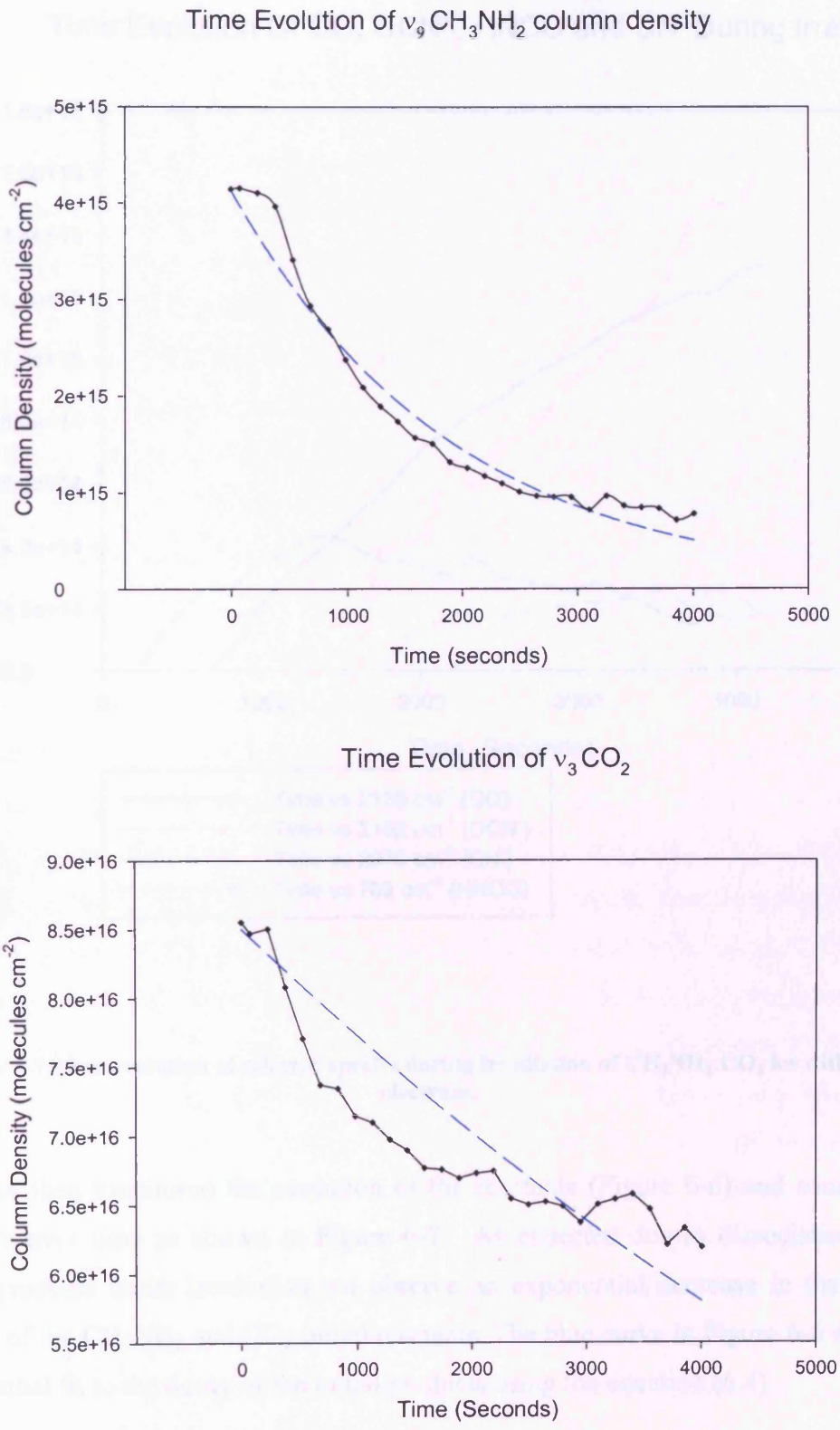

Figure 6-6 Time Evolution of CH_3NH_2 and CO_2. Exponential fits are shown in blue.

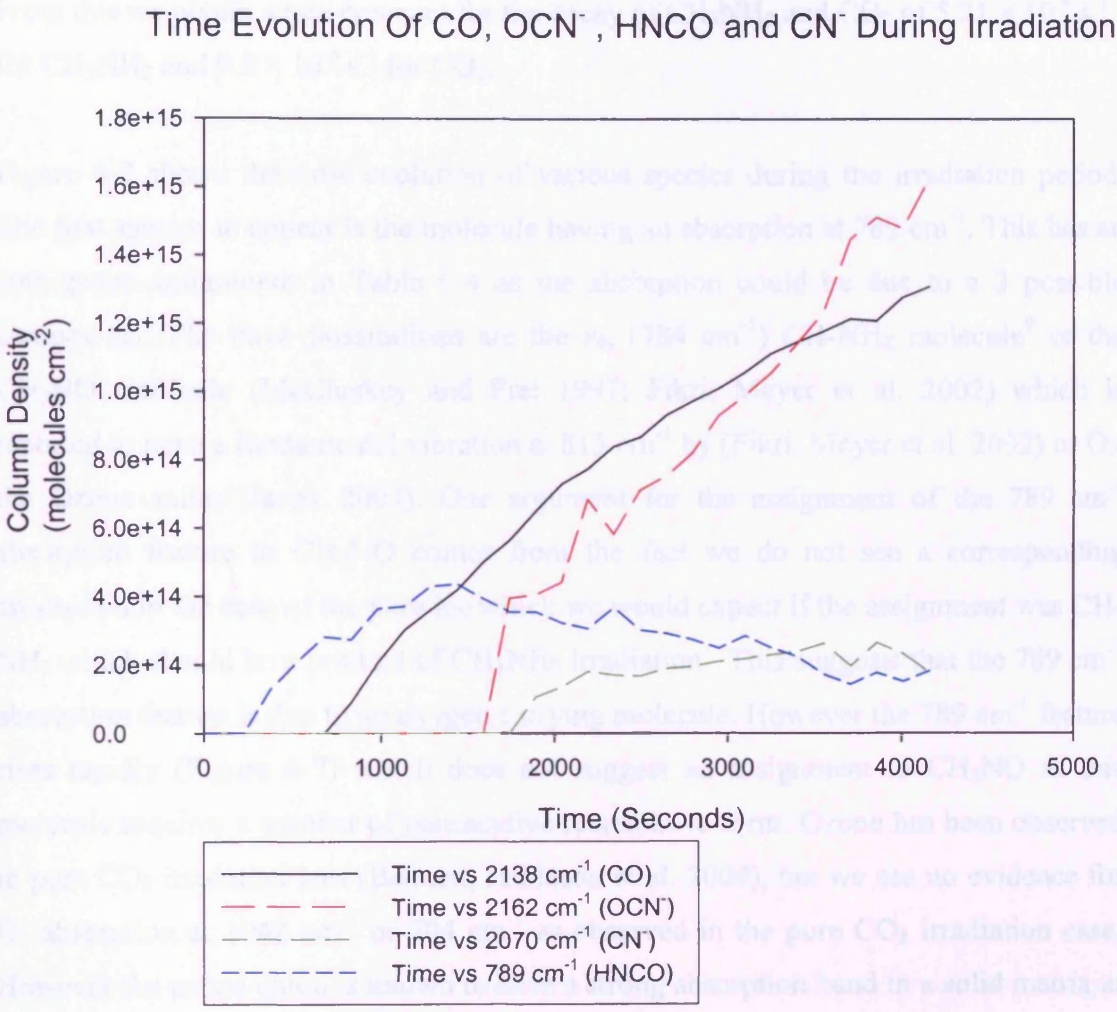

Figure 6-7 Time evolution of selected species during irradiation of CH_3NH_2:CO_2 ice with 5 keV electrons.

We have then monitored the evolution of the reactants (Figure 6-6) and some of the products over time as shown in Figure 6-7. As expected due to dissociation of the initial products under irradiation we observe an exponential decrease in the column density of the CH_3NH_2 and CO_2 initial reactants. The blue curve in Figure 6-6 shows an exponential fit to the decay of the initial products using the equation (6.4)

$$y = ae^{(-bx)} \tag{6.4}$$

From this we obtain a rate constant for the decay of CH_3NH_2 and CO_2 of 5.21×10^{-4} s^{-1} for CH_3NH_2 and 9.5×10^{-5} s^{-1} for CO_2.

Figure 6-7 shows the time evolution of various species during the irradiation period. The first species to appear is the molecule having an absorption at 789 cm^{-1}. This has an ambiguous assignment in Table 6-4 as the absorption could be due to a 3 possible compounds. The three possibilities are the ν_9, (784 cm^{-1}) CH-NH_2 molecule[9] or the CH_2NO molecule (McCluskey and Frei 1997; Fikri, Meyer et al. 2002) which is reported to have a fundamental vibration at 815 cm^{-1} by (Fikri, Meyer et al. 2002) or O_3^- the Ozone anion (Jacox 2003). One argument for the assignment of the 789 cm^{-1} absorption feature to CH_2NO comes from the fact we do not see a corresponding absorption in the case of the pure ice which we would expect if the assignment was CH-NH_2 which should be a product of CH_3NH_2 irradiation. This suggests that the 789 cm^{-1} absorption feature is due to an oxygen carrying molecule. However the 789 cm^{-1} feature rises rapidly (Figure 6-7) which does not suggest an assignment to CH_2NO as this molecule requires a number of consecutive reactions to form. Ozone has been observed in pure CO_2 irradiated ices (Bennett, Jamieson et al. 2004), but we see no evidence for O_3 absorption at 1042 cm^{-1} or 704 cm^{-1} as observed in the pure CO_2 irradiation case. However the ozone anion is known to have a strong absorption band in a solid matrix at 795 cm^{-1}. (Lugez, Thompson et al. 1996); (Peterson, Mayrhofer et al. 1990) so an argument can be made for an assignment to the ozone anion, O_3^-. The last possibility is the HNCO molecule. This has a strong absorption at 796 cm^{-1} (Johnson, Richter et al. 2003) with an absorption coefficient of 236.1 km mol^{-1}. We do not see any evidence for the strongest absorption ν_2 (2267 cm^{-1}, A=666 km mol^{-1}). This could be due to the overlap with a CH_3NH_2 / CO_2 feature at 2276 cm^{-1}. HNCO is a candidate for the 789 cm^{-1} absorption feature based on the other products seen after irradiation. One possible route to the observed OCN^- product is as a result of proton transfer from isocyanic acid (HNCO), (Novozamsky, Schutte et al. 2001); (Hudson, Moore et al. 2001). The presence of both HNCO and OCN^- in the ice matrix suggests that the 789 cm^{-1} carrier could be due to HNCO absorption. As time increases the column density of 789 cm^{-1} feature falls coincidentally with a rise in the production of OCN^- and CN^-. This can not

[9] Personal Communication from Prof. Yoshihiro Osamura [osamura@rikkyo.jp]

this can not be fully explained from the current observations, but suggests the HNCO is taking part in an additional reaction with a faster reaction rate than the production of HNCO thus leading to the overall decrease in the HNCO column density. We also note the column density of OCN^- rapidly becomes much greater than the observed HNCO column density. If our OCN^- was forming as a result of de-protonation of HNCO then we would not expect there to be an enhanced OCN^- column density compared to the HNCO. This could suggest another pathway to OCN^- is competing with the HNCO pathway.

One possible route to OCN^- comes from the recombination of CN^- with oxygen.

$$O(^1D/^3P) + CN^- \ (^1\Sigma) \rightarrow OCN^- (^1\Sigma)$$

The oxygen atom can be formed from the dissociation of CO_2.

$$CO_2 (X\ ^1\Sigma_g^+) \rightarrow CO (X\ ^1\Sigma^+) + O(^3P)$$
$$CO_2 (X\ ^1\Sigma_g^+) \rightarrow CO (X\ ^1\Sigma^+) + O(^1D)$$

Depending on the energy transfer from the electron to the CO_2 molecule the oxygen atom can form in one of two states (Bennett, Jamieson et al. 2004), either the (^{3}P) ground state or the excited (^{1}D) state. This presents two possibilities for the formation of OCN^- from CN^-. Either the (^{1}D) or the (^{3}P) state can react. Calculations (B3LYP/6-311G(d,p) basis set) show that O (^{1}D) + CN^- will react without an energy barrier. O (^{3}P) + CN^- is endoergic by 540.8 kJ/mol.

Figure 6-7 shows the time evolution of carbon dioxide, CO. CO is a primary reaction product of the irradiation of CO_2. (Bennett, Jamieson et al. 2004) As such we would expect CO to form virtually instantly upon the start of irradiation. The unexpected time delay shown in Figure 6-7 could be due to the methylamine background which occurs in the region of the CO feature as shown in
Figure 6-8 preventing us from observing any CO before the CO concentration exceeds the methylamine background.

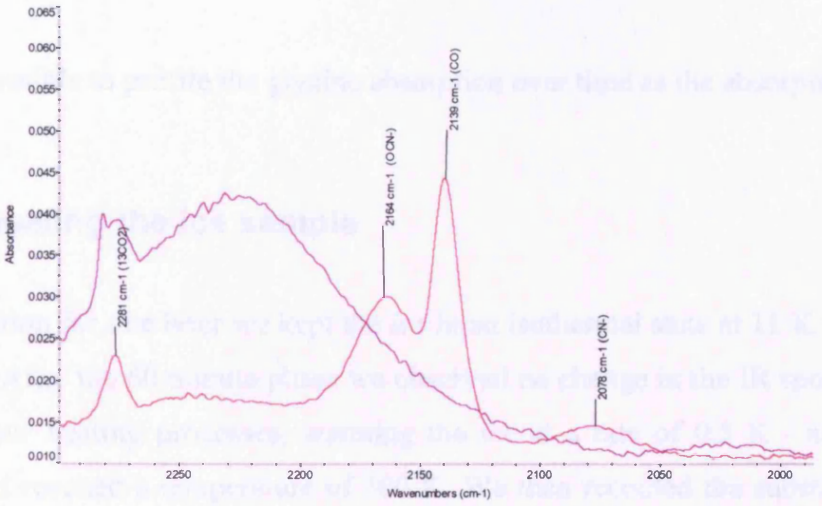

Figure 6-8 2140 cm^{-1} CO feature before and after 1 hr of irradiation. The red curve shows the sample after 1 hr of irradiation. The purple curve is before irradiation.

The most dramatic observation in our processed ice sample evidence for the symmetric COO stretch of zwitter-ionic glycine at 1381 cm^{-1}. (Figure 6-9) The position of the peaks is in good agreement with previous measurements of these species (Rosado, Duarte et al. 1998) listing the ν_s COO feature at 1367 cm^{-1} from theoretical calculations and at 1401 cm^{-1} from an experimental determination.

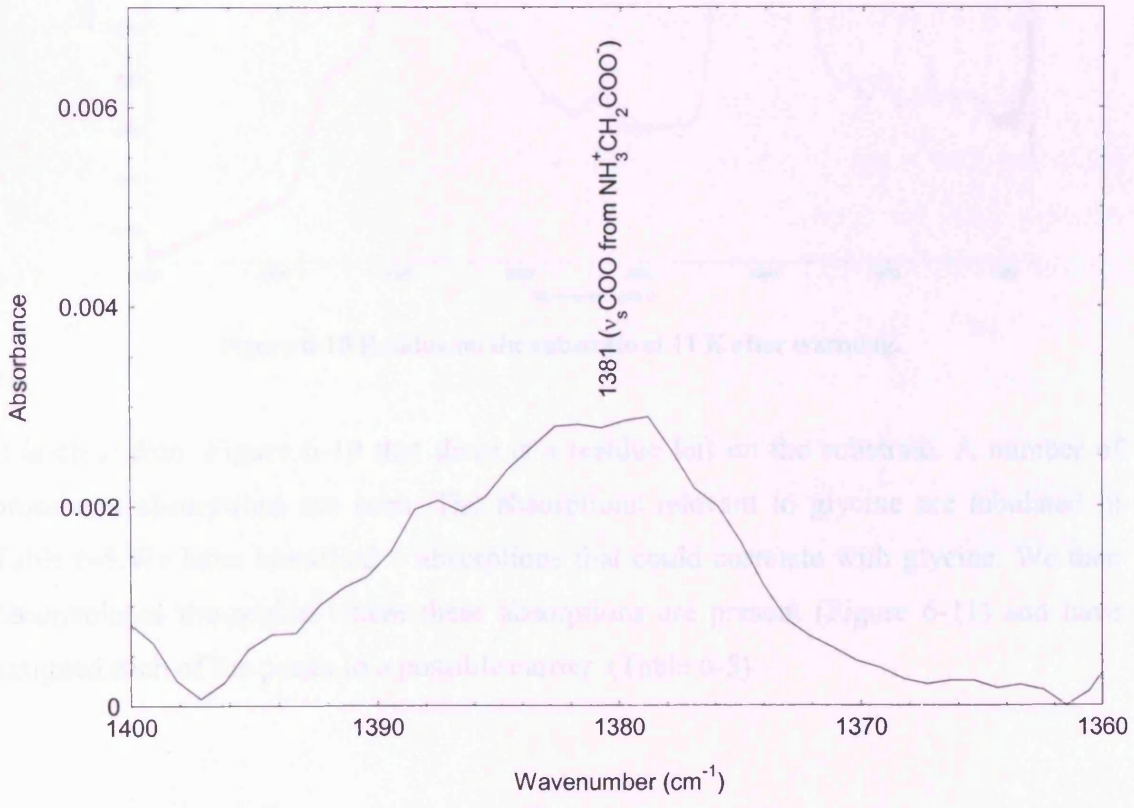

Figure 6-9 1381 cm^{-1} glycine absorption at 11 K

It was not possible to profile the glycine absorption over time as the absorption feature is too weak.

6.3.3 Annealing the Ice sample

After irradiation for one hour we kept the ice in an isothermal state at 11 K for a further 60 minutes. After the 60 minute phase we observed no change in the IR spectrum. Then we started our heating processes, warming the ice at a rate of 0.5 K / min until the substrate had reached a temperature of 300 K. We then recooled the substrate to 11 K and recorded an infrared scan. This is shown in Figure 6-10

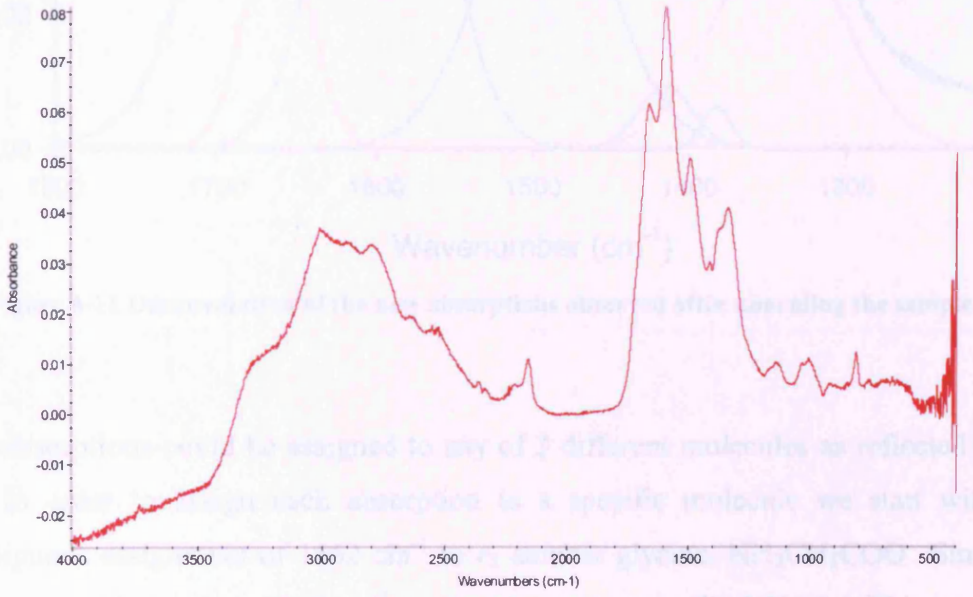

Figure 6-10 Residue on the substrate at 11 K after warming.

It is clear from Figure 6-10 that there is a residue left on the substrate. A number of prominent absorptions are seen. The absorptions relevant to glycine are tabulated in Table 6-5.We have identified 5 absorptions that could correlate with glycine. We then deconvoluted the region where these absorptions are present (Figure 6-11) and have assigned each of the peaks to a possible carrier. (Table 6-5)

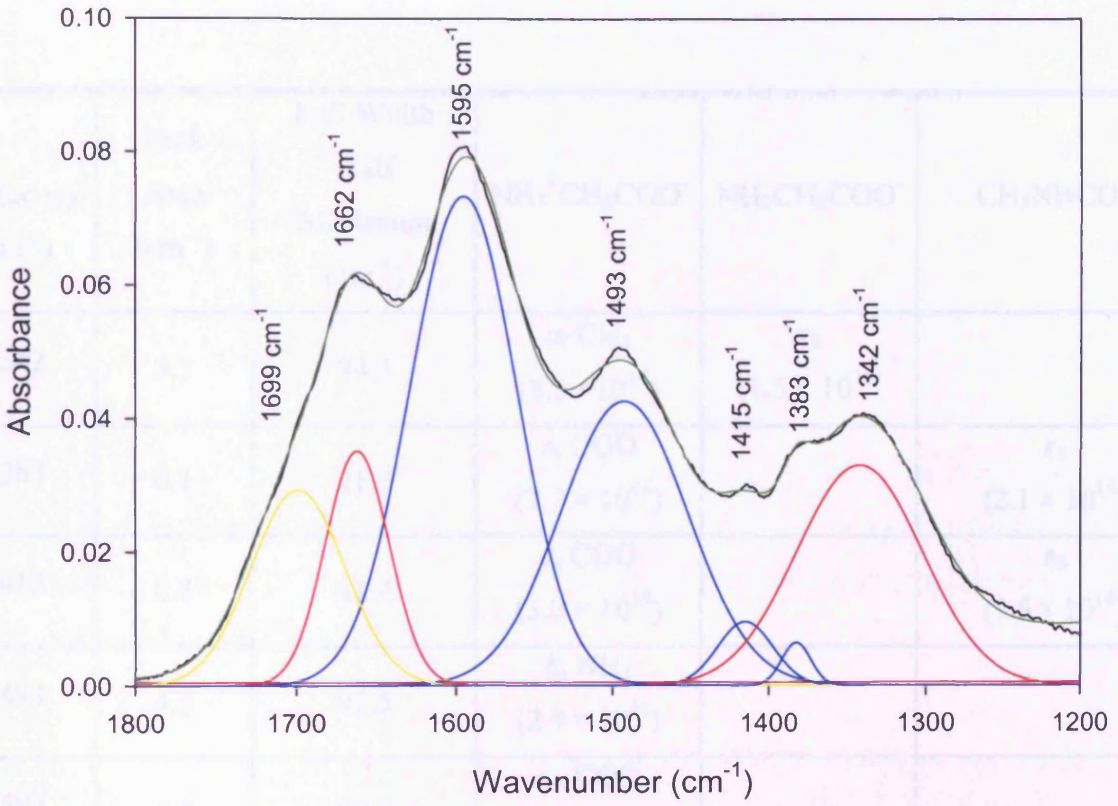

Figure 6-11 Deconvolution of the new absorptions observed after annealing the sample.

These absorptions could be assigned to any of 3 different molecules as reflected in the table. In order to assign each absorption to a specific molecule we start with the unambiguous assignment of 1662 cm^{-1} to ν_5 anionic glycine, $NH_2CH_2COO^-$. Similarly we can assign the peak at 1699 cm^{-1} to the glycine isomer $CH_3NHCO_2^-$. This isomer is also assigned to the 1383 cm^{-1} peak. The similarity in column density suggests the reassignment of the 1383 cm^{-1} peak to $CH_3NHCO_2^-$ The total column density of $CH_3NHCO_2^-$ is then $3.8 \pm 2 \times 10^{14}$ molecules cm^{-2} . We can then assign the peaks at 1342 , 1493 and 1595 cm^{-1} to the glycine zwitter ion, giving us a total column density of $4.5 \pm 3 \times 10^{16}$ molecules cm^{-2}.

Table 6-5 Absorptions at 11 K after warming. Column densities are in parenthesis in units of molecules cm^{-2}.

Frequency (cm^{-1})	Peak Area (cm^{-1})	Full Width Half Maximum (cm^{-1})	$NH_3^+CH_2COO^-$	$NH_2CH_2COO^-$	$CH_3NHCO_2^-$
1342	3.3	94.3	ω CH_2 (8.5×10^{16})	ν_9 (1.5×10^{15})	
1383	0.1	21.5	ν_s COO (7.7×10^{14})		ν_8 (2.1×10^{14})
1415	0.4	41.4	ν_s COO (3.0×10^{15})		ν_6 (1.5×10^{14})
1493	4.3	95.5	δ_s NH_3 (2.9×10^{16})		
1595	6.2	80.0	ν_{as} COO (2.1×10^{16})		
1662	1.7	46.9		ν_5 (7.3×10^{14})	
1699	2.1	68.5			ν_5 (7.8×10^{14})

6.3.4 Discussion

We have now established the possible presence of glycine in our ice sample. We see some evidence for either glycine or a glycine isomer at 11 K. Upon thermal processing of our ice sample we find an enhanced column density of glycine. But how can this glycine form ?

Initially we expect methylamine to lose hydrogen via either C-H bond cleavage or C-N bond cleavage. (6.5). We can confirm the release of hydrogen in the ice matrix from mass spectrum data recorded during the experiment. Figure 6-12 shows a steady release of hydrogen during the 60 minutes irradiation time, which then falls during the 60 minutes isothermal state. Once heating commences hydrogen is again released. This indicates the release of hydrogen is a direct result of electron induced processes during the first 60 minutes of irradiation.

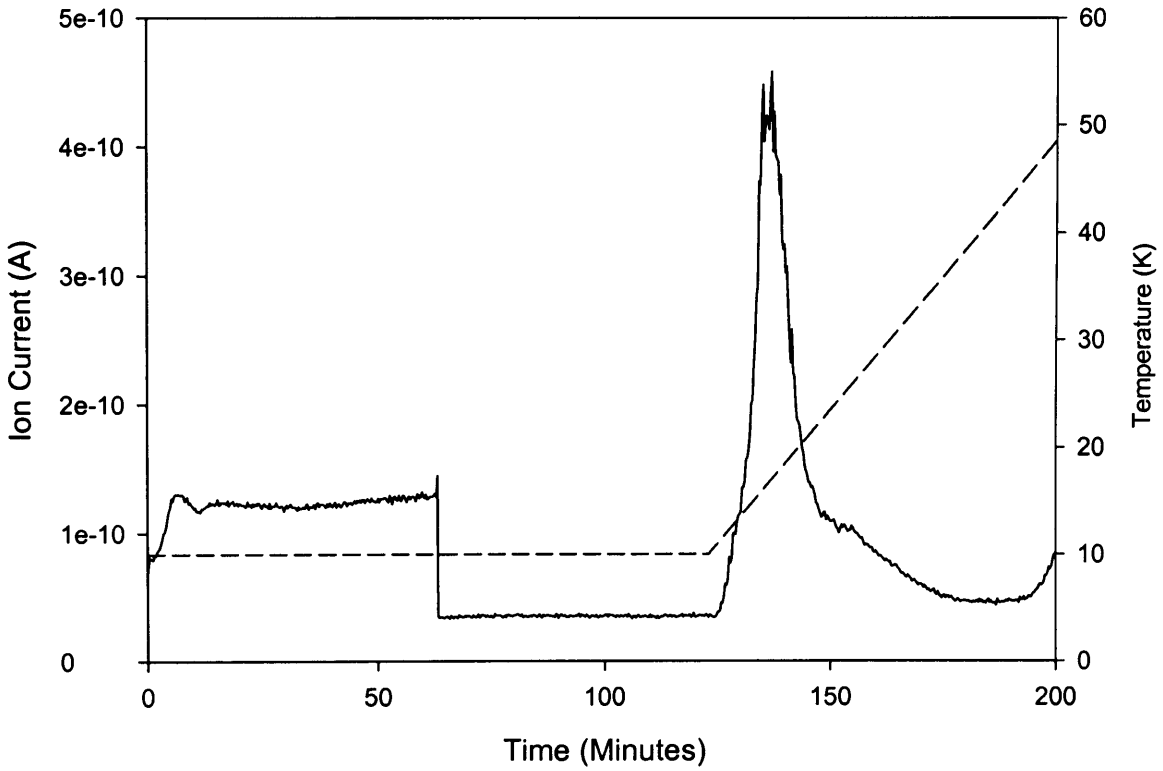

Figure 6-12 Mass spectrum data showing the evolution of H_2 with warming of the ice sample. The dotted line represents the heating profile.

$$CH_3NH_2(X^1A') \rightarrow CH_2NH_2(X^2A') + H(^2S_{1/2})$$

$$CH_3NH_2(X^1A') \rightarrow CH_3NH(X^2A') + H(^2S_{1/2}) \qquad (6.5)$$

This forms two distinct products. Calculations show both reactions are endoergic by 369 kJ mol^{-1} and 394 kJ mol^{-1}, respectively, with the aminomethyl radical, $CH_2NH_2(X^2A')$, more stable by 25 $kJmol^{-1}$ compared to the methyl amino radical, $CH_3NH(X^2A')$. The hydrogen released by such a reaction will be superthermal to the 11 K surroundings and can overcome the addition barrier of 113 $kJmol^{-1}$ of the reaction to form the $HOCO(X^2A')$ radical (6.6) (Morton and Kaiser 2003); (Yu, Muckerman et al. 2001). This HOCO radical was observed in the preliminary experiments as the solid phase surroundings stabilise the radical.

$$CO_2(X^1\Sigma_g^+) + H(^2S_{1/2}) \rightarrow HOCO(X^2A') \qquad (6.6)$$

In order to form glycine the HOCO radical has to recombine with the CH_2NH_2 radical. Since this is a radical-radical reaction there will be no entrance barrier to such a reaction making it feasible at 11 K. These radicals are immobile at 11 K (only hydrogen atoms are mobile) so reactions between HOCO and CH_2NH_2 can only occur when they are in neighbouring sites in the ice matrix with the correct geometry. This accounts for the low column density at 11 K and the subsequent rise in column density on thermal processing. Warming the ice allows radicals to move and recombine enhancing our column density.

Alternatively glycine can be formed via the reaction of CO_2 with CH_3NH or CH_2NH_2. The possible reactions are shown in Figure 6-13. Reactions (1) and (2) show the possible isomers of HOCO that can be formed. Reactions (3) to (6) show how the possible glycine isomers observed can be formed.

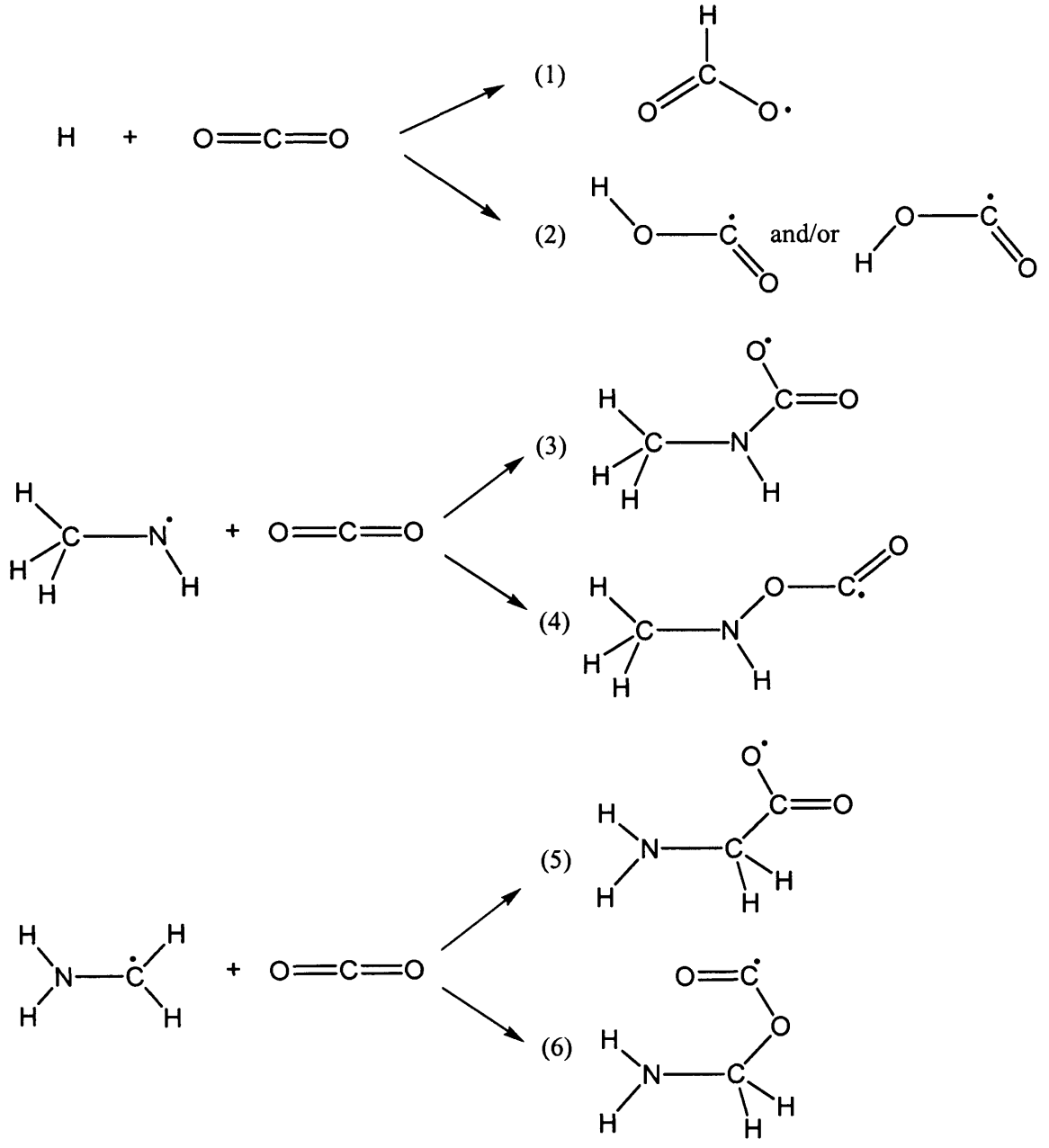

Figure 6-13 Some of the possible pathways to glycine based on our initial reactants and observed products.

6.3.5 Conclusions.

Our experiments have provided the evidence for a possible mechanism of glycine formation in the interstellar medium. Our proposed formation mechanism is not the only mechanism. Other possible routes to glycine include the recombination of amino radicals with a radical derived from acetic acid. (6.7)

$$NH_2(X^2B_1) + CH_2COOH(X^2A') \rightarrow H_2NCH_2COOH(X^1A') \qquad (6.7)$$

Or acetic acid itself can react with a superathermal NH radical. (6.8)

$$NH(X^3\Sigma^+) + CH_3COOH(X^1A') \rightarrow H_2NCH_2COOH(X^1A') \qquad (6.8)$$

Acetic acid has already been discovered in the interstellar medium (Mehringer, Snyder et al. 1997; Remijan, Snyder et al. 2003) and so it is not difficult to see that it too could be an important source of glycine in the ISM. It is planned to investigate these processes in future work.

6.4 Ultraviolet Irradiation of a CH_3NH_2: CO_2 ice mixture

6.4.1 Introduction

We will now investigate the effects of ultraviolet photon irradiation on a CH_3NH_2:CO_2 mixture. We irradiated our CH_3NH_2 and CO_2 mixture (the same mixture used in chapter 5), using the UV1 beamline in Aarhus (Chapter 5, Chapter 3) as a source of UV photons. Instead of collecting transmission spectra with UV light and a photomultiplier tube we used a Nicolet FTIR Spectrometer to collect infrared spectra of our sample before and after irradiation.

6.4.2 Experimental

Before starting any infrared measurements it is necessary to purge the spectrometer with an infrared inert gas such as nitrogen to minimise the absorption by atmospheric water and carbon dioxide vapour. After 24 hours the spectrometer is sufficiently purged and the effect of water vapour in our spectrum is minimised. Having cooled our CaF_2 substrate to 25 K we then record an infrared spectra of the clean substrate. This is shown in Figure 6-14.

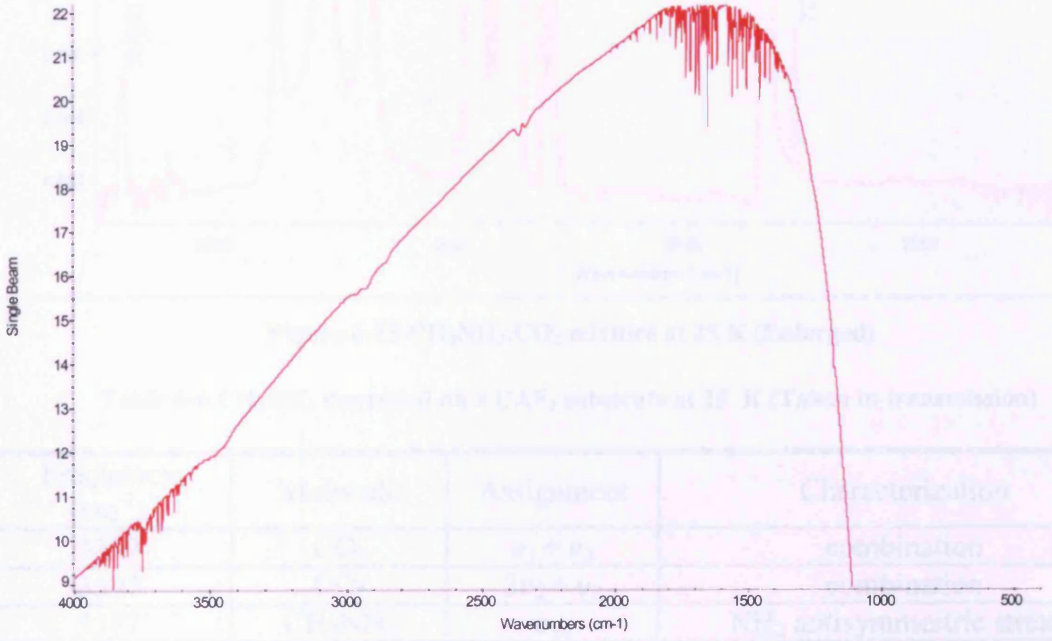

Figure 6-14 Background infrared scan though a clean cooled CaF_2 substrate at 25 K

It is clear there is still some water contamination in the spectra especially when compared to the spectrum obtained on a similar Nicolet FTIR during the electron irradiation experiments, (Figure 6-1) the infrared spectrometer at the University of Hawaii was purged by a drying unit. The extra water removal around 1500 cm^{-1} is clearly visible when comparing the two. However as long as the water vapour levels are constant then the error introduced by the water vapour is small.

We then deposited the CO_2 / CH_3NH_2 mixture onto the clean substrate (5 mbar of 7:1 gas mixture of CH_3NH_2:CO_2.) The results of this deposition are shown in Figure 6-15 and tabulated in Table 6-6

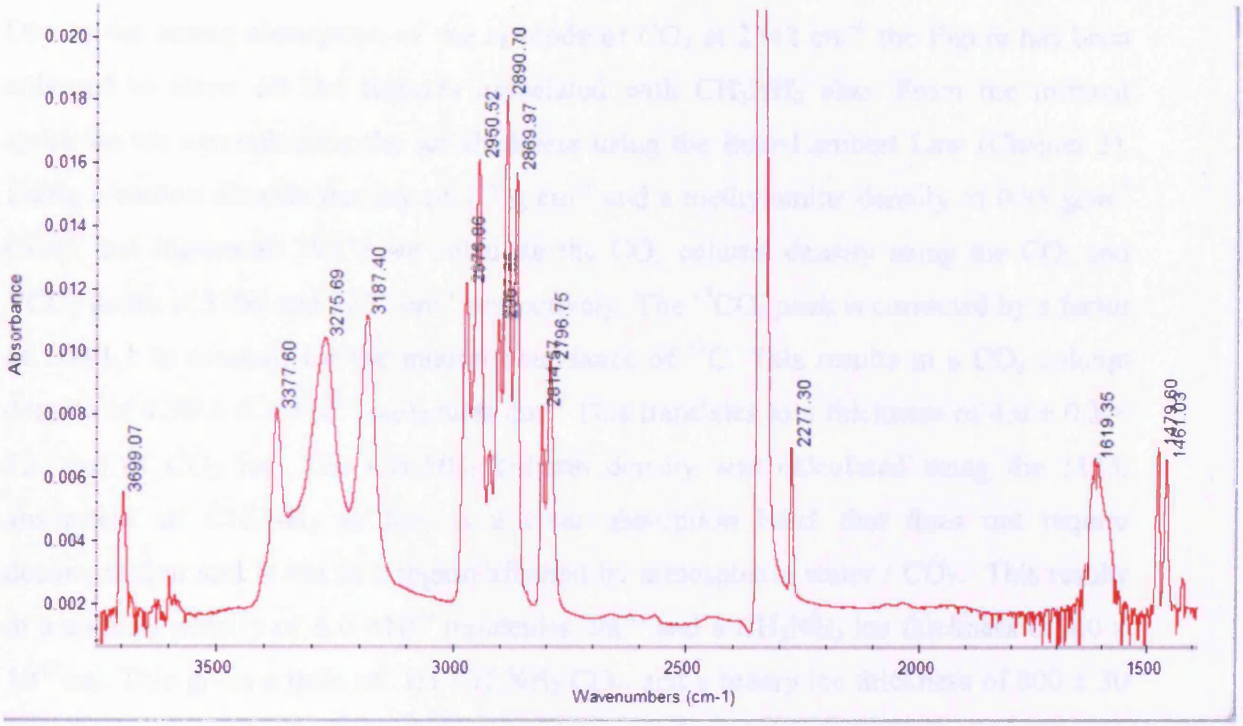

Figure 6-15 CH_3NH_2:CO_2 mixture at 25 K (Enlarged)

Table 6-6 CH_3NH_2 deposited on a CAF_2 substrate at 25 K (Taken in transmission)

Frequency (cm^{-1})	Molecule	Assignment	Characterization
3699	CO_2	$\upsilon_1 + \upsilon_3$	combination
3597	CO_2	$2\upsilon_2 + \upsilon_3$	combination
3377	CH_3NH_2	υ_{10}	NH_2 antisymmertric stretch
3276	CH_3NH_2	υ_1	NH_2 symmetric stretch
3189	CH_3NH_2	(?)	
2977	CH_3NH_2	(?)	
2950	CH_3NH_2	υ_{11}	CH_3 antisymmetric stretch
2927	CH_3NH_2	(?)	
2908	CH_3NH_2	(?)	
2890	CH_3NH_2	υ_2	CH_3 antisymmetric stretch
2870	CH_3NH_2	(?)	
2814	CH_3NH_2	(?)	
2797	CH_3NH_2	υ_3	CH_3 symmetric stretch
2342	CO_2	υ_3	asymmetric stretch
2277	$^{13}CO_2$	$\upsilon_3(^{13}CO_2)$	isotope peak
1619	CH_3NH_2	υ_4	NH_2 scissor
1480	CH_3NH_2	υ_5	CH_3 antisymmetric deformation
1461	CH_3NH_2	υ_{12}	CH_3 antisymmetric deformation
1424	CH_3NH_2	υ_6	CH_3 symmetric deformation

Due to the strong absorption of the ν_2 mode of CO_2 at 2342 cm^{-1} the Figure has been enlarged to show all the features associated with CH_3NH_2 also. From the infrared spectrum we can calculate the ice thickness using the Beer-Lambert Law (Chapter 3). Using a carbon dioxide density of 1.7 g cm^{-3} and a methylamine density of 0.85 gcm^{-3} (Atoji and Lipscomb 1953) we calculate the CO_2 column density using the CO_2 and $^{13}CO_2$ peaks at 3706 and 2277 cm^{-1} respectively. The $^{13}CO_2$ peak is corrected by a factor of 100/1.1 to account for the natural abundance of ^{13}C. This results in a CO_2 column density of $9.39 \pm 0.7 \times 10^{16}$ molecules $cm^{-2.}$ This translates to a thickness of $4.0 \pm 0.3 \times 10^{-6}$ cm of CO_2 ice. The CH_3NH_2 column density was calculated using the 1153, absorption of CH_3NH_2 as this is a clear absorption band that does not require deconvolution and is not in a region affected by atmospheric water / CO_2. This results in a column density of 6.6×10^{16} molecules $cm^{-2.}$ and a CH_3NH_2 ice thickness of 4.0 x 10^{-6} cm. This gives a ratio of 1:1 CH_3NH_2:CO_2. and a binary ice thickness of 800 ± 30 nm.

As an aside we note the differences in the sample of CH_3NH_2 in transmission mode to the sample taken in reflectance. An overlay of the two spectra, one of CH_3NH_2 in transmission the other in reflection is shown in Figure 6-16.

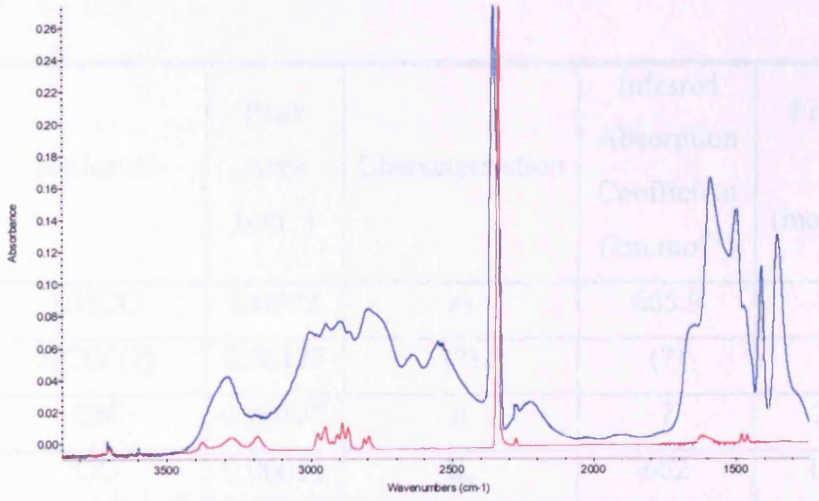

Figure 6-16 Comparison between the reflectance and transmission spectrum of CH_3NH_2 at T < 25 K. Blue spectra is taken in reflection, red in transmission.

We observe new bands appearing in the reflectance spectrum that are not seen in transmission. However it should be noted that the CH_3NH_2 sample was much thinner (445 nm) in the case of the reflectance experiment with a much greater proportion of CH_3NH_2 compared to CO_2. In our transmission experiment we had a much thicker ice sample but a ~ 1:1 mixture of CH_3NH_2:CO_2. This could account for any differences seen between the two spectra. Differences in the spectra could also be attributed to a metal surface selection rule.

We then rotated our sample to face the light source and irradiated the sample for 7 hours. The irradiation wavelength was selected to be 145 nm. (Photon energy of 825 kJ.mol^{-1}) 145 nm corresponds to a strong photoabsorption cross section of CH_3NH_2 (Figure 5-40) with an average flux of 4 x 10^9 photons s^{-1} cm^{-2} . After each hour of the irradiation process we recorded an infrared spectrum. After irradiation was complete the sample was warmed to 300 K then recooled and an infrared scan taken. We note now that *no* residue was seen on the substrate after the heating process.
As the irradiation progresses at 25 K we observe a number of new infrared absorptions. These are tabulated in Table 6-7

Table 6-7 New Infrared absorptions at 25 K after 7 hours irradiation of CH_3NH_2:CO_2 ice mixture at 25 K by 145 nm photons. For absorptions with uncertain assignments all possible assignments are given.

Wave number (cm^{-1})	Molecule	Peak Area (cm^{-1})	Characterisation	Infrared Absorption Coefficient (km.mol^{-1})	Final Column Density (molecules cm^{-2})
2232	HNCO	0.0092	ν_2	665.9	1.9×10^{14}
2110	NCO^- (?)	0.00127	(?)	(?)	(?)
	CN^-	0.00127	σ	7	2.5×10^{15}
2140	CO	0.00051	Σ_g	662	1.06×10^{14}
1285	CH_4	0.00629	ν_4	19.8	4.4×10^{15}
	$CHNH_3$	0.00629	ν_6	29	3.0×10^{15}
	C-NH_3 ($^3A_1$)	0.00629	ν_2	44	2.0×10^{15}

We have calculated the column densities of the new species found after irradiation using the Beer Lambert law. (Chapter 3) Infrared absorption coefficients were obtained using the NIST Computational Chemistry Comparison and Benchmark Data Base (Johnson, Richter et al. 2003) from ab initio calculations using the B3LYP 6-311G* basis set. Figure 6-17 shows 3 absorption features in the ice after 7 hours of irradiation. As can be seen the appearance of the band at 2232 cm-1 is extremely clear.

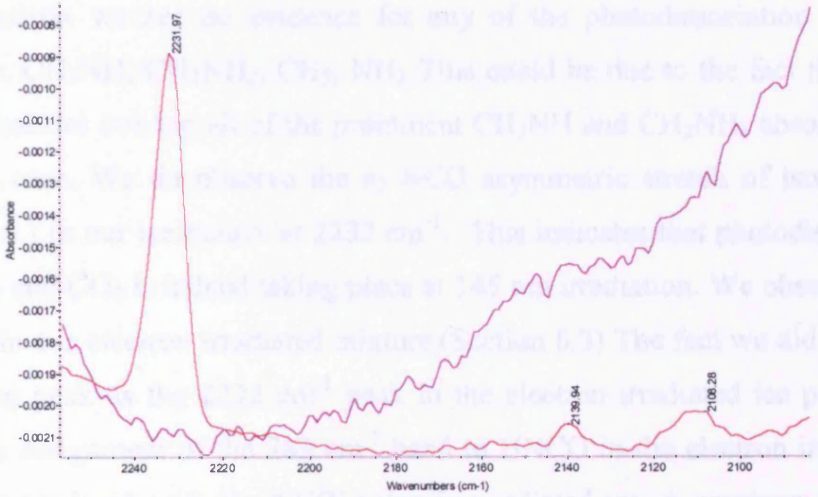

Figure 6-17 IR spectrum shown in red of the result of 7 hours irradiation of CH_3NH_2:CO_2 ice mixture at 145 nm. The spectrum in purple is the unirradiated ice.

6.4.3 Discussion

The UV irradiation of the CH_3NH_2 mixture triggers the dissociation of CH_3NH_2 and CO_2. The pathways for CH_3NH_2 dissociation are

$$CH_3NH_2(X^1A') \rightarrow CH_2NH_2(X^2A') + H(^2S_{1/2}) \quad (a)$$

$$CH_3NH_2(X^1A') \rightarrow CH_3NH(X^2A') + H(^2S_{1/2}) \quad (b)$$

$$CH_3NH_2(X^1A') \rightarrow CH_3(X^2A'') + NH_2(X^2B_1) \quad (c)$$

Previous experiments on the photodissociation of CH_3NH_2 in the gas phase at 222 nm have shown that pathway (a) is the most dominant, followed by pathway (b) Pathway C is the least likely pathway with only a small fraction of photons able to dissociate the C-N bond (Waschewsky, Kitchen et al. 1995). However there is no reason to suspect that

the solid phase is similar to the gas phase in this case, especially under single wavelength irradiation.

The carbon dioxide will also dissociate via one of the following pathways

$$CO_2\,(X^1\Sigma_g^+) \rightarrow CO\,(X^1\Sigma^+) + O\,(^1D) \qquad (d)$$

$$CO_2\,(X^1\Sigma_g^+) \rightarrow CO\,(X^1\Sigma^+) + O\,(^3P) \qquad (e)$$

In the ice matrix we see no evidence for any of the photodissociation products of CH_3NH_2. i.e. CH_3NH, CH_2NH_2, CH_3, NH_2. This could be due to the fact that CH_3NH_2 absorption features overlap all of the prominent CH_3NH and CH_2NH_2 absorptions as in the electron case. We do observe the ν_2 NCO asymmetric stretch of isocyanic acid, HNCO ($X\ ^1A'$) in our ice matrix at 2232 cm^{-1}. This indicates that photodissociation of the CH_3NH_2 and CO_2 is indeed taking place at 145 nm irradiation. We observed HNCO at 789 cm^{-1} in our electron irradiated mixture.(Section 6.3) The fact we did not observe such a strong peak as the 2232 cm^{-1} peak in the electron irradiated ice perhaps casts doubt on the assignment of the 789 cm^{-1} band to HNCO in the electron irradiated ice. We also tentatively identify the NCO^- anion in irradiated ice. A previous study on the photodissociation of HNCO in solid Xe by (Pettersson, Khriachtchev et al. 1999) identified NCO^- as a product of HNCO dissociation at 2124.5 cm^{-1}. If HNCO is present in our ice samples then it may be photolysed itself to produce NCO^-. Alternatively the 2110 cm^{-1} feature can be assigned to the CN^- feature which was observed at 2078 cm^{-1} in the electron irradiated case. The reason for any shift if the absorption is due to CN^- is unclear, but could be due to the enchanced presence of CO_2 in the ice matrix.

One possible formation route to HNCO could be as shown in (f)

$$NH_2\,(^2B_1) + CO_2\,(X^1\Sigma_g^+) \rightarrow HNCO\,(X\ ^1A') + OH\,(^2\Pi_i) \qquad (f)$$

The NH_2 radical could be formed from the cleavage of the CN bond in CH_3NH_2, which requires 350 kJ mol^{-1}. The reaction (f) is endoergic by 138.2 kJ mol^{-1}. Thus our photons should provide enough energy for this process to occur.

It is notable that the species present after UV irradiation are different from those present in electron irradiation of a similar mixture. However in the electron case we had a larger excess of CH_3NH_2 in our mixture compared to CO_2 which could account for any differences seen. We note there is also very little destruction of CO_2 compared to CH_3NH_2. After 7 hours of irradiation our final column densities of CO_2 and CH_3NH_2 are 9.13 $\times 10^{16}$ molecules cm^{-2} and 6.2 $\times 10^{16}$ molecules cm^{-2} respectively. A decrease of 3 % and 6 % respectively. The destruction of CH_3NH_2 is more efficient at 145 nm than CO_2. The relative lack of CO_2 dissociation compared to the electron case means there are fewer $O(^1D)$ and $O(^3P)$ atoms which may play a critical role in forming some of the products observed in the electron irradiation case. It is also possible that selective photolysis such as ours may induce an imbalance in the production of $O(^1D)$ and $O(^3P)$. Further studies at different wavelengths are required to determine the role that $O(^1D)$ and $O(^3P)$ may play in reaction mechanisms.

As in the case with the electron irradiation of our mixture we would expect to see traces of HOCO in our ice matrix. The photolysis of CH_3NH_2 should release hydrogen atoms into the ice which should then recombine with CO_2 to form HOCO. The lack of HOCO could be due to the enhanced temperature compared to the electron case (25 K cf. 11 K) as the HOCO is know to be very temperature sensitive. We are also lacking evidence of the H_2CNH molecule and OCN^- which is a prominent feature in our electron irradiated ices. The lack of OCN^- could be simply be due to the smaller concentration of CH_3NH_2 in the UV case, or due to the aforementioned lack of O(3P) atoms. If we assume OCN^- is formed via the reaction of O + CN^- recall we earlier stated is O (^1D) + CN^- will react without an energy barrier and O (^3P) + CN^- is endoergic by 540.8 kJ mol^{-1}. If we are observing CN^- at 2110 cm^{-1} the lack of OCN^- could indicate we have no $O(^1D)$ atoms in our ice matrix, or any oxygen atoms released from CO_2 dissociation are in the $O(^3P)$ state and lack the kinetic energy to overcome the barrier to formation.

Most importantly the aim of the experiment was to look for the formation of the amino acid glycine. We see no evidence for glycine in our current preliminary UV experiments in contrast to our electron irradiation experiments where we see evidence for glycine and glycine isomers. However this could be partly due to some of the problems associated with purging the spectrometer. In order to look for the small absorption

features of glycine it is necessary that there is almost no contamination from atmospheric CO_2 and H_2O as the absorptions overlap. Due to the portable nature and design of our experiment it is currently very difficult to eliminate the atmospheric CO_2 and H_2O absorptions to a sufficient level. It should also be noted that in the electron case we saw the majority of our glycine absorption features after we had warmed to 300 K allowing recombination of radicals. We were then left with an organic residue on the substrate. The substrate in the electron irradiation case was a silver mono-crystal. This may be better suited to retaining the residue than our CaF_2 substrate used in the UV irradiation case. Upon warming of the mixture after UV irradiation we see no evidence for any residue. Due to our use of the open cycle helium refrigeration system a controlled warming is difficult to archive as we have to manually adjust the flow of helium into the cryostat as the resistive heater does not provide enough power to totally warm the cryostat to high temperatures with a full load of helium in the system. Future modification of a sapphire disk to the sample mount (Chapter 7) will allow a more controlled warming of the sample. Rapid warming of our UV irradated sample may have destroyed any chance of glycine formation by stripping the top layers of the ice where the irradiation products were formed (recall that UV photons do not penetrate as deeply into the ice as electrons do)

6.4.4 Conclusions

In conclusion our UV irradiation experiments have shown there is much future work to be carried out on the UV irradiation of our CH_3NH_2:CO_2 ice mixture. A longer irradiation time or a more intense source coupled with careful heating may yield glycine formation. Further irradiation at specific wavelengths may allow the mechanism of glycine formation to be additionally refined.

Chapter Seven

Conclusions and Future Work

"**Conclusion** /nm./: the place where you got tired of thinking."

In the course of this thesis work we have designed and built an apparatus to simulate the conditions of the interstellar medium. In this concluding chapter we will evaluate the performance of the apparatus and identify the main areas for improvement, we will then review some of the conclusions from each of the three irradiation studies described in this thesis and discuss a future work programme

7.1 Experimental Evaluations.

The apparatus designed to simulate conditions in the ISM has fulfilled the major design requirements. It is capable of simulating the pressures and temperatures of the interstellar medium achieving a base temperature of ~20 K. (Chapter 5) and pressures in the region of 10^{-10} mbar. Our Oxford instruments temperature sensor coupled with a dual thermocouple has proved to be a reliable method of measuring the temperature especially when compared to the fragile Rhodium-Iron sensor.

The thin ice layers of all our samples are currently prepared by deposition of the vapour onto a cooled CaF_2 crystal substrate. Thickness of the sample is then assessed using a laser technique. However the current gas dosing system could benefit from some modifications. Currently all gas dosing is done by a hand controlled precision leak

valve, with practice it is possible to produce deposition times that are consistent over a range of experiments on the same day, however an electronically controlled dosing system would allow totally reproducible depositions time after time. Our mixing volume is also currently too small, using a larger t-piece is a simple modification to our existing system.

Our experiments have shown that the use of helium transported from a dewar instead of a closed cycle helium refrigerator has resulted in the use of a large amount of liquid helium. An expensive undertaking. The main use of the helium comes when heating the cryostat. In order to have a controlled heating of the sample we must keep the cryostat full of liquid helium while the sample is heating. This is extremely inefficient and uses a lot of helium. If however we were to place a sapphire disk acting as a thermal diode between the sample mount and cryostat we could perform a controlled heating of the substrate by placing a cartridge heater onto the sample mount and yet maintain the cryostat at base temperature of 20 K. We would not have to heat the whole cryostat and waste liquid helium.

Any experiment is totally reliant on its detection method. Our current detection methods are infrared and UV spectrometry. During the course of this PhD we have used two infrared spectrometers. Both spectrometers have highlighted the importance of correctly purging the spectrometer. Due to the fact the chamber is placed into the compartment of the spectrometer we expose the spectrometer beam path to air, making measurements susceptible to atmospheric fluctuations. The ion-irradiation experiments have shown that in order to obtain more qualitative results the beam path must be totally purged. We have designed a method of purging the beam path between the CaF_2 windows and the spectrometer and initial tests suggest it is effective at reducing the interference from atmospheric water in our spectrum. We are also in the process of purchasing a permanent drying unit to replace the liquid nitrogen that we have been using as a purge medium which will hopefully improve the purge. The most effective method of water removal though is simply to wait and allow the spectrometer to fully purge. After purging the system for 24 hours plus a noticeable improvement in the spectrum is visible. The drying unit will allow us to have a constant purge running over the course of an experiment without changing liquid nitrogen dewars and breaking the purge. An

important factor also highlighted in our infrared studies is the range limitation currently imposed on our system by the CaF_2 windows and substrate we use. The identification of molecules could be greatly aided by extending our range to lower wavelength regions, for example by the use of KBr windows. This also requires the use of an alterative detector to detect the lower infrared regions. We have already purchased a MCT (Mercury Cadmium Telluride) detector with a range of ~ 5000 - 720 cm^{-1} which coupled with new windows will allow us to detect many additional species in our infrared spectra.

Our main use of UV spectroscopy has been at the UV1 beam line in Aarhus. The synchrotron and a photomultiplier tube have proved to be excellently suited to our system and have provided consistent results. One possible area of improvement lies in our choice of substrate. At present we can only achieve a lower limit of ~125 nm with low sensitivity in this region. By changing our substrate and entrance window (perhaps to LiF_2) to the Synchrotron we could perhaps extend the range to 110 nm. But this is still limited by the design of the synchrotron itself, as there is a LiF_2 window in place on the beamline. An alternative solution to UV irradiation using the synchrotron is a UV lamp. We have purchased a Deuterium lamp that will provide a high photon flux and enable us to decrease our irradiation times. However one disadvantage of a UV lamp is it is not wavelength selectable, making it harder to determine some of the underlying mechanisms of molecular formation in our ices.

Our ion irradiation studies performed at Queens University Belfast were carried out towards the beginning of the PhD and highlighted some of the initial problems with the design of the system. However we were successful in attaching the system to the ion source and we have reproduced some of the results of other groups who have studied the ion irradiation of water:CO_2 ice mixtures. We have also studied, we believe for the first time, the effect of ion mass on the production of CO and H_2CO_3 in heavy ion (noble gas) irradiation of H_2O:CO_2 water ice mixture at temperatures relevant to the outer solar system planets. We have also studied the irradiation of Water with multiply charged ions and we see evidence for trapping and formation of CO in multiple sites. There is some evidence of a charge dependant energy effect in that we have seen a greater yield when irradiating with the multiply charged ion. However in order to

confirm this we need to obtain a ground state ion beam without the high metastable fraction.

During the course of this PhD, we have begun to build a "library" of ultraviolet spectra in the solid phase. In most cases the ultraviolet spectra in the solid phase of common molecules of astrophysical interest is not well known. We have measured the ultraviolet spectra of a number of molecules of astrophysical interest, in some cases for the first time in the solid phase. In addition to this we have used begun to use a laser thickness technique with our equipment to measure the thickness of films deposited. This technique can also be extended to the infrared to enable us to measure our own infrared absorption coefficients in the future. From our ultraviolet spectra we have observed the effects that phase changes can have on a solid sample, for example the vibration structure observed in SO_2 on annealing. It has also highlighted that attention should be paid to the method of deposition; in particular deposition rates may be critical. In order to accurately simulate the conditions of interstellar space deposition times should be as long as practically possible.

Our electron irradiation studies began with the aim of trying to create a simple amino acid, glycine, from a binary ice mixture. We believe we have succeeded in creating the amino acid glycine and in understanding some of the processes involved in the formation of this amino acid. This is only the first step though in a study of the formation of biologically relevant compounds in the ISM. Our CH_3NH_2:CO_2 ice mixture was not representative of a true interstellar ice mixture which will likely be water dominated. The experiment should be repeated with a more complex ice mixture perhaps similar to the one used by (Munoz Caro, Meierhenrich et al. 2002) in their UV irradiation experiments which formed amino acids. They used a mixture of H_2O:CH_3OH:NH_3:CO:CO_2 = 2:1:1:1:1. It could also be advantageous to repeat the experiment using low energy electrons to better simulate the conditions in the ISM. Secondary electrons released for example by cosmic ray tracks, could play an important role in interstellar chemistry and these low energy events need to be further studied.

7.2 Other Modifications / Future work.

One possible improvement to the portable ices system would be the addition of an additional detection method such as a Quadrupole Mass Spectrometer (QMS). This could allow us to detect products released from the ice on warming and any products sputtered from the surface during irradiation. It would also allow the detection of non infrared detectable species such as H_2 and O_2. The small size of our chamber though would perhaps make this impractical. In order to mount a QMS we would have to extend the cube upwards, either using an additional cube or a six way cross to mount the QMS. This would also require investment in a z motion feedthrough to lower and raise the ice sample for warming, deposition and irradiation.

7.3 The Urey-Miller Experiment

As a complimentary project to the main body of research during this thesis. We have decided to recreate one of the famous and classic experiments in Astrobiology, The "Urey-Miller" experiment. There are two main theories on the formation of life on earth, one states that the building blocks for life were formed outside of our planet and brought to Earth on comets. The other alternative to life being delivered to earth on comets is of course that life originated here on Earth. The most famous experiment which set out to prove that prebiotic molecules could be formed in the early earth was the Urey-Miller experiment. In the 1950's Stanley Miller and his colleague Harold Urey conceived an experiment to try and re-create some of the organic compounds that make up life on Earth. (Miller and Urey 1959) By simulating the conditions of the primitive Earth they were able to create a number of organic compounds, specifically the amino acids Glycine, α-alanine and β-alanine were identified. To simulate the primitive earth they built a glass vessel containing an "ocean", "atmosphere" and an energy source. Lightning was chosen as an energy source from all the available sources Table 7-1

Table 7-1 Energy Sources on the Earth. (adapted from (Brack 1998))

Source	Energy (cal $cm^{-2} yr^{-1}$)
Total Radiation from Sun	260,000
Ultraviolet Light	
$\lambda < 2500$ Å	570
$\lambda < 2000$ Å	85
$\lambda < 1500$ Å	3.5
Electric Discharges	4
Cosmic Rays	0.0015
Radioactivity (to 1 km Depth)	0.8
Volcanoes	0.13

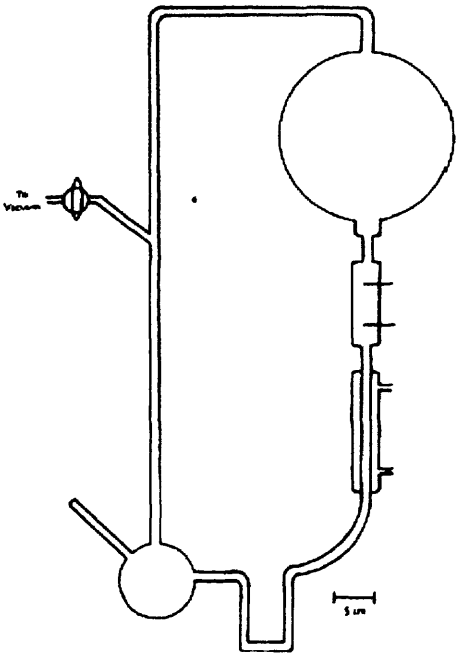

Figure 7-1 The Urey-Miller Experiment (After (Miller and Urey 1959)). The glass vessel to the lower left of the picture is used for the water reservoir. Sparking of the mixture occurs to the below the large bulb to the top right which contains the mixture of gases used to simulate the atmosphere.

The atmosphere used in their experiments was a mixture of hydrogen, H_2, methane, CH_4 and ammonia, NH_3. The experiment was allowed to run for a week, the water was heated to drive circulation around the system and the spark was run constantly. After one week the water was removed from the vessel and analysed using chromatography. Three amino acids were identified in the mixture, Glycine, α-alanine and β-alanine. The experiment seemed to prove that it was possible to create amino acids in the primitive

earth atmosphere simply by the electrical discharges prevalent at the time. However it is now thought that the composition of the Earth's early atmosphere was very different from that strongly reducing mixture used by Urey and Miller in the 1950's. Current predictions on the state of the earth's atmosphere predict that the earth would have had an early atmosphere very similar to volcanic outgassing today. So we will soon aim to repeat the Urey Miller experiment using different gas compositions, perhaps including a gas mixture similar to the composition of Titans atmosphere. During the course of this PhD we built a replica version of the Urey-Miller experiment which will be tested in due course. A photograph of our version can be seen in Figure 7-2

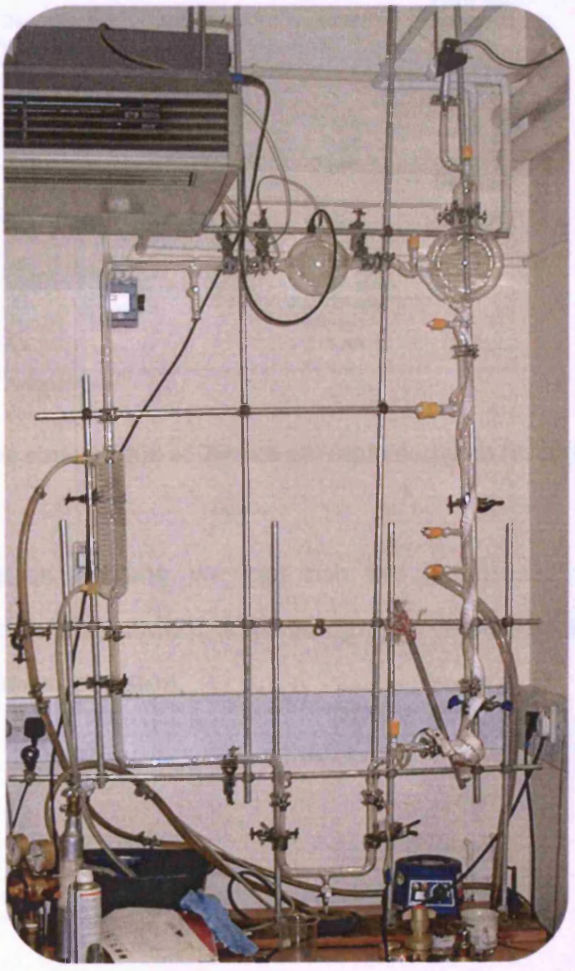

Figure 7-2 Our recreation of the Urey-Miller experiment. The atmosphere bulb can be seen top right with the water reservoir bottom right.

We use a high voltage power supply connected to two tungsten electrodes to provide the spark for the experiment. A water reservoir is heated by using heating tapes wrapped around the glass bulb and pipe. We will use the Urey Miller to simulate a composition of gases similar to the conditions found in volcanic outgassing. i.e. CO_2 and N_2 with some traces of CO, H_2 and reduced sulphur gases. Alternatively we can simulate the atmosphere of Titan (which is though to be similar to the atmosphere of the early Earth)

TABLE 11. Composition of the atmosphere of Titan (Strobel, 1985).

Constituent	Volume mixing ratio		
N_2		0.76–0.98*	
	Surface	*Stratosphere*	*Thermosphere* (3900 km)
CH_4	0.02–0.08	≤0.026	0.08 ± 0.03
Ar	<0.16		<0.06
Ne	<0.002		<0.01
CO	60 ppm		<0.05
H_2	0.002 ± 0.001		
C_2H_6		20 ppm	
C_3H_8		1–5 ppm	
C_2H_2		3 ppm	~0.0015 (3400 km)
C_2H_4		0.4 ppm	
HCN		0.2 ppm	<0.0005 (3500 km)
C_2N_2		0.01–0.1 ppm	
HC_3N		0.01–0.1 ppm	
C_4H_2		0.01–0.1 ppm	
CH_3C_2H		0.03 ppm	
CO_2		1–5 ppb	

*Preferred value.

Figure 7-3 The composition of Titan's atmosphere (taken from (Levine 1988))

Once the experiment is running we can use the techniques of infrared and UV spectroscopy coupled with modern chromatography techniques to determine what products are formed in our solution.

7.4 Conclusions

In conclusion we have designed and built an apparatus to simulate the conditions of the interstellar medium. The experiment has been successfully attached to a variety of irradiation sources and we have measured the UV spectra of some ices of astrophysical important and performed some of the first experiments using multiply charged and heavy ion irradiation of an astrophysical ice mix. We have demonstrated the production of the simplest amino acid glycine from a simple binary ice mixture and taken the first steps in understanding the mechanism of the production of biologically relevant molecules in the interstellar medium. The work is this thesis should provide a solid foundation for future work and further investigations.

References

Atkins, P. W. (1998). Physical Chemistry. Oxford, Oxford University Press.

Atoji, M. and W. N. Lipscomb (1953). "On the Crystal Structures of Methylamine." Acta Cryst. **6**: 770.

Ayotte, P., R. S. Smith, et al. (2001). "Effect of porosity on the adsorption, desorption, trapping, and release of volatile gases by amorphous solid water." Journal of Geophysical Research **106**: 33387-33392.

Baek, S. J., K.-W. Choi, et al. (2002). "Vibrational structures of predissociating methylamines (CH_3NH_2 and CH_3ND_2) in [A-tilde] states: Free internal rotation of CH_3 with respect to NH_2." The Journal of Chemical Physics **117**(22): 10057-10060.

Banwell, C. N. (1983). Fundamentals of Molecular Spectroscopy. London, McGraw-Hill.

Baratta, G. A. and M. E. Palumbo (1998). "Infrared optical constants of CO and CO_2 thin icy films." Optical Society of America Journal **15**: 3076-3085.

Beegle, L. W., J. M. Ajello, et al. (1999). "High resolution emission spectroscopy of the A $^1\Pi$ - X $^1\Sigma^+$ fourth positive band system of CO excited by electron impact." Astronomy and Astrophysics **347**: 375-390.

Bennett, C. J., C. Jamieson, et al. (2004). "Untangling the formation of the cyclic carbon trioxide isomer in low temperature carbon dioxide ices." Phys. Chem. Chem. Phys. **6**(4): 735 - 746.

Bludsky, O., P. Nachtigall, et al. (2000). "The calculation of the vibrational states of SO_2 in the electronic state up to the $SO(^3\Sigma^-)+O(^3P)$ dissociation limit." Chemical Physics Letters **318**(6): 607-613.

Brack, A. (1998). The Molecular Origins Of Life: *Assembling Pieces of the Puzzle*. Cambridge, Cambridge University Press.

Brand, J. C. D., P. H. Chiu, et al. (1976). "Sulfur dioxide: Rotational constants and asymmetric structure of the C^1B_2 state." Journal of Molecular Spectroscopy **60**: 43-56.

Brith, M. and O. Schnepp (1965). "The Absorption Spectra Of Solid CO and N_2." Molecular Physics **9**: 473.

Brown, R. D., P. D. Godfrey, et al. (1979). "A search for interstellar glycine." Monthly Notices of the Royal Astronomical Society **186**: 5P-8P.

Brucato, J. R., M. E. Palumbo, et al. (1997). "Carbonic Acid by Ion Implantation in Water/Carbon Dioxide Ice Mixtures." Icarus **125**: 135-144.

Cazaux, S. and A. G. G. M. Tielens (2004). "H_2 Formation on Grain Surfaces." Astrophysical Journal **604**: 222-237.

Chen, F. Z. and C. Y. R. Wu (2004). "Temperature-dependent photoabsorption cross sections in the VUV-UV region. I. Methane and ethane." Journal of Quantitative Spectroscopy and Radiative Transfer **85**(2): 195-209.

Clements, J. H. (1935). "On the Absorption Spectrum of Sulphur Dioxide." Physical Review **47**: -50224-232.

Collings, M. P., J. W. Dever, et al. (2002). Laboratory Surface Science: The Key to the Gas-Grain Interaction. NASA Laboratory Astrophysics Workshop.

Crovisier, J., D. Bockele-Morvan, et al. (2004). "The composition of ices in comet C/1995 O1 (Hale-Bopp) from radio spectroscopy. Further results and upper limits on undetected species." Astronomy and Astrophysics **418**: 1141-1157.

Dawes, A. (2003). Spectroscopic Study of Photon, Ion And Electron Stimulated Molecular Synthesis In Astrophysical Ices. Physics And Astronomy, University College London: 251.

Dawes, A., M. P. Davis, et al. (2004). "Formation of carbon monoxide and carbon dioxide during 2-4 keV C^+ and C^{++} irradaton of water ice." Icarus **Publication Pending**.

D'Hendecourt, L., M. Jourdain de Muizon, et al. (1996). "ISO-SWS observations of solid state features towards RAFGL 7009S." Astronomy and Astrophysics **315**: L365-L368.

d'Hendecourt, L. B., L. J. Allamandola, et al. (1985). "Time dependent chemistry in dense molecular clouds. I - Grain surface reactions, gas/grain interactions and infrared spectroscopy." Astronomy and Astrophysics **152**: 130-150.

Di Francesco, J., M. R. Hogerheijde, et al. (2002). "Abundances of Molecular Species in Barnard 68." Astronomical Journal **124**: 2749-2755.

Durig, J. R., S. F. Bush, et al. (1968). "Infrared and Raman Investigation of Condensed Phases of Methylamine and Its Deuterium Derivatives." The Journal of Chemical Physics **49**(5): 2106-2117.

Ehrenfreund, P. and S. B. Charnley (2000). "Organic Molecules in the Interstellar Medium, Comets, and Meteorites: A Voyage from Dark Clouds to the Early Earth." Annual Review of Astronomy and Astrophysics **38**: 427-483.

Falk, M. (1987). "Amorphous solid carbon dioxide." The Journal of Chemical Physics **86**(2): 560-564.

Federman, S. R., D. L. Lambert, et al. (2003). "Further Evidence for Chemical Fractionation from Ultraviolet Observations of Carbon Monoxide." Astrophysical Journal **591**: 986-999.

Fikri, M., S. Meyer, et al. (2002). "An experimental and theoretical study of the product distribution of the reaction CH_2 (X^3B_1) + NO." Faraday Discuss **119**: 223-242.

Fourikis, N., K. Takagi, et al. (1974). "Detection of Interstellar Methylamine by its 2₀₂-€€gt;1₁₀ A_{a^-} State Transition." Astrophysical Journal **191**: L139.

Fourikis, N., K. Takagi, et al. (1974). "Detection of Interstellar Methylamine by its 2_{02} -> 1_{10} A_a- State Transition." Astrophysical Journal **191**: L139.

Fraser, H. J., M. P. Collings, et al. (2004). "Using laboratory studies of CO-H_2O ices to understand the non-detection of a 2152 cm^{-1}band in the spectra of interstellar ices." Monthly Notices RAS **353**(1): 59-68.

Gerakines, P. A., M. H. Moore, et al. (2000). "Carbonic acid production in H_2O:CO_2 ices. UV photolysis vs. proton bombardment." Astronomy and Astrophysics **357**: 793-800.

Gerakines, P. A., M. H. Moore, et al. (2001). "Energetic processing of laboratory ice analogs: UV photolysis versus ion bombardment." Journal of Geophysical Research **106**: 33381-33386.

Gerakines, P. A., W. A. Schutte, et al. (1995). "The infrared band strengths of H_2O, CO and CO_2in laboratory simulations of astrophysical ice mixtures." Astronomy and Astrophysics **296**: 810.

Gerakines, P. A., D. C. B. Whittet, et al. (1999). "Observations of Solid Carbon Dioxide in Molecular Clouds with the Infrared Space Observatory." Astrophysical Journal **522**: 357-377.

Golomb, D., K. Watanabe, et al. (1961). "Absorption Coefficients of Sulfur Dioxide in the Vacuum Ultraviolet." The Journal of Chemical Physics **36**(4): 958-960.

Hagiwara, K., K. Hikasa, et al. (2002). "Review of Particle Physics." Physical Review D (Particles and Fields) **66**(1): 010001-974.

Henning, T. and H. Mutschke (1997). "Low-temperature infrared properties of cosmic dust analogues." Astronomy and Astrophysics **327**: 743-754.

Herzberg, G. (1966). Molecular Spectra and Molecular Structure Vol III. Electronic Spectra And Electronic Structure Of Polyatmoic Molecules, D.Van Nostrand Company Inc.

Hollis, J. M., F. J. Lovas, et al. (2000). "Interstellar Glycolaldehyde: The First Sugar." Astrophysical Journal **540**: L107-L110.

Hubin-Franskin, M.-J., J. Delwiche, et al. (2002). "Electronic excitation and optical cross sections of methylamine and ethylamine in the UV--VUV spectral region." The Journal of Chemical Physics **116**(21): 9261-9268.

Hubin-Franskin, M.-J., J. Delwiche, et al. (1998). "Outer-Valence-Shell spectoscopy of methylamine by the electron energy loss method." J. Phys. B: At. Mol. Opt. Phys **21**: 189-202.

Hudson, R. L., M. H. Moore, et al. (2001). "The Formation of Cyanate Ion (OCN^-) in Interstellar Ice Analogs." Astrophysical Journal **550**: 1140-1150.

Jacox, M. E. (2003). Vibrational and Electronic Energy Levels of Polyatomic Transient Molecules. NIST Standard Reference Database. Gaithersburg MD. **69**.

Johnson, R. D., U. Richter, et al. (2003). NIST Computational Chemistry Comparison and Benchmark DataBase. R. D. Johnson, NIST.

Johnson, R. E. and T. I. Quickenden (1997). "Photolysis and radiolysis of water ice on outer solar system bodies." Journal of Geophysical Research(102): 10985-10996.

Kaifu, N., M. Morimoto, et al. (1974). "Detection of Interstellar Methylamine." Astrophysical Journal **191**: L135.

Kaiser, R. I. (2002). "Experimental Investigation on the Formation of Carbon-Bearing Molecules in the Interstellar Medium via Neutral-Neutral Reactions." Chem. Rev **102**(5): 1309-1358.

Klinger, J., D. Benest, et al. (1985). Ices in the solar system; Proceedings of the Advanced Research Workshop, Nice, France, January 16-19, 1984. NATO ASIC Proc. 156: Ices in the Solar System.

Kouchi, A., T. Yamamoto, et al. (1994). "Conditions for condensation and preservation of amorphous ice and crystallinity of astrophysical ices." Astronomy and Astrophysics **290**: 1009-1018.

Krasnopolsky, V. A. and J. B. Pollack (1994). "H2O-H2SO4 system in Venus' clouds and OCS, CO, and H2SO4 profiles in Venus' troposphere." Icarus **109**: 58-78.

Krimigis, S. M., D. G. Mitchel, et al. (2002). "A nebula of gases from Io surrounding Jupiter." Nature **415**: 994-996.

Kuan, Y.-J., S. B. Charnley, et al. (2003). "Interstellar Glycine." Astrophysical Journal **593**: 848-867.

Lacy, J. H., J. S. Carr, et al. (1991). "Discovery of interstellar methane - Observations of gaseous and solid CH4 absorption toward young stars in molecular clouds." Astrophysical Journal **376**: 556-560.

Leger, A., M. Pirre, et al. (1994). "Relevance of oxygen and ozone detections in the search for primitive life in extra solar planets." Advances in Space Research **14**: 117-.

Levine, J. S. (1988). The atmospheres of the earth and the other planets: Origin, evolution and composition. Origins of Solar Systems.

Lugez, C. L., W. E. Thompson, et al. (1996). "Matrix isolation study of the interaction of excited neon atoms with O_3: Infrared spectrum of O^-_3 and evidence for the stabilization of O_2 ... O^+_4." The Journal of Chemical Physics **105**(6): 2153-2160.

Mauersberger, R., C. Henkel, et al. (1995). "Dense gas in nearby galaxies. VIII. The detection of OCS." Astronomy and Astrophysics **294**: 23-32.

McCluskey, M. and H. Frei (1997). "Transfer of methylene from ketene to nitric oxide by photoexcitation of reactant pairs in solid argon below the CH2:C:O dissociation limit." Journal of Physical Chemistry **97**(20): 5204 - 5207.

Mebel, A. M., S.-H. Lin, et al. (1997). "Theoretical study of vibronic spectra and photodissociation pathways of methane." The Journal of Chemical Physics **106**(7): 2612-2620.

Mehringer, D. M., L. E. Snyder, et al. (1997). "Detection and Confirmation of Interstellar Acetic Acid." Astrophysical Journal **480**: L71.

Meyer, B. (1971). Low Temperature Spectroscopy. New York, Elsevier Publishing Company Inc.

Miller, S. L. and H. C. Urey (1959). "Organic Compound Synthesis on the Primitive Earth." Science **130**: 245-251.

Monahan, K. M. and W. C. Walker (1974). "Photoabsorption of solid carbon dioxide from 7 to 12 eV." The Journal of Chemical Physics **61**(10): 3886-3889.

Monahan, K. M. and W. C. Walker (1975). "Vacuum ultraviolet absorption spectra of solid N_2O and CO_2 at 53 K." The Journal of Chemical Physics **63**(4): 1676-1681.

Monahan, K. M. and W. C. Walker (1975). "Vacuum ultraviolet absorption spectra of solid OCS at 53 K." Journal of Chemical Physics **63**: 5126-5130.

Morton, R. J. and R. I. Kaiser (2003). "Kinetics of suprathermal hydrogen atom reactions with saturated hydrides in planetary and satellite atmospheres." Planetary and Space Science **51**(6): 365-373.

Mumma, M. J., M. A. Disanti, et al. (1996). "Detection of Abundant Ethane and Methane, Along with Carbon Monoxide and Water, in Comet C/1996 B2 Hyakutake: Evidence for Interstellar Origin." Science **272**: 1310-1314.

Munoz Caro, G. M., U. J. Meierhenrich, et al. (2002). "Amino acids from ultraviolet irradiation of interstellar ice analogues." Nature **416**: 403-406.

Nastasi, M., M. J. W., et al. (1996). Ion-Solid Interactions: Fundamentals and Applications. Cambridge, Cambridge University Press.

Noll, K. S., T. L. Roush, et al. (1997). "Detection of ozone on Saturn's satellites RHEA and Dione." Nature **388**: 45-47.

Novozamsky, J. H., W. A. Schutte, et al. (2001). "Further evidence for the assignment of the XCN band in astrophysical ice analogs to OCN^-. Spectroscopy and deuterium shift." Astronomy and Astrophysics **379**: 588-591.

P.A. Gerakines, M. H. Moore, et al. (2000). "Carbonic acid production in H2O:CO2 ices." Astrononmy & Astrophysics **357**: 793-800.

Palumbo, M. E. and G. Strazzulla (1993). "The 2140/cm band of frozen CO - Laboratory experiments and astrophysical applications." Astronomy and Astrophysics **269**: 568-580.

Peterson, K. A., R. C. Mayrhofer, et al. (1990). "The potential energy and dipole moment surfaces of NF_2 and O_3^- by complete active space self-consistent field." The Journal of Chemical Physics **93**(7): 5020-5028.

Pettersson, M., L. Khriachtchev, et al. (1999). "Photochemisty Of HNCO in Solid Xe: Channels of UV Phtolysis and Creationg of H_2NCO Radicals." J. Phys. Chem. A. **103**: 9154-9162.

Post, B. J., R. S. Schwartz, et al. (1952). "The Crystal Structure Of Sulfur Dioxide." Acta Cryst. **5**: 372.

Quirico, E., B. Schmitt, et al. (1996). "Spectroscopy of some ices of astrophysical interest: SO2, N2 and N2: CH4 mixtures." Planetary and Space Science **44**(9): 973-986.

Rabalais, J. W., S. P. McGlynn, et al. (1971). "Electronic spectroscopy of isoelectronic molecules. II. Linear triatomic groupings containing sixteen valence electrons." Chem. Rev **71**(1): 73-108.

Remijan, A., L. E. Snyder, et al. (2003). "A Survey of Acetic Acid toward Hot Molecular Cores." Astrophysical Journal **590**: 314-332.

Robert Wu, C. Y., B. W. Yang, et al. (2000). "Measurements of High-, Room-, and Low-Temperature Photoabsorption Cross Sections of SO2 in the 2080- to 2950-A Region, with Application to Io." Icarus **145**(1): 289-296.

Robin, M. B. (1974). Higher Excited States of Polyatmoic Molecules. London, Academic Press. Inc.

Rosado, M. T., M. L. T. S. Duarte, et al. (1998). "Vibrational spectra of acid and alkaline glycine salts." Vibrational Spectroscopy **16**(1): 35-54.

Sandford, S. A. and L. J. Allamandola (1990). "The physical and infrared spectral properties of CO2 in astrophysical ice analogs." Astrophysical Journal **355**: 357-372.

Sandford, S. A., M. P. Bernstein, et al. (2001). "The Abundances of Solid N_2 and Gaseous CO_2 in Interstellar Dense Molecular Clouds." Astrophysical Journal **548**: 836-851.

Spoon, H. W. W., L. Armus, et al. (2004). "Fire and Ice: Spitzer Infrared Spectrograph (IRS) Mid-Infrared Spectroscopy of IRAS F00183-7111." Astrophysical Journal Supplement Series **154**: 184-187.

Steinfeld, J. I., J. S. Francisco, et al. (1998). Chemical Kinetics And Dynamics. Paramus, NJ, Prentice Hall.

Strazzulla, G., L. G., et al. (2003). "Implantation of carbon and nitrogen ions in water ice." Icarus **164**(1): 163-169.

Strobel, D. F. (1969). "Photochemistry of methane in the jovian atmosphere." Journal of Atmospheric Sciences **26**: 906-911.

Taylor, D. P. and E. R. Bernstein (1995). "On the low lying excited states of methyl amine." The Journal of Chemical Physics **103**(24): 10453-10464.

Taylor, R. V., W. C. Walker, et al. (1980). "Photodissociative production of $O(^1S)$ from N_2O and $S(^1S)$ from OCS in rare gas matrices." Journal of Chemical Physics **72**: 6743-6748.

Tielens, A. G. G. M. and L. J. Allamandola (1987). Evolution Of Interstellar Dust. Physical Processes in Interstellar Clouds. G. E. Morfill and M. Scholer, Kluwer Academic Pub: 333-376.

Trassl, R., F. Broetz, et al. (1999). An All-Permanent Magnet 10 GHz "Multi-Mode" ECR Ion Source for the Production of Metallic Ions. 14th International Workshop on ECR Sources, ECRIS99, Geneva, CERN.

Turner, B. E. (1989). "A molecular line survey of Sagittarius B2 and Orion-KL from 70 to 115 GHz. I - The observational data." Astrophysical Journal Supplement Series **70**: 539-622.

Turner, B. E. (1991). "A molecular line survey of Sagittarius B2 and Orion-KL from 70 to 115 GHz. II - Analysis of the data." Astrophysical Journal Supplement Series **76**: 617-686.

van Dishoeck, E. F. and J. H. Black (1988). "The photodissociation and chemistry of interstellar CO." Astrophysical Journal **334**: 771-802.

Vandaele, A. C., Simon, P. C., Guilmot, J. M.,Carleer, M. , Colin, R. (1994). "SO_2 absorption cross section measurement in the UV using a Fourier transform spectrometer." Journal of Geophysical Research **99**: 25599-25606.

Wang, J.-H., K. Liu, et al. (2000). "Vacuum ultraviolet photochemistry of CH_4 and isotopomers. II. Product channel fields and absorption spectra." The Journal of Chemical Physics **113**(10): 4146-4152.

Waschewsky, G. C. G., D. C. Kitchen, et al. (1995). "Competing Bond Fission and Molecular Elimination Channels in the Photodissociation of CH3NH2 at 222 nm." Journal of Physical Chemistry **99**(9): 2635 - 2645.

Westley, M. S., G. A. Baratta, et al. (1998). "Density and index of refraction of water ice films vapor deposited at low temperatures." Journal of Chemical Physics **108**: 3321-3326.

Whalley, E. and J. E. Bertie (1967). "Optical Spectra of Orientationally Disordered Crystals. I. Theory for Translational Lattice Vibrations." The Journal of Chemical Physics **46**(4): 1264-1270.

Woon, D. E. (2002). "Pathways to Glycine and Other Amino Acids in Ultraviolet-irradiated Astrophysical Ices Determined via Quantum Chemical Modeling." Astrophysical Journal **571**: L177-L180.

Yoshino, K., J. R. Esmond, et al. (1996). "Absorption cross section measurements of carbon dioxide in the wavelength region 118.7-175.5 nm and the temperature dependence." Journal of Quantitative Spectroscopy and Radiative Transfer **55**(1): 53-60.

Yu, H.-G., J. T. Muckerman, et al. (2001). "A theoretical study of the potential energy surface for the reaction OH+CO->H+CO2." Chemical Physics Letters **349**(5-6): 547-554.

Ziegler, J. F. (2003). SRIM -The Stopping And Range Of Ions In Matter - *http://www.srim.org/*.

Appendix A – List of Conference / abstracts/posters and talks and papers.

Abstracts / Posters /Talks

Davis,M.P, Dawes, A, Hoffmann, S.V., Holtom, P., Mason, N.J., McCullough,R.W., Williams, I.D. "Laboratory Studies of Ion, Photon, and Electron Irradiated Astrophysical Ice Analogues" presented at: "UK Astrobiology Symposium 2003, Cambridge, March 2003 and Workshop on the Solid State Astrochemisrty of Star Forming Regions, Leiden, The Netherlands (April 2003)

Dawes, A., P. Holtom and N. J. Mason (2003). "Laboratory studies of molecular synthesis in astrophysical ices." EGS - AGU - EUG Joint Assembly, Abstracts from the meeting held in Nice, France, 6 - 11 April 2003, abstract #6581: 6581.

Holtom, P. (2004) "The formation of the amino acid glycine in extraterrestrial ices", National Astronomy Meeting (NAM), Milton Keynes. 2004

Holtom, P. (2004) "The formation of the amino acid glycine in extraterrestrial ices" EPIC Meeting, Austria. 2004

Publications

Dawes, A. M., N.J., Tegeder, P, Holtom, P. (2003). Laboratory studies of astrophysical molecules; a new UCL apparatus. Electron scattering from atoms, molecules, nuclei and bulk matter. C. T. W. a. N. J. Mason, Plenun Press: 329-344

Dawes, A., Holtom, P., Mason, N.J. (2003). "Study of condensed phase molecules and molecular synthesis in astrophysical environments." Recent. Res. Devel. Chem. Physics 4: 519-532.

Publications Pending. (Intended journal of submission in parenthesis)

A. Dawes, M. P. Davis, P. D. Holtom, R. W. McCullough, B Seredyuk, R. Trassl I. Williams and N. J. Mason (2004). "Formation of carbon monoxide and carbon dioxide during 2-4 keV C^+ and C^{++} irradiation of water ice." (Icarus)

Philip D. Holtom, Chris J. Bennett, Yoshihiro Osamura, Nigel J. Mason, and Ralf I. Kaiser, *et al.* (2005). "Mechanistical studies on the formation of the amino acid glycine in extraterrestrial ices." (Astrophysical Journal)

Philip D. Holtom, Chris J. Bennett, Yoshihiro Osamura, Nigel J. Mason, and Ralf I. Kaiser. (2005). "Untangling the formation of the OCN^- radical in interstellar ice mixtures" (?)